EPRI-NASA Cooperative Project on
Stress Corrosion Cracking of Zircaloys

NP-717
Research Project 455-1

Final Report, March 1978

Prepared by

950 5365

SRI INTERNATIONAL
333 Ravenswood Avenue
Menlo Park, California 94025

Principal Investigators
D. Cubicciotti
R. L. Jones

Prepared for

Electric Power Research Institute
3412 Hillview Avenue
Palo Alto, California 94304

EPRI Project Managers
J. T. A. Roberts
H. Ocken
Nuclear Power Division

EPRI-NASA Cooperative Project on Stress Corrosion Cracking of Zircaloys

MASTER

ELECTRIC POWER RESEARCH INSTITUTE

ABSTRACT

This report presents the results of EPRI RP 455, a 30-month program of research aimed at developing improved understanding of the stress corrosion cracking (SCC) mechanism considered responsible for pellet-cladding interaction (PCI) nuclear fuel failures. PCI failures originate at the fuel side of the Zircaloy cladding, and therefore, the major objective of EPRI Project 455 was to define the SCC mechanism of Zircaloy in environments relevant to those at the inside surface of operating fuel cladding. The work was conducted in complementary programs at SRI International, NASA-Ames Research Center, and, under subcontract, Argonne National Laboratory and Massachusetts Institute of Technology.

The results of examinations of the inside surfaces of irradiated fuel cladding from two power reactors showed that Zircaloy cladding can be exposed during service to a number of potentially aggressive substances. Zircaloy samples were screened at reactor operating temperatures for susceptibility to SCC induced by such substances. The most aggressive were iodine, cadmium, and iron-contaminated cesium. Detailed studies were made of iodine-induced SCC of well-characterized samples of Zircaloy sheet and tubing. The results of experiments on pressurized, cladding-grade tubes indicated that a threshold stress must be exceeded for iodine SCC to occur. The threshold stress was sensitive to the microstructure of the Zircaloy and probably to in-reactor irradiation, but was not affected by the presence of an oxide film or by iodine concentration within the range studied. The existence of a threshold stress indicates that crack formation probably is the key step in iodine SCC. A detailed investigation of the crack formation process showed that the cracks responsible for SCC failure nucleated at locations in the metal surface that contained higher than average concentrations of alloying elements and impurities.

A four-stage model of iodine SCC is proposed based on the experimental results and the relevance of the observations to FCI failures is discussed.

FOREWORD

The main source of limitations on plant capacity factor attributed to fuel is designated "pellet-clad interaction" (PCI). While failure rates have been kept to modest levels, this has been achieved largely by the utilities adhering rigidly to vendor "recommendations" on permissible rates of overall and local changes in power levels. These limitations, while workable, are expensive in terms of plant output lost during slow increase in power. For example, for some BWR's up to 6% availability is lost per year.

Observations of PCI-induced failures have strongly supported the belief that fission products generated in the fuel contribute to crack initiation and growth in the fuel rod cladding, thus implicating stress corrosion cracking (SCC) as a failure mechanism. It appears that the release of fission product species (most likely iodine or cadmium) and an applied stress combine to produce failures associated with power-ramps. The quantitative relative contributions of chemistry and stress remain to be resolved.

RP 455 was initiated with SRI International and the NASA-Ames Research Center to investigate the mechanisms of Zircaloy SCC in environments simulating those at the inside surface of operating fuel cladding. Argonne National Laboratory and the Massachusetts Institute of Technology served as subcontractors for specific measurements and analyses.

Examination of the inner diameter surfaces of cladding (from two commercial power reactors) showed that the Zircaloy cladding may be exposed to a number of mobile fission product species. Laboratory testing suggested that the most aggressive of these are iodine, cadmium and iron-contaminated cesium. Detailed studies of SCC

BLANK PAGE

crack initiation and crack propagation were made on Zircaloy sheet and tubing in iodine environments. Cracks initiate at sites in the Zircaloy substrate which contain a high local concentration of alloying elements or at impurities that likely have been introduced during tube processing. A threshold stress (well below the yield stress of irradiated cladding) must be exceeded for SCC to occur in the presence of iodine. The data suggest that the threshold stress is the minimum stress value required to nucleate cracks at the sites noted above. A model of SCC was proposed based on the experimental data. The results of this study support the prospects of remedies based on the following objectives: (a) in the midterm, improving the cladding inner surface quality, and reducing fission product release from the fuel pellet through changes in pellet composition or structure: and (b) in the long term, developing a fuel design that incorporates a barrier between the fuel and cladding. Some combinations of these remedies are expected to permit specifying and producing fuel rods capable of reaching present lifetime targets without maneuvering restrictions, and longer lifetimes probably with some restrictions.

J.T.A. Roberts

H. Ocken

EPRI RP 455 Project Managers

ACKNOWLEDGMENTS

The research reported below represents a truly cooperative effort by a large number of people from several organizations. Although it is not possible to acknowledge in detail the part played by every individual, the authors sincerely thank the people listed below, each of whom contributed in some substantive way to the planning, performance, or interpretation of the work.

F. W. Yaggee

R. V. Strain

R. F. Mattas

S. Greenberg

C. E. Johnson

Massachusetts Institute of Technology:

   S. Namba (Visiting Scientist from Osaka Prefecture, Osaka, Japan)

Stanford University:

   L. E. Eiselstein

   A. K. Miller

   C. Schmidt

Failure Analysis Associates:

   E. Smith (Consultant from UMIST, Manchester, England)

CONTENTS

LIST OF FIGURES

LIST OF TABLES

BLANK PAGE

UNITS

In this report the International System of units (SI units) is used. The conversion factors from other systems of units are available in most handbooks and in the publication "The International System of Units" by E. A. Mechtly (NASA-SP-7012).

For certain units frequently used in this report, the conversion factors are listed below for convenience.

Stress or Pressure

$$\text{ksi} = 0.145 \times \text{MPa}\,(\text{MN}/\text{m}^2)$$
$$\text{torr} = 7.5 \times 10^{-3} \times \text{Pa}\,(\text{N}/\text{m}^2)$$

Stress Intensity

$$\text{ksi}\,\sqrt{\text{inch}} = 0.91 \times \text{MPa} \cdot \text{m}^{1/2}\,(\text{MN}/\text{m}^{3/2})$$

Temperature

$$^{\circ}\text{C} + 273.2 = \text{K}$$
$$(5/9)\,(^{\circ}\text{F} + 459.7) = \text{K}$$
$$590\ \text{K} = 317\,^{\circ}\text{C} = 602\,^{\circ}\text{F}$$
$$630\ \text{K} = 357\,^{\circ}\text{C} = 674\,^{\circ}\text{F}$$

Section 1

INTRODUCTION AND SUMMARY

BACKGROUND

When a Zircaloy-clad uranium dioxide (UO_2) fuel rod that has been irradiated in a light water nuclear power reactor to a significant fraction of its rated life is subjected to a power increase, failure of the cladding sometimes occurs. It is now generally agreed that this type of fuel failure, which is termed pellet-cladding interaction (PCI) failure, is due to stress corrosion cracking (SCC) of the cladding. Cracking originates at the inside surface of the cladding and is thought to result from tensile stresses imposed on the cladding by fuel thermal expansion during the power ramp combined with chemical attack by fission products and impurities released from the UO_2 fuel.

The incidence of PCI failures can be kept acceptably low by using the very slow rates of local and overall power change recommended by nuclear fuel vendors. However, this solution is expensive because of the substantial costs associated with the operation of the plant at partial capacity throughout the long periods while the power is being slowly increased. Thus, there is an important need to understand and improve the SCC behavior of Zircaloy cladding so that increased operational flexibility and reduced costs can be achieved while maintaining the frequency of fuel failure at an acceptably low level. The research program described in this report was intended to meet that need.

EPRI Project RP 455, the EPRI-NASA Cooperative Project on Stress Corrosion Cracking of Zircaloys, was initiated on 1 May 1975 with the overall objectives of

- Investigating correlations between clad surface inhomogeneities and preferred sites of oxide film penetration

- Establishing the mechanisms of stress corrosion crack initiation and propagation in reactor-relevant environments.

- Developing a mechanistic model of SCC that could be used in fuel performance codes to predict in-reactor failure thresholds.
- Identifying possible remedies for SCC.

In pursuit of these objectives, complementary research programs were undertaken at SRI International (SRI), NASA-Ames Research Center (NASA-Ames) and, under sub-contract, Argonne National Laboratory (ANL) and Massachusetts Institute of Technology (MIT).

The results of these research programs and our interpretation of them are presented in detail in this report. The remainder of this section summarizes the major findings. To allow easy cross correlation with the detailed descriptions given later in the report, the summary is divided into subsections that correspond to the major report sections.

SUMMARY OF RESULTS

Characterization of Deposits on the Inside Surfaces of LWR
Fuel Cladding (Section 2)

This study was undertaken to generate information on the nature of the chemical environment to which the inside surfaces of LWR fuel cladding are exposed during reactor service.

Scanning electron microscope examinations were made in the ANL hot cells of the deposits on the inside surfaces of power reactor cladding from two sources. One lot of cladding was from some fuel rods that had failed by PCI (Maine Yankee), whereas the second lot of cladding (H.B. Robinson) was from unfailed rods.

The predominant types of deposits found on the inside surfaces of Maine Yankee cladding were:

- Sharply defined stripes that were formed opposite cracks in the fuel. The stripes consisted of a band of particles of various sizes and compositions, presumed to represent such compounds as Cs_2UO_4 (or similar Cs-U-O compounds), Cs_2O, CsI, Cs_2Te and mixtures of them, as well as particles containing manufacturing impurities. On either side of the central band was a parallel band of tiny nodules ($\sim$ 1-2 μm) that were intimately attached to the surface and contained Cs, U, and Te.

- Heavy deposits of a ceramic-like material that contained mainly U and Cs (and presumably oxygen) and were located opposite pellet-pellet interfaces.

- Occasional circular mound deposits that appeared to consist of the same ceramic material as the pellet-pellet interface deposits.

- Pieces of fuel bonded to the cladding by the same Cs-U ceramic material.

The likely mechanism of transport of fission products from the fuel to the Maine Yankee cladding was through the vapor. The volatilities of the fission product compounds were estimated on the basis of the compounds expected to be present in light of the oxygen potential calculated for the system. The substances observed on the cladding were in accord with those volatilities.

The H.B. Robinson cladding was relatively clean and free of fission products although traces of cesium were occasionally observed. The only noteworthy features were regions of greater oxidation of the cladding, which apparently occurred where UO_2 was in contact with the cladding either as small particles or where fuel pellets touched it.

These examinations and associated chemical modeling studies showed that there are several chemical substances present or likely to be present in significant amounts in the service environment experienced by fuel cladding which are potentially embrittling to Zircaloy. For example, a simple calculation of the amount of iodine that might be released if the fuel temperature attained high enough values after a burnup of about 10,000 MWd/MTU showed that local concentrations could reach values as much as ten times the minimum required to induce SCC in laboratory tests.

It was not possible to identify a single substance as the active agent in PCI failures. Candidates considered likely were iodine (released from CsI by radiolysis), cadmium and possibly iron (in liquid cesium). Iodine was chosen to be the active agent in most of the laboratory studies of SCC discussed below because its aggressiveness was more reproducible than that of the other substances.

Characterization of Experimental Materials (Section 3)

SRI International was responsible for procurement, distribution, and characterization of the Zircaloy sheet, plate, and tubing needed for the experimental phases of both EPRI Projects RP 455 and 456.[*] Three types of nuclear grade Zircaloy tubing with dimensions and characteristics typical of BWR and PWR fuel cladding were obtained from Sandvik Special Metals Corp.[+] Thirty-five lots of Zircaloy sheet and plate were fabricated by Teledyne Wah Chang Albany Corp., using a range of schedules intended to produce controlled variations in key metallurgical characteristics, such as microstructure and crystallographic texture. The chemical compositions of all the tube, sheet, and plate materials were in accordance with ASTM B353-77.

Twenty-eight of the sheet, plate, and tubing products were screened to determine their optical microstructures, hardnesses, and basal pole figures. As anticipated, the microstructures of the thicker products generally were coarser than those of the thinner products and the thinner products generally were harder. The basal pole figures of the tubing materials showed the familiar $\pm30°$ texture. The reduction schedule intended to reproduce this texture in sheet and plate was successful as was the schedule designed to generate a high basal pole density in the sheet normal direction. However, the schedule that was intended to generate a high basal pole density in the long transverse direction was found to be unsuccessful. Through-thickness texture variations could be detected in all products but were particularly noticeable in the thickest plate materials.

Additional characterization studies on the tubing materials included

- Biaxial tensile tests at ~ 600 K that indicated yield stresses ranging from 210 to 490 MPa and burst stresses from 370 to 550 MPa, dependent primarily on alloy heat treatment.

---

[*]Zircaloy Inelastic Deformation Project, with General Electric (NP 500), Stanford University (NP 507) and MIT.
[+]The tubing was from the special lots procured by EPRI for RP 251, 249, 355, and 507, and also used by NRC-RSR in its Zircaloy Program.

- Measurements of hoop residual stresses at room temperature that indicated predominantly compressive residual stresses in the inner part of the tube wall and resulted in peak residual stress estimates of ~ 100 MPa in all three tubing materials.

- Profilometry measurements and SEM examinations of the topography of the tubing surfaces that indicated roughnesses in accordance with the manufacturer's specifications and revealed the presence of considerable numbers of large second-phase particles and inclusions in and near the inside surface which proved to be important in the crack formation stage of iodine SCC (see below).

Crack Formation in Zircaloys Exposed to Iodine (Section 4)

The processes involved in the formation of cracks in Zircaloy samples stressed in iodine at reactor fuel cladding operating temperatures were studied using a new technique. A spherical indenter was used to produce a small, well-defined area of tensile strain in a sample surface exposed to iodine. The sample surface was cleaned by argon ion milling and the topography and chemical composition of the small strained area were characterized by scanning electron microscopy.

Preliminary experiments were conducted on stress-relieved Zircaloy-4 sheet samples. Subsequently, more detailed investigations were conducted on samples of stress-relieved Zircaloy-4 and Zircaloy-2 tubing and annealed Zircaloy tubing at 630 K and 590 K, which are typical cladding temperatures during reactor operation. In the absence of iodine, cracking was observed only under the most severe mechanical conditions and was probably attributable to creep-rupture failure. When iodine was present, cracks were formed under much milder mechanical conditions but not in the complete absence of strain. Therefore, we attributed the cracks formed in the presence of iodine to SCC.

Two distinctly different types of iodine-induced cracks were observed in all four materials tested. One type, classified as small cracks, was observed in all samples strained in iodine, and in occasional samples relatively large cracks were also observed. The small cracks generally seemed to form at microstructural inhomogeneities (such as certain grain boundaries in recrystallized material) that would be expected to be associated with large local stress concentrations in a material undergoing plastic flow. These cracking sites were not associated with any

detectable chemical inhomogeneities in the metal. The frequency of occurrence of the small cracks increased with increasing iodine pressure but was not very dependent on strain (indenter load) or time under load. We did not find either an iodine pressure or a plastic strain below which cracks did not form. The lowest imposed values of these variables in the present tests were 0.03 Pa I_2 and $\sim 1\%$ strain. In experiments with pressurized tubes we found similar small cracks at stresses well below the threshold stress for iodine-induced failure. Therefore, it appears likely that these cracks do not propagate.

The larger cracks were observed in about 30% of the samples and differed from the small cracks in that they were consistently associated with local concentrations of impurities or alloying elements. We presume that the erratic appearance of these larger cracks was related to the probability of there being a site containing a susceptible chemical inhomogeneity within a randomly located ~ 1 mm^2 area of sample surface (i.e., the area of the strained region produced by the randomly positioned indenter). Because of their relatively infrequent appearance, we were unable to determine whether any of the experimental variables affected the frequency or size of the larger cracks. In experiments with pressurized tubes, the larger cracks appeared only at stresses above the threshold stress for iodine-induced failure. Therefore, it appears likely that propagation of this type of crack leads to iodine SCC failure.

In preoxidized specimens, metal cracks always were associated with oxide cracks, which suggests that mechanical fracture of the oxide is a necessary precursor to the formation of a crack in the metal. However, iodine seemed to be able to penetrate very thin oxide films in the absence of any applied stress.

Mechanical cracking of oxide films at ~ 600 K was briefly studied. Oxide cracking was detectable at a tensile strain of ~ 0.4 percent and the number of cracks in the oxide increased systematically at higher strains. The frequency of cracks depended on oxide thickness--oxides around 2 μm thick were cracked more severely than either thicker or thinner oxides.

The results of this study of iodine-induced crack formation indicate that local concentration of alloying elements and impurities in the metal surface play a key role in the crack formation process. Although the origin of these local chemical inhomogeneities is not certain, it seems possible that they are formed in tubing as a result of surface contamination picked up during tube reduction.

Iodine-Induced Failure of Internally Pressurized Zircaloy Tubes (Section 5)

Tube pressurization experiments were conducted on three types of unirradiated, nuclear cladding grade Zircaloy tubing and one type of irradiated Zircaloy fuel cladding in inert and iodine-containing environments at ~ 600 K. The objective of these tests was to learn more about the threshold conditions required for iodine SCC failure of thin-walled Zircaloy tubes.

The results of tests on preflawed and unflawed specimens of unirradiated stress-relieved Zircaloy-4 exposed to iodine at 630 ± 5 K (a typical PWR cladding service temperature) indicated that hoop stress was a more useful parameter than either stress intensity or diametral (hoop) strain for predicting iodine-induced failure. The data supported a relationship between hoop stress and failure time that strongly suggested a threshold hoop stress for iodine SCC at about 300 MPa. At stresses just above this threshold, iodine-induced failures occurred in much shorter times and at much smaller strains than creep-rupture failures. The iodine SCC and creep rupture failure times and failure strains converged at higher stresses and became similar at stresses close to the burst stress.

The behavior of unirradiated stress-relieved Zircaloy-2 specimens pressurized in the presence of iodine at 590 ± 5 K (a typical BWR cladding service temperature) was qualitatively similar to that of the stress-relieved Zircaloy-4 specimens at ~ 630 K. The threshold stress for iodine SCC of the stress-relieved Zircaloy-2 was ~ 330 MPa and the failure times at stresses above threshold were somewhat longer than for the stress-relieved Zircaloy-4, perhaps because of the different test temperatures. The tests on unirradiated stress-relieved Zircaloy-2 also indicated that decreasing the iodine concentration from ~ 6.0 to ~ 0.06 mg I_2 per cm^2 of Zircaloy surface tended to increase the failure time but did not significantly increase the SCC threshold stress.

Annealed (recrystallized) unirradiated Zircaloy-2 specimens showed a threshold stress for iodine SCC of about 280 MPa in tests at 590 ± 5 K. The threshold stress was not affected by a preoxidation treatment that formed a 1.5-μm thick oxide film. The annealed Zircaloy-2 was found to be susceptible to iodine SCC only within a narrow range of stresses just above the threshold. At higher stresses, ductile failures were observed in specimens stressed in the presence of iodine, and it was concluded that crack blunting due to plastic flow suppressed iodine SCC at strain rates above about 3×10^{-5} sec^{-1}. Some of the specimens tested in the susceptible range of stresses failed in periods of only a few minutes. Because the annealed Zircaloy-2 exhibited both a smaller threshold stress and shorter failure times, it was considered more susceptible than the stress-relieved Zircaloy-2 to iodine SCC in tube pressurization tests at ~ 590 K.

The results of a limited number of tests on specimens of irradiated Zircaloy-4 fuel cladding were qualitatively consistent with the trends in behavior exhibited by the unirradiated, stress-relieved Zircaloy-4 specimens. The threshold stress for the irradiated cladding at 630 ± 5 K appeared to be about 200 MPa-- ~ 30 percent less than the threshold stress for the unirradiated Zircaloy-4 and a much smaller fraction of the yield stress. In addition, the failure times for the irradiated specimens seemed to be shorter. Tests on preflawed specimens of the irradiated Zircaloy-4 suggested that K_{Iscc} for iodine SCC of irradiated Zircaloy at reactor operating temperatures was not dramatically smaller than the values of 9 to 10 MPa$\cdot$m$^{1/2}$ that have been obtained for unirradiated Zircaloy.

Although the results suggested that irradiation significantly increased the susceptibility of Zircaloy-4 to failure by iodine SCC, proof of the deleterious effect of in-reactor service and a proper assessment of the severity of any such effect must await the results of additional experiments on irradiated and unirradiated specimens from the same tubing lot. Such experiments are being undertaken by ANL as part of an ongoing EPRI project (RP 1027, "Characterization of Irradiated Zircaloys").

Fractographic observations generally were indicative of a transgranular mode of SCC crack growth in both irradiated and unirradiated materials, although some

features suggestive of intergranular growth were observed in unirradiated annealed Zircaloy-2 specimens. Corrosive attack of Zircaloy by the test environment was apparent on the fracture surfaces, and the inside surfaces of the specimens were pitted. The stress corrosion cracks in specimens tested close to the threshold stress showed little indication of branching, but highly branched cracks were observed in specimens tested at stresses well above the threshold stress.

The results of these pressurization tests on thin-walled Zircaloy tube specimens generally seemed more consistent with the concept that the threshold stress is an intrinsic property of the material/environment system related to the formation of an SCC crack than with the alternative idea that the threshold stress is the minimum stress that is capable of maintaining a critical rate of plastic strain.

SCC Screening Tests in Several Environments (Section 6)

The SCC susceptibility of stress-relieved Zircaloy-4 was screened in a number of environments using different test methods. Most of the screening tests were performed at NASA-Ames Research Center using sheet and plate specimens but the aggressiveness of cesium and, to a lesser extent, cadmium was also investigated at SRI in tests on tubing specimens.

The gases H_2, I_2, Br_2, and Cl_2 and the liquid metals Cs and Cd were shown to be capable of promoting subcritical crack growth in stress-relieved Zircaloy-4 at fuel cladding service temperatures. Further, evidence was found that I_2, Br_2, and Se are all capable of severely corroding Zircaloy-4 at reactor operating temperatures in the absence of stress. The metals Se, Sn, Te, Sb, and Ag did not cause crack extension in statically loaded specimens. It was difficult to compare the aggressiveness of the substances that caused subcritical crack growth because the differeing natures of the cracking processes and the differing characteristics of the various substances necessitated the use of different test methods.

The halogens were the only substances that caused crack extension in statically loaded specimens at ∼ 630 K. They seemed to be similar to each other in their aggressiveness toward Zircaloy and their presence resulted in very similar

fracture surfaces that exhibited a mixture of cleavage and ductile rupture. The threshold stress intensities (K_{Iscc}) for the halogens were estimated to be about 9 MPa·m$^{1/2}$ at ~ 630 K, and iodine-induced cracking proved to be essentially immune to the presence of oxygen.

In contrast, cadmium and cesium were aggressive toward Zircaloy at cladding service temperatures only when steps were taken to reduce the oxygen contents of the test environments to very small values. Furthermore, cesium and cadmium embrittled Zircaloy only in rising stress tests and cesium had to be contaminated with a trace of iron before embrittlement was observed. K_{Iscc} for cadmium cracking at 633 K was estimated to be about 20 MPa·m$^{1/2}$, but this value was believed to be an over-estimate. In tests on smooth specimens, cadmium and iron-contaminated cesium generally caused embrittlement at stresses just above the yield stress, although on two occasions much smaller failure stresses were observed in the iron-contaminated cesium environment.

Gaseous hydrogen proved to be much more aggressive toward Zircaloy at ambient temperature than at cladding operating temperatures. Hydrogen was capable of promoting subcritical crack growth in statically loaded specimens at room temperature, but an alternating stress was required to obtain crack extension at ~ 570 K.

Because the halogens promoted slow crack growth in statically loaded specimens and seemed to be insensitive to the presence of contaminants, the results of the screening tests could be interpreted as indicating that the halogens are more aggressive towards Zircaloy-4 than the other elements that were screened. However, in rising load tests both Cd and Fe-contaminated Cs caused embrittlement under conditions where I_2 was not aggressive.

Discussion and Conclusions, (Section 7)

A model of iodine SCC of thin-walled Zircaloy tubes was developed based on the experimental results. The model consists of four steps, namely oxide penetration, crack formation, crack propagation, and cladding rupture.

Iodine is capable of penetrating very thin oxide films in the absence of an applied stress but a strain threshold of a few tenths of one percent must be exceeded to mechanically fracture the oxide before iodine can penetrate films with thicknesses in the micrometer range. The number of oxide cracks increases systematically at higher strains and depends somewhat on oxide thickness. Because the threshold stress for iodine SCC of annealed Zircaloy in tube pressurization experiments is well above the stress required to fracture the oxide, oxide penetration is not believed to be the key step in iodine SCC.

Crack formation in the metal surface occurs beneath cracks in the oxide if the applied stress exceeds a threshold value. Crack formation, which we regard as the critical step in the overall iodine SCC process, occurs at spots in the metal surface where there are locally high concentrations of alloying elements and impurities. The exact mechanism of crack formation is uncertain, but rapid chemical reaction to form brittle mixed metal iodides may be involved. The threshold stress for crack formation depends on microstructure and probably also on irradiation, but is insensitive to iodine concentration in the range 6 to 0.06 mg/cm^2 Zircaloy surface.

As the crack nuclei grow, the stress required for their continued propagation falls. Initially, the applied stress must be large enough to maintain the net section stress above the crack formation threshold stress, but when the cracks are deeper than 100 to 200 μm, conditions at the crack tip become dominant and continued propagation at lower net section stresses becomes possible. In stress-relieved materials, propagation occurs by transgranular cleavage and ductile tearing, whereas recrystallized materials sometimes exhibit intergranular propagation. The cracks propagate on a surface perpendicular to the hoop stress and become more branched at larger stresses. The crack growth rate depends on stress and microstructure and probably also on irradiation, temperature and iodine concentration. The role of iodine in crack propagation is uncertain. It seems most probable that the presence of iodine at the crack tip leads to a reduction in the strength of metal-metal bonds.

Crack propagation continues until the stress state in the uncracked ligament exceeds an instability criterion. Shear failure then occurs on a surface inclined at about

45° to the hoop stress. At applied stresses near the burst stress, instability occurs when the net section stress exceeds the burst stress. At smaller applied stresses, the net section stress at instability approaches three times the yield stress.

The most important observations with respect to PCI failure are as follows:

- Significant quantities of several potentially aggressive substances can reach the surface of fuel cladding under normal design conditions.

- Iodine stress corrosion cracks form at specific sites in the metal surface.

- A stress threshold exists for iodine SCC below which Zircaloy tubing is immune to failure.

The significance of each of these observations with regard to possible remedial measures for PCI failure is discussed and it is concluded that several of the PCI remedies now under development have potential for significantly reducing the incidence of PCI failures of LWR fuel cladding.

Section 2

CHARACTERIZATION OF DEPOSITS ON THE INSIDE
SURFACES OF LWR FUEL CLADDING

INTRODUCTION

It is generally agreed that PCI fuel cladding failures originate at the inside surface of the cladding and are a result of the combined action of mechanical stress and a chemically aggressive environment. However, it has not yet been possible to identify the specific chemical substances that play the active role in the cladding failure process, at least partly because the nature of the environment to which the inside surface of the cladding is exposed during reactor service is poorly understood. The present study of the inside surface of cladding after reactor irradiation was undertaken to help elucidate that environment and identify possible PCI agents.

Examinations were made of the deposits on the inside surfaces of power reactor cladding from two sources. One lot of cladding was from a fuel assembly in Maine Yankee Core I that had suffered PCI cladding failures. The other lot of cladding was from a fuel assembly in H.B. Robinson which had operated at low average power levels and had shown no evidence of PCI failures. The examinations were made in the hot cells at Argonne National Laboratory; the observations and our interpretation of them are summarized below. A more detailed account was presented in a previous EPRI document (2-1) and some of the major findings have been published (2-2).

OBSERVATIONS

Maine Yankee Core I Rods

Some of the unpressurized fuel rods in Maine Yankee Core I exhibited PCI failures. Comprehensive examinations of rods from that core were conducted by Combustion Engineering Inc. for the Electric Power Research Institute and are reported in

Reference 2-3. Pieces of cladding from the same batch were provided for the present examination. The rods had been irradiated to about 13 GWd/MTU at linear powers less than 300 W/cm (9 kW/ft). The rods examined (JCN 196 and HBU 169) both showed high (about 15%) fission gas release and peaks of gamma activity from Cs^{137} at positions corresponding to pellet-pellet interfaces. One length of cladding from rod JCN 196 was examined extensively. A piece taken from rod HBU 169 was also examined and similar results were obtained.

The general nature of the deposits on the inside of the cladding can be seen in the optical photograph, Figure 2-1, which shows the inside surface of the cladding after the rod had been slit open and the fuel removed. The deposits were of three types: (a) sharply defined linear stripes, which occurred opposite cracks in the fuel; (b) concentrations of more massive deposits at the locations of pellet-pellet interfaces; and (c) circular, mound-like deposits at random locations. In addition, there were occasional chips of fuel that strongly adhered to the cladding.

Small pieces of cladding were examined in a scanning electron microscope (SEM). The SEM was a Model U1 made by ETEC (Hayward, California) and modified to control alpha as well as beta-gamma radioactivity. The SEM was equipped with an energy dispersive x-ray analyzer (Kevex Corp., Burlingame, California) with a gold collimator, as described by Wolff and Wolf (2-4), which served to reduce the background radiation reaching the detector, thus allowing analyses of samples with greater levels of activity. Samples of cladding as large as 0.5 cm x 0.5 cm could be examined, although occasionally they were too radioactive for the Kevex detector and had to be cut into smaller pieces for elemental analyses.

The Kevex energy dispersive analyzer could analyze the x-ray fluorescence arising from elements heavier than Na. Oxygen could not be analyzed, but it was assumed to be present in all of the surface layers because of their ceramic or crystalline appearance and because of the strong avidity for oxygen of the elements present (Zr, U, Cs). The sensitivity of the instrument was such that 1 to 5% of an element could be detected. The 20 keV electron beam used probably penetrated of the order of 1 μm into the surface being examined; therefore, the analyses of thin surface
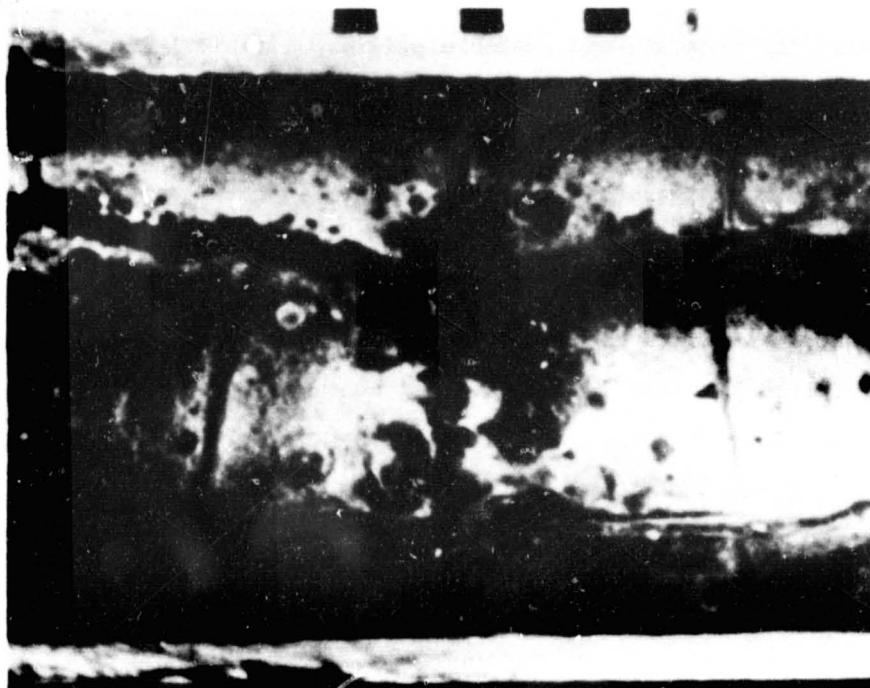
SA-4197-310

FIGURE 2-1 OPTICAL PHOTOGRAPH OF THE INNER SURFACE OF A SECTION OF
CLADDING FROM A MAINE YANKEE CORE I ROD (JCN 196)

Width of photo corresponded to 1.5 cm of cladding length. The vertical
band of deposits occurred at a pellet interface. The thin line deposits were
opposite fuel cracks.

features included some of the substrate material. The shades of gray observed in SEM photos are established by the relative electron emissions from the surfaces and are generally not the same as would be recorded by an optical photograph of the same surface. The rods were sectioned and samples were prepared in hot cells. Caution was exercised to avoid contamination of sample surfaces, but occasional features were observed that were obviously introduced in the hot cell.

The SEM examination was concentrated on the distinctive features seen in Figure 2-1 so as to reveal their nature and probable origin. A typical linear deposit (type a) is shown in greater detail in Figure 2-2. The stripe, which is horizontal in the figure, consists of two parallel gray bands about 0.1 mm apart. Between the two bands there seems to be a concentration of particles of random size and shape.

The areas above and below the band in Figure 2-2 represented the majority of the cladding surface. The dark regions showed only Zr and had a smooth, wavy surface typical of oxidized Zircaloy. The particles contained U and Cs and were apparently particles of UO_2 fuel that had reacted with some Cs.

Figure 2-3 shows the nature of a linear deposit in greater detail. The upper two-thirds of the figure shows the structure of a gray band consisting of tiny nodules ($\sim$ 1 to 2 μm diameter and $\sim$ 1 μm apart) closely attached to the substrate, which was presumably a surface coating of ZrO_2 on the Zircaloy. The nodules contained mainly Zr (partly observed due to penetration of the electron beam through the nodules), and some U, Cs, and Te. The large dark particle near the center of the photo showed only U on analysis and was apparently a chip of UO_2 fuel stuck to the surface. The almost white, angular particles contained U and Cs and were probably a cesium uranate (possibly Cs_2UO_4). The lower one-third of the photo was part of the region separating two bands of nodules. Particles observed in those bands included pieces of UO_2, particles of cesium uranate that were sometimes crystalline and sometimes amorphous, occasional small cubic crystals that were found to be CsI (by comparison of the x-ray fluorescence spectrum with that from a standard CsI crystal), and some amorphous-looking deposits (typical of that near the bottom, center of Figure 2-3) that contained Cs and Te and were presumed to be Cs_2Te. Occasionally small amounts of Fe, Mn, Cu, and Cl were observed in some of the amorphous deposits.
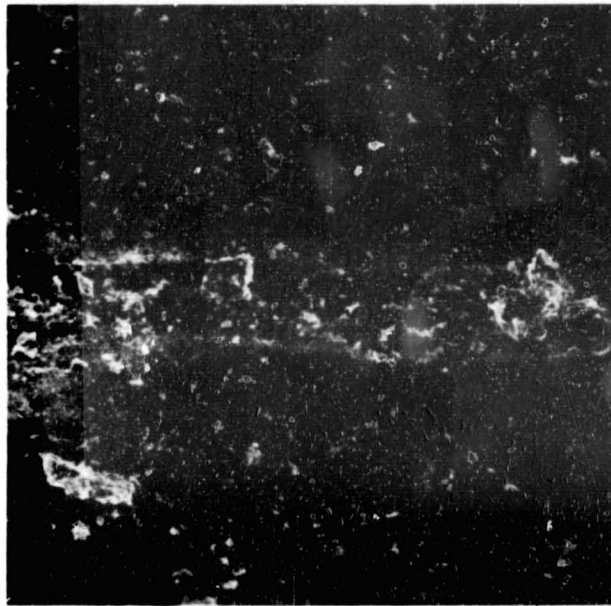
SA-4197-311

FIGURE 2-2   SEM PHOTOGRAPH OF A LINEAR DEPOSIT
Width of photo = 0.5 mm.
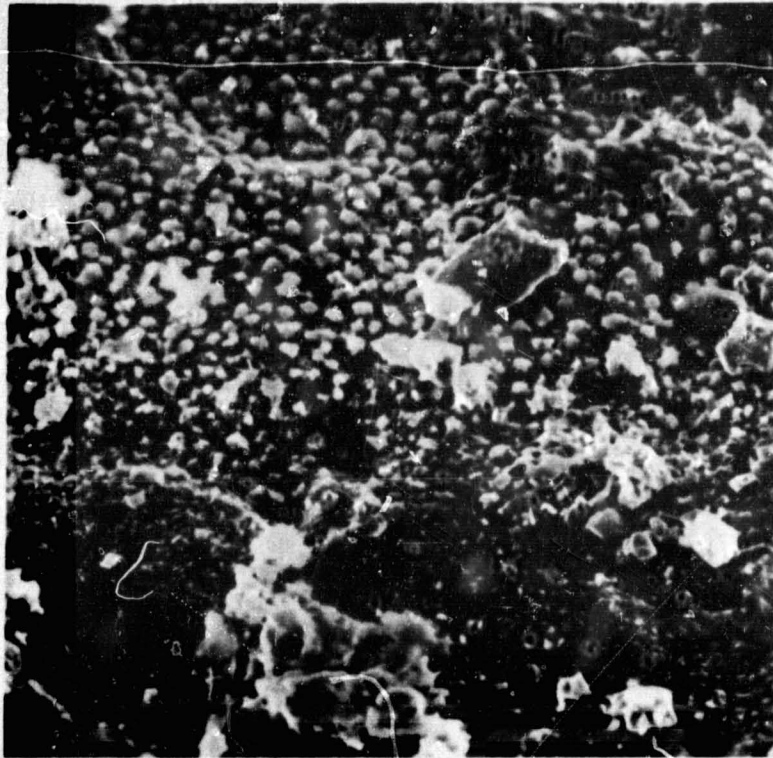
SA-4197-312

FIGURE 2-3   SEM PHOTOGRAPH OF A SECTION OF A LINEAR DEPOSIT
Width of photo = 75 μm.

The deposits found opposite pellet-pellet interfaces (type b) generally contained larger amounts of material and were much more radioactive than the linear deposits found opposite fuel cracks. As noted above, intense peaks of Cs^{137} activity were observed at pellet-pellet interfaces in gamma scans of the cladding. A massive deposit of the type found opposite pellet-pellet interfaces is shown in Figure 2-4 and in greater detail in Figure 2-5. The material looks like a brittle ceramic substance that was molten at some stage and had cracked during solidification. SEM analyses showed only U and Cs in proportions that varied through the thickness of the deposit. The Cs:U ratio was largest in the material adjacent to the cladding and smallest in the material nearest the fuel. A transverse metallographic section of one massive deposit was prepared that showed the deposit to consist of a duplex layer. Electron microprobe analysis of the section showed that the layer nearest the cladding contained uranium and cesium while the layer nearest the fuel contained principally uranium with some cesium and other fission products. The ceramic appearance of the material suggested it was an oxide.

The small circular mound deposit in the lower right corner of Figure 2-4 is shown in greater detail in Figure 2-6. It was representative of the type c deposits observed to occur randomly over the surface. Another example is shown in Figure 2-7. Those mounds were found to consist of essentially the same material as the massive deposits, showing the same brittle fracture and duplex structure, with greater cesium concentrations next to the cladding.

A piece of fuel adhering to the cladding is shown in Figure 2-4. The fuel was distinguishable by its grain size ($\sim 2 \ \mu$m) and structure; analysis showed only U. Fuel chips were apparently cemented to the cladding by some of the Cs-U ceramic material, which was observed at the base of the chip. Near the base of the ceramic material, as well as near the base of the circular mounds, small bands of nodules, similar to those in the stripes, were often observed.

In some regions the small dot-like features shown in Figure 2-8 were observed. Those small dots ($\sim$ hundreds of nanometers in diameter) contained U and Zr only and were quantitatively different from the nodules shown in Figure 2-3 which contained
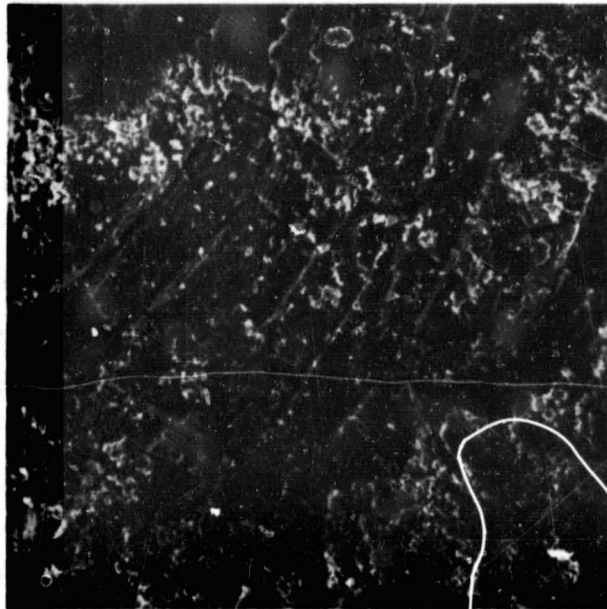
SA-4197-313

FIGURE 2-4   SEM PHOTOGRAPH OF A PELLET INTERFACE DEPOSIT
Width of photo = 5 mm.
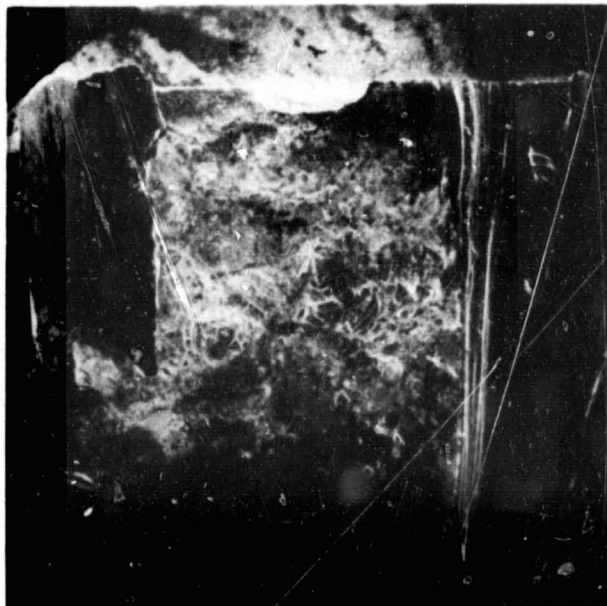
SA-4197-314

FIGURE 2-5   SEM PHOTOGRAPH OF INTERFACE DEPOSIT MATERIAL
Width of photo = 220 μm.
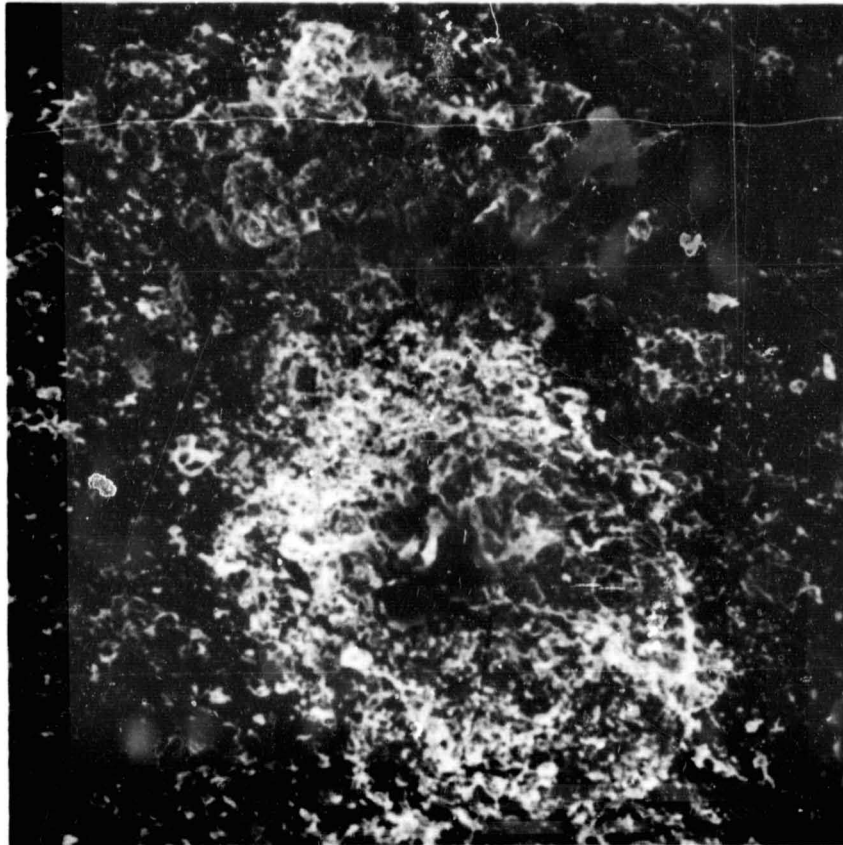
SA-4197-315

FIGURE 2-6   SEM PHOTOGRAPH OF CIRCULAR MOUND DEPOSIT FROM LOWER
RIGHT CORNER OF SAMPLE IN FIGURE 2-4

Width of photo = 270 μm.
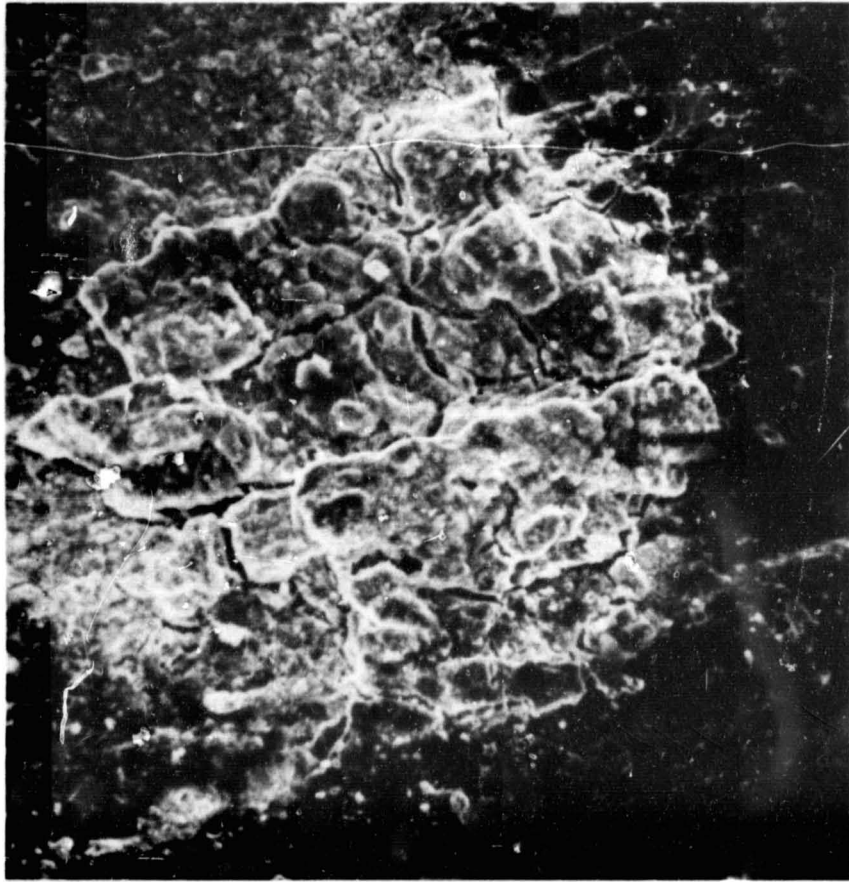
SA-4197-316

FIGURE 2-7   SEM PHOTOGRAPH OF ANOTHER EXAMPLE OF A CIRCULAR
MOUND DEPOSIT
Width of photo = 300 μm.
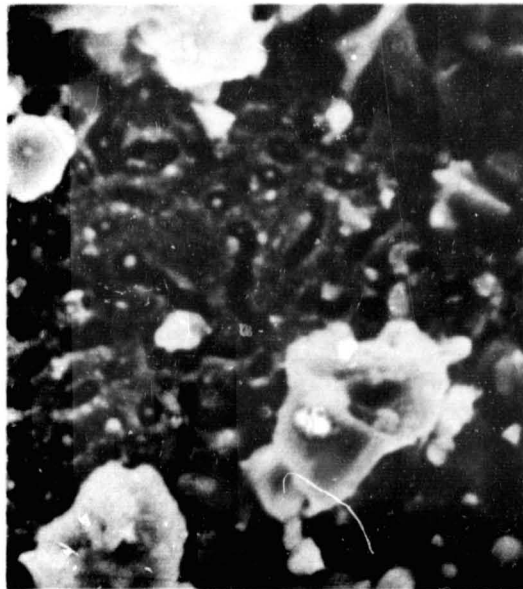
SA-4197-317

FIGURE 2-8   SEM PHOTOGRAPH OF DOT-LIKE PARTICLES
Width of photo = 12 μm.

U, Cs, and Te. The small dots in Figure 2-8 seem to be particles of UO_2 that were reacting with the ZrO_2 surface layer.

H.B. Robinson Rod

Cladding from the H.B. Robinson reactor was studied as part of the NRC-LWR safety program. Two pieces were obtained from a rod designated F-7, which had been irradiated to an average burnup of 28 GWd/MTU at an average power of 230 W/cm (7 kW/ft) (2-5). Axial gamma scans showed no peaks of Cs activity and fission gas release in those rods was small (< 1%).

SEM examination showed that the inner surfaces of the cladding were relatively clean and free of deposits. Figure 2-9 shows the general appearance. The majority of the surface was covered with a dark gray zirconium oxide. There were occasional lighter gray patches of various sizes and shapes, some of which were several millimeters in longest dimension, where apparently fuel pellets or pieces of fuel had pressed against the cladding. Also, the surface was sprinkled with small crystals. None of the prominent features found on the Maine Yankee cladding (stripes opposite fuel cracks, pellet-pellet interface deposits, or circular mounds) were observed on these samples of H.B. Robinson cladding. Also, no fission products were detected in any of the features or particles on the surface except for an occasional trace of cesium. The only elements generally observed were uranium, in the light grey patches and small particles, and of course zirconium. (In one small spot a stain containing iron was noted, which may have been formed after the rod was opened. In another spot a particle presumed to be alumina was found embedded in the surface.)

Figure 2-10 shows one of the gray patches in greater detail. The light gray regions near the lower right and upper left sections of the photo contained mainly U with some Zr. They were apparently areas where fuel had pressed against the cladding, had reacted with it, and then been detached from it, leaving some UO_2 behind. The dark areas with white ridges contained mainly Zr with some U. They were apparently regions of enhanced oxidation of the Zircaloy, possibly due to a higher local temperature where the fuel pressed against the cladding. The upper part of the photo shows the smooth, oxidized Zircaloy surface that is characteristic of the large majority of the cladding surface.
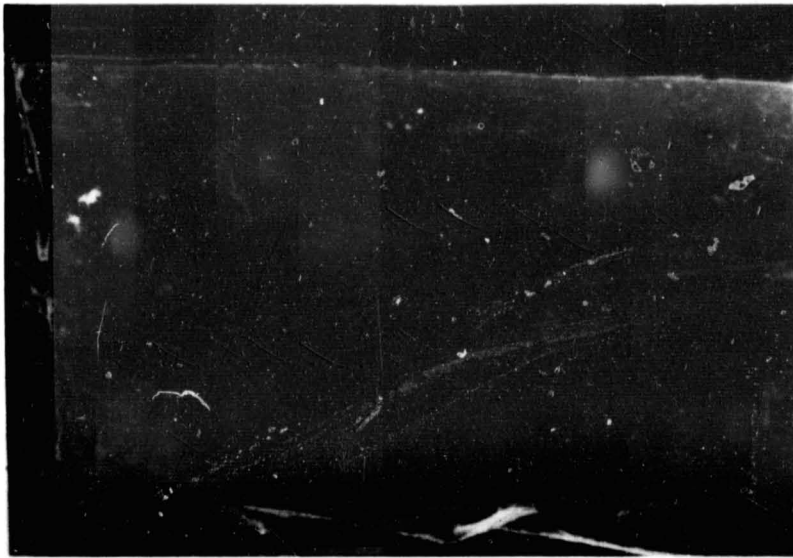
SA-4197-318

FIGURE 2-9   SEM PHOTOGRAPH OF INNER SURFACE OF CLADDING FROM
H.B. ROBINSON ROD

Width of photo = 8 mm.

The type of light gray surface seen just to the lower left center of Figure 2-10 is shown at higher magnification in Figure 2-11. The small, light crystals contained mainly U and were apparently grains of UO_2 fuel. The worm-like material was ZrO_2 containing variable proportions of UO_2. The detailed structure of those worm-like features indicates they were caused by the reaction of UO_2 with ZrO_2. The UO_2 apparently became incorporated into the ZrO_2 which resulted in a faster local oxidation.

The horizontal white line in Figure 2-9 is shown at higher magnification in Figure 2-12. It consisted of the worm-like material containing U as well as Zr. Presumably that structure was originally a scratch on the cladding surface made during fuel rod loading. The scratched area apparently oxidized somewhat more rapidly than the unscratched areas due to the interaction of UO_2 particles with the fresher Zircaloy surface.

The majority of the surface was covered with somewhat undulating, black zirconium oxide, sprinkled with occasional white particles of UO_2. Figure 2-13 shows such a surface, which is interesting because of the cracks in the surface zirconia layer that were associated with intimately attached UO_2 particles. The white particles were rich in uranium and were probably grains of UO_2. Those fused to the surface were apparently in the process of diffusing into the zirconia, and we presume that the diffusion process gradually resulted in the formation of the worm-like material.

Thus, the H.B. Robinson cladding had no significant deposits of fission products. The UO_2 apparently reacted with the cladding in spots where there was good contact. Where pellets or pieces of fuel were pressed against the cladding, some bonding occurred. The bonds generally broke so as to leave some UO_2 on the cladding when the rod was opened; however, occasionally the zirconia surface oxide was pulled away from the cladding metal. When small particles of UO_2 were in intimate contact with the cladding, they apparently could react with its surface oxide, which resulted in an accelerated oxidation.
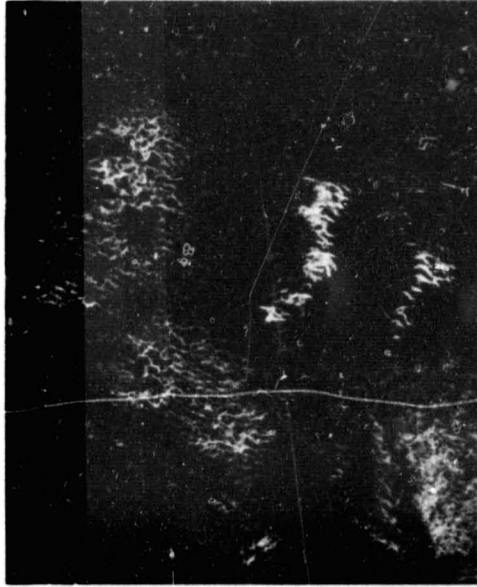
SA-4197-319

FIGURE 2-10   SEM PHOTOGRAPH OF AN AREA
OF FUEL-CLADDING CONTACT

Width of photo = 330 μm.
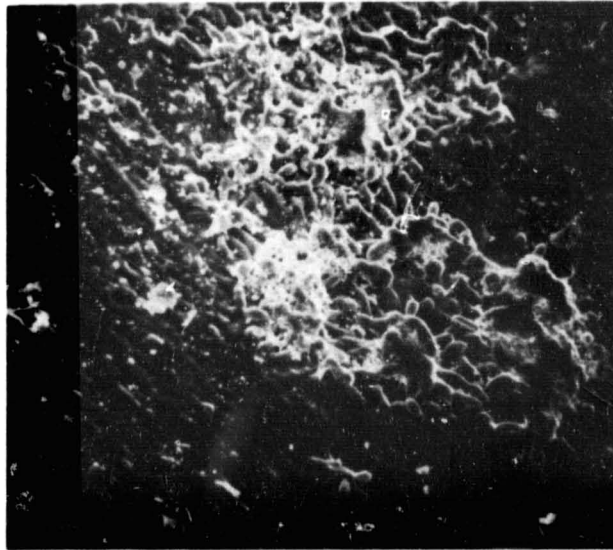
SA-4197-320

FIGURE 2-11   SEM PHOTOGRAPH OF A GRAY PATCH

Width of photo = 180 μm.
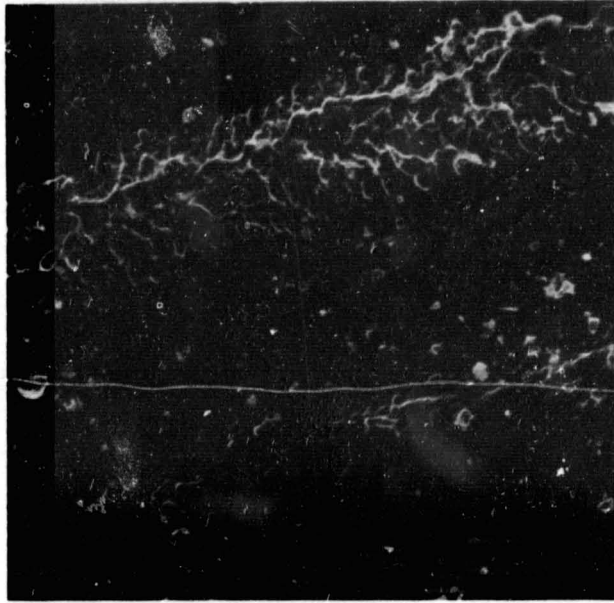
SA-4197-321

FIGURE 2-12   SEM PHOTOGRAPH OF DETAIL OF SCRATCHED REGION
Width of photo = 200 μm.
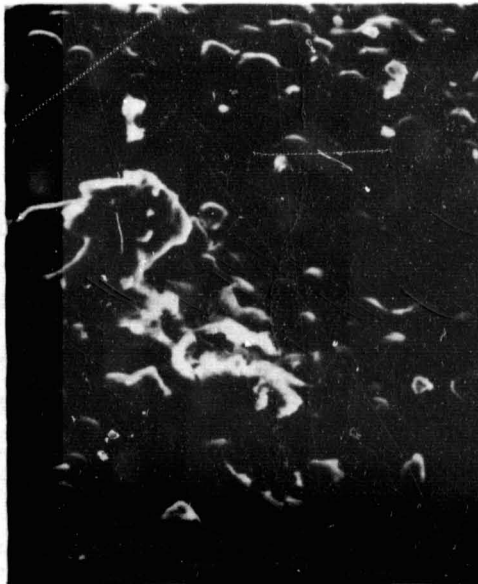
SA-4197-322

FIGURE 2-13   SEM PHOTOGRAPH OF CRACKS IN SURFACE OXIDE
Width of photo = 45 μm.

MECHANISM OF FORMATION OF DEPOSITS

The deposits on Main Yankee cladding appeared to have been formed mainly by vapor transport. That is, the substances deposited were first released from the fuel and transported through the gas to the cladding. The release of volatile fission products occurs during fuel restructuring. There is some evidence that the fractional release of fission products is the same as that of the fission gases (Xe and Kr) (2-6). Accordingly, we shall assume that the release of volatile fission products (and manufacturing impurities) from the UO_2 fuel occurs by mechanisms similar to those of the fission gases so that the fraction of volatile fission products released is the same as that of fission gases. That assumption is supported by the Maine Yankee rods examined (10 to 13% fission gas release and many deposits) compared with the Robinson rod ($<$ 1% gas and very few deposits). Another important factor is the volatility of the fission product, which, in turn, is a function of its chemical state in the system. Thus in our model, fission product release is related to the fraction of fission gas released and the chemical states of the fission products.

The fission gas release fraction for the Maine Yankee rods studied was about 10 to 13%, a relatively large value that was related to the relatively high temperatures reached in the fuel [$\sim$ 1900 K at the center (2-3)]. Thus, fission product compounds with significant vapor pressure at $\sim$ 1900 K would be expected to be released to the same fraction as the permanent gas fission products. Presumably the fraction released from the hotter fuel center was larger than that from the cooler periphery. The volatile compounds would be expected to travel radially from the hotter regions, through open porosity in the fuel, along fuel cracks or pellet interfaces and finally deposit on the cladding, the coolest surface available. There was no evidence (2-3) for axial migration, indicating that once the deposits formed, they were not significantly volatile at cladding temperatures. In particular, Cs^{137} activity was concentrated at pellet interface positions and no significant amount was observed at the lower end of undefected fuel rods in gamma scans made before the rods were opened. This suggests that there were no significant amounts of liquid Cs in the Maine Yankee rods. The released Cs was apparently all combined in solid forms.

Chemical States

The behavior, especially the volatilities, of the fission products will depend on their chemical states in the fuel, which will be governed in turn by the oxygen potential in the system. Fuel pellets initially have a stoichiometry of about $UO_{2.002}$. As the uranium is fissioned, the oxygen becomes partitioned among the fission products, those with greater avidity for oxygen forming oxides and others going into elemental states, on the basis of equilibrium thermodynamics. The free energies of formation of the oxides are shown in Figure 2-14. The ordinate of that figure gives the oxygen potential at which an element will be oxidized. From the inventory of fission products, one can estimate the oxygen potential expected in the system. The method has been applied to fast reactor fuels and is described in Reference 2-10. LWR fuels differ from fast reactor fuels in that the spectrum of fission products for UO_2 includes more oxygen-avid elements and also because the Zircaloy cladding is a strong oxygen getter. The rate of uptake of oxygen by the cladding is determined by the kinetics of formation of oxide films on zirconium, which are parabolic for moderate burnup (2-11). We estimate that at a burnup of 1.5 at.% oxidation of cladding will consume about 0.0015 O/U units of oxygen for a typical fuel rod geometry. (One O/U unit represents one gram atom of oxygen per gram atom of uranium.)

The chemical states* of the fission products and the amounts of oxygen combined by them are shown in Table 2-1. Certain fission products are very oxygen-avid and will certainly be oxidized (Item 2 of Table 2-1). They (plus the oxygen taken by the cladding) consume 0.027 O/U units of oxygen at 1.5% burnup. The total amount of oxygen made available because of U fission is 0.030 O/U units at

---

*The chemical states of the fission products in UO_2 fuel are not well known. A first assessment as to whether an element would be expected to be oxidized or not will be made on the basis of the data in Figure 2-14 (which is an iterative process of estimating the oxygen potential and amounts of fission products oxidized). However, the data of Figure 2-14 refer to the elements and oxides in pure states. When the fission products are incorporated in UO_2 they may have different oxidation states that are formed at somewhat different oxygen potentials (see Reference 2-10). The assumptions used in Table 2-1 provide a first approximation to the calculation..
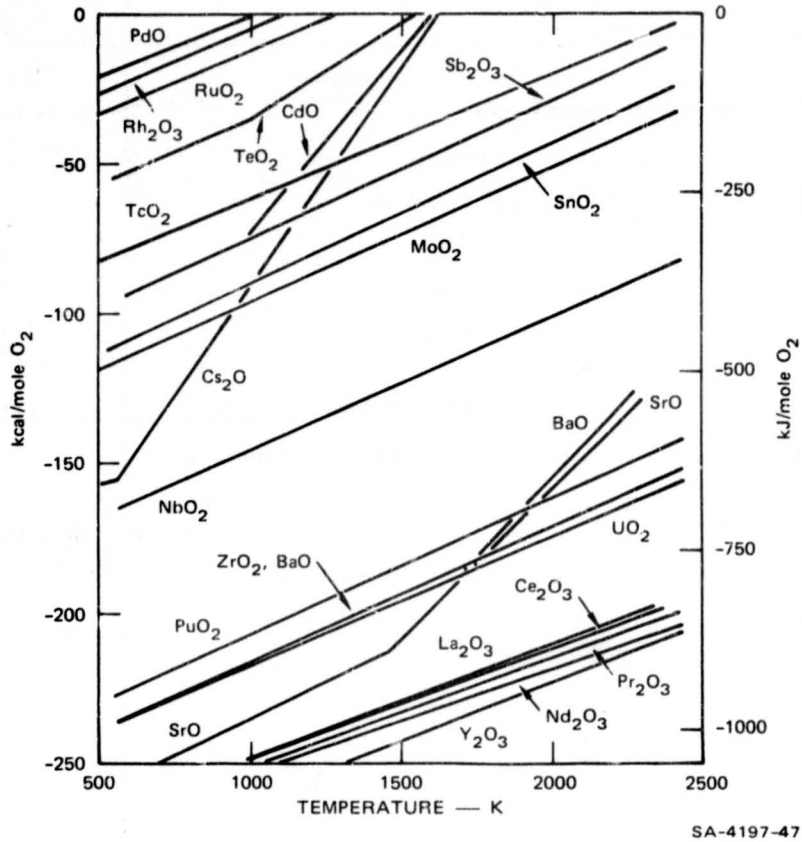
FIGURE 2-14   STANDARD FREE ENERGIES OF FORMATION OF PURE
SOLID METAL OXIDES

Data from References 2-7 and 2-8, except for Cs_2O from
Reference 2-9. (Uncertainties are of the order of 30 kJ.)
The high-temperature branches of the curves for TeO_2,
Cs_2O, BaO, CdO, and SrO represent formation of the solid
oxides from the gaseous elements at one atmosphere.

Table 2-1

OXYGEN INVENTORY CALCULATION

Oxygen Sink			Amount of Oxygen Used (O/U Units)[1] at 1.5 % Burnup
1. Cladding oxidation			0.0015
2. Fission products with very stable oxides (i.e., completely oxidized)			
Oxides	Fission Yield[2]	Oxygen per Metal[3]	
(4) RE_2O_3, Y_2O_3	0.55	1.5	0.0124
BaO, SrO	0.13	1.0	0.0020
ZrO_2	0.37	2.0	0.0111
NbO_2	0.006	2.0	0.0002
Total combined oxygen =			0.0272
3. Fission product oxides of intermediate stability			
Cs + Rb:	0.21		
	−0.013 (amount combined as iodide and bromide)		
	−0.058 (amount combined as Cs_2Te and Cs_2Se)		
Cs_2UO_4	0.14	1.0	0.0021
MoO_2	0.25	2	0.0007
4. Fission products with unstable oxides (i.e., not oxidized)			
Sn, Sb, Cd	0.003		
Tc	0.061		
Ru	0.093		
Rh	0.049		
Pd, Ag	0.016		
Xe, Kr	0.238		

[1] Burnup of 1.5% is equivalent to about 14 GWd/MTU, which provides 0.030 O/U units of oxygen.

[2] Data from Reference 2-12.

[3] This column gives the number of oxygen atoms reacted per fission product metal atom to give the oxide in the first column. Note that in Cs_2UO_4 each U initially has two oxygen atoms and only one O per Cs is needed.

[4] RE represents the rare earth elements.

that burnup. The difference (0.003) is available to be applied to the formation of the next higher oxides (Figure 2-14), which would appear to be Cs_2O at lower temperatures and MoO_2 at higher temperatures. However, the situation is somewhat more complex. Because of the stability of the halides of Cs and Rb, (which will be treated together with Cs), it is assumed that Br and I will react with Cs in preference to oxygen. Also it is assumed that Te and Se will react with Cs in preference to O_2 [as is the case for K compounds (2-8)]. Another complication arises in that Cs can form the relatively stable Cs_2UO_4. Figure 2-15 shows the oxygen potentials for formation of Cs_2UO_4 vapor at 10^{-2} atmospheres.* Also the stoichiometry of the UO_2 is a function of the oxygen potential of the system. Blackburn (2-13) has provided a model for calculating the stoichiometry as a function of oxygen potential. Curves for various UO_2 stoichiometries is as well as the curve for Mo oxidation are given in Figure 2-15. According to Figure 2-15, for temperatures corresponding to the majority of the fuel, Cs should be oxidized at lower oxygen potentials than Mo. Therefore, in the inventory calculation (Table 2-1), after the Cs oxidation 0.0007 units of oxygen remain for Mo oxidation. Since elemental Mo will remain, some of the oxygen of the $UO_{2.002}$ will be used to oxidize Mo and the stoichiometry of the fuel will decrease accordingly. This leads to the conclusion that the oxygen potential of the system is buffered by the Mo/MoO_2 couple. That conclusion is strengthened by the experimental results of Adamson et al. (2-14) who found the oxygen potentials of irradiated LWR fuels to be in the range of -460 to -540 kJ/mol (compare Figure 2-15).

---

*It is assumed that the partial pressure of Cs in the fuel rod at these burnups is about 10^{-2} atm. That assumption is based on the argument that no liquid Cs was present; hence, the pressure must have been less than the vapor pressure of Cs ($\sim 10^{-1.7}$ atm) at cladding temperatures (~ 650 K) and Cs seemed to be vapor transported throughout the rods.
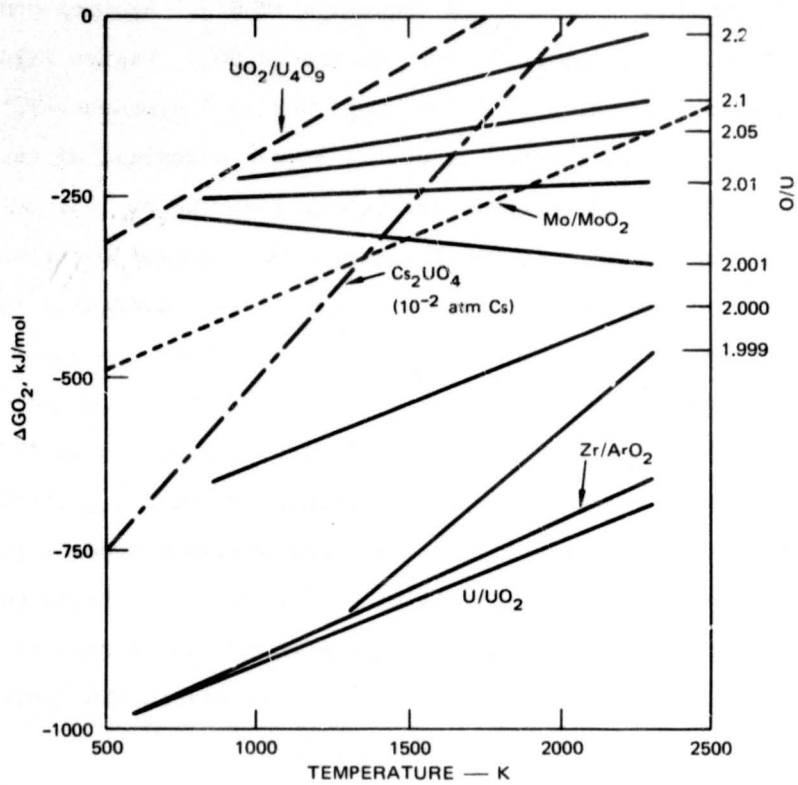
FIGURE 2-15   OXYGEN POTENTIALS FOR UO_{2+x} FROM BLACKBURN/MODEL
(FULL LINES) AND FOR FORMATION OF SOME SOLID OXIDES
AND FOR THE REACTION $2Cs(g) + O_2 + UO_2(s) = Cs_2UO_4(s)$

Data from References 2-7, 2-8, 2-9. (Uncertainties are of the
order of ±50 kJ.)

Volatilities

The fission product compounds, as indicated in Table 2-1, are classified according to their volatilities in Table 2-2. Substances in Classes I and II are sufficiently volatile to be vapor transported from the fuel during normal operation (fuel temperatures $\sim$ 1500 K at the center to $\sim$ 1000 K at the outer surface). Those in Class III might be expected to be transported if the fuel operated at temperatures higher than normal. Substances in Class IV would not be expected to be vapor transported during reactor operation.

As indicated earlier, the release of even the very volatile noble gases (Xe, Kr) does not occur during normal rod operation even to relatively large burnup. That is, the kinetics of release of fission products must be a controlling factor. We will assume that the release of volatile fission products is comparable to that of the fission gases and the fraction released will be the same for all the compounds in Classes I and II.

The volatility and chemical form of Cs need special consideration. No gaseous Cs-U-O compounds were observed in a mass spectrometer study made by Johnson (2-16) of the vaporization of Cs_2UO_4; only gaseous Cs and Cs_2O were found. The thermodynamics of vaporization to those species are given by the following data (2-7, 2-8, 2-9, 2-15, 2-17):

$$Cs_2UO_4(s) = Cs_2O(g) + UO_2(s) + 3/2\ O_2$$

$$\Delta G^\circ = 691400 - 483T\ (J/mol)$$

$$Cs_2UO_4(s) = 2Cs(g) + UO_2(s) + 2O_2$$
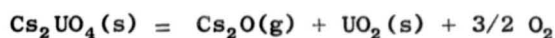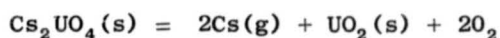
$$\Delta G^\circ = 98900 - 618T\ (J/mol)$$

If we assume that the Cs_2UO_4 was heated to about 2000 K, because of a temperature excursion in the fuel, and that the volatile products (Cs_2O, Cs, O_2) were confined in voids until fuel restructuring released them, very large pressures could build up before the release and the predominant species released would be gaseous Cs_2O. The pressure of atomic Cs expected is less than 1% of the Cs_2O.

Table 2-2

VOLATILITY CLASSIFICATION OF FISSION PRODUCT COMPOUNDS[1]

Compound Classification	Vapor Pressure (Atm)	
	1000K	2000 K
I Very volatile (permanent gases)		
Xe, Kr		
II Moderately volatile		
CsI, RbI, CsBr, RbBr	10^{-3}	1
Cs_2Te, Cs_2Se[2]	10^{-3}	1
Cd	0.5	$\gg 1$
Sb	10^{-3}	1
Ag	10^{-8}	0.1
(Cs pressure over Cs_2UO_4)[3]	10^{-3}	$\gg 1$
III Moderately nonvolatile		
Sn	$\sim 10^{-10}$	$10^{-3.3}$
Pd	$\sim 10^{-10}$	10^{-3}
BaO	$\sim 10^{-10}$	$10^{-3.5}$
MoO_2	$< 10^{-10}$	10^{-4}
IV Nonvolatile (pressure $< 10^{-4}$ atm at 2000 K)		
Ru, Rh, Tc, Mo		
Rare-earth oxides		
SrO		
ZrO_2, NbO_2		

[1] Data from References 2-7, 2-8, and 2-15.
[2] Estimated to be comparable to the halides.
[3] See text.

Deposit Formation

We believe that the formation of deposits such as CsI and Cs_2Te opposite fuel cracks resulted from several events--release of fission products from the fuel center when its temperature exceeded a threshold value, reaction of released atoms in the gas phase to form stable molecules, transport in the gas along fuel cracks, and deposition on the cladding (the coolest local surface available). In addition to those compounds, one would expect to find Cd, Sb, Sn, Ag, and possibly Pd, some of which were observed. The low fission yields of those elements makes their detection difficult. The presence of the trace impurities observed is in accord with the model because the impurities observed have sufficient volatilities to be vapor transported as elements (Mn, Cu) or compounds (Fe-Cl, or possibly Fe-Te).

The small crystals containing Cs and U (presumably as Cs-U oxide) probably were formed from particles of UO_2 that had broken away from fuel pellets, adhered to the cladding, and reacted with a cesium-bearing vapor species to form the Cs-U oxide.

The small nodules arranged in bands opposite fuel cracks and occasionally at the base of other deposits on the cladding appeared to be sites of greater zirconium oxidation, which was likely enhanced by the presence of the Cs-U-Te material that was always associated with nodules. We speculate that some volatile compound of Cs, U, Te, (and possibly O) exists that carries those elements to the cladding. That compound then reacts with the surface zirconium oxide on the cladding and locally accelerates the cladding oxidation to form the observed nodules.

A model for the formation of the more massive Cs-U ceramic deposits must consider the transport of Cs, O, and U. We propose the following model, which is illustrated in Figure 2-16. When the center of the fuel became hot enough to release fission products, gaseous Cs_2O was evolved. It was transported to the gaps between pellets, and then to the cladding at pellet interfaces, where it deposited to form type b deposits. The deposit, according to this model, was originally rich in Cs_2O, but at some time it came in contact with the fuel. The Cs_2O melted and dissolved some UO_2 to form a higher melting solid that solidified into the observed deposit.

FUEL GAP CLADDING

HIGH
TEMPERATURE
REGION
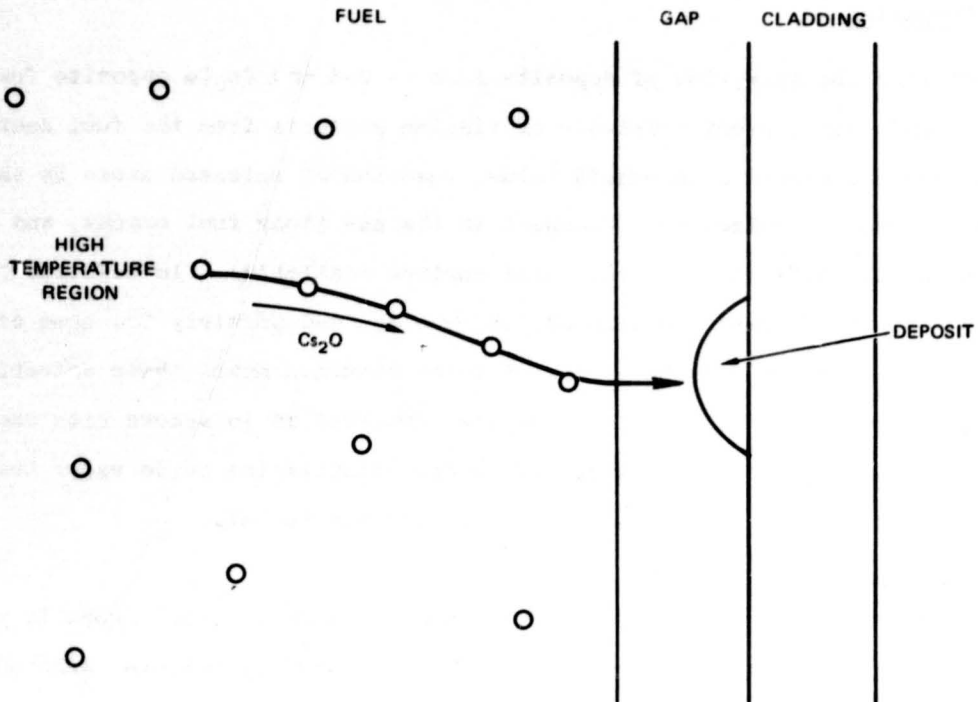
Cs_2O

DEPOSIT

(a) Cs_2O VAPOR RELEASED FROM HOT CENTRAL FUEL TRAVELS ALONG FUEL CRACKS
OR INTERCONNECTED POROSITY AND FINALLY DEPOSITS ON CLADDING

UO_2 REACTS
WHERE DEPOSIT
TOUCHES FUEL

Cs–U–O
COMPOUNDS

Cs_2O RICH
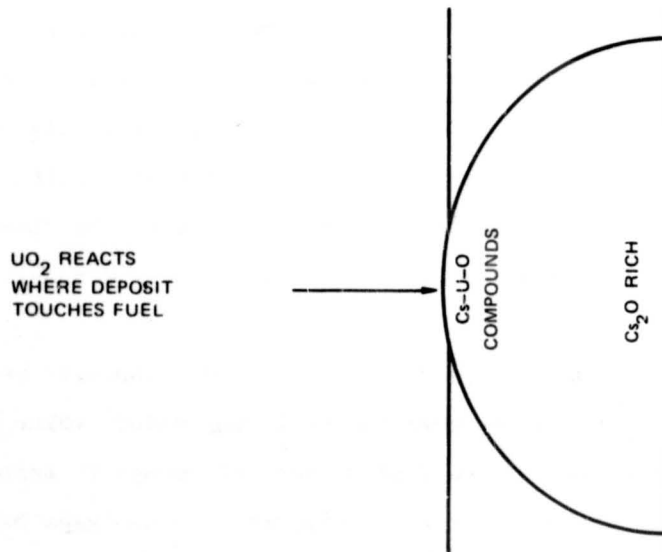
(b) WHEN FUEL TOUCHES DEPOSIT, THE Cs_2O MELTS AND REACTS WITH UO_2

SA-4197-61R

FIGURE 2-16   SCHEMATIC DIAGRAM FOR FORMATION OF CERAMIC DEPOSITS

(Melting point of $Cs_2O \sim 730$ K; cladding temperature ~ 650 K; and fuel surface ~ 1000 K). The layered structure and melted appearance of those deposits are in accord with the proposed model.

The circular deposits (type c) were very similar to type b deposits and were probably formed by a similar mechanism, except that the deposits occurred at locations other than pellet-pellet interfaces. Presumably there were local paths in the fuel (interconnected porosity perhaps coupled with cracks) through which the Cs_2O could escape from the hot regions to the cladding, which would account for the localized nature of those deposits.

The bonding of fuel to cladding by the ceramic-like substance is in accord with the model. In particular, when the deposited Cs_2O was melted by the fuel the resultant solidified substance acted as a cement between the fuel and cladding. When the rod was opened, the bond was broken at the weakest region--either in the cement or in the fuel pellet. Regions of both types were observed.

The H.B. Robinson cladding had only small amounts of fission product deposits, probably because fission products had not been released from the fuel. The volatility of the fission products probably was not the factor that prevented their release, since only little of the very volatile rare gases had escaped. The worm-like ZrO_2 structures and wrinkled regions on the surface represent areas of accelerated oxidation of the cladding caused by UO_2. Apparently UO_2 and ZrO_2 in close contact interdiffused and local oxidation was accelerated either because the resulting oxide was less protective or because oxygen was more readily available from the UO_2. (The nodules seen on the Main Yankee cladding were probably initial states of a similar accelerated oxidation, in that case caused by a Cs-U-Te deposit.) Interdiffusion of UO_2 and ZrO_2 where fuel pellets were in close contact with the cladding probably was involved in the fuel-clad bonding observed in the Robinson rod.

Relevant Literature Information

There are very few literature reports of the nature of deposits on LWR fuel rod cladding. Bazin et al. have investigated the radial redistribution of fission products in experimental PWR-like fuel rods (2-18). They found U, Zr, Cs, and some I, Te, Pd, and Ba in the fuel-clad gap. A reaction layer (sometimes a duplex layer) formed in the gap, and they delineated a threshold region as a function of linear power and burnup above which the reaction layer formed. Their curve is shown in Figure 2-17. The peak fuel rod power during the operation of the Maine Yankee Core I fell substantially below their threshold; yet we observed reaction layers similar to theirs, indicating there is some important factor not included in their correlation. We believe that fuel temperature is more fundamental than linear power in view of the Maine Yankee Core I experience (2-3). That is, the release of fission products from fuel probably occurs by mechanisms that are thermally activated and therefore the temperature attained by the fuel is a primary variable. The temperature of the fuel depends on the linear power but also on the geometry of the fuel rod, especially the fuel-cladding gap and associated gap thermal conductivity. Therefore, a correlation of fuel temperature and burnup with the formation of reaction layers may give a better defined threshold. The H.B. Robinson rod operating conditions fell on the threshold line drawn by Bazin. No reaction layers were observed in that rod.

Another relevant paper is the GE report of the examination of some BWR rods (2-19). Those investigators observed some fuel-clad bonding and a reaction layer in rods that had operated at maximum power levels of 420 W/cm (12.6 kW/ft) to burnups of 34 GWd/MTU. Those conditions fall above the Bazin threshold, in agreement with his correlation (2-18). Videm and Lunde have briefly reported features similar to those shown above for the Robinson cladding (2-20). An observation made on the Main Yankee rod (2-3) as well as on some GE rods (2-19) is that the zirconium oxide layer on the cladding in regions of fuel-clad bonding is much thicker than the ZrO_2 layer in other areas that did not show fuel-clad bonding. These results indicate that where the deposits on the cladding had bonded, the growth of the ZrO_2 layer was accelerated. In the Robinson rod we also found that the contact of UO_2 on the ZrO_2 caused accelerated oxidation.
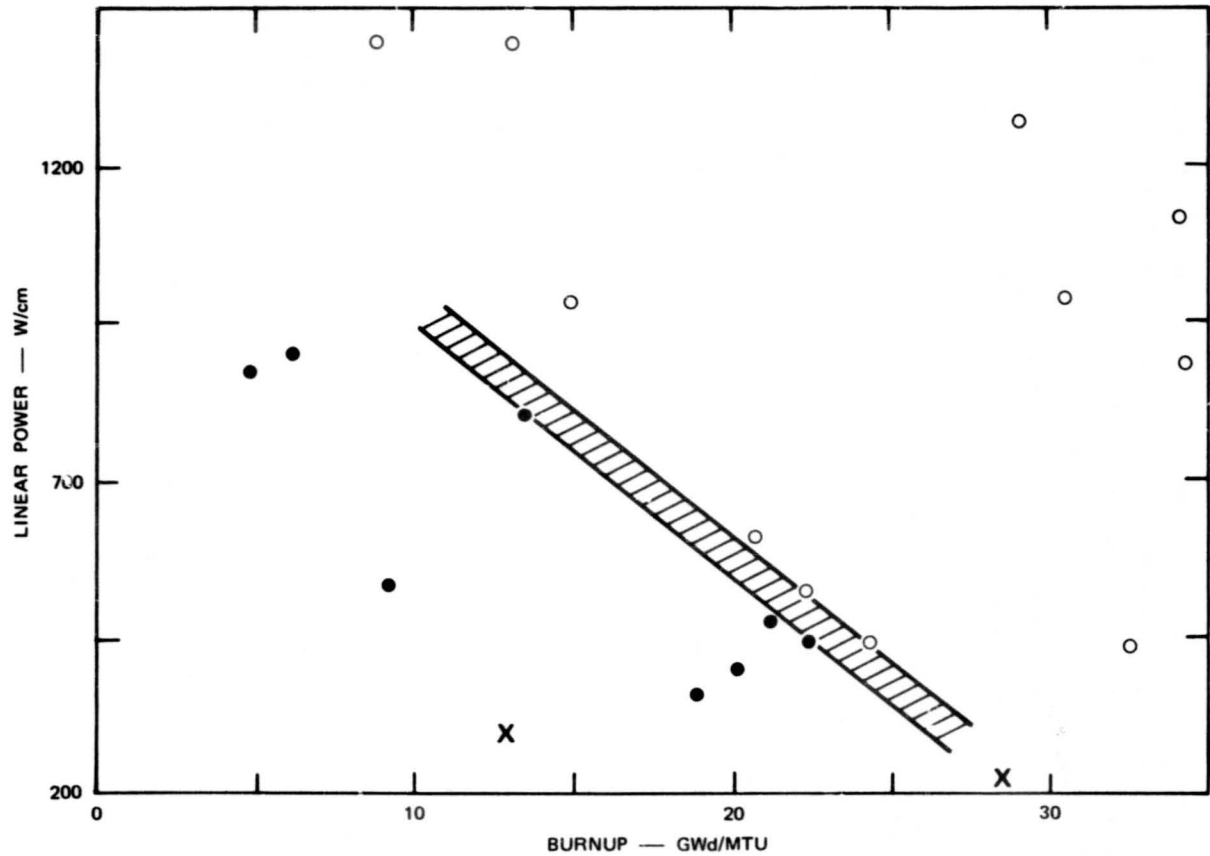
FIGURE 2-17 CONDITIONS FOR FORMATION OF FUEL-CLAD REACTION LAYER FROM BAZIN ET AL

Open circles represent rods with a reaction layer. Full circles rods with no reaction layer. Cross hatched band separates regions of layer formation and nonformation. Crosses indicates conditions for rods examined in present study. Left hand cross for Maine Yankee, right hand for H. B. Robinson.

SA-4197-63

RELATION TO IN-REACTOR STRESS CORROSION CRACKING OF ZIRCALOY

Several of the substances deposited on the cladding are embrittling or potentially so to Zircaloy:

- Cesium iodide. Free iodine is known to embrittle Zircaloy (2-21) and radiolytic decomposition of CsI can liberate iodine (2-22).

- Cadmium. It has recently been shown that Cd can embrittle Zircaloy (2-23). We did not detect Cd in any deposits, although in the SEM, the x-ray fluorescence spectrum of U would probably have obscured that of Cd.

- Iron. Fe in liquid Cs has been observed to be very embrittling to Zircaloy (2-24). Iron can occur as a trace impurity in UO_2.

- Cesium. Liquid Cs can embrittle Zircaloy under some conditions (2-25) and although liquid cesium itself was not present in the rods, it is possible that some other form of cesium may be aggressive.

In addition, other substances found or potentially present in the deposits may be embrittling to Zircaloy. For example, the semimetals (Te, Se, Sb, As) and B group metals (Ag, Cd, In, Sn, Pb) are embrittling to steels, whereas Cd and Ag embrittle Ti alloys. They may also be embrittling to Zircaloy.

As part of the assessment of the importance of these substances as PCI-active agents, we should consider whether the quantities that reach the cladding are sufficient to embrittle it. Estimates for some elements are presented below. It was found that the major concentrations of fission product deposits occurred at locations such as pellet-pellet interfaces and opposite fuel cracks, where analysis indicates that stresses and strains also are concentrated. Therefore, the estimates below are of the amounts of some fission products and impurities that might be encountered at such locations in the cladding surface.

Iodine

In the fuel rod environment, iodine (and bromine, which will act like iodine) is mainly combined as CsI because of the large availability of Cs. CsI alone does not cause SCC of Zircaloy under fuel rod operating conditions. However, in the intense radiation flux in a reactor, CsI undergoes radiolytic decomposition and releases iodine (2-26), and that combination can cause SCC of Zircaloy (2-27).

An estimate of the amount of iodine that might be available at the inner cladding surface can be made as follows. The fission yield of iodine is about 1 atomic percent. Therefore, at 1 percent burnup (9500 MWd/MTU), there will be about 0.8 mg I generated in a typical UO_2 fuel pellet (assumed to be 1.2 cm diameter by 1.2 cm long). We further assume that about 10% of that iodine is released from the fuel because of a temperature rise in the fuel. (Fission gas release of about 10 to 13% was observed in Main Yankee rods and it is reasonable to expect that a similar fraction of volatile substances in the fuel--CsI in this case--would be released. See Reference 2-6). The CsI probably would escape from the fuel center, travel along pellet-pellet interfaces, and deposit on the cladding opposite. If we assume the deposits will occur primarily in a narrow circumferential ring ($\sim$ 0.1 mm wide, or $\sim$ 0.04 cm^2 area), the surface density of the CsI would be about 4 mg/cm^2. The fraction decomposed by radiolysis is unknown, but in electron beams decomposition of as much as 10% has been observed (2-27). The surface concentration of iodine on the cladding at the pellet-pellet interface is thus estimated to be of the order of 0.2 mg/cm^2 and should be roughly proportional to the burnup.

Clearly, this estimate is only approximate because of the many assumptions required in the calculation. However, it is noteworthy that the value obtained is well in excess of the 0.005 mg/cm^2 figure reported by Busby et al. (2-29) to be sufficient to cause iodine SCC of Zircaloy.

Cadmium

A comparable estimate of the cadmium concentration at the cladding can be made. In the fuel rod environment, elemental cadmium should be stable and will be released from the fuel as the vapor. Grubb (2-23) found that elemental Cd, as well as Cd dissolved in liquid Cs, caused embrittlement of Zircaloys and the aggressiveness of the element was confirmed in our screening tests (Section 6).

The yield of Cd is about 0.05 percent of the U fissioned; therefore, at one percent burnup the inventory of Cd is about 35×10^{-3} mg per pellet (1.2 cm diameter by 1.2 long). If Cd is released, most of it will deposit as droplets of liquid on the cladding inner surface opposite pellet-pellet interfaces, because the melting point (549 K) is lower than the typical cladding operating temperature. (A small fraction

of the Cd, less than a few percent, will remain as vapor in the void volume available in the fuel rod, and we neglect that fraction.) If 10 percent of the Cd in the fuel pellet is released and deposits in a circumferential ring ~ 0.1 mm wide, the surface concentration will be about 0.1 mg Cd per cem^2 Zircaloy. Therefore, the amount of Cd available is comparable to the amount of free iodine.

Iron

Iron dissolved in liquid cesium at concentrations as low as 0.1 percent was found (2-24) to embrittle Zircaloy, as reported in Section 6. Iron is a manufacturing impurity in UO$_2$ fuel. Its vapor pressure is large enough that it can be released from the fuel and vapor transported to the cladding. As indicated above, there should be no liquid Cs present in the fuel rod to dissolve the Fe; however, it is probable that iron vapor could act in the same way as iron dissolved in Cs and thus is a potential SCC agent.

The amount of Fe in UO$_2$ fuel does not increase with burnup. Levels of Fe impurity of 25 ppm are not unlikely in fuel. That level corresponds to 0.4 mg Fe per pellet. If 10 percent of that amount were released during a fuel temperature rise, and deposited on the cladding at pellet-pellet interfaces in a ring 0.1 mm wide, the surface concentration would amount to about 1 mg Fe per cm^2 of Zircaloy. In the observed embrittlement of Zircaloy rings (2-24) by 0.1% Fe in liquid Cs, the amounts of Fe involved were approximately 3 mg Fe per cm^2 of Zircaloy, that is, the same order of magnitude as the amount available in the fuel rod, assuming Fe impurity levels in the fuel to be in the range 25 to 100 ppm.

Thus, several chemical substances present in the service environment experienced by fuel cladding are potentially embrittling to Zircaloy. It is not possible at this time to specify which one is the active agent in PCI failures. In fact, there may be more than one active agent under different operating regimes. High on the list of active agents are iodine, cadmium, and iron, not only because of their availability but also because of the similarity of the fractography of cracks induced by those substances with the fractography of PCI fractures. We chose to use iodine to provide the embrittling environment in the tests of Zircaloy behavior

reported below in Sections 4 and 5 because it was easier to control than either cadmium or iron and also because, at the time the tests were undertaken, the embrittling nature of the latter two substances was not well enough established.

REFERENCES

2-1   D. Cubicciotti et al., "The Nature of Fission Product Deposits Inside Light-Water-Reactor Fuel Rods," Topical Report, EPRI Project RP 455-1, November 1976.

2-2   D. Cubicciotti et al., "The Nature of Fission Product Deposits Inside LWR Fuel Rods," to be published in Proceedings ANS Topical Meeting on water Reactor Fuel Performance held in St. Charles, Illinois May 9-11, 1977.

2-3   N. Fuhrman et al., "Evaluation of Fuel Performance in Main Yankee Core I," EPRI Report NP 218, November 1976.

2-4   U. E. Wolff and C. R. Wolf, "Collimator for Energy-Dispersive X-ray Analysis of Radioactive Materials in a Scanning Electron Microscope." Proc. Ninth Annual Conference of the Microbeam Analysis Society, Ottawa, Ontario, Canada, July 22-26, 1974.

2-5   R. G. Sacks et al., "Light Water Safety Research Program: Quarterly Progress Report, April-June 1975," ANL-75-58, p. 45, 1975; July-September 1975, ANL 75-72, p. 43, 1975.

2-6   F. Garzarolli et al., "KWU Observations and Hypothesis of PCI Failures," IAEA Specialists Meeting on Pellet-Cladding Interaction for Water Reactors, June/July 1977 Vienna, Austria. See also: J. A. Turnbull et al., J. Nucl. Mat. 67, 301 (1977); 58, 31 (1975), and papers in Session 5 of "Physical Metallurgy of Reactor Fuel Elements," J. E. Harris and E. C. Sykes, eds., The Metals Society, London, 1975.

2-7   D. D. Wagman et al., NBS Technical Note 270 (Parts 3 to 7), 1968 to 1973, U.S. Government Printing Office, Washington, D.C.; and NBSIR 76-1034, PB PB 254460, Nat. Tech. Information Serv., Springfield, Virginia, 1976.

2-8   O. Kubaschewski, E. Evans, and C. Alcock, "Metallurgical Thermochemistry," 4th Ed. (Pergamon Press, Oxford, England, 1967).

2-9   P. O'Hare et al., "Calorimetric Studies on Actinide Compounds," in Thermodynamics of Nuclear Materials, 1974, Vol. II, P. 447 (International Atomic Energy Agency, Vienna, 1974); J. Chem. Thermo., 6, 135, 263 (1974).

2-10 D. R. Olander, "Fundamental Aspects of Nuclear Reactor Fuel Elements," TID26711-P1, Nat. Technical Information Serv., Springfield, Virginia, 1976.

2-11 D. L. Douglass, "The Metallurgy of Zirconium," Atomic Energy Review, Supplement 1971, International Atomic Energy Agency, Vienna, 1971.

2-12 M. E. Meek and B. F. Rider, "Compilation of Fission Product Yields," Report NEDO-12154, General Electric Co., San Jose, California 1972.

2-13 P. E. Blackburn, "Oxygen Pressures Over Fast Breeder Reactor Fuel," J. Nucl. Mat., <u>46</u>, 244 (1973).

2-14 M. Adamson et al, "Oxygen Redistribution and its Measurement in Irradiated Oxide Fuels," in <u>Thermodynamics of Nuclear Materials 1974</u>, Vol. I, p. 59 (International Atomic Energy Agency, Vienna, 1974).

2-15 JANAF Thermochemical Tables, The Dow Chemical Co., Midland, Michigan, March 1977.

2-16 I. Johnson, in "Argonne National Laboratory Annual Progress Report, Chemical Engineering Division, July 1974 to June 1975," ANL 75-48, P. 18, March 1976.

2-17 A. V. Gusarov et al., Teplofiz Vys. Temp. <u>5</u>, 584 (1967), Chem. Abstr 68: 6984z.

2-18 J. Bazin et al., "Comportment et Etat Physico-chemique des Produits de Fission," Bull. Info. Sci. Tech., CEA, France, <u>196</u>, 55 (1974), Translated in NRC-TR-1, U.S. Nuclear Reg. Comm. Also, Trans. Am. Nucl. Soc. <u>20</u>, 235 (1975).

2-19 F. H. Megerth et al., "Zircaloy Clad UO_2 Fuel Rod Evaluation Program Report," GEAP 10371, General Electric Co., San Jose, California (June 1971).

2-20 K. Videm and L. Lunde, "Stress Corrosion Cracking of Zircaloy Fuel Cladding Tubes under Power Ramps in Lab Tests," to be published in Proceedings ANS Topic. Meeting on <u>Water Reactor Fuel Performance</u> held in St. Charles, Illinois, May 9-11, 1977.

2-21 B. Cox and J. C. Wood, "Iodine Induced Cracking of Zircaloy Fuel Cladding, in <u>Corrosion Problems in Energy Conservation and Generation</u>, p. 275, C. . Tedmon, Ed. (The Electrochemical Society, Princeton, New Jersey, 1974).

2-22 D. Cubicciotti and J. H. Davies, "Release of Iodine From Iodide Salts by Gamma Radiolysis," Nuclear Science and Eng., <u>60</u>, 314 (1976).

2-23 W. T. Grubb, "Cadmium Metal Embrittlement of Zircaloy-2," Nature, 265, 36, (1977).

2-24 B. C. Syrett, D. Cubicciotti, and R. L. Jones, "Embrittlement of Zircaloy-4 by Liquid Cesium at 300°C," <u>Zirconium in the Nuclear Industry</u>, p.281, ASTM publication STP 633, Philadelphia, Pa., 1977.

2-25 J. C. Wood et al., "Environmentally Induced Fracture of Zircaloy by Iodine and Cesium," J. Nuclear Mat., <u>57</u>, 155 (1975).

2-26 D. Cubicciotti and J. H. Davies, Nuclear Science and Engineering <u>60</u>, 314 (1976).

2-27 J. S. Armijo et al., "Irradiation Tests to Characterize the PCI Failure Mechanism," <u>Proceedings: ANS Topic Meeting on Water Reactor Fuel Performance</u>, St. Charles, Illinois, May 1977.

2-28 L. W. Hobbs, "Surface and Defect Properties of Solids," Vol. 4, p. 152, M. W. Roberts and J. M. Thomas, eds. (Chem. Soc., London, 1975).

2-29 C. C. Busby, R. P. Tucker, and J. E. McCauley, J. Nuclear Materials 55, 64 (1975).

Section 3

CHARACTERIZATION OF EXPERIMENTAL MATERIALS

INTRODUCTION

SRI International was assigned responsibility for procurement, distribution, and characterization of the Zircaloy sheet, plate, and tubing needed for the experimental phases of EPRI Projects RP 455 and RP 456. The purpose of assigning this responsibility to one organization was to ensure that the five participants* in the two EPRI projects would all study comparable materials.

The Zircaloy tubing required for SRI's testing program was supplied by Sandvik Special Metals Corp. from the special lots of tubing ordered by EPRI. Three types of tubing were obtained: stress-relieved Zircaloy-4 (lot number 7FD11), stress-relieved Zircaloy-2 (7AH11-H), and annealed Zircaloy-2 (7AH11-S). The nominal outside diameter of the 7FD11 tubing was 10.92 ± 0.05 mm and the wall thickness was 0.635 ± 0.05 mm. The corresponding nominal dimensions for the 7AH11-H and 7AH11-S tubing lots were 12.52 ± 0.05 mm and 0.86 ± 0.08 mm.

Lists of estimated requirements for sheet and plate products (needed for fracture mechanics experiments on RP 455 and mechanical anisotropy studies on RP 456) were obtained from all of the participants in RP 455 and RP 456 and were compiled into a single master list by SRI. The final list, consisting of 35 distinct items, was based on a matrix of two compositions (Zircaloy-2 and Zircaloy-4) by three basal textures (basal pole maxima at $0°$, $\pm 30°$, and $\pm 90°$ with respect to the plate normal) by three thicknesses (12.7 mm, 3.2 mm, and 0.8 mm) by three heat

---

* NASA-Ames, GE, Stanford University, MIT, and SRI.

treatments (none, stress-relieved, and annealed). The flat products were fabricated by Teledyne Wah Chang Albany Corp. (TWCA) and shipped to SRI for distribution.

EXPERIMENTAL MATERIALS AND FABRICATION HISTORIES

Table 3-1 lists the tube and flat products obtained for use on projects RP 455 and RP 456 and shows ingot numbers, fabrication schedules, and heat treatments. The Sandvik lot numbers and TWCA sales order numbers are used for identification. Tables A-1, A-2, and A-3 in Appendix A provide details of the reduction schedules used for the 12.7-mm, 3.2-mm, and 0.8-mm flat products, respectively. The three different reduction schedules (C, J, and K) used by TWCA for each thickness were based on suggestions by D. Lee of GE and were intended to generate the ±90° (Schedule C), ±30° (Schedule J), and 0° (Schedule K) basal pole distributions mentioned previously.

Ingots were rotary forged, extruded, and cold worked to fabricate the tubes. Although detailed tube fabrication schedules were not provided by Sandvik, the procedures used were reportedly typical of those used for the manufacture of commercial nuclear fuel cladding and included a final cold reduction of about 60 percent prior to heat treatment and straightening (3-1). Accordingly, the Schedules C, J, and K used for the 0.8-mm sheets also included a final cold reduction of 60 percent. Unfortunately, an error was made when TWCA scaled the schedules for the 3.2-mm sheets and the final cold reduction in this case was 40 percent rather than the desired 60 percent. It was not considered feasible to include a 60 percent cold reduction in the rolling schedules used for the 12.7-mm plates; hence a warm reduction of 60 percent was used as shown in Table A-1.

PRIMARY CHARACTERIZATION

To allow cross correlation of the results of experiments on sheet, plate, and tubing, we evaluated certain key characteristics of the experimental materials. Ingot compositions were obtained from TWCA and most of the products were subjected to a primary characterization screening consisting of

- Optical metallography (3 orthogonal sections)
- Vickers diamond pyramid hardnesses (3 orthogonal loading directions)
- Basal texture determination.

Table 3-1

TUBE AND FLAT PRODUCTS OBTAINED FOR USE ON EPRI PROJECTS RP 455 and RP 456

Alloy	Ingot No.	Product Form	Identification Number[1]	Fabrication Schedule[2]	Heat Treatment[3]	Primary Characterization[4]	Product Chemistry
Zircaloy-4	394597Q	Tube	7FD11	–	Hard	x	x
Zircaloy-2	395481Q	Tube	7AH11-S	–	Soft	x	x
			7AH11-H	–	Hard	x	x
Zircaloy-2	397598Q	12.7 mm Plate	9908-1A	C	Hard	x	
			9908-1B	C	Soft	x	
			9908-2A	J	Hard	x	
			9908-2B	J	Soft	x	
			9908-3A	K	Hard	x	
			9908-3B	K	Soft	x	x
Zircaloy-2	397598Q	3.2 mm Sheet	9908-4A	C	None		
			9908-4B	C	Hard	x	x
			9908-4C	C	Soft	x	
			9908-5A	J	None		x
			9908-5B	J	Hard	x	
			9908-5C	J	Soft	x	
			9908-6A	K	None		
			9908-6B	K	Hard	x	
			9908-6C	K	Soft	x	
Zircaloy-2	397598Q	0.8 mm Sheet	9912-1A	C	Hard	x	
			9912-1B	C	Soft	x	
			9912-2A	J	Hard	x	
			9912-2B	J	Soft	x	x
			9912-3A	K	Hard	x	
			9912-3B	K	Soft	x	
Zircaloy-4	397523Q	12.7 mm Plate	9912-4A	J	None		
			9912-4B	J	Hard	x	x
Zircaloy-4	397523Q	3.2 mm Sheet	9912-5A	C	None		
			9912-5B	C	Hard	x	
			9912-6A	J	None		x
			9912-6B	J	Hard	x	
			9913-1A	K	None		
			9913-1B	K	Hard	x	
Zircaloy-4	397523Q	0.8 mm Sheet	9913-2A	C	None		
			9913-2B	C	Hard	x	
			9913-3A	J	None		x
			9913-3B	J	Hard	x	x
			9913-4A	K	None		
			9913-4B	K	Hard	x	

[1] Sandvik lot number or TWCA sales order number.
[2] See Tables A-1 to A-3 for fabrication schedules used for flat products.
[3] None = as rolled, Hard = 4 hours at 770 ± 5 K; Soft = 2 hours at 840 ± 5 K.
[4] Optical microstructure, Vickers diamond pyramid hardness and basal texture.

Table 3-1 identifies the products that were screened and also indicates those whose compositions were analyzed after fabrication. Detailed information on the results of the primary characterization studies can be found in Appendix A. A summary of the observations is presented below.

Ingot and Product Compositions

The chemical compositions of the four ingots used to fabricate the tube and flat products listed in Table 3-1 are presented in Tables A-4 to A-7. The contents of the alloying elements and major impurities were all in accordance with normal nuclear cladding specifications, (ASTM B353-77) and no significant differences were found between the chemical compositions of the ingots used for the sheet and plate products and those used for the tubing.

At SRI's request, TWCA analyzed the three tubing products and an arbitrary but representative group of the sheet and plate products. These analyses were restricted to the interstitial impurities oxygen, nitrogen, and hydrogen, which are the only elements whose contents are likely to change significantly during fabrication (3-2). The data obtained are presented in Table A-8. Although the interstitial impurity levels generally increased slightly during fabrication, the final contents were within normal nuclear specifications in all cases. It was concluded that no significant differences existed between the chemical compositions of the tube products and those of the corresponding sheet and plate products.

Basal Textures

Basal pole figures for the 28 products that were subjected to the primary characterization screening are presented in Appendix A as Figures A-1 to A-28. Each of these basal textures was obtained at the midplane (sheet and plate products) or midwall (tube products) using a technique similar to that described by Holland (3-3). Values of the texture parameter f, defined as

$$f = \Sigma \, V_i \, \cos^2 \alpha_i \qquad\qquad (3-1)$$

(Where V_i is the volume fraction of material with basal poles α_i degrees from a reference direction) are listed in Figures A-1 to A-28 for the three principal

tube or plate directions. The validities of the textures and f-numbers were verified by the acceptable agreement achieved in a limited round-robin in which the same plate specimens were characterized by GE, MIT, and SRI.

The basal textures of the two lots of stress-relieved tubing (7FD11 and 7AH11-H) are very similar. Both show maximum basal pole intensities of six times random centered at about ±33° from the radial direction towards the tangential direction, a "hole" in the basal pole distribution centered in the radial direction, and an essentially zero density of basal poles in the axial direction. The higher heat treatment temperature used for the 7AH11-S lot of Zircaloy-2 tubing results in only minor changes in texture--the radial "hole" disappears and the position of the basal pole peaks shifts to about ±27° from the radial direction.

Schedule J, which was intended to produce sheet and plate materials with basal textures similar to those of tubing, was generally successful in a qualitative sense; however, with a few exceptions, the Schedule J sheet and plate textures are somewhat less intense than those of the tubes. Schedule K, which was intended to produce a symmetrical basal pole distribution centered in the plate normal direction, also was generally successful, although some of the Schedule K materials have textures that show two near-normal peaks rather than one. Also, the 12.7-mm Schedule K plates show much less intense textures than the thinner materials, presumably because of the difference in working temperature.

Schedule C was not successful in producing the desired high basal pole intensity in the plate transverse direction. The textures of the Schedule C materials were similar to those of the Schedule J materials for sheets and plates of all thicknesses. No explanation emerged for the present lack of success with Schedule J which previously had been used successfully by Lee (3-4).

Optical Microstructures and Diamond Pyramid Hardnesses

Optical microstructures (three orthogonal sections) and Vickers diamond pyramid hardnesses (5-kg load--three orthogonal loading directions) are shown in Appendix A for the 28 materials that were screened (Figures A-1 to A-28). The optical

microstructures of the tubing materials are as expected, and the type and degree of mechanical anisotropy indicated by the hardness measurements is consistent with the basal pole distributions. The microstructures of the sheet and plate materials generally are coarser than those of the equivalent tubing and the hardnesses are somewhat lower. These trends are particularly apparent for the warm-worked 12.7-mm plates. These plates also showed the very pronounced mechanical fibering or layering illustrated in Figure 3-1. It is apparent in Figure 3-1 that the etching characteristics of the layers differ. Since this effect persisted in fully annealed plates but was not apparent in fully annealed bar stock (Figure 3-1) some segregation of the alloying constituents may have been present in the plates. No attempt was made to confirm this possibility.

SECONDARY CHARACTERIZATION

To provide additional information on the metallurgical characteristics of the experimental materials, we examined in more detail a few important aspects of selected products. With the exception of an investigation of through-thickness texture variations in one of the 12.7-mm plate materials, these additional characterization studies were confined to the tubing materials.

Through-Thickness Basal Texture Variations

The computer program used at SRI to reduce crystallographic texture data is equipped with a statistical subroutine that indicates the existence of texture variations through the thickness of the material being characterized. All the Schedule J and Schedule C sheet and plate products and all three tubing materials appeared to contain such texture variations, but the indication was most pronounced in the case of the 12.7-mm-thick Schedule J plates. The nature of the texture variations was therefore explored further for the 9908-2B plate lot (annealed Zircaloy-2) by determining pole figures at different depths below the plate surface. The results obtained are shown in Figure 3-2. The basal texture at the plate surface shows a strong pole concentration centered in the plate normal direction, whereas at the midplane the maximum basal pole concentration is split and is centered at about ±30° from the plate normal. It is evident in Figure 3-2 that the surface texture
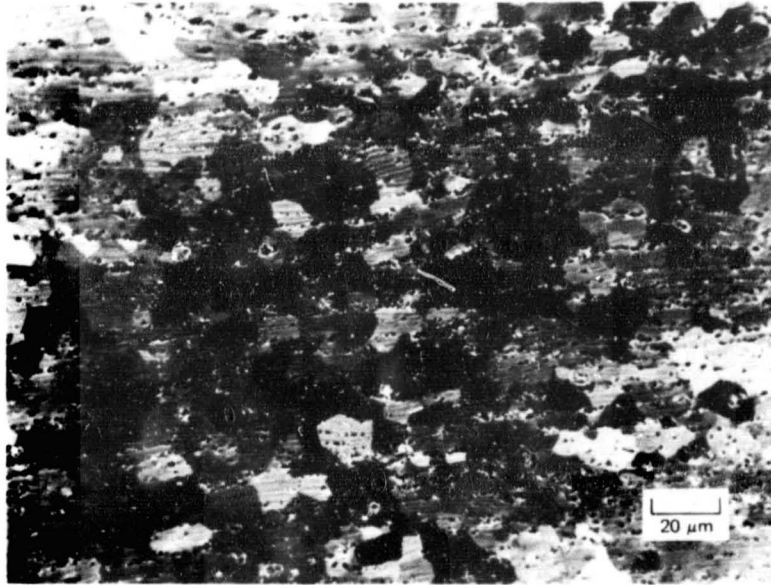
(a) 9912-4A PLATE RECRYSTALLIZED AT 870 K
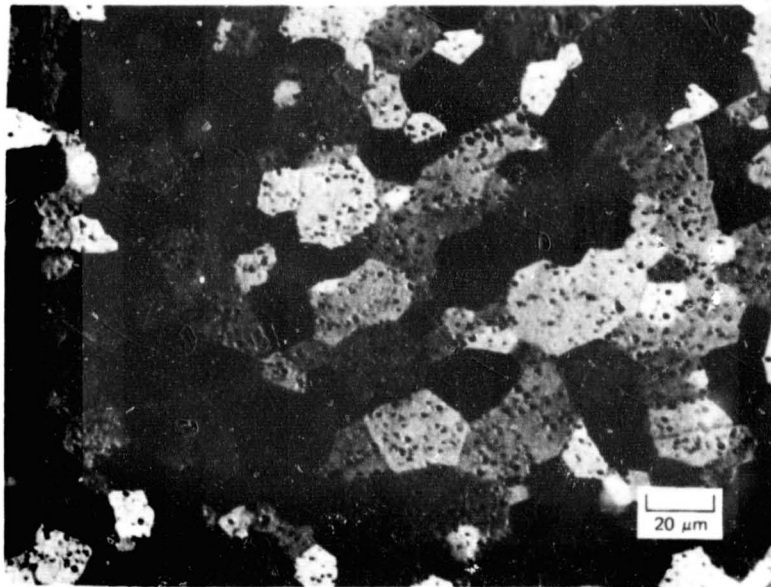
(b) 6-mm-DIAMETER ROD RECRYSTALLIZED AT 870 K
(Note absence of striations present in the plate.)

SA-4197-248

FIGURE 3-1   OPTICAL MICROGRAPHS OF LONGITUDINAL SECTIONS
THROUGH ZIRCALOY-4 PRODUCTS
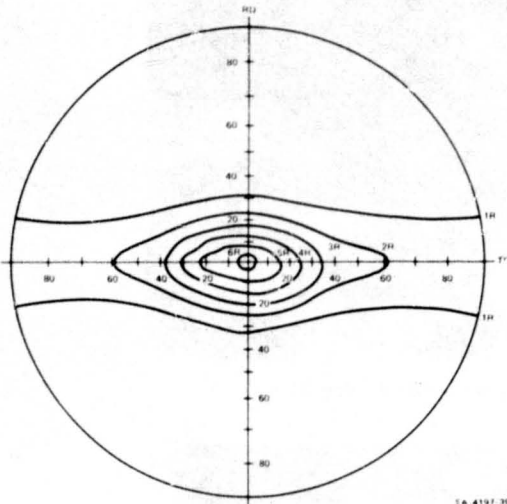
(a) AT THE SURFACE
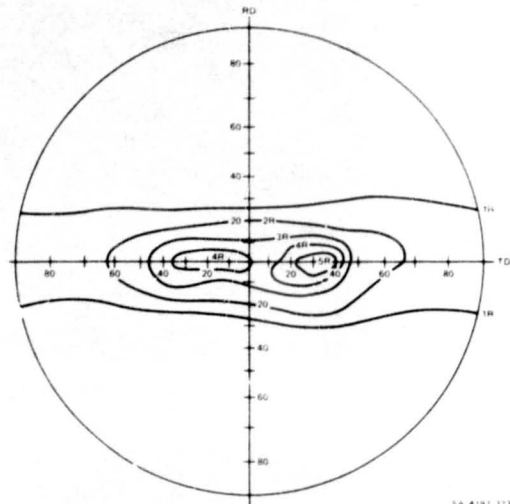
(b) 0.13 mm BELOW THE SURFACE
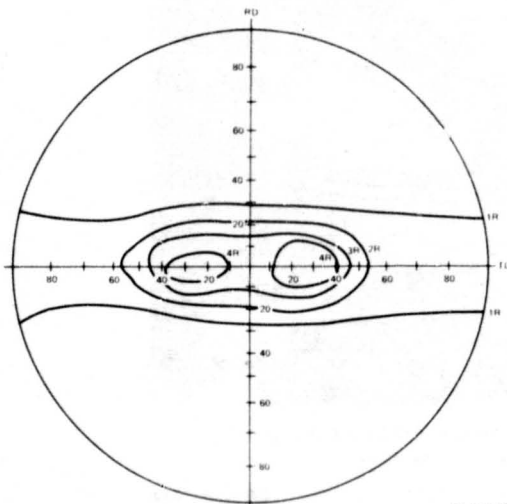
(c) 0.28 mm BELOW THE SURFACE
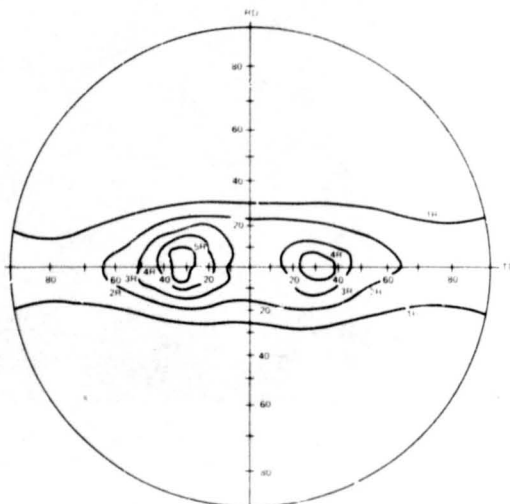
(d) 6.35 mm BELOW THE SURFACE

FIGURE 3-2   BASAL POLE FIGURES FOR 9908-2B ZIRCALOY-2 PLATE

does not persist far into the body of the plate. The basal pole split is already apparent at a depth of 130 μm below the plate surface and is essentially fully developed at a depth of 280 μm.

Although no other products were investigated in detail, the computer output indicated that the nature of the texture variations in the Schedule J and Schedule C sheets and plates and in the tubes was qualitatively similar to that illustrated in Figure 3-2. Therefore, we can conclude that the basal pole orientations of all those materials was more strongly radial (normal) near the surface than indicated by the midwall (midplane) pole figures presented in Appendix A.

Biaxial Tensile Tests on Tubing

The biaxial stress-strain behavior of the three lots of tubing was evaluated with a simple but tedious test method. First, the diameter of a length of tubing was accurately measured. Next, the tubing length was heated to the desired test temperature* and pressurized with helium to a predetermined pressure at a rate of about 100 kPa/sec. After reaching the predetermined level, the pressure was immediately reduced to a small value, the temperature of the specimen was returned to room temperature, and the new diameter was measured. The entire procedure was repeated for increasing maximum pressure levels until the specimen burst. The averaged data obtained from duplicate tests are shown in Figure 3-3 and Table 3-2. As expected, the fully annealed Zircaloy-2 tubing (Sandvik lot number 7AH11-S) is considerably weaker and more ductile at 590 K than the stress-relieved Zircaloy-2 tubing (7AH11-H). More surprising is the observation that the stress relieved Zircaloy-4 tubing (7FD11) is detectably weaker and less ductile at 630 K than the stress-relieved Zircaloy-2 tubing (7AH11-H) at 590 K. The difference in test temperature probably accounts for the small strength differential. However, the lower ductility of the 7FD11 tubing most likely is due to its smaller wall thickness

---

*The Zircaloy-2 tubings were tested at 590 ± 5 K (a typical BWR cladding service temperature) and the Zircaloy-4 tubing was tested at 630 ± 5 K (a typical PWR cladding service temperature). As will become apparent later, these test temperatures were used consistently throughout the program.
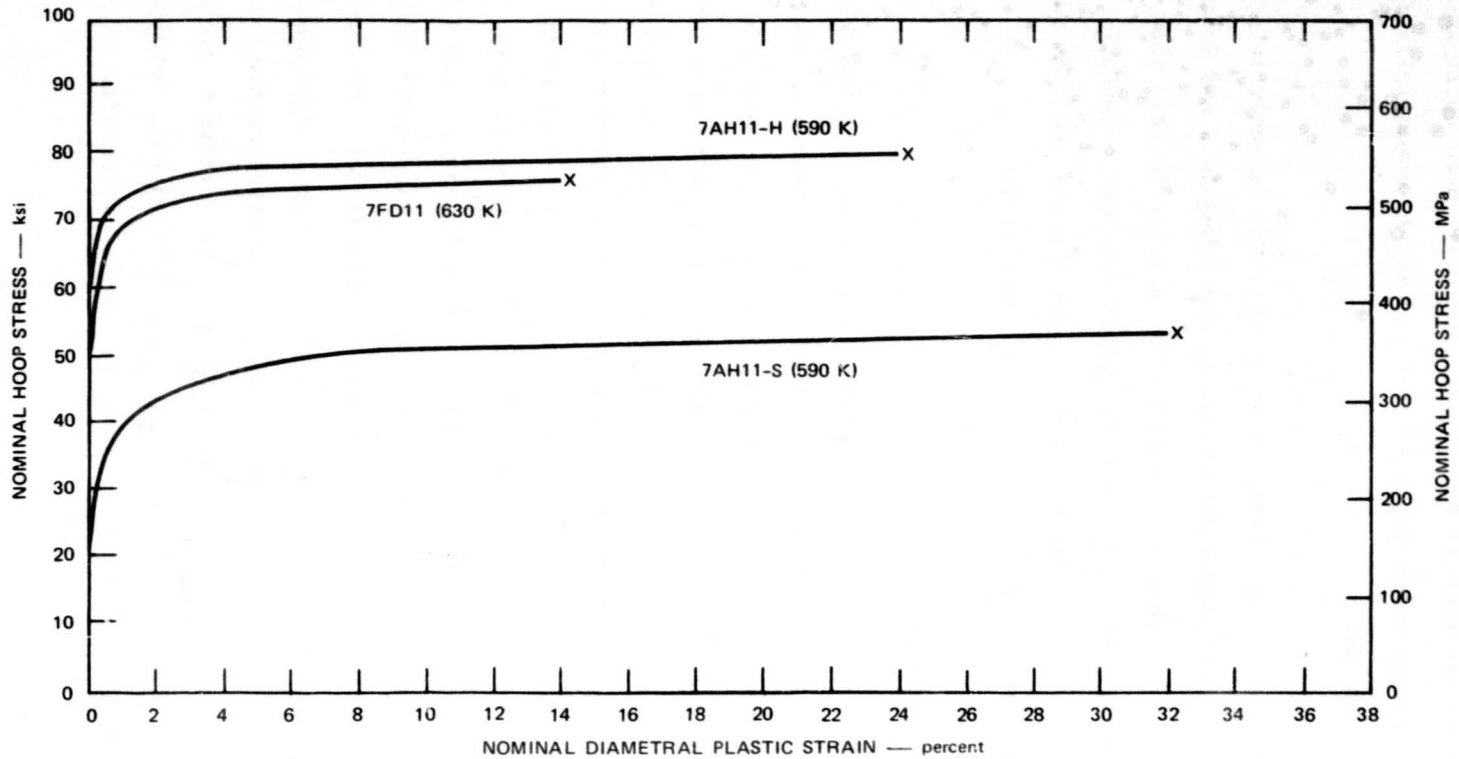
SA-4197-209

FIGURE 3-3   HOOP STRESS VERSUS DIAMETRAL STRAIN FOR THREE TYPES OF ZIRCALOY
TUBING UNDER INTERNAL PRESSURIZATION

Curves are smoothed averages of duplicate tests. See Table 3-2 for variability.

Table 3-2

MECHANICAL PROPERTIES OF THREE TYPES OF TUBING UNDER INTERNAL PRESSURIZATION AT REACTOR OPERATING TEMPERATURES[1]

Lot Number	Description	Test Temperature	Proportional Limit (MPa)	0.2% Plastic Offset Yield Stress (MPa)	Burst Stress (MPa)	Uniform Diametral Strain (%)	Total Diametral Plastic Strain (%)
7FD11	Sandvik Zircaloy-4, stress relieved 4 hours at 770 ± 5 K	630 ± 5 K	280 + 20	410 + 5	525 ± 5	4 ± 1	14 ± 5
7AH11-H	Sandvik Zircaloy-2, stress relieved 4 hours at 770 ± 5K	590 ± 5 K	300 ± 20	4?0 ± 5	550 ± 5	4 ± 1	24 ± 5
7AH11-S	Sandvik Zircaloy-2, annealed 2 hours at 840 ± 5 K	590 ± 5 K	140 ± 20	210 ± 5	370 ± 5	5 ± 1	32 ± 5

[1] Values listed are arithmetic means of duplicate tests. Estimated uncertainties are as indicated.

(which would tend to reduce nonuniform strain), because the higher test temperature used for the Zircaloy-4 tubing would normally be expected to enhance ductility.

Residual Stresses in Tubing at Room Temperature

Estimates of the residual stresses in the tubes were obtained by cutting several ~ 1-cm-long rings randomly from each tubing lot, measuring the outside diameter D_0, slitting the rings axially using a diamond saw, and measuring the new diameter D. Crampton's formula (3-5)

$$\sigma_r = \frac{Et}{1-\nu^2} \left(\frac{1}{D_o} - \frac{1}{D} \right) , \tag{3-2}$$

(where E and ν are Young's Modulus and Poisson's ratio, respectively, and t is the wall thickness of the tube) was used to estimate the magnitude of σ_r, the residual hoop stress. The mean data obtained in 5 tests on each tubing are shown in Table 3-3.

Table 3-3

RESIDUAL STRESSES IN TUBING MATERIALS
AT ROOM TEMPERATURE

Tubing Lot	D_o (mm)	D (mm)	t (mm)	σ_r[1] (MPa)
7FD11	10.92	11.07	0.63	86 ± 4
7AH11-S	12.52	12.7	0.864	104 ± 5
7AH11-H	12.52	12.67	0.864	88 ± 5

[1] Mean of five determinations and range of observed variation.

All the tubes contain considerable residual hoop stresses that probably originate from tube straightening, which is the final fabrication step and is performed after annealing. The behavior of rings of the 7FD11 tubing was noticeably more consistent than that of rings of either 7AH11-S or 7AH11-H, indicating that the residual hoop stress in the 7FD11 tubing was less variable along the length of the tube. The ring diameter increased when the ring was slit axially for all three materials, indicating that the residual stresses in the inside part of the tube wall were predominantly compressive, whereas the residual stresses nearer to the outside surface were predominantly tensile. However, these experiments do not allow us to conclude that the residual hoop stress at the inside surface is compressive. Crampton's formula assumes that a linear stress gradient exists through the tube wall, but as Wood et al have pointed out, there are an infinite number of through-wall stress distributions that can account for a given change of ring diameter following axial slitting (3-6). To determine the residual stress distribution that actually exists, it is necessary to follow the change in ring diameter that occurs as material is progressively removed from the ring wall. This time-consuming procedure was regarded as beyond the scope of the present screening tests and was not undertaken.

Topography of Tubing Surfaces

Profilometry measurements and scanning electron microscope (SEM) observations were combined to characterize the topography of the inside and outside surfaces of ramdomly selected sections of the 7FD11 Zircaloy-4 tubing. The profilometer traces in Figure 3-4 show, as expected, that the circumferentially ground outside surface of the tubing was considerably rougher than the pickled inside surface in the axial direction. However, the circumferential traces show similar roughnesses for the inside and outside surfaces. The arithmetic average (AA) roughness values given in Figure 3-4 are based on the definition given in American Standards Association Standard B46.1 (1962).

SEM micrographs of the outside tube surfaces showed the relief typical of an as-ground surface. As shown in Figure 3-5, the inside surface contained a surprisingly high density of defects with sizes ranging from 1 to 10 μm. The other tubing
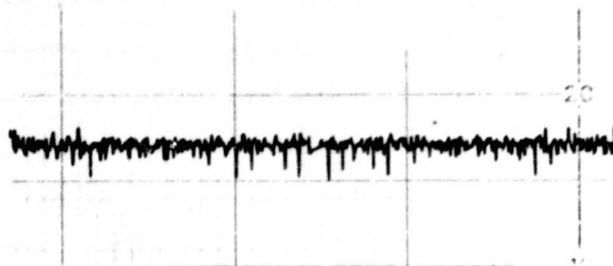
(a) AXIAL DIRECTION ON OUTSIDE SURFACE.
Roughness (AA) ≈ 25 μin.
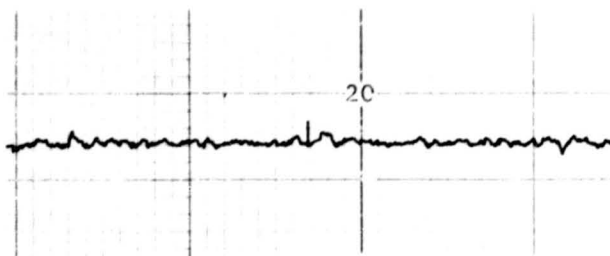
(b) AXIAL DIRECTION ON INSIDE SURFACE.
Roughness (AA) = 11 μin.
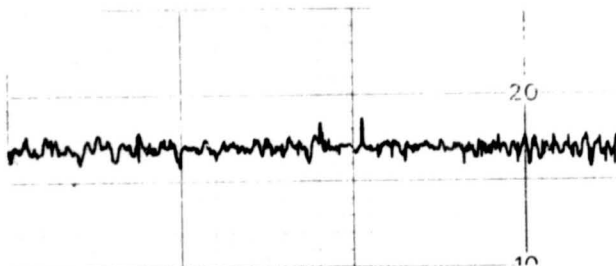
(c) CIRCUMFERENTIAL DIRECTION ON OUTSIDE SURFACE.
Roughness (AA) = 22 μin.
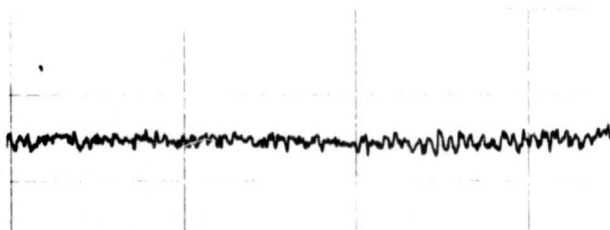
(d) CIRCUMFERENTIAL DIRECTION ON INSIDE SURFACE.
Roughness (AA) = 20 μin.

SA-4197-41

FIGURE 3-4   PROFILOMETER TRACES OBTAINED FROM THE
SURFACES OF 7FD11 ZIRCALOY-4 TUBE LENGTHS
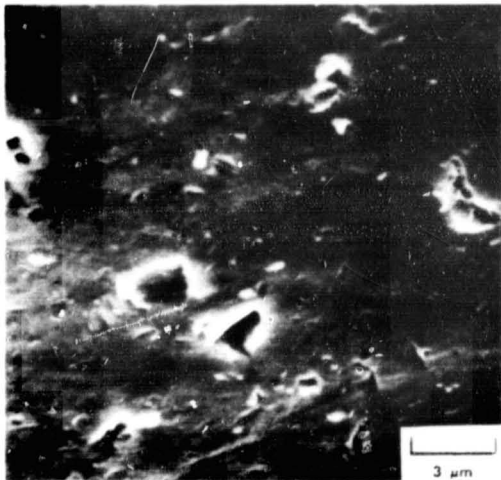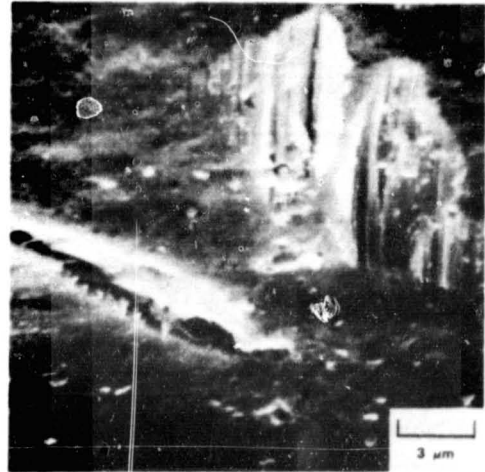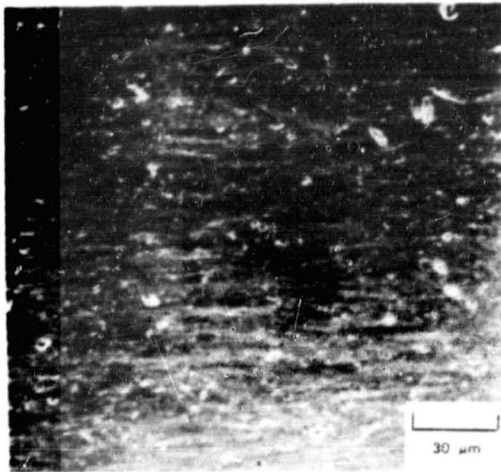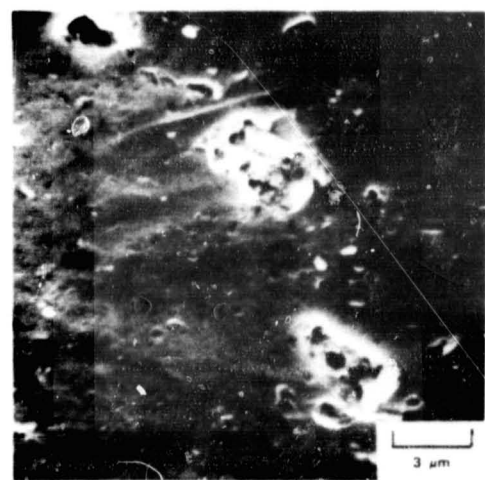
FIGURE 3-5   SEM MICROGRAPHS AT TWO MAGNIFICATIONS SHOWING TYPICAL AREAS
OF THE PICKLED INSIDE SURFACE OF 7FD11 ZIRCALOY-4 TUBING

materials were not characterized in detail but appeared qualitatively similar in SEM examinations.

In addition to the characterization studies summarized above, a considerable body of information on the surface and near-surface characteristics of the tubing materials was developed during our crack initiation studies. Some important observations made during those studies regarding distributions of large second-phase particles and inclusions in and near the tubing inside surface, are discussed in Section 4 of this report.

REFERENCES

3-1 T. D. Naylor, Sandvik Special Metals Corp., Private Communication (1977).

3-2 R. E. Grammer, Teledyne Wah Chang Albany Corp., Private Communication (1976).

3-3 J. R. Holland, "The Use of Computer Techniques to Plot Pole Figures," Advances in X-ray Analysis, 4, 74-84 (1961).

3-4 D. Lee, "Ductility of Textured Zircaloy-2," Trans. ASM., 61, 742 (1968).

3-5 D. K. Crampton, Trans. AIME, 79, 233-255 (1930).

3-6 J. C. Wood, J. Nuclear Mat., 45, 105-122 (1972/73).

Section 4

CRACK FORMATION IN ZIRCALOYS EXPOSED TO IODINE

INTRODUCTION

The results of tube pressurization experiments (see, for example, Section 5) lead
to the conclusion that a threshold stress must be exceeded before iodine can induce
stress corrosion cracking (SCC) of internally pressurized, thin-walled Zircaloy
tubes. This suggests that crack formation may be the key step in iodine-induced
SCC of the Zircaloy tubes used for light water reactor fuel cladding (4-1) and may
also be important in the PCI fuel cladding failure process. Therefore, we undertook
the present study to understand how stress corrosion cracks form in thin-walled
Zircaloy tubes. Principal emphasis was placed on iodine SCC but a few exploratory
tests were conducted with cadmium because the SCC screening tests (Section 6) indi-
cated that, under certain conditions cadmium was as aggressive toward Zircaloy as
iodine. A related study was undertaken under subcontract by Professor S. Namba
during his visit to MIT. The results of that work are reported in Appendix B.

Cox and Wood (4-2) suggest that penetration of the surface oxide either chemically
or, in the case of thick oxide layers, by mechanical cracking, is an essential
precursor to iodine-induced crack formation. Penetration of the oxide allows con-
tact between the iodine and the underlying metal, which then can undergo a high-
temperature chemical reaction leading to the formation of a sharp notch large
enough to propagate under the combined action of stress and environment. Cox and
Wood (4-2) report that fractographic observations on specimens that have undergone
crack propagation to final fracture provide useful information on the predominantly
transgranular microprocesses involved in crack propagation. However, the fracture
topography in the crack formation region usually is greatly affected by chemical
attack during the long exposure period while the crack propagates to final fracture.

As a result, the nature of the fracture microprocesses leading to crack formation have not been clearly defined, although Cox and Wood indicate that intergranular attack may be involved.

Because of the problems encountered by previous investigators (4-2) in defining the mechanism of initial crack penetration from fracture surface observations, we developed a new technique for studying crack formation. In this technique, a modification of a mechanical test devised by van der Schaaf (4-3) is used to subject a small, well-defined area of test sample surface to conditions expected to lead to stress corrosion crack information. Then corrosion products are removed from the sample surface by argon ion milling, and the topography and chemistry of the small area of interest are characterized in detail using the scanning electron microscope (SEM) and energy dispersive x-ray (EDX) analysis.

MATERIALS AND TEST METHODS

Preliminary experiments were conducted on disc samples of the 9913-3B lot of stress-relieved 0.8-mm Zircaloy-4 sheet. Subsequent detailed investigations were made using lengths of the 7FD11, 7AH11-S, and 7AH11-H lots of Zircaloy tubing. Characterization information on these four experimental materials can be found in Section 3 and Appendix A.

The system used for the tests on tubing is illustrated in Figure 4-1. The central part of the tube sample was heated in a small furnace. The test temperatures chosen were 590 K for Zircaloy-2 tubing and 630 K for Zircaloy-4 tubing because these are approximately the temperatures of operation of BWR and PWR claddings. The sample was strained locally by pressing a 1.6-mm-diameter steel ball against its outside surface. A lever system and a known dead weight were used to generate accurate indenter loads. The direction of motion of the indenter was parallel to the diameter of the tube and perpendicular to its length. As the tube wall was strained by the indenter, a small dimple (typically 1-2 mm in diameter) developed on the inside surface of the tube that was exposed to an Ar-I_2 gas stream flowing through the tube interior. The mixed gas was dried over Drierite before entering the tube sample in the vicinity of the dimple location. The tube sample could be evacuated to
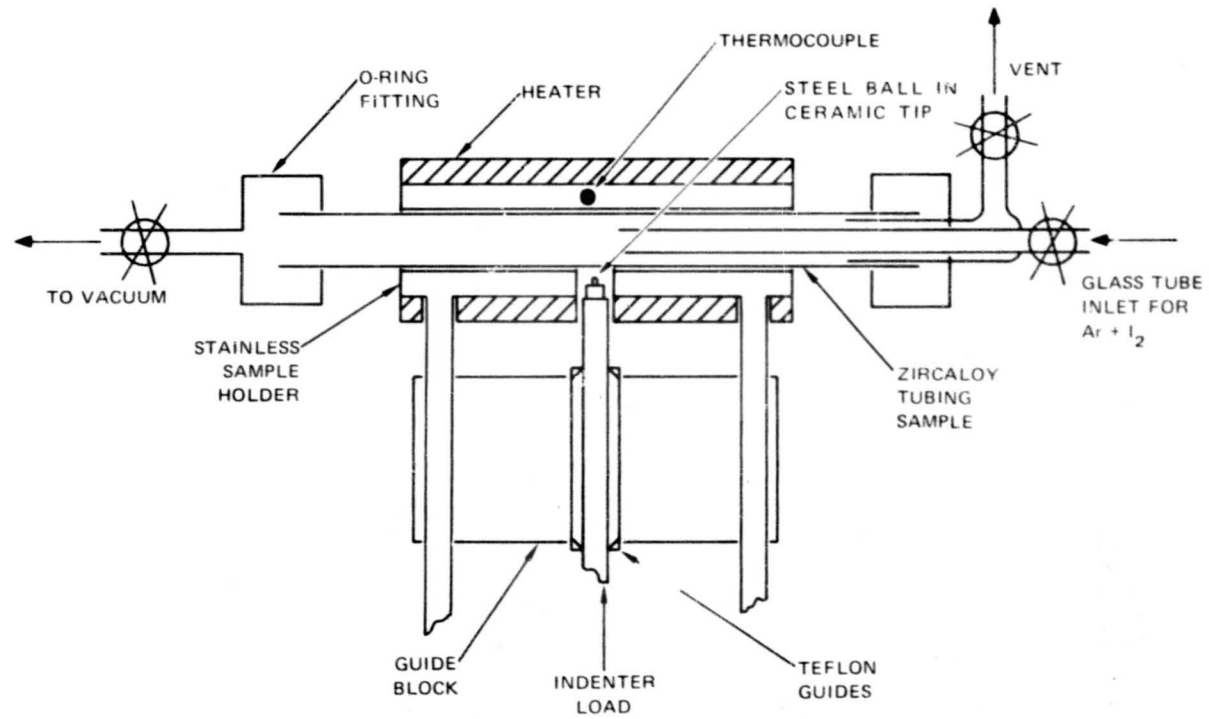
FIGURE 4-1   SCHEMATIC DIAGRAM OF INDENTER APPARATUS FOR TUBING SAMPLES

SA-4197-172

remove air and water vapor before starting the gas flow. Adjusting the position of the sample relative to the indenter allowed several dimples to be produced (under the same or different conditions as desired) in a single tube length.

The apparatus used for sheet samples is shown in Figure 4-2. The loading system described above was used to press the indenter into the center of a 10-mm-diameter disc sample. When the sample was under load, it pressed against a gold O-ring gasket, which in turn pressed against a support ring in the base of the molybdenum environmental chamber. Argon gas carrying I_2 flowed through the environmental chamber, which was heated to the desired test temperature. Thus, the dimple that developed on the side of the disc sample remote from the indenter was exposed to the combined action of an Ar-I_2 gas mixture and a biaxial tensile stress.

After the test, the samples were sectioned to recover the dimpled areas, which were then cleaned of surface oxide and corrosion products by argon ion milling. Milling was accomplished using an RF Bias DC Sputter Etch System (Materials Research Corp., Orangeburg, New York) at 820 volts, 300 watts in an Ar pressure of 0.3 Pa. Under those conditions, material was removed from the sample surface at approximately 1 μm per hour. In addition to cleaning off corrosion products, Ar-ion milling served to remove oxide films that had been preformed on some of the samples. The outlines of cracks that had been formed in the surface oxide due to the local strain generated by the indenter were etched into the sample surface during the ion milling step. Therefore, the relative locations of oxide and metal cracks could be observed. Figure 4-3 shows optical micrographs of the central regions of dimples in Zircaloy-4 sheet before and after Ar-ion milling. The initial surface had a preformed oxide film about 2-μm thick, which developed the cracking pattern shown in Figure 4-3a. Figure 4-3b shows the appearance of the metal surface after the oxide was removed by ion milling. Grooves were ion-etched into the metal surface beneath the cracks in the oxide.

The ion-etched surfaces of the dimples were examined in a scanning electron microscope (Cambridge Research Lab) equipped with an energy dispersive x-ray fluorescence analyzer (EDAX Corp.) capable of detecting elements heavier than Na at concentrations greater than about one percent.

CONTROLLED GAS ENVIRONMENT

Mo HOLDER

HEATER

SAMPLE

INDENTER BALL

HEATER

Mo HOLDER

SA-4197-146
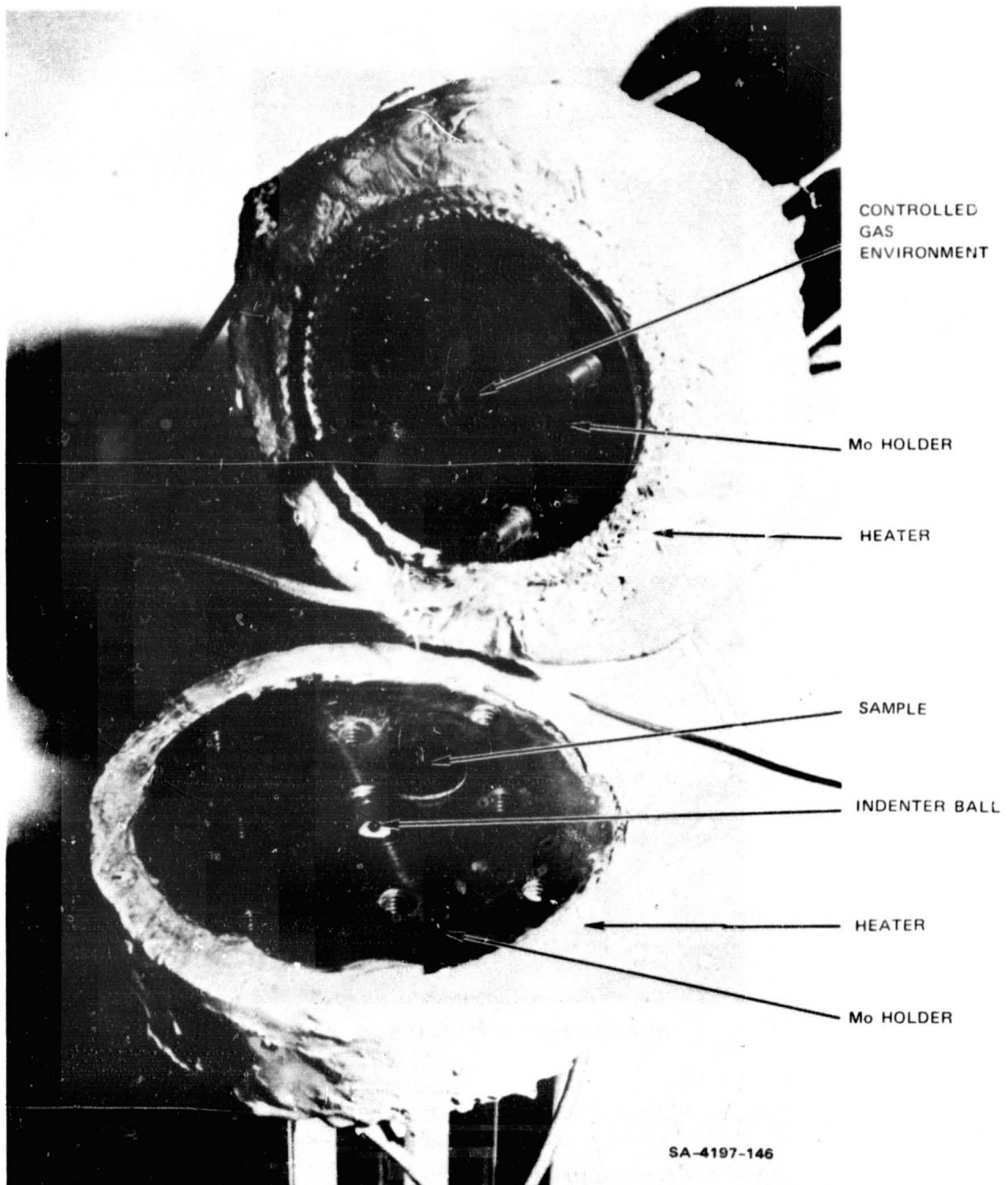
FIGURE 4-2   PHOTOGRAPH OF THE INDENTER APPARATUS FOR SHEET SAMPLES
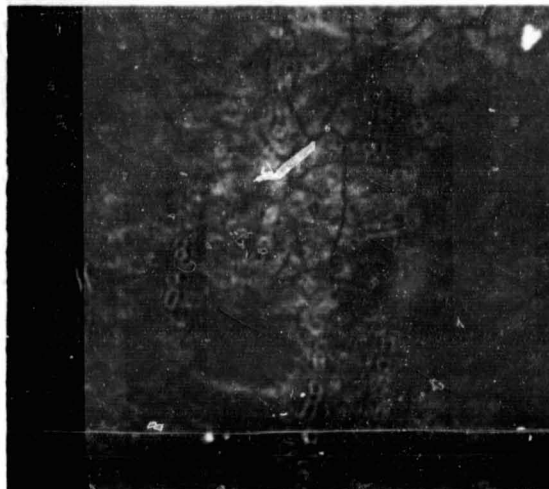
(a) BEFORE Ar-ION MILLING
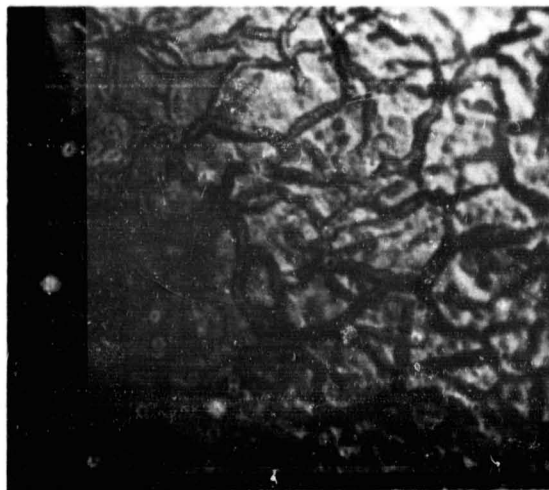
(b) AFTER Ar-ION MILLING FOR 2.8 HR

SA-4197-287

FIGURE 4-3   OPTICAL PHOTOGRAPHS OF TYPICAL DIMPLE CENTERS IN PREOXIDIZED
ZIRCALOY-4 SHEFT (50-kg LOAD, 40 Pa I_2, 570 K)

Width of each photograph = 0.2 mm

The local plastic strains at the dimples were quantified as a function of indenter load for each of the experimental materials by making optical measurements of the distortion of a grid of lines that had been scribed on the surfaces of specially prepared test samples. These measurements confirmed our expectations that the central region of the dimple was subjected to an almost perfectly balanced biaxial tensile stress and that the strain at the center of the dimple increased systematically with increasing indenter load.

RESULTS

Preliminary Work on Zircaloy-4 Sheet (9913-3B)

An initial series of tests was made with stress-relieved Zircaloy-4 sheet samples. In these tests the temperature was 570 K and the indenter load was 50 kg, which was sufficient to produce a dimple about 2 mm in diameter and 50 to 100 μm high. The tensile plastic strain near the dimple center was found to be 3 to 5 percent. The samples were exposed for times ranging from 5 to 200 minutes to either Ar or to Ar containing I_2 at a partial pressure of 40 Pa. The sample surfaces were oxidized at 670 K for 3 hours to form a thin, black oxide film prior to the tests.

No cracks were found in samples tested without I_2 present. In samples exposed to I_2, two kinds of cracks were observed in the metal surface. Small cracks were found in all samples exposed to iodine. In occasional samples, relatively large cracks were also observed. These larger cracks were associated with relatively large local concentrations of impurities (Al, Si, Ti) or alloying additives (Fe, Cr). Metal cracks of both types were found to be associated with cracks in the oxide.

Figures 4-4 and 4-5 show typical examples of the two types of cracks. Figures 4-6 shows an example of the larger type of crack in which the cracks in the metal followed oxide cracks and radiated out from a region containing elements other than Zr. Another such region is shown in Figure 4-7. The granular lumps in Figure 4-7 were typical of regions containing higher-than-normal concentrations of alloying additives and impurities. Similar features were also observed in samples that had not been exposed to I_2, but there were no cracks associated with those features
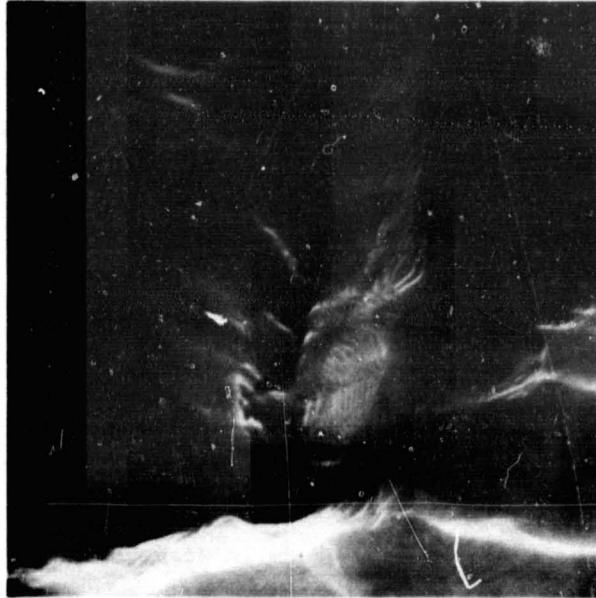
(a) 50-kg LOAD, 40 Pa I_2, 200 MIN, 570 K
Photograph width = 0.9 μm.

(b) 50-kg LOAD, 40 Pa I_2, 60 MIN, 570 K
Photograph width = 9 μm.

SA-4197-288

FIGURE 4-4   TYPICAL SMALL CRACKS IN PREOXIDIZED ZIRCALOY-4 SHEET
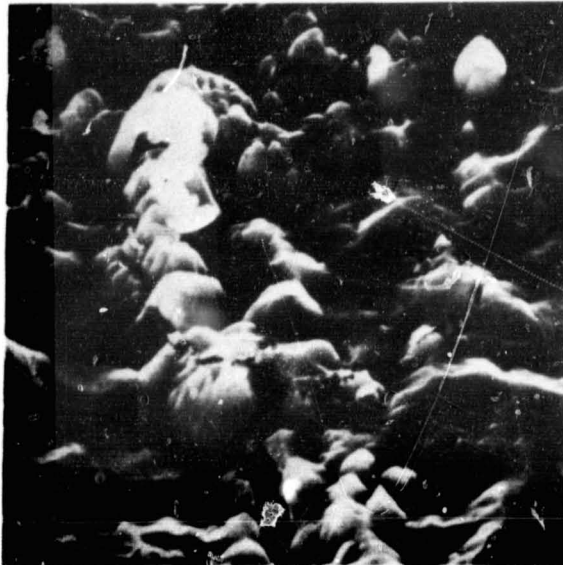
SA-4197-289

FIGURE 4-5   LARGE CRACK ASSOCIATED WITH IMPURITIES — PREOXIDIZED ZIRCALOY-4 SHEET, 50-kg LOAD, 40 Pa I_2, 20 MIN, 570 K

Light-gray granular lumps contained several percent Si, Fe, Cr, and some Al. Dark-gray matrix was only Zr. Width of photograph = 20 μm.
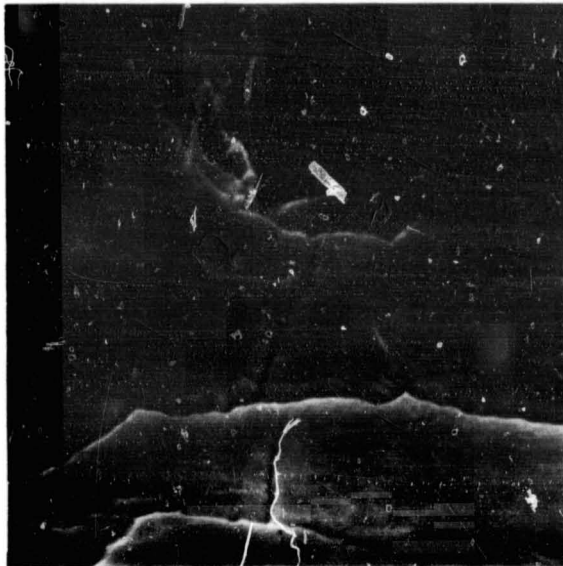
SA-4197-290

FIGURE 4-6   LARGE CRACK ASSOCIATED WITH IMPURITIES — PREOXIDIZED ZIRCALOY-4 SHEET, 50-kg LOAD, 40 Pa I_2, 60 MIN, 570 K

Ridge contained several percent Si, Al, and some Fe, Cr. Some oxide layer still present on surface (after 2 Hr. ion milling). Width of photograph = 20 μm.
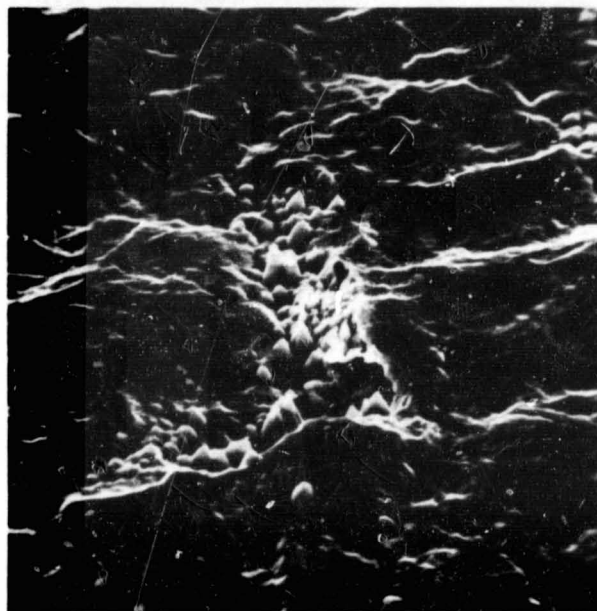
SA-4197-291

FIGURE 4-7   LARGE CRACK ASSOCIATED WITH IMPURITIES — PREOXIDIZED ZIRCALOY-4
SHEET, 40-kg LOAD, 50 Pa I_2, 30 MIN, 570 K

Light-gray granular lumps associated with crack contained several percent Ti, Fe, Cr.
Dark-gray matrix contained only Zr. Width of photograph $\doteq$ 100 μm.

since there was no iodine. The distinctive shape resulted from the ion milling process--apparently the regions with unusually high concentrations of alloying elements and impurities were more resistant to ion milling than the Zr matrix.

Grubb (4-4, 4-5) observed that Cd can cause embrittlement of Zircaloys; accordingly, we made a few tests in which pieces of Cd were placed on the surface of samples in an argon gas stream. The behavior in these tests was indistinguishable from that observed in tests made with Ar alone. In other tests, a stick of Cd was rubbed against the surfaces of samples (either preoxidized or as-received) before placing them in the test apparatus. In those samples many surface cracks were formed. Figure 4-8 shows a dimple formed on a sample that had been preoxidized, rubbed with Cd and tested, ion milled, and examined. The Cd seemed to have reacted in patches (light gray areas in Figure 4-8a) and where the oxide surface film had cracked to form granules of Zr-Cd intermetallic compounds. There were many surface cracks in the metal associated with the intermetallics in the strained region (Figure 4-8b). Apparently Cd caused cracks to form after it had been rubbed into the Zircaloy surface, but not when it was simply placed on the surface. We presume that the small amounts of oxygen present during the tests were sufficient to form films that prevented reaction of Cd with Zr except when the Cd was forced into intimate contact with the Zr metal by abrasion. No further tests were made with Cd because its aggressiveness toward Zircaloy was not reproducible in the present type of test.

Annealed Zircaloy-2 Tubing (7AH11-S)

A series of 80 tests was performed with samples of annealed Zircaloy-2 tubing. The parameters varied and the values used in the tests are given in Table 4-1. Two types of cracks in the metal surface were again observed: small cracks that occurred fairly routinely and a smaller number of relatively large cracks that were always associated with local concentrations of impurities in the metal surface.

Figure 4-9 shows micrographs of typical dimple centers. The grain structure of this recrystallized material is clearly evident. Many of the grains show features that we believe were caused by coplanar slip with a vector inclined to the sample surface. Other grains are featureless, which may indicate that their basal planes
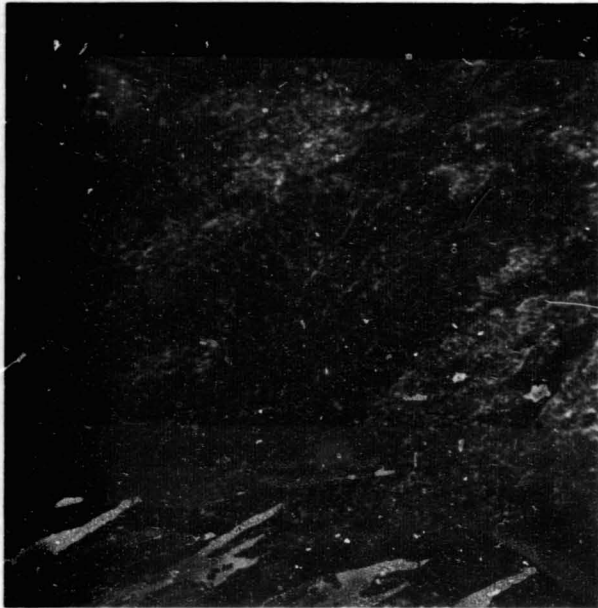
(a) **DIMPLE IS NEAR CENTER OF PHOTOGRAPH**
Sharp lines are oxide crack pattern etched into metal surface. Patches of light-gray in surrounding surface were Zr–Cd intermetallic. Width of photograph = 2 mm.
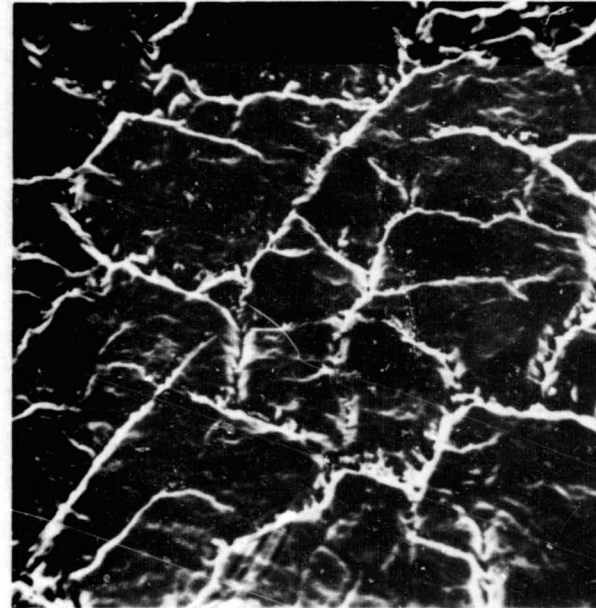
(b) **DIMPLE CENTER**
Metal cracks occurred at bottoms of oxide cracks where granular lumps of Zr–Cd intermetallic (light-gray lumps) formed. Width of photograph = 0.2 mm.

SA-4197-292

FIGURE 4-8   DIMPLE IN PREOXIDIZED ZIRCALOY SAMPLE RUBBED WITH Cd, 50-kg LOAD, 30 MIN, 610 K, Ar-ION MILLED

Table 4-1

VALUES OF PARAMETER USED IN INDENTER TESTS

Material	Iodine Pressures, Pa	Indenter Loads, kg	Percent Strain at Dimple Center	Times min	Surface Conditions	Temperature kelvins
Annealed Zircaloy-2 Tubing (7AH11-S)	0 0.03 0.4 4 40	30 40 50 70	3 ± 1 5 ± 1 8 ± 1 13 ± 1	5 30 180 1000	(1) (2) (3) (4)	590 ± 5
Zircaloy-4 Tubing (7FD11)	0 0.4 4 40	20 30 40 50	2 ± 1 4 ± 1 7 ± 1 11 ± 1	5 30 180 1000	(1) (2)	630 ± 5
Stress-Relieved Zircaloy-2 Tubing (7AH11-H)	0 0.03 0.4 4 40	40 50 70 100	2 ± 1 5 ± 1 11 ± 1 18 ± 1	30	(1) (2)	590 ± 5

Surface conditions:

(1) As received.

(2) Oxidized 3 hours at 670 K--oxide film ~ 0.2 μm thick, as calculated from literature data.

(3) Oxidized 5 hours at 770 K--oxide film ~ 1.5 μm thick, determined by weight-gain measurements.

(4) Oxidized 100 hours at 770K--oxide film ~ 5 μm thick, determined by weight-gain measurements.

(and their close packed slip directions) were parallel to the surface and to the applied tensile stress. Typical examples of small cracks can be seen in the figure. Those cracks usually extended one or two grains in length and almost always occurred at the boundaries of the featureless grains. We suggest that this indicates that such boundaries are subjected to unusually high local stresses during plastic deformation.

The frequency of occurrence of the small, integranular cracks was found to be larger, the greater the iodine partial pressure in the test environment. No cracks were observed in most of the tests in the absence of iodine; however, in the longest tests (1000 min, 30 kg) there were occasional indications of grain boundary separation.

The frequency of the small cracks in as-received samples was quantitatively found to increase slightly with increasing indenter load. However, as is evident from comparison of Figures 4-9a and 4-9b, the most noticeable effect of increasing the indenter load was to widen the cracks. Transgranular cracks were occasionally observed at large loads. The application time of the indenter load was not an important variable. Cracks occurred within the 5-minute period of the shortest test and the crack frequency for as-received samples was essentially independent of the time for which the indenter load was applied.

The results reported above were obtained with as-received specimens, presumably with an air-formed oxide film of the order of tens of nanometers thick. The as-received samples also suffered general corrosion, in addition to crack formation in environments containing iodine. Apparently, iodine somehow penetrated the thin oxide films during the tests. Since Zircaloy cladding in fuel rods has on its inside surface an oxide film of the order of micrometers thick, indenter tests were also run to investigate how thicker oxide films influence crack initiation.

Samples with three different oxide film thicknesses that were stressed under the same conditions of iodine pressure, load, time, and temperature are shown in Figure 4-10. Figure 4-10a shows a sample that was preoxidized to form an oxide

(a) AS RECEIVED, ANNEALED ZIRCALOY-2, 40-kg LOAD, 40 Pa I_2, 30 MIN, 590 K, ION MILLED 60 MIN
Width of photograph = 100 μm.
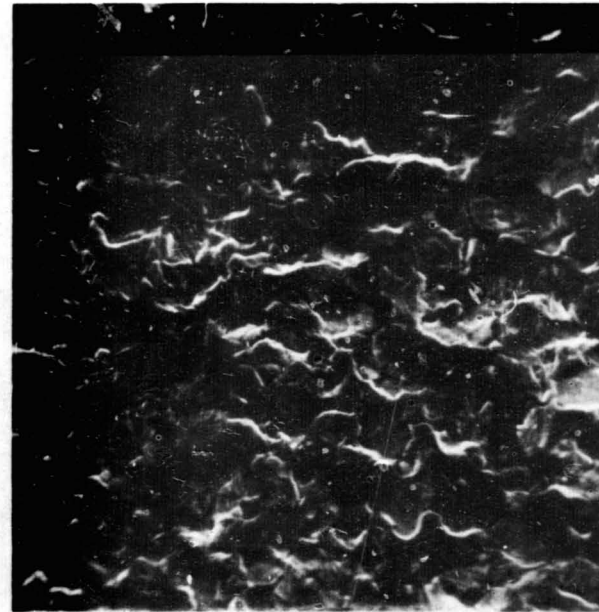
(b) AS IN (a) BUT WITH 70-kg LOAD
Width of photograph = 100 μm.

SA-4197-293

FIGURE 4-9   TYPICAL SMALL CRACKS IN ANNEALED ZIRCALOY-2 TUBING
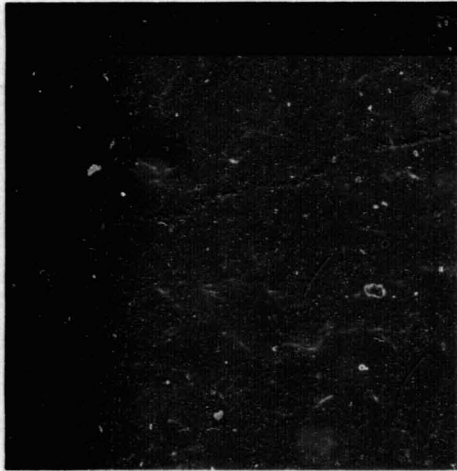
(a) ANNEALED ZIRCALOY-2 WITH 0.2-μm OXIDE 40 Pa I_2, 30-kg load, 30 min, 590 K, ion milled 60 min. The wrinkle marks are imprints of oxide cracks. Small metal cracks are present but difficult to discern. Width of photograph = 100 μm.
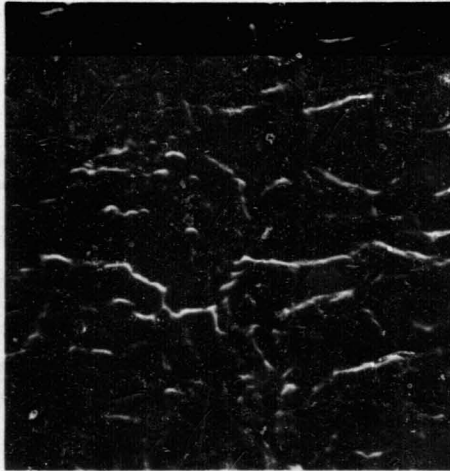
(b) ANNEALED ZIRCALOY-2 WITH 1.5 μm OXIDE 40 Pa I_2, 30-kg load, 30 min, 590 K, ion milled 150 min. Grooves are imprints of oxide cracks. A metal crack runs approximately vertically through the center. Granular lumps near center contain a few percent Fe. Width of photograph = 50 μm.
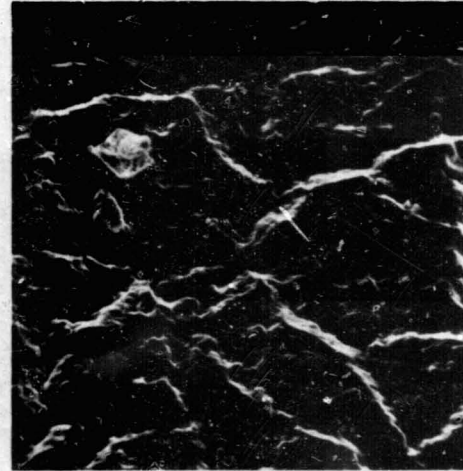
(c) ANNEALED ZIRCALOY-2 WITH 5-μm OXIDE 40 Pa I_2, 30-kg load, 30 min, 590 K, ion milled 390 min. Grooves are imprints of oxide cracks. Metal cracks are present but difficult to distinguish. Width of photograph = 100 μm.

SA-4197-294

FIGURE 4-10   TYPICAL SMALL METAL CRACKS FORMED ON PREOXIDIZED ZIRCALOY-2 SAMPLES

~ 0.2 μm thick. The surface of the metal shows some wrinkles, which were the result of oxide cracks ion-milled into the metal surface. Small cracks are present in the metal grain boundaries. With a thicker oxide (about 1.5 μm), the cracks in the metal generally were located at the bottom of oxide cracks, as shown in Figure 4-10b. The metal grain boundaries were difficult to see and it was hard to tell whether the cracks were intergranular or transgranular. Similar results were obtained with the thickest oxide studied (about 5 μm thick). Figure 4-10c shows the metal surface under a heavily oxidized specimen. The metal cracks were difficult to see so that only the larger cracks in the metal surface could be detected.

The most severe cracks in the metal always seemed to be associated with concentrations of alloying elements and impurities. The cracks shown in Figures 4-9 and 4-10 occurred in chemically "normal" regions in the metal and were rather small. Some specimens exhibited more severe cracking in regions containing higher than normal concentrations of foreign elements, principally Fe, Cr, Al, Si, and sometimes Sn, Mn, and Ti.

Figure 4-11 shows examples of severe cracking. The granular material in the largest cracks contained iron and impurity elements and is clearly associated with the cracks. Iodine was observed frequently in that granular type of material, but never in the matrix metal. While examining some unstressed surfaces, we found evidence that the granular material formed only when iodine was present and only in regions that contained impurities or alloying additives at levels of a few percent or more. Figure 4-12 shows the growth of granules after exposure to iodine of a region surrounding an inclusion that was rich in Fe and Cr. The granules contained a few percent Fe. Inclusions rich in Fe and impurity elements were also frequently observed after ion milling of surfaces that had not been exposed to iodine.

Zircaloy-4 Tubing (7FD11)

A series of 34 tests was made with stress-relieved Zircaloy-4 tubing. The values of the test parameters are given in Table 4-1. Because the stress-relieving temperature for this tubing was fairly low (770 K), oxide films thicker than ~ 0.2 μm could not conveniently be formed by thermal oxidation without affecting the
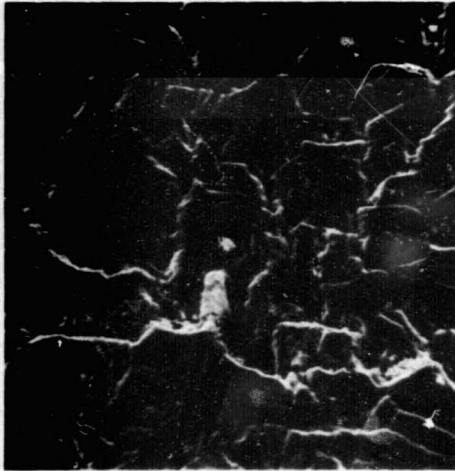
(a) ANNEALED ZIRCALOY-2 WITH 1.5 μm OXIDE 40 Pa I_2, 70–kg load, 30 min, 590 K, ion milled 330 min. Severe metal cracks formed under oxide cracks. The associated granular material contained several percent Fe, and some Al, Sn, and Ti. Width of photograph = 100 μm.
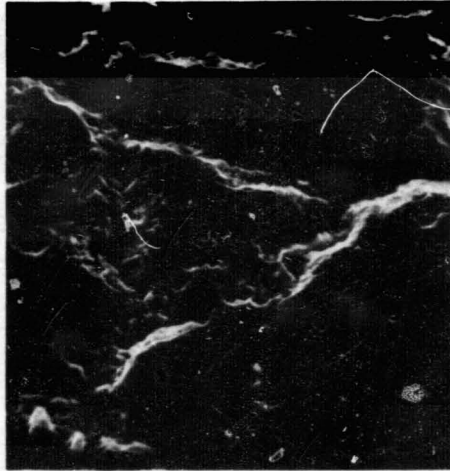
(b) ANNEALED ZIRCALOY-2 WITH 5–μm OXIDE 40 Pa I_2, 40–kg load, 30 min, 590 K, ion milled 330 min. The granular lumps associated with the metal cracks contain a few percent Fe, Cr, and Ti. Width of photograph = 100 μm.
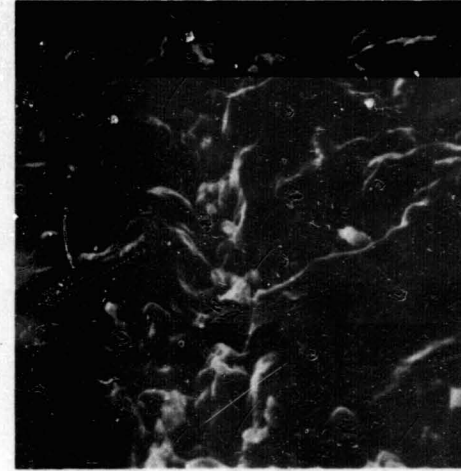
(c) ANNEALED ZIRCALOY-2 WITH 5–μm OXIDE 40 Pa I_2, 40–kg load, 30 min, 590 K, ion milled 300 min. The granular lumps in the cracks contained a few percent Fe, I, Cr, and Mn. The matrix material was only Zr. Width of photograph = 50 μm.

SA-4197-295

FIGURE 4-11 METAL CRACKS ASSOCIATED WITH IMPURITIES IN PREOXIDIZED SAMPLES OF ZIRCALOY-2

4-18
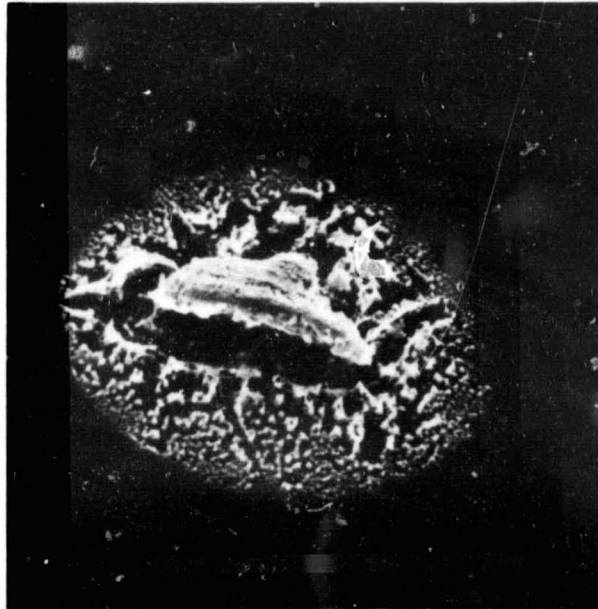
SA-4197-296

FIGURE 4-12   GRANULAR MATERIAL FORMED NEAR AN INCLUSION IN AN UNSTRESSED
REGION OF STRESS-RELIEVED ZIRCALOY-2

As-received, 40 Pa I_2, 100 min, 590 K, ion milled 30 min. The inclusion near the
center contained > 20% Fe + Cr. The small, surrounding granules contained a few
percent Fe. The matrix material was only Zr. Width of photograph = 100 μm.

mechanical properties of the material (in contrast to the case of annealed Zircaloy, which had been heat treated at 840 K).

Figure 4-13 shows the nature of the metal surface at a typical dimple after ion milling. Metal grains were not distinguishable in SEM photos of this material. There were two types of cracks--the small ones shown in Figure 4-13 and the larger ones shown in Figure 4-14. The frequency of the small cracks increased with iodine pressure and also seemed to increase somewhat with load and time under load. The large cracks (Figure 4-14) were again associated with local concentrations of additives or impurities. Because the presence of an impurity concentration in the dimple region was not a controllable parameter, the influence of test variables on the frequency of the large cracks could not be established.

Samples that had a preformed oxide film are shown in Figure 4-15. Most of the lines in the sample surfaces are grooves etched into the metal at oxide cracks; however, some cracks in the metal are present. The larger ones in Figure 4-15b are associated with granular lumps of Fe-containing material.

In some samples the depths of the cracks were estimated by repeated ion milling and SEM examination. Most of the cracks appeared to be about 10 μm deep but a few cracks penetrated into the metal at least twice that far.

Usually, no cracks were observed in samples indented in the absence of iodine. However, samples subjected to high indenter loads (40 and 50 kg) and long times under loads (1000 minutes) in the absence of iodine exhibited small surface defects that tended to be holes rather than cracks. We believe that these defects indicate the initiation of ductile creep-rupture failure.

Figure 4-16 shows some pits observed in an unstrained region of a Zircaloy-4 tube sample. Similar pits can be seen in Figure 4-13b, which shows the strained surface of the same sample. The pits do not appear to be associated with metal cracks. Before ion milling, the pits were covered with mounds of corrosion products, and the surfaces around the pits had a layer of corrosion product containing Fe and Al. We believe that the original metal surface contained local spots rich in Fe and Al,
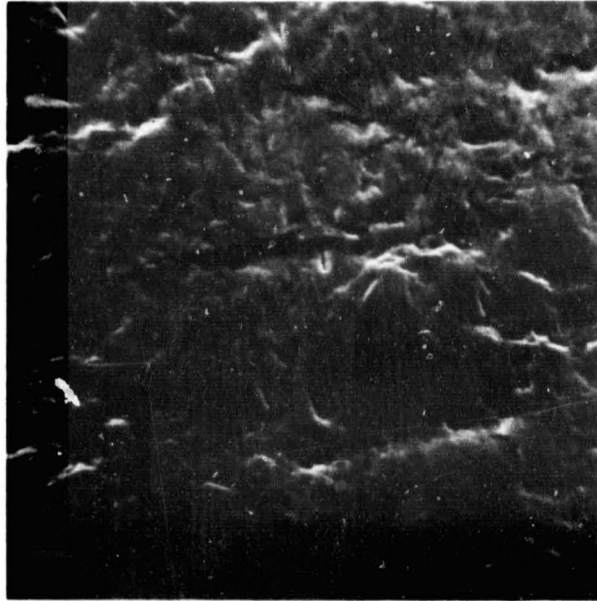
(a) AS RECEIVED, 40 Pa I_2, 40-kg LOAD, 1000 MIN, 630 K, ION MILLED 45 MIN
Width of photograph = 100 μm.
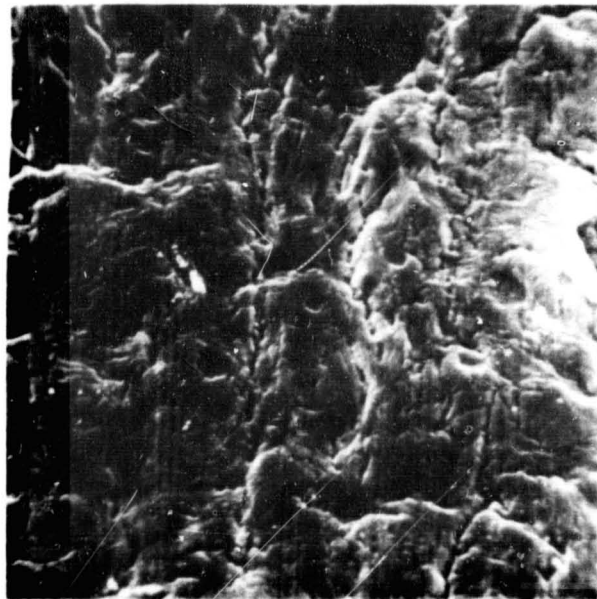
(b) AS RECEIVED, 4 Pa I_2, 50-kg LOAD, 30 MIN, 630 K, ION MILLED 45 MIN
Width of photograph = 100 μm.

SA-4197-297

FIGURE 4-13   TYPICAL SMALL CRACKS IN STRESS-RELIEVED ZIRCALOY-4
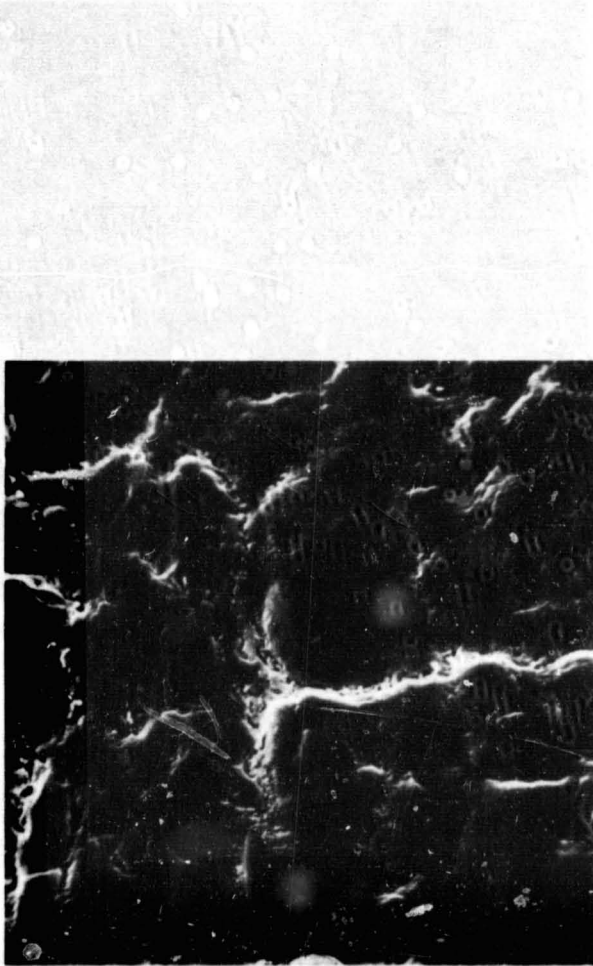
SA-4197-298

FIGURE 4-14   CRACKS ASSOCIATED WITH IMPURITIES IN ZIRCALOY-4

As received, 40 Pa I_2, 50 kg load, 30 min, 630 K, ion milled 45 min. Granular
material in the cracks is typical of Fe-rich material. Width of photograph = 100 μm.
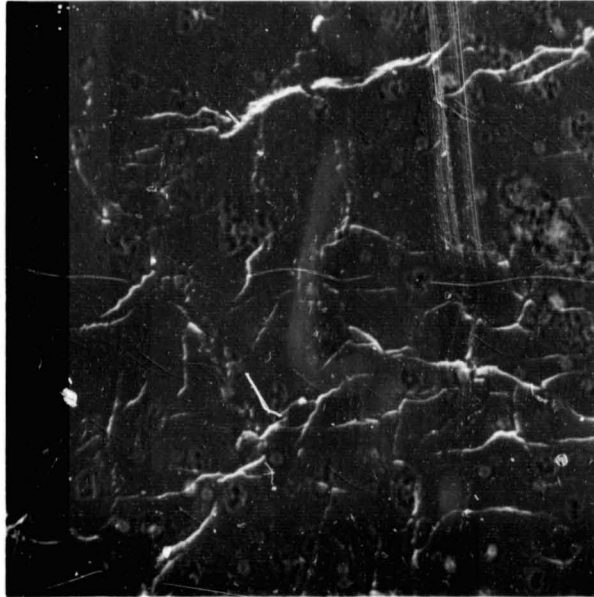
(a) STRESS-RELIEVED ZIRCALOY-4, 0.2 μm OXIDE
40 Pa I_2, 40-kg load, 30 min, ion milled 45 min. Small cracks possibly with some impurity. Width of photograph = 100 μm.
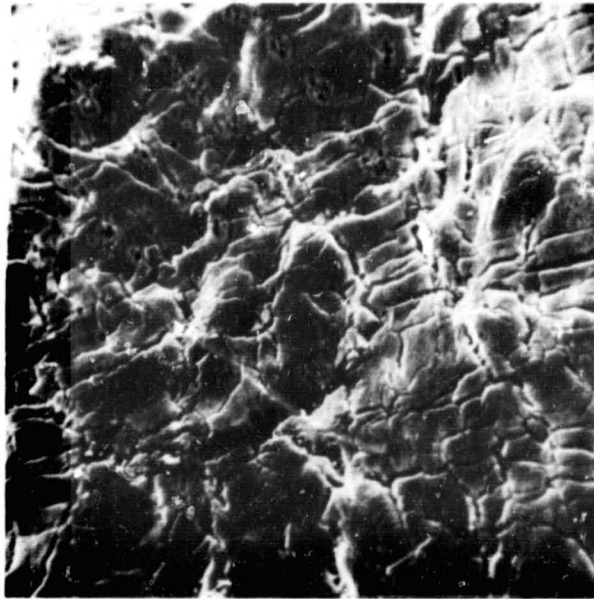
(b) SAME AS (a) BUT WITH 50-kg LOAD
Large metal cracks associated with Fe-rich granules. Width of photograph = 100 μm.

SA-4197-299

FIGURE 4-15   METAL CRACKS IN PREOXIDIZED ZIRCALOY-4 TUBING SAMPLES

and that attack by iodine generated AlI_3 and FeI_2 (probably ZrI_4 also), which were volatile at the test temperature and coated nearby surfaces.

Stress-Relieved Zircaloy-2 Tubing (7AH11-H)

A series of 28 tests was performed with stress-relieved Zircaloy-2 tubing. The values of the test parameters are given in Table 4-1.

In this material, as in the others, two kinds of cracks appeared--small ones that were randomly distributed and occasional larger ones associated with concentration: of impurities or alloying additives. No cracks were observed in the absence of iodine. Figure 4-17 shows a typical surface with small cracks. The frequency of these cracks increased with iodine pressure; increased load resulted in wider cracks with a slight increase in frequency. Figure 4-18 shows the surface of a preoxidized sample that contained some of the larger cracks. The association of these cracks with local concentrations of impurities and alloying additives is clearly apparent.

Cracking of Oxide Films

During this study of crack initiation, we obtained some information about the mechanical behavior of the preformed oxide films. The frequency of oxide cracks in the dimple region was determined for a number of the indenter test specimens. A random line counting technique developed by Smith and Guttman (4-5) was used to measure the crack frequency.

Effect of Strain. The oxide cracking frequency (i.e., length of oxide crack per unit surface area) is shown as a function of the strain imposed by the indenter in Figure 4-19. The oxide cracking frequencies were measured at the centers of the dimples formed in indenter tests on Zircaloy-4 tubing at different loads. The oxide crack frequency increases linearly with plastic strain above about 2 percent. Other tests demonstrated that at 630 K the oxide began to crack at total strains (elastic plus plastic) of the order of 0.4 percent. The dashed line in the figure indicates the onset of oxide cracking in that strain region.

SA-4197-300

FIGURE 4-16   CORROSION PITS FORMED IN UNSTRESSED AREA OF ZIRCALOY-4 TUBING

Exposed to 4 Pa I_2, 120 min, 630 K, ion milled 45 min. The white lumps in the pits contained a few percent Fe and some I. Before ion milling the whole surface was covered with a layer containing Fe, Al, and I and had mounds of corrosion product over the pits. Width of photograph = 50 μm.
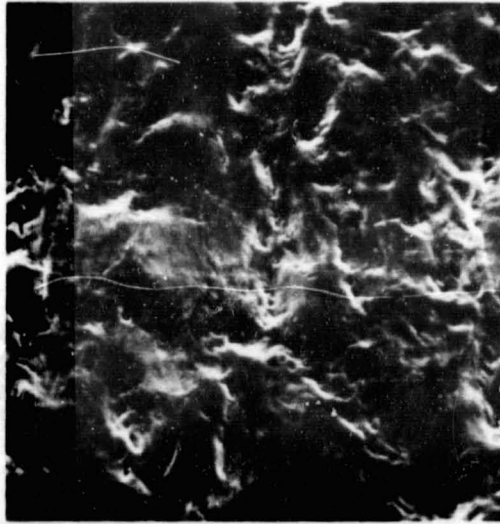
SA-4197-301

FIGURE 4-17   TYPICAL SURFACE OF STRESS-RELIEVED ZIRCALOY-2 SHOWING
SMALL CRACKS

As received, 40 Pa I_2, 100-kg load, 30 min, 590 K, ion milled 30 min.
Width of photograph = 100 μm.
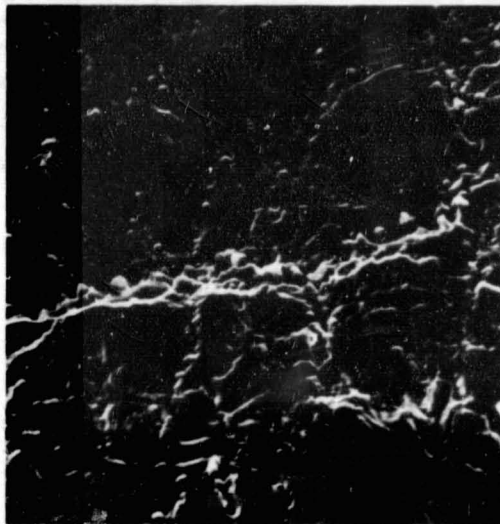
SA-4197-302

FIGURE 4-18   LARGE CRACKS AND ASSOCIATED IMPURITIES IN THE SURFACE OF A
PREOXIDIZED SAMPLE OF STRESS-RELIEVED ZIRCALOY-2

0.2-μm oxide, 40 Pa I_2, 70-kg load, 30 min, 590 K ion milled 120 min.
The lumps in the cracks contain several percent I, Fe, and Cr. Width of
photograph = 100 μm.
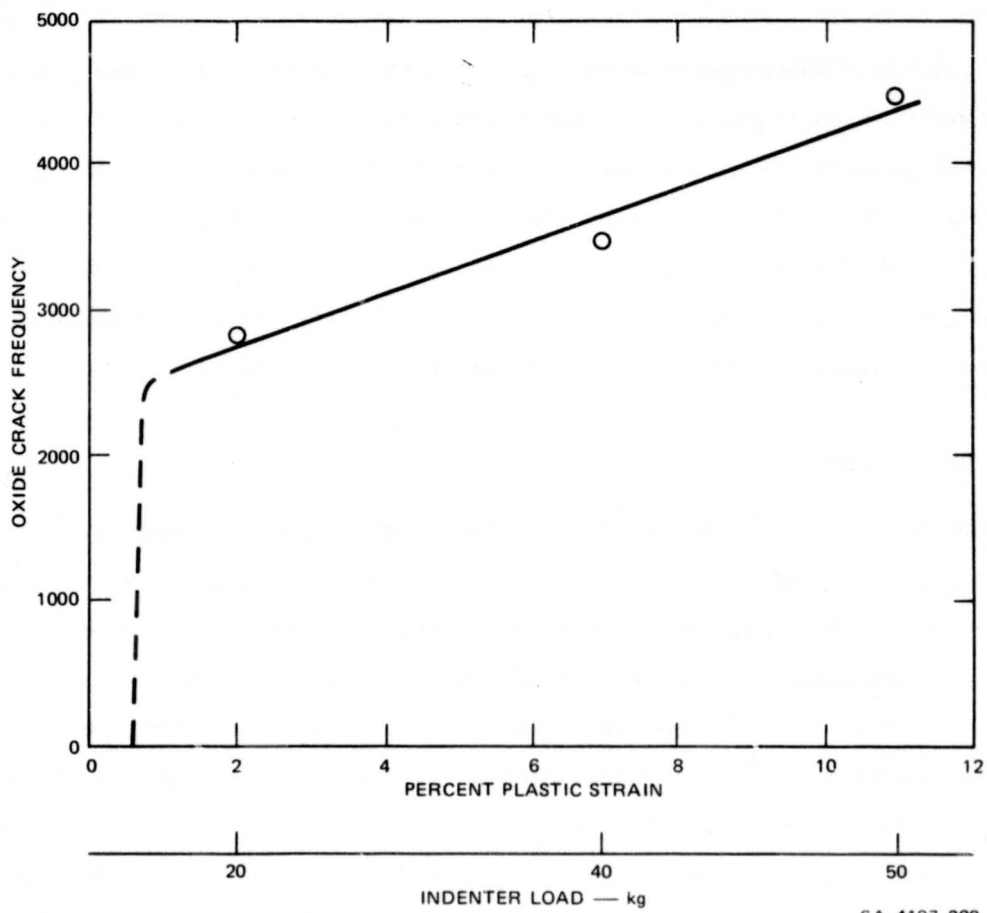
FIGURE 4-19   OXIDE CRACKING FREQUENCY OBSERVED WITH SLIGHTLY OXIDIZED
ZIRCALOY-4 TUBING AS A FUNCTION OF STRAIN (LOAD)

Effect of Oxide Thickness. The frequencies of oxide cracks were measured on films of various thickness. The thinnest oxide studied was the air-formed film on "as-received" materials, which was estimated to be less than 0.1 μm thick. The other oxides were formed as described above. The dependence of oxide cracking frequency on oxide thickness at constant strain and temperature is shown in Figure 4-20. Our interpretation of the results is indicated by the dashed lines in the figure. During the thermal oxidation of Zircaloys, the nature of the oxide film changes when it reaches a thickness of 2 to 3 μm. The thicker films are less protective. The change in oxide cracking frequency between thin films and thick films shown in Figure 4-20 probably is related to the change in the protectiveness of the oxide film observed in thermal oxidation. The results indicate that oxide films about 1 to 2 μm thick show a greater frequency of cracking than either thicker films (about 5 μm) or thinner films (less than 0.5 μm thick), possibly because of the nature of the stresses generated in the oxides when they are formed.

DISCUSSION AND CONCLUSIONS

In the absence of iodine, cracks were observed only under the most severe combinations of indenter load and time under load. These cracks probably were attributable to creep-rupture failure. When iodine was present, cracks were formed under much less severe mechanical conditions but only in the strained dimple regions of the samples. Cracks were not observed in the unstrained parts of test samples exposed to iodine, although pitting attack sometimes occurred in such regions (Figure 4-16). Therefore, both the presence of iodine and mechanical deformation were required to form the cracks shown in Figures 4-4 through 4-7, 4-9 through 4-11, 4-13 through 4-15, 4-17, and 4-18. Hence, we can conclude that these cracks are a manifestation of iodine-induced SCC.

Two types of iodine-induced cracks were observed in all four materials tested. Small cracks were observed in all samples strained in iodine and relatively large cracks were also observed in some samples.

The small cracks generally seemed to form at microstructural inhomogeneities (such as certain grain boundaries in recrystallized material) that would be expected to
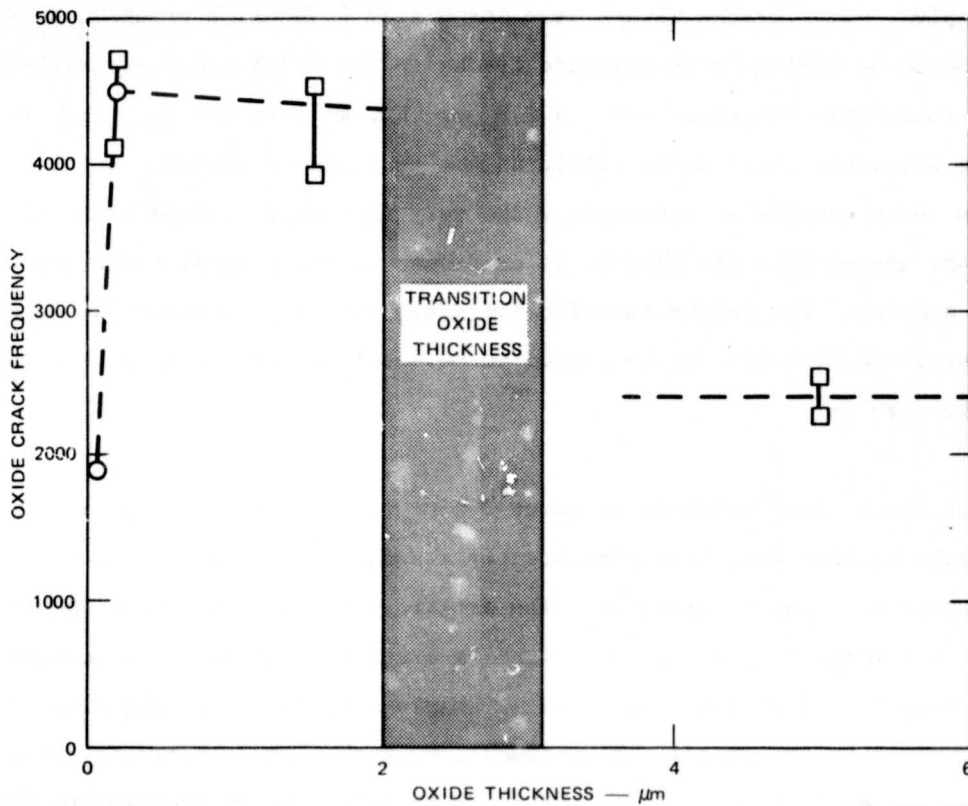
FIGURE 4-20   OXIDE CRACKING FREQUENCY AS A FUNCTION OF OXIDE
THICKNESS AT CONSTANT STRAIN AND TEMPERATURE

be associated with large local stress concentrations in material undergoing plastic flow. These cracking sites were not associated with any chemical inhomogeneities that could be detected in the SEM. The frequency of occurrence of the small cracks increased with increasing iodine pressure but was not very dependent on strain (indenter load) or time under load. We did not find either an iodine pressure or a plastic strain below which cracks did not form. The lowest imposed values of these variables in the present tests were 0.03 Pa I_2 and $\sim 1\%$ strain. In preoxidized samples, metal cracks always were associated with oxide cracks. We suspect that it would be difficult to initiate cracks in the metal under noncracked oxide films of reasonable thickness (say, ≥ 0.5 μm), but we have not confirmed this by examining specimens strained so little as not to crack the oxide. However, iodine does seem to be capable of penetrating the very thin oxide formed at room temperature on the as-received Zircaloy-4, as evidenced by the general corrosion of as-received samples. The depths to which the small cracks penetrated the metal was not investigated, but the cracks seemed to be about as deep as they were long (typically ≤ 10 μm).

The larger cracks were observed in about 30% of the samples and differed from the small cracks in that they were consistently associated with local concentrations of impurities or alloying elements. The erratic occurrence of these larger cracks probably is related to the chance of finding a suitable chemical inhomogeneity within a randomly located ~ 1 mm^2 area of sample surface (i.e., the area of the dimple produced by the randomly positioned indenter). The relatively infrequent occurrence of these cracks made it difficult to determine whether any of the experimental variables affected their frequency or size. However, the preoxidized samples showed a clear association between the locations of oxide and metal cracks. Although the cracks associated with chemical inhomogeneities were larger than the other types of cracks, they did not seem to extend more than about 20 μm into the metal. This may indicate that the tensile stress decreased rapidly below the dimple surface or that neither of the two types of crack nuclei observed in the present work is capable of propagating. However, if the threshold stress for iodine SCC observed in tube pressurization tests (see Section 5) is associated with crack formation [as suggested by Ranjan and Smith (4-1)], the crack nuclei

that are important in the overall iodine-SCC process should be formed only at stresses above the threshold stress. We therefore performed the additional experiment described below.

Two lengths of annealed Zircaloy-2 tubing (7AH11-S) were pressurized for 30 minutes at 590 K in the presence of iodine. The pressures were such that the nominal hoop stresses were 210 MPa and 310 MPa which are respectively below and above the threshold stress for iodine SCC of this tubing under internal pressurization ($\sim$ 280 MPa--see Section 5). After exposure, samples were cut out, and the inside surfaces were ion milled to remove corrosion products and then examined in the SEM. Small intergranular cracks similar to those shown in Figure 4-9 were observed in both samples. Larger cracks associated with local chemical inhomogeneities occurred at many sites in the sample stressed at 310 MPa, but were not observed in the sample stressed at 210 MPa. An example of a larger crack is shown in Figure 4-21. The crack is clearly associated with a local impurity concentration and follows along what appear to be the boundaries of the impurity-rich region. The crack in Figure 4-21 is indistinguishable in appearance from those observed in the indenter tests (see Figures 4-5 and 4-11). These results indicate that the larger cracks observed in the indenter experiments are capable of propagating and that the threshold stress for iodine SCC is associated with their formation.

The chemistry of the metal-environment system evidently plays a dominant role in iodine-induced crack initiation. Apparently, iodine reacts more readily with regions containing a few percent of certain elements than with zirconium itself. Since iodine was found in material near cracks even after surface layers had been ion-milled away, iodine probably was incorporated into the lattice in these regions. Perhaps the structure was modified by the presence of the foreign elements, allowing iodine to be accommodated more easily than in zirconium. In the presence of zirconium at these temperatures, iodine will react to form gaseous ZrI_4, which will in turn react to form solid iodides, such as $ZrI_{0.9}$, $ZrI_{1.6}$ and others (4-7). It has also been found that gaseous ZrI_4 reacts readily with certain metals (Cu, Ag, Ti) to form iodide compounds involving Zr and the other metal (4-8, 4-9). The
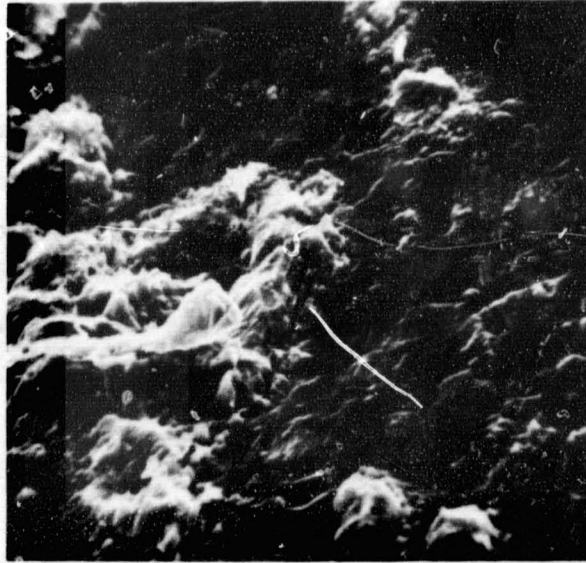
(a)   SHOWING THE WAY THE CRACK FOLLOWS THE RIDGE OF SLOWLY MILLED MATERIAL

Width of photograph = 45 μm.
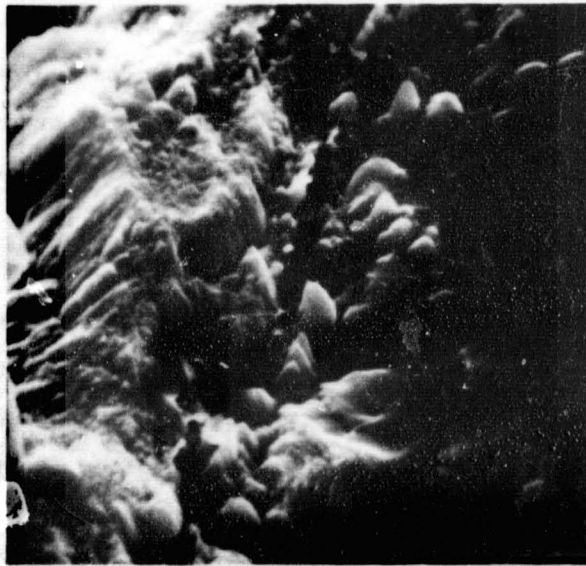
(b)   A HIGHER MAGNIFICATION VIEW OF THE UPPER PART OF THE CRACK

The spires in the center contained abnormal concentrations of Sn, Ti, and Fe.
Width of photograph = 9 μm.

SA-4197-324

FIGURE 4-21   A LARGER CRACK OBSERVED IN AN ANNEALED ZIRCALOY-2
PRESSURE TEST SPECIMEN STRESSED AT 310 MPa IN THE
PRESENCE OF IODINE

Iodine partial pressure clearly would affect the rate of such reactions and this may explain why the frequency of cracking in constant time tests depends on iodine pressure.

The present results are consistent with the crack formation mechanism suggested by Cox and Wood (4-2). Because ZrO_2 is thermodynamically very stable with respect to iodine, penetration of the oxide is a necessary first step in the cracking process. At reactor operating temperatures, penetration of oxide films a few micrometers in thickness appears to require that the material be strained a few tenths of one percent, whereas iodine seems to be able to penetrate thinner oxide films in the absence of an applied stress. The mechanism involved in the latter case is not known.

Once the iodine reaches the metal, it reacts to form ZrI_4. The ZrI_4 reacts in turn with susceptible sites (e.g., local impurity concentrations or second phase particles such as described in References 4-10 and 4-11), and produces mixed iodide compounds of Zr plus impurities. The iodide presumably penetrates into the metal in the impurity-containing regions and, possibly because of a volume increase or because of weakening of intermetallic bonds, the local material fractures if the applied stress exceeds a certain level, resulting in the formation of a sharp crack.

A similar process may account for the formation of the small cracks observed. No detectable chemical inhomogeneities were associated with these cracks. However, segregation of iron to the surface of dilute zirconium-iron alloys has been reported (4-12) and it seems possible that segregation of iron and other elements to preferred sites such as grain boundaries occurs in Zircaloys. Such segregation would make the grain boundaries more reactive toward iodine than the bulk, leading to the formation of compounds in the grain boundary. During plastic flow, weakened boundaries that experienced particularly severe local stresses (associated with the orientations of the adjacent grains and the anisotropy of Zircaloy) would fail. Presumably, the small crack nuclei formed in this way (which apparently are formed at applied stresses well below the threshold stress for iodine-SCC failure of

pressurized tubes) do not propagate because the microstructural configuration required to achieve a sufficiently severe local stress concentration exists only at a few isolated grain boundaries in the material.

In investigations of iodine SCC of Zircaloys using stressed ring specimens, the stressing mandrels usually have been made either of aluminum alloys or stainless steel--both of which contain elements found to be associated with the larger crack nuclei observed in this study. Also Wood has reported that iron is a catalyst for iodine SCC of Zircaloy (4-13). In some of our SEM examinations we found evidence that Al and Fe are transported by iodine. Possibly transport of those elements as iodides with the subsequent formation of Zr-metal iodides at local sites initiated cracks under those conditions.

Some of the regions in which we detected abnormally high concentrations of alloying elements and impurities were surprisingly large in size. In particular we found a 2-cm length of 7FD11 Zircaloy-4 tubing that contained 20 to 40% Fe over much of the inside surface. We also observed aluminum-rich particles ranging in size up to 0.3 mm buried in the inside surfaces of all three types of tubing. Because these features are connected with the initiation of the larger type of iodine-induced cracks, their origin is of interest.

A possible source of the aluminum-rich particles could be the alumina grit that sometimes is used to grit blast the inside surface of the tubing prior to final pickling. However, it is somewhat surprising that any aluminum contamination picked up in this way is not removed by the subsequent acid pickling. Perhaps insufficient material is removed to free the most deeply buried particles. In this connection, it is interesting to note that Picklesimer observed particles of lapping compound buried 50 to 100 μm below the surface of a Zircaloy-2 plate that had been lapped with 180- to 200-mesh particles on a copper wheel (4-14).

It is likely that any significant segregation of iron in the original Zircaloy ingot would be homogenized during ingot forging, which involves temperatures above the $\alpha \rightarrow \beta$ transus where iron is very mobile. Therefore, the observed iron segregation must arise at a later stage in the tube-making process. The most likely

source of iron contamination to which the tube I.D. is exposed is the tool-steel mandrel used in rocking reduction steps and indeed the mandrels used for intermediate reductions do show evidence of surface deterioration (4-15). However, here again it is surprising that any iron transferred from the mandrel to the tube surface is not removed by the acid pickling that follows each reduction step. Thus, we cannot convincingly account for the presence of chemical inhomogeneities of the type observed in the inside surfaces of Zircaloy tubing. However, because these inhomogeneities are preferred sites for the formation of iodine-induced stress corrosion cracks, more work is warranted to elucidate their origin and to develop methods of eliminating them.

REFERENCES

4-1 G. V. Ranjan and E. Smith, "Fracture of Zircaloy Cladding During Power Ramps by Interaction with Uranium Dioxide Pellets in Water Reactor Fuel Rods," Proceedings: ANS Topical Meeting on Water Reactor Fuel Performance, St. Charles, Illinois, May 1977.

4-2 B. Cox and J. C. Wood, "Iodine Cracking of Zircaloy Fuel Cladding--A Review," in Corrosion Problems in Energy Conversion and Generation, Craig S. Tedman, Jr. ed. (Electrochemical Soc., New York, 1974), p. 275.

4-3 B. van der Schaaf, "Fracture of Zircaloy-2 in an Environment Containing Iodine," in Zirconium in Nuclear Applications, ASTM STP 551, American Society for Testing and Materials, 1974, pp. 479-494.

4-4 W. T. Grubb, Nature, 265, 36 (1977).

4-5 W. T. Grubb and M. H. Morgan, III, "Cadmium Embrittlement of Zircaloy-2," Proceedings: ANS Topical Meeting on Water Reactor Fuel Performance, St. Charles, Illinois, May 1977.

4-6 C. S. Smith and L. Guttman, Trans. TMS-AIME, 197, 81 (1953).

4-7 D. Cubicciotti et al., "Thermodynamics of Zirconium Iodides at Elevated Temperatures," Proceedings: Symposium on Metal-Halide Chemistry at High Temperatures, October 1977, Electrochemical Society, Princeton, New Jersey, 1978.

4-8 Z. A. Bhatti, D. B. Copley, and R.A.J. Shelton, "Titanium-Zirconium Triiodides, J. Less Common Metals 18, 99 (1969).

4-9 K. Lascelles and R.A.J. Shelton, "Formation of Compounds $M_{1/4}M'_{3/4}I_3$ by the Reaction of ZrI_4 and HfI_4 with Copper and Silver," J. Less Common Metals, 25, 49 (1971).

4-10 J. B. van der Sande and A. L. Bement, "An Investigation of Second Phase Particles in Zircaloy-4 Alloys," J. Nucl. Mat., 52, 115 (1974).

4-11 P. Rao, J. L. Walker, and E. F. Koch, "Intermetallic Particles in Zircaloy-2 and Zircaloy-4," Report 76CRD 183, General Electric Co., Schenectady, New York, 1977.

4-12 R. S. Polizzotti and J. J. Burton, "Surface Segregation in Alloys: Dilute Binary Iron/Zirconium Solid Solutions," J. Vac. Sci. Technol., 14, 347 (1977).

4-13 J. C. Wood, "Factors Affecting Stress Corrosion Cracking of Zircaloy in Iodine Vapor," J. Nucl. Mat., 45, 105 (1972).

4-14 M. Picklesimer, U. S. Nuclear Regulatory Commission, Private Communication.

4-15 T. D. Naylor, Sandvik Special Metals Corp., Private Communication.

Section 5

IODINE-INDUCED FAILURE OF INTERNALLY
PRESSURIZED ZIRCALOY TUBES

INTRODUCTION

Because the propagation of stress corrosion cracks usually is quite rapid, compo-
nent failure is often imminent as soon as crack growth begins. This is particu-
larly true for PCI failure of nuclear fuel cladding, where crack propagation for
a distance of only a few hundred micrometers leads to penetration of the cladding
wall. It is therefore important to determine whether any threshold conditions
exist that must be satisfied before fission-product-induced stress corrosion
cracking (SCC) of thin-walled Zircaloy tubes can occur at reactor operating
temperatures.

Novak and Rolfe (5-1) showed that the growth of a sharp, deep flaw in an elasti-
cally stressed specimen exposed to a corrosive medium was determined by the magni-
tude of the elastic stress field at the flaw tip (as described by the opening
mode stress intensity K_I) rather than by the nominal tensile stress applied to the
specimen. From studies on SCC in maraging steels, they concluded (5-1) that
flaw growth would not occur unless K_I exceeded a threshold value termed K_{Iscc}.

Novak and Rolf's conclusion has since been verified for many cases of SCC and in
some instances, values of K_{Iscc} measured in the laboratory have aided in designing
against SCC failure. However, application of the K_{Iscc} concept to SCC of fuel clad-
ding is problematical because the preexisting surface flaws present in nuclear
grade Zircaloy tubing are very tiny (see, for example, Figure 3-5). This limits
the magnitude of the stress intensity that can be generated at the flaw tip and
increases the likelihood that a parameter other than stress intensity will control
the onset of SCC. In fact, it has often been observed in other metal/environment

systems that environment-assisted growth of very small flaws can proceed at nominal stress intensities well below K_{Iscc} and that stress is a more useful SCC threshold criterion than stress intensity (5-2).

The objective of the work described in this section of the report was to determine whether stress, stress intensity, or some other parameter such as strain or strain rate could be used as a threshold criterion for SCC failure of Zircaloy tubing. As explained earlier, iodine was chosen as the test environment because of its consistent and reproducible aggressiveness toward Zircaloy. Internal pressurization was selected as the test method because it allows accurately known states of general stress and local stress intensity to be generated in tubing specimens. A particular objective of the work was to define at least a preliminary threshold criterion for iodine-induced failure of irradiated Zircaloy tubing, since relatively little published information is available on this aspect of the SCC behavior of irradiated cladding (5-3). Pressurization experiments on irradiated power reactor cladding were therefore conducted under subcontract in the hot cells at Argonne National Laboratory (ANL).* A parallel series of tests was conducted at SRI on unirradiated material to help set the test conditions for the hot cell tests and to investigate the effects of material, environment, and test variables.

MATERIALS AND TEST METHOD

The tests at SRI were conducted on stress-relieved Zircaloy-4 tubing (7FD11) at 630 ± 5 K (PWR cladding service temperature) and on stress-relieved and annealed Zircaloy-2 tubings (7AH11-H and 7AH11-S, respectively) at 590 ± 5 K (BWR cladding service temperature). The metallurgical characteristics, dimensions, and compositions of those three tubing lots are discussed in Section 3 and Appendix A. The tests at ANL were conducted at 630 K on stress-relieved Zircaloy-4 (7FD11) and on irradiated Zircaloy-4 cladding from the H.B. Robinson reactor (HBR Zircaloy-4). Unfortunately, no information was available regarding the fabrication history or

---

*This work formed the basis for an expanded project at ANL to characterize the mechanical and SCC behavior of power reactor cladding, RP 1027.

metallurgical characteristics of the HBR cladding, but we presume that it was metallurgically similar to the 7FD11 Zircaloy-4 which had a similar inside diameter and wall thickness. The fast neutron fluence to which the HBR Zircaloy-4 specimens had been exposed was estimated to be about 3.6×10^{21} neutrons/cm^2, based on the position of the test specimens in the fuel rod and the known peak flux.

The unirradiated test specimens were about 13 cm long and the irradiated specimens were 10 cm to 15 cm long. All the Zircaloy-2 specimens were tested in the unflawed (as received) condition. 7FD11 Zircaloy-4 and HBR Zircaloy-4 specimens were tested both in the unflawed condition and with machined preflaws present. The outside diameters of unflawed, unirradiated specimens were reduced by about 250 μm in the central ~ 3 cm of their length to ensure that failure occurred at a location remote from the pressure fittings. The nominal dimensions of the preflawed Zircaloy-4 specimens are shown in Figure 5-1. Figure 5-2 illustrates the shape and dimensions typical of actual machined preflaws, based on examinations of polyvinyl acetate replicas, supplemented by the results obtained from two specimens that were serially sectioned.

All unirradiated specimens were prepared for testing by successively soaking them with methanol, acetone, and ethanol, followed by etching for 10 seconds in a solution consisting of 45 parts of 70% HNO_3 45 part of 3% H_2O_2, and 9 parts of 48% HF. After etching, the specimens were thoroughly rinsed twice in deionized water and then dried with an air blast. Measurements of inside and outside diameter were made at several locations prior to testing. One of the 7AH11-S Zircaloy-2 specimens was oxidized before testing for 5 hours at 770 K to form an oxide film ~ 1.5 μm thick. All the other unirradiated specimens were tested as etched. Most of the HBR Zircaloy-4 specimens were prepared for testing by removing the fuel, cleaning the tubing lengths, and machining the preflaws (when used).

Figure 5-3 shows the tube pressurization system used for the tests at SRI. The ANL system differed in detail but was similar in overall function and capabilities. The air-driven gas booster (Haskel model AG) was used to pressurize the bottled high-purity helium to ~ 100 MPa and pump it to the reservoir. Gage No. 1 allowed
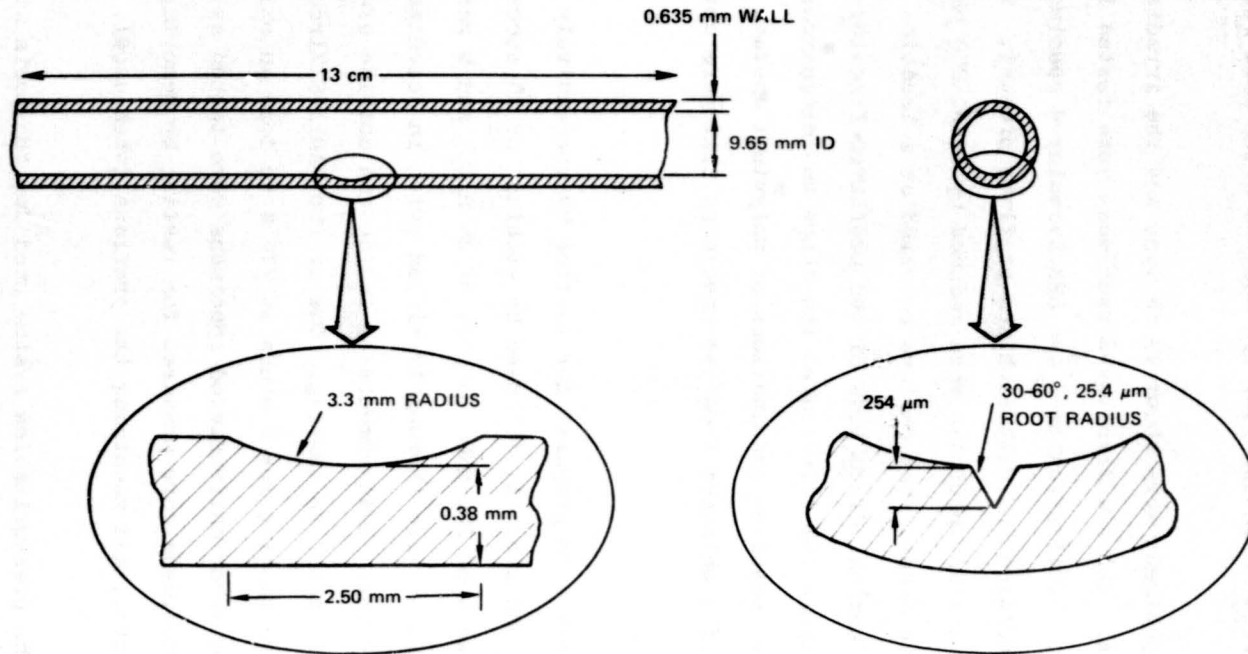
FIGURE 5-1   NOMINAL PREFLAWED TUBE BURST SPECIMEN

~2.2 mm

0.635 mm

~100 μm

~70°, ~50 μm
ROOT RADIUS
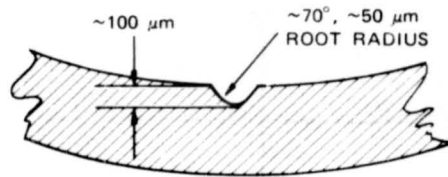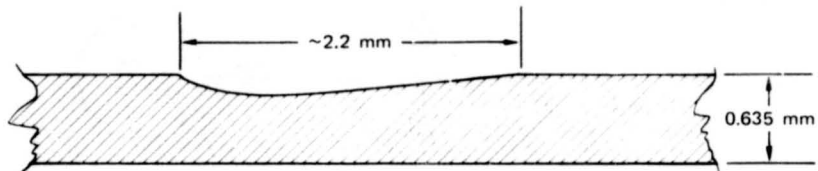
SA-4197-72R

FIGURE 5-2   ACTUAL SHAPE AND DIMENSIONS OF A TYPICAL MACHINED DEFECT
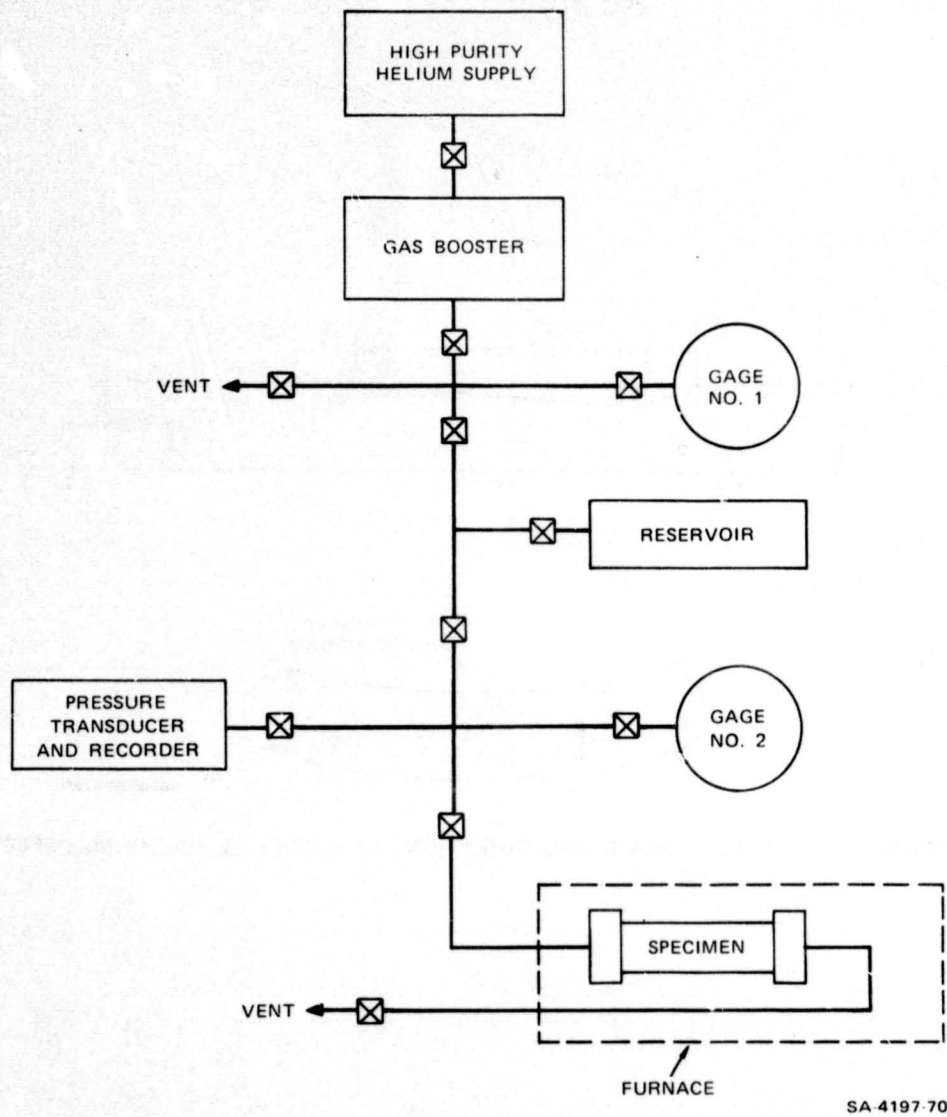
FIGURE 5-3   SCHEMATIC OF THE TUBE PRESSURIZATION SYSTEM USED AT
SRI INTERNATIONAL

the reservoir pressure to be determined at any time. The specimen was pressurized from the reservoir and the specimen pressure was monitored as a function of time by the pressure transducer (BLH Type DHF) and the chart recorder (H.P. Model 7100B). Gage No. 2 provided a means of accurately calibrating the response of the pressure recording system. When the recorded pressure was calibrated against Gage No. 2 at a system pressure of ~ 10 MPa, the recorded pressure and Gage No. 2 reading were essentially identical over the entire working range of the system.

The test specimen was connected to the pressurization system via specially modified stainless steel fittings (Swagelok) and was located in the center zone of a three-zone electric furnace (Lindberg Hevi-duty). To minimize the pressurized volume in the hot parts of the system, small-bore tubing was used for the inlet and outlet lines and a Vycor volume-displacing mandrel was placed inside the test specimen. Safety features included a sealed stainless steel chamber (which completely enclosed all of the hot parts of the test system) as well as the usual overpressure releases, gage snubbers, etc.

To perform a test, the test specimen was loaded with 250, 25, 2.5, or 0 mg of iodine (~ 6, 0.6, 0.06, 0 mg of iodine per cm^2 of exposed Zircaloy surface), a volume-displacing mandrel was inserted, and the specimen was connected to the pressure system. Before a test was begun, the specimen was successively pressurized (with high purity helium) to ~ 7 MPa and vented a total of at least 10 times at room temperature and twice at ~ 380 K to reduce the partial pressures of air and water vapor inside the specimen. Also, the sealed stainless steel chamber was evacuated and backfilled with helium several times to provide a protective atmosphere outside the specimen. After the final evacuation, the chamber was backfilled to a slightly positive helium pressure, and the specimen was brought up to the desired test temperature (590 ± 5 K or 630 ± 5 K). Then the specimen was pressurized with high purity helium using one of the three types of pressure-time histories shown in Figure 5-4. Most of the tests were conducted using Type 2 or Type 3 pressure histories. Type 2 tests were used to approximately define the pressure/failure time relationship, and Type 3 tests were used to generate more exact data. Type 1 tests were used to prove the pressure system and to determine the short time burst pressures for the various types of tubing. Specimen failure was signaled by an
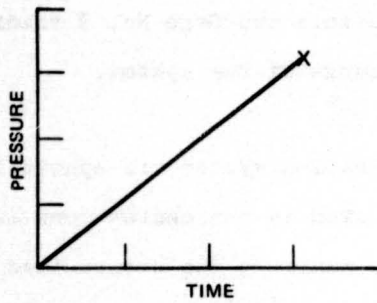
TYPE 1: PRESSURE RAMP
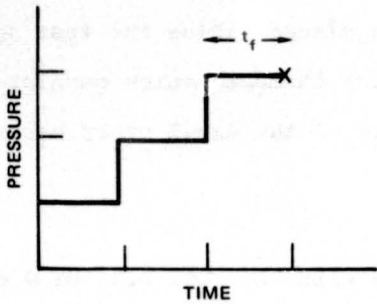
TYPE 2: INCREMENTAL PRESSURIZATION
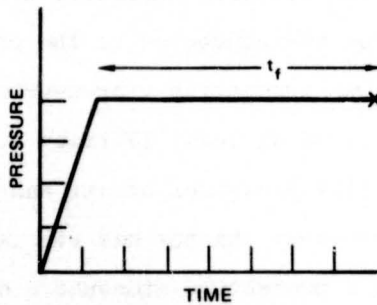
TYPE 3: RAPID PRESSURE RAMP FOLLOWED
BY HOLD AT CONSTANT PRESSURE

SA-4197-71R

FIGURE 5-4   THREE TYPES OF PRESSURE-TIME CURVES EMPLOYED IN THE TUBE
PRESSURIZATION TESTS

abrupt pressure decrease in the pressure-time trace, and the time to failure t_f was determined from the trace as indicated in Figure 5-4.

Creep of the test specimens during long-term tests resulted in detectable pressure decreases. However, because the change of specimen volume was small compared with the total volume of pressurized gas, the pressure decreases were never greater than about 3% of the initial pressure.

Fractographic observations were made on some of the failed specimens. To obtain samples suitable for scanning electron microscope (SEM) examination, a ring section containing the failure region was cut from the failed specimen. The ring was cut axially so that the failure region was at the apex of one of the two half rings. Then the failure section was broken open by bending the half ring that contained the failure site. In addition, a few unirradiated specimens were transversely sectioned through the failure region and examined by optical metallography.

RESULTS

7FD11 Zircaloy-4

The results obtained in the pressurization tests at 630 K on the unirradiated 7FD11 Zircaloy-4 tubing are presented in Table 5-1. The listed values of nominal hoop stress, σ_{nom}, were calculated from the standard expression for the hoop stress at the inside surface of an internally pressurized cylinder:

$$\sigma_{nom} = \left(\frac{R_i^2 + R_o^2}{R_o^2 - R_i^2} \right) P_f, \tag{5-1}$$

Where R_i and R_o are the internal and external radii, respectively, of the cylinder and P_f is the internal pressure. The estimated uncertainty in the values of σ_{nom} is ±4%. The values of the net section stress, σ_{net}, for preflawed specimens were calculated from the expression

$$\sigma_{net} = \frac{\sigma_{nom}}{1 - \frac{a}{w}} \tag{5-2}$$

Table 5-1

RESULTS OF PRESSURIZATION TESTS AT 630 K ON 7FD11 ZIRCALOY-4 TUBING SPECIMENS

Specimen Number[1]	Test Type[2]	Amount of Iodine (mg)	Preflaw Depth (μm)	Pressurization History[3]				Failure Strain (%)	Failure Type[4]	Failure Location[5]
				Time (hr)	σ_{nom} (MPa)	σ_{net} (MPa)	K_{Inom} (MPa·m$^{1/2}$)			
Zr-4-1	1	0	-	-	525†	-	-	~14	Ductile	C
Zr-4-2	1	0	-	-	500†	-	-	~16	Ductile	C
Zr-4-3*	1	0	-	-	500†	-	-	~15	Ductile	C
Zr-4-4*	1	0	-	-	510†	-	-	~16	Ductile	C
Zr-4-5	1	0	100	-	450	535†	9.3†	~3	Ductile	P
Zr-4-6	1	0	85	-	450	520†	8.6†	~4	Ductile	P
Zr-4-7*	1	0	60	-	485	530†	7.7†	~5	Ductile	P
Zr-4-8*	1	0	90	-	430	500†	8.4†	~4	Ductile	P
Zr-4-9*	1	0	105	-	455	545†	9.6†	~5	Ductile	P
Zr-4-10*	1	0	75	-	490†	550	8.8	~3	Ductile	NP(C)
Zr-4-11	3	0	100	0.3†	450	535†	9.3	3.0	Ductile	P
Zr-4-12	3	0	85	4.6†	390	450†	7.4	2.9	Ductile	P
Zr-4-13	3	0	90	82†	335	390†	6.6†	3.0	Ductile	P
Zr-4-14	2	250	85	0.5	335	385	6.3			
				0.5	390	450	7.4			
				0.2†	450	515†	8.5†	2.8	SCC-1	P
Zr-4-15	2	250	65	1.0	310	345	5.1			
				1.0	365	410	6.0			
				0.5†	420	470†	6.9†	2.5	SCC-2	P
Zr-4-16	2	250	95	24	235	275	4.7			
				24	245	285	4.9			
				24	260	305	5.2			
				20†	270	315†	5.4†	1.4	SCC-1	P
Zr-4-17	2	250	95	168	225	260	4.3			
				168	250	290	4.8			
				21.6†	280	325†	5.4†	1.6	SCC-1	P
Zr-4-18	3	250	75	2.9†	335	380†	6.0†	0.75	SCC-1	P
Zr-4-19	3	250	120	4.6†	245	305†	5.6†	0.35	SCC-2	P
Zr-4-20	3	250	65	19.2†	280	315†	4.6†	0.45	SCC-1	P
Zr-4-21*	2	250	85	24	170	190	3.3			
				24	225	260	4.3			
				8.7†	280	320†	5.4†	0.4	-	-
Zr-4-22*	3	250	110	6.7†	275	335†	6.0†	-	-	-
Zr-4-23*	3	250	80	5.6†	275	315†	5.1†	0.3	-	-
Zr-4-25	3	250	-	24	315	-	-			
				16.6†	330*	-	-	3.9	SCC-2	C
Zr-4-26	3	250	-	100	290	-	-			
				19.4†	305†	-	-	3.4	SCC-1	C
Zr-4-27	2	250	-	27.6†	320†	-	-	1.5	SCC-2	C
Zr-4-28	2	250	-	34.1†	310†	-	-	1.6	SCC-1	C

[1] Specimens identified with an asterisk* were tested by ANL, other specimens tested by SRI.
[2] See Figure 5-4 and text.
[3] Values identified with a dagger† are associated with specimen failure.
[4] One ductile failure mode and two stress corrosion cracking (SCC) failure modes were observed. See text for discussion.
[5] C signifies failure in the central portion of the specimen where the stress state is known; P signifies failure at the preflaw; NP signifies failure remote from the preflaw (with the actual location shown in parentheses).

where a is the maximum depth of the machined defect (measured optically after completion of the test) and w is the wall thickness (= $R_0 - R_i$). The estimated uncertainty in the values of σ_{net} is ±6%.

The nominal mode I stress intensity, K_{Inom}, at the pressure P_f associated with the presence of a machined preflaw of depth a was obtained from the calibration curve shown in Figure 5-5. The calibration curve is based on the three-dimensional finite element solution reported by Kobayashi et al. (5-4) for a pressurized, semielliptical sharp internal crack in an internally pressurized cylinder, and shows the maximum mode I stress intensity as a function of a/w for a specimen geometry similar to that of the nominal specimen (Figure 5-1). It should be noted that the finite element calculations that lead to Figure 5-5 are based on an ideally sharp crack, whereas the experimental flaws are quite blunt. Therefore the actual stress intensities generated in the specimens must be less than the estimates given in Table 5-1.

Also listed in Table 5-1 are estimates of the diametral (≡ hoop) plastic strain at failure, ϵ_f, obtained using the formula

$$\epsilon_f = \frac{R_f - R_0}{R_0} \quad , \tag{5-3}$$

where R_f is the external radius following failure. The minimum detectable strain was found to be 0.001 (i.e., 0.1%).

The initial group of ten Type 1 tests on 7FD11 Zircaloy-4 specimens demonstrated that:

- The burst stress at 630 K for unflawed specimens of 7FD11 Zircaloy-4 tubing was ~ 500 MPa (specimens Zr-4-1 through Zr-4-4 in Table 5-1).

- Similar results were obtained in tests at SRI and ANL on unflawed specimens (specimens Zr-4-1 through Zr-4-4) and for tests on specimens preflawed by SRI (specimens Zr-4-5 through Z4-4-8).

- Specimens preflawed by SRI (specimens Zr-4-7 and Zr-4-8) and by ANL (specimens Zr-4-9 and Zr-4-10) behaved similarly when tested by ANL.
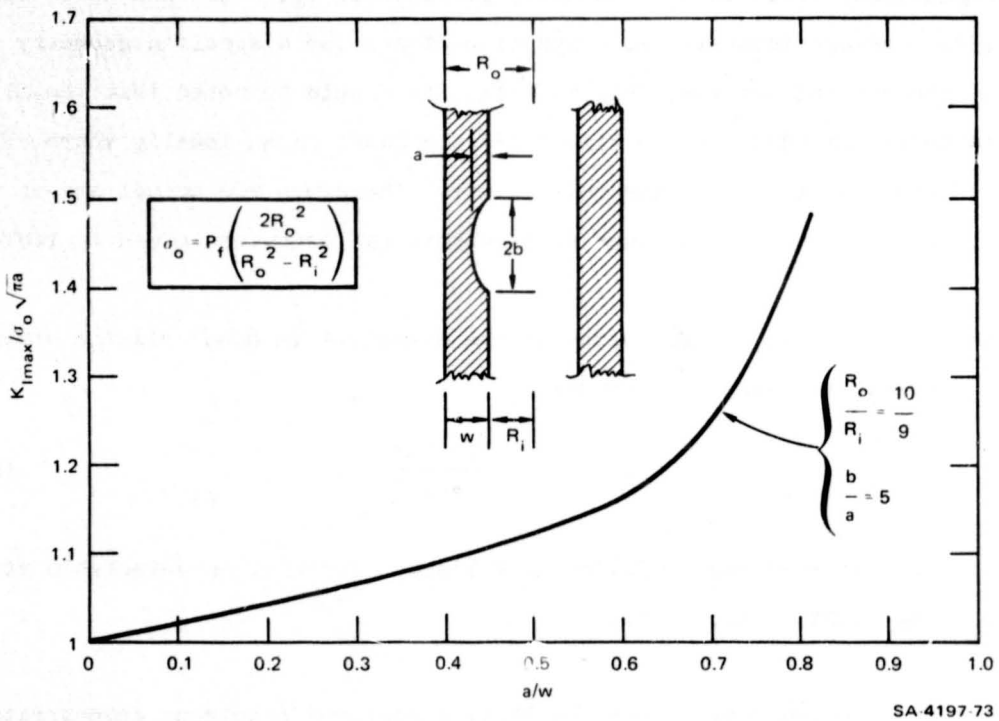
FIGURE 5-5   STRESS INTENSITY CALIBRATION CURVE FOR A PRESSURIZED, INTERNAL, SEMIELLIPTICAL SURFACE CRACK IN AN INTERNALLY PRESSURIZED CYLINDER (FROM REFERENCE 5-4)

- 7FD11 Zircaloy-4 was notch insensitive at 630 K as indicated by the observation that the values of σ_{net} for preflawed specimens at failure generally were larger than the values of σ_{nom} for unflawed specimens at failure.

The subsequent group of three Type 3 tests (specimens Zr-4-11 through Zr-4-13 in Table 5-1) was used to define the creep-rupture behavior of preflawed specimens of 7FD11 Zircaloy-4 at $\sim$ 630 K in the absence of an aggressive environment. As expected, the data in Table 5-1 show that the time to creep-rupture failure increases rapidly as the applied hoop stress is decreased.

Specimens Zr-4-1 through Zr-4-13 all exhibited failures consisting of an axial split in the tube wall on a plane lying at an angle of $\sim$ 45° to the tube radial direction. SEM fractography (Figure 5-6) showed that these failures were entirely ductile in nature and confirmed that failure occurred by a shear microprocess, as suggested by the $\sim$ 45° inclination of the macroscopic fracture plane. Failure of unflawed specimens in pressure ramp tests was preceded by considerable ballooning of the specimen--the local strain at failure was typically $\sim$ 15 percent, whereas the diametral strain in the uniform region of the specimen was only 3 to 5 percent. The presence of a preflaw effectively eliminated the ballooning and resulted in failure strains that consistently fell in the 3 to 5 percent range.

With the exception of specimen Zr-4-10, all of the preflawed specimens failed at the preflaw location. Therefore, the values of σ_{net} and K_{Inom} for the preflawed specimens should provide a more meaningful description of the stress state leading to failure than σ_{nom}. However, since none of the K_{Inom} values meet the ASTM-recommended acceptance criteria (5-5), their significance is questionable.[*] As indicated

---

[*]ASTM Recommended Test Method E-399-72 defines the specimen dimensions required to ensure that at a given nominal stress intensity, the crack tip conditions in a material of given yield stress closely approximte a linear elastic, plane strain state. The maximum stress intensities that could be generated in the present preflawed tubing specimens under conditions that would be considered acceptable by ASTM were $\sim$ 3 MPa·m$^{1/2}$ for 7FD11 specimen and $\sim$ 5 MPa·m$^{1/2}$ for H.B. Robinson specimens, the precise values depending on the actual flaw size.
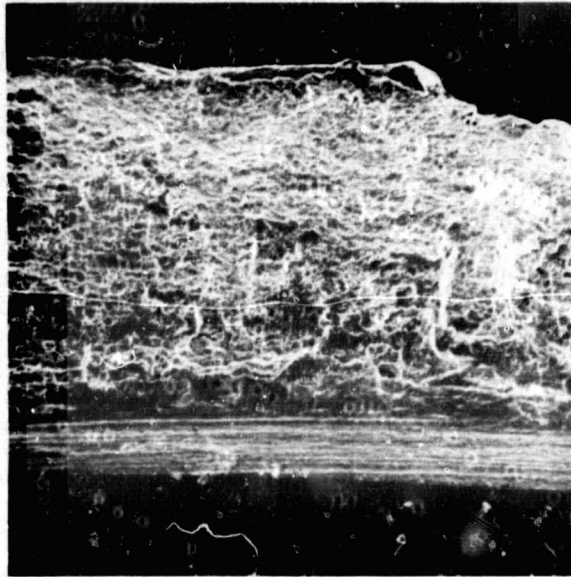
(a) SHOWING PART OF THE PREFLAW AND THE INCLINED FRACTURE
SURFACE (100x)
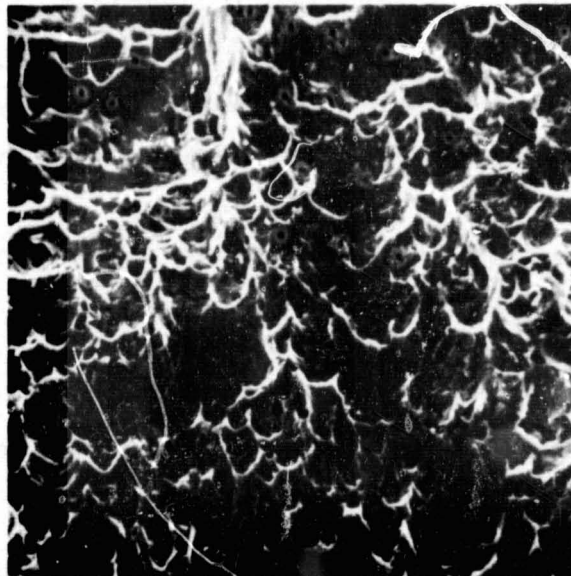
(b) TYPICAL AREA OF SHEAR FRACTURE (100X)

SA-4197-74

FIGURE 5-6   SEM FRACTOGRAPHS OF SPECIMEN Zr-4-11
PRESSURIZED TO FAILURE AT 630 K
IN PURE HELIUM

in Table 5-1, the value of σ_{nom} for specimen Zr-4-10 (the preflawed specimen that failed remote from the preflaw) is considered to provide a more useful description of the stress state associated with failure than either σ_{net} or K_{Inom}.

Specimens Zr-4-14 through Zr-4-23 all contained preflaws and all were pressurized to failure at ~ 630 K after they were loaded with 250 mg of iodine. A combination of test types was used in tests at both SRI and ANL. As shown in Table 5-1, the data obtained at SRI and ANL are completely consistent for specimens preflawed by SRI. Moreover, the behavior of the specimen that was preflawed by ANL (Zr-4-23) was indistinguishable from that of two other specimens tested by ANL that had been preflawed by SRI(Zr-4-21 and Zr-4-22). Thus, the slight differences in the methods used to preflaw and test specimens at SRI and ANL, which were due to the limitations of the equipment available in the ANL hot cells, did not result in any detectable changes in the behavior of 7FD11 Zircaloy-4 test specimens.

The smallest values of σ_{net}, K_{Inom}, and ε_f that were associated with iodine-induced failure within the maximum test duration of 168 hours were 305 MPa, 6.4 MPa·m$^{1/2}$, and 0.3 percent, respectively. Again, none of the values of K_{Inom} associated with specimen failure satisfy the acceptance criteria recommended by ASTM and so these data should be interpreted with caution.

Two types of SCC failures were observed in the preflawed specimens Zr-4-14 through Zr-4-23. The majority of specimens showed pinhole failures (termed SCC-1 in Table 5-1), but two showed short axial splits (SCC-2 in Table 5-1). Optical metallography (Figure 5-7) and SEM fractography (Figure 5-8) showed well-defined axially oriented SCC regions (usually approximately semielliptical in shape) emanating from the pre-flaws and terminating in a ductile tear or blowout, but revealed no explanation for the two types of final failure. The higher magnification fractograph in Figure 5-8b shows the brittle nature of the SCC microfracture process (compare with Figure 5-6b). The fracture path appears to be transgranular, but the well-defined cleavage and fluting features reported by others (5-3) are not apparent. Most of the fracture surfaces and all of the inside surfaces of the tubes were oxide covered, probably due to the posttest hydrolysis of iodide films formed during the test. The inside surfaces of the specimens showed evidence of pitting attack, and elemental analysis

0.5 mm
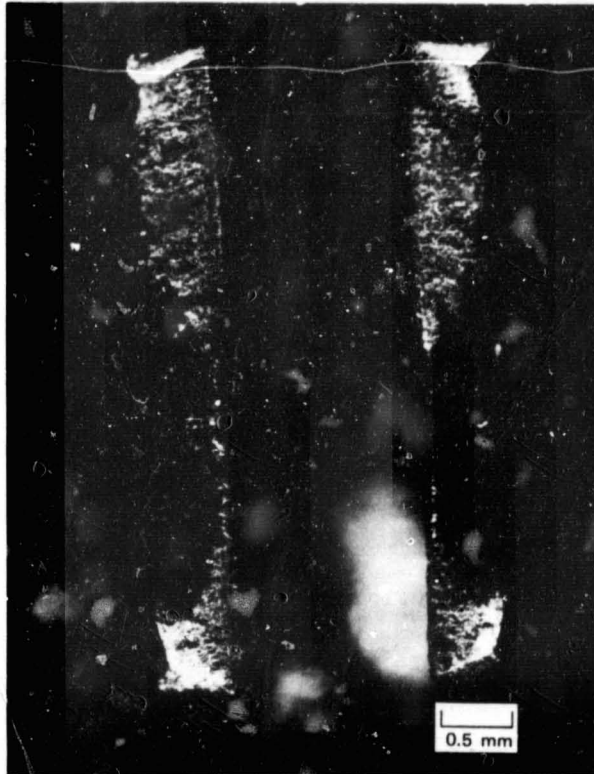
SA-4197-303

FIGURE 5-7   OPTICAL FRACTOGRAPH OF SPECIMEN Zr-4-18 SHOWING A WELL-DEFINED
REGION OF SCC THAT PENETRATED ALMOST COMPLETELY THROUGH
THE TUBING WALL
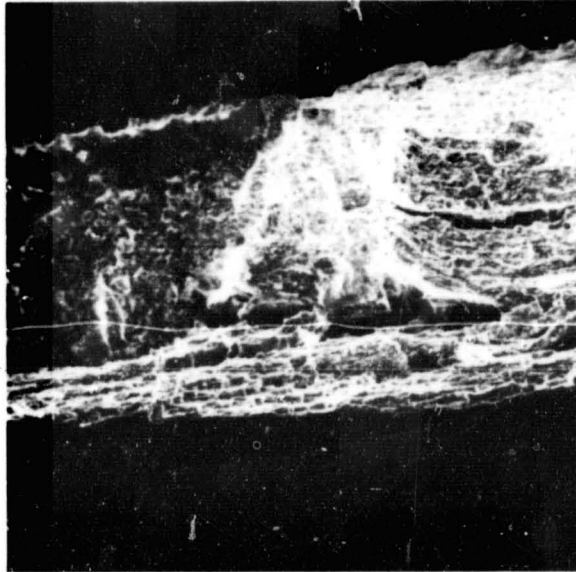
(a) GENERAL VIEW AT 100x SHOWING THE TUBE I.D., PART OF THE PREFLAW, THE SCC REGION, AND THE BLOWOUT REGION ASSOCIATED WITH THE FINAL PINHOLE FAILURE. NOTE THE PITTING OF THE TUBE I.D.
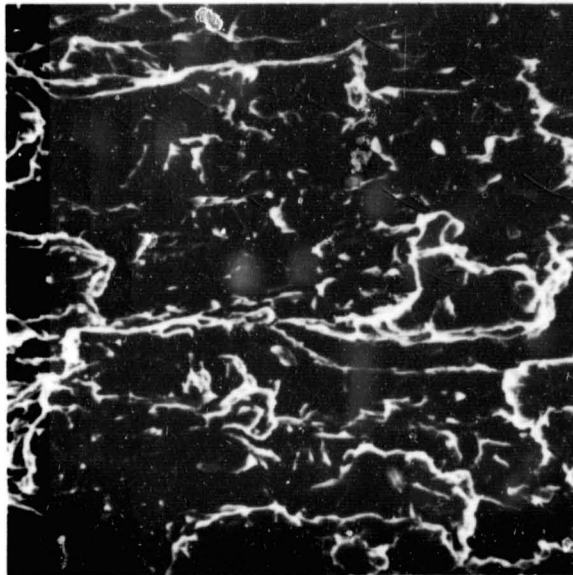
(b) TYPICAL AREA IN THE SCC REGION (1000X)

SA-4197-75

FIGURE 5-8   SEM FRACTOGRAPHS OF SPECIMEN Zr-4-14 PRESSURIZED TO FAILURE AT 630 K IN THE PRESENCE OF IODINE

indicated that the presence of iron on both the inside surfaces and fracture surfaces. We presume that this iron originated in the stainless steel pressure tubing and fittings and was transported to the specimen via an iodide vapor, probably FeI_2.

Optical metallography of cross sections through several fracture surfaces indicated the features typified by Figure 5-9. The SCC regions generally were approximately parallel to the radial direction (i.e., perpendicular to the hoop stress), whereas the ductile overload parts of the fracture surfaces usually were inclined at about 45° to the radial direction. The SCC cracks were more branched and penetrated a shorter distance through the cladding wall in specimens tested at higher stresses.

All of the preflawed specimens tested by SRI in the presence of iodine that are included in Table 5-1 failed at the preflaw. However, another specimen that contained a 50-μm deep preflaw failed under one of the pressure fittings after 20 hours at the relatively low nominal hoop stress of 260 MPa ($\sigma_{net} \approx 280$ MPa). SEM fractography revealed the large calcium-rich inclusion shown in Figure 5-10, which may have provided a more severe stress concentration than the comparatively blunt machined preflaw. This result was not included in Table 5-1 because the stress state in the tubing beneath the pressure fittings cannot be accurately estimated.

A final group of four unflawed specimens of 7FD11 Zircaloy-4 (Zr-4-25 through Zr-4-28) was tested under similar conditions to those used for the preflawed specimens to determine the conditions needed to promote iodine SCC in the absence of an artificial preflaw. The smallest hoop stress at which failure was observed in test times up to 100 hours was 305 MPa and the smallest value of strain at failure was 1.5 percent. Pinhole failures and short axial splits were both observed in these tests but no detailed fractography was performed.

HBR Zircaloy-4

The results of the tube pressurization tests at ANL on the irradiated HBR Zircaloy-4 are summarized in Table 5-2. This cladding presented difficulties because of its ovality, which presumably resulted from creepdown during service. The HBR tubing

100 µm

FINAL DUCTILE
REGION

IODINE-SCC
REGION

PREFLAW
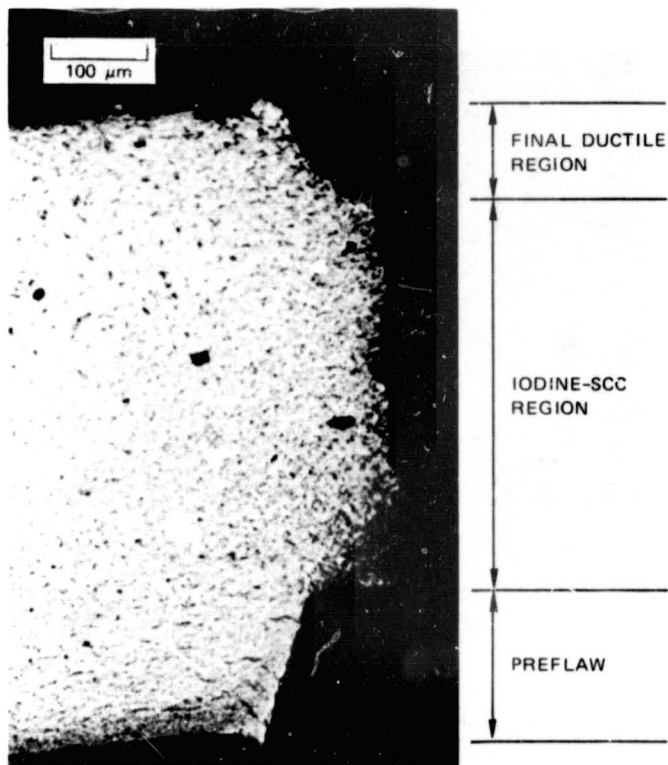
SA-4197-304

FIGURE 5-9   CROSS SECTION THROUGH THE FRACTURE SURFACE OF SPECIMEN
Zr-4-17 (7FD11 ZIRCALOY-4)
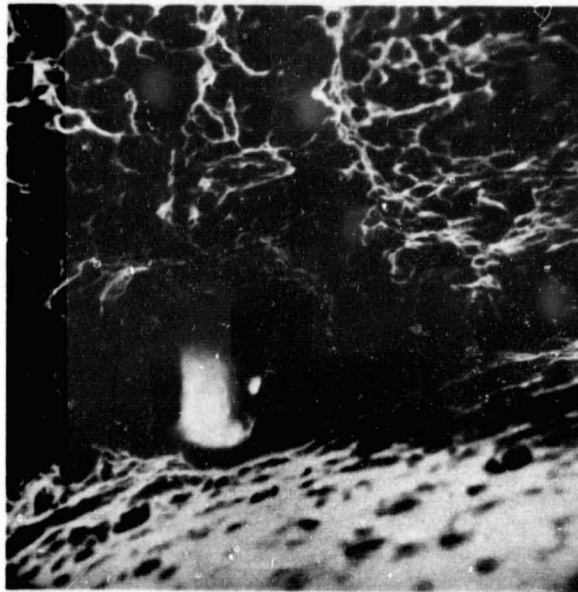
SA-4197-77

FIGURE 5-10   A LARGE CALCIUM-RICH INCLUSION AND POSSIBLE SCC INITIATION
SITE AT THE INNER EDGE OF THE FRACTURE SURFACE OF A
7FD11 SPECIMEN

The lower part of the micrograph is the tube ID.

sections were found to be out of round by up to 250 μm, which made it difficult to obtain a good pressure seal. In fact, two specimens that were prepared for testing were never pressurized because a leak-tight seal could not be achieved when the fittings were tightened to the maximum torque available in the hot cell. Moreover, those specimens that could be satisfactorily sealed showed a marked tendency to develop leaks at or near the seals during testing. These leaks proved to be due to SCC failures in the highly strained regions in the tubing beneath the pressure fittings. We believe that the ovality of the tubing caused an unusually severe stress state in these regions, thus resulting in rapid SCC. Because of these problems, only one of the first three specimens tested generated useful quantitative information on the conditions leading to iodine-induced SCC failure (see Table 5-2).

To alleviate the problems associated with the ovality of the HBR tubing, the ends of subsequent specimens were annealed and rounded using a specially modified Jacobs lathe chuck. None of the three specimens prepared in this way developed leaks at or near the fittings during testing.

The smallest value of stress associated with the failure of an HBR Zircaloy-4 specimen containing iodine was 200 MPa. The same stress level also resulted in the failure of specimen HBR-6, which was tested without removing the fuel or adding iodine. However, since iodine was detected on the fracture surface of specimen HBR-6 and fractography indicated an SCC failure, it is likely that residual iodine and iodides remaining in the system from previous tests were responsible.

Because only one preflawed specimen (HBR-1) failed at the preflaw, only one value of K_{Inom} was obtained that was associated with a failure. This value (7.9 MPa$\cdot$m$^{1/2}$) was found to be marginally unacceptable in terms of the ASTM-recommended acceptance criteria (5-5). The smallest values of failure strain observed in these tests were 0.25 percent (for a preflawed specimen that failed remote from the preflaw) and 0.4 percent (for an unflawed specimen).

SEM fractography of several of the specimens revealed that the details of the fracture surfaces generally were almost totally obscured by thick iodine-containing layers that were presumed to be corrosion products. The failure near the pressure

Table 5-2

RESULTS OF PRESSURIZATION TESTS AT ANL ON IRRADIATED H. B. ROBINSON ZIRCALOY-4 CLADDING SPECIMENS AT 630 K

Specimen Number	Test Type [1]	Amount of Iodine (mg)	Preflaw Depth (μm)	Pressurization History [2]				Failure Strain (%)	Remarks
				Time (hr)	σ_{nom} (MPa)	σ_{net} (MPa)	K_{Inom} (MPa·m$^{1/2}$)		
HBR - 1 (155BD-1)	2	250	200	24	80	115	2.4		Developed leaks at both ends after 5.2 hours at 110 MPa. Cut and resealed twice. Final fracture (SCC-2 type) at preflaw.
				24	95	140	2.9		
				5.2	110	160	3.3		
				0.53†	260	380†	7.9†	0.8	
HBR-2 (155CA-1)	2	250	80	0.53	195	220	3.7		Test aborted because of end leaks
				2.0	~195	220	3.7		
				0.5	~195	220	3.7	-	
HBR-3 (155CA-3)	3	250	30	0.5	195	205	2.2	≥ 0.25	SCC-1 failures at both pressure fittings
HBR-4 (155BD-3)	2	250	60	24	195	215	3.1		SCC-2 failure away from preflaw
				10.5†	205†	225	3.3	0.25	
HBR-5 (155BD-5)	3	250	-	14.3†	200†	-	-	1.1	SCC-1 failure in central region
HBR-6 (155BD-4)	3	0	-	7.4†	200†	-	-	0.4	Specimen contained fuel. Long axial split near center

[1] See Figure 5-4 and text.

[2] Values identified with a dagger† are associated with specimen failure.

seals in specimen HBR-3 was found to be better preserved, perhaps because that region was partially protected from the test environment. Figure 5-11 is a typical view of one of the failures in specimen HBR-3 and shows the mixture of the transgranular cleavage and plastic tearing that is often associated with iodine SCC of Zircaloys (5-3). Note that the appearance of the fracture surface in Figure 5-11 is similar (although better preserved) to that of the unirradiated specimen in Figure 5-8b.

7AH11-S and 7AH11-H Zircaloy-2

Unflawed specimens of both 7AH11-S and 7AH11-H Zircaloy-2 were pressure-tested at ~ 590 K in the presence of iodine to determine the influence of environmental and metallurgical variables on iodine SCC. The results obtained for 7AH11-H specimens are summarized in Table 5-3.

The first 7AH11-H specimen was pressure ramped to failure in the absence of iodine to establish the burst stress and the strain to ductile failure at 590 K. This specimen showed the ductile shear type of failure mode described earlier. Specimens Zr-2H-2 and Zr-2H-3 were subjected to incremental pressurization tests (Type 2 in Figure 5-4) after being loaded with 250 mg of iodine. The results of these tests defined the pressure range of interest for the 10 subsequent tests, which were constant pressure tests (Type 3 in Figure 5-4) on specimens containing 250 mg of iodine. The behavior of these 10 specimens was remarkably systematic, with progressively increasing times to failure observed as the nominal hoop stress was gradually decreased. The lowest hoop stress at which an iodine-induced failure occurred in this group of tests was 329 MPa--specimen Zr-2H-13 survived intact for 218 hours at a hoop stress of 320 MPa. The smallest strain to failure was 0.3 percent, and the failure strain values showed a minimum at intermediate failure times.

All of the 7AH11-H Zircaloy-2 specimens failed near the center of the region with the reduced outside diameter. As in the case of Zircaloy-4 specimens, two different iodine SCC failure modes were observed. Pinhole failures were usually observed in low stress tests, with higher hoop stresses tending to favor the formation of axial splits. However, Table 5-3 shows some exceptions to this trend. A very limited

SA-4197-305
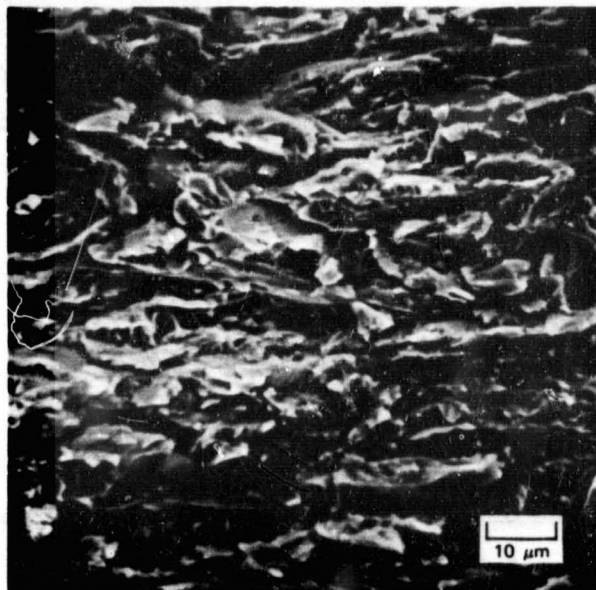
FIGURE 5-11   FRACTURE SURFACE OF SPECIMEN HBR-3 (IRRADIATED
ZIRCALOY-4 CLADDING) TESTED IN THE PRESENCE OF
IODINE AT 630 K

Table 5-3

RESULTS OF PRESSURIZATION TESTS AT 590 K ON 7AH11-H ZIRCALOY-2 TUBING SPECIMENS

Specimen Number	Test Type[1]	Amount of Iodine (mg)	Pressurization History[2]		Failure Strain (%)	Failure Type[3]
			Time (hr)	σ_{nom} (MPa)		
Zr-2H-1	1	0	–	550†	24	Ductile
Zr-2H-2	2	250	0.5	384		
			0.5	416		
			0.5	448		
			0.5	480		
			0.25†	512†	~6	SCC-2
Zr-2H-3	2	250	48	322		
			48	335		
			48	348		
			12.3†	361†	0.9	SCC-1
Zr-2H-4	3	250	4.6†	451†	3.3	SCC-2
Zr-2H-5	3	250	16.7†	390†	0.7	SCC-2
Zr-2H-6	3	250	17.5†	359†	0.4	SCC-2
Zr-2H-7	3	250	27.5†	356†	0.3	SCC-2
Zr-2H-8	3	250	33.7†	348†	0.4	SCC-2
Zr-2H-9	3	250	34.0†	343†	0.4	SCC-1
Zr-2H-10	3	250	86.6†	339†	0.7	SCC-1
Zr-2H-11	3	250	82.0†	336†	0.7	SCC-1
Zr-2H-12	3	250	90.8†	329†	1.0	SCC-1
Zr-2H-13	3	250	218	320	–	–
Zr-2H-14	3	25	57.2†	336†	0.7	SCC-1
Zr-2H-15	3	2.5	166.2†	338†	1.2	SCC-2

(1) See Figure 5-4 and text.

(2) Values identified with a dagger† are associated with specimen failure.

(3) All failures occurred within the central gage region of the specimen.

SEM study failed to reveal any significant difference between the fracture micro-processes involved in the two types of failure. In all the specimens examined, the appearance of the SCC fracture region was very similar to that of the 7FD11 Zircaloy-4 specimens (see Figure 5-8), and the final fracture regions all showed the elongated dimples characteristic of ductile shear fracture irrespective of whether the final failure led to the formation of a pinhole or an axial split.

Two final specimens of 7AH11-H Zircaloy-2 were used for a brief investigation of the influence of iodine concentration. Specimen Zr-2H-14 was loaded with 25 mg of iodine and was pressurized at a hoop stress of 336 MPa. Failure occurred after 57.2 hours which is within the range of failure times for similarly stressed speci-mens containing 250 mg I_2 (34 to 82 hours, see Table 5-3). Specimen Zr-2H-15 was similarly stressed but contained only 2.5 mg of iodine. This specimen failed after 166.2 hours, significantly longer than the failure times of specimens containing 25 and 250 mg I_2.

The results of the pressurization tests at 590 K on the unflawed 7AH11-S Zircaloy-2 tubing specimens are presented in Table 5-4. Again, the first test was used to define the stress required to burst the tubing and the resultant failure strain when the specimen was subjected to a pressure ramp in the absence of iodine. The seven subsequent tests were Type 2 (incremental pressurization) tests on specimens containing 250 mg of iodine. Unlike the other three materials investigated, it was difficult to induce iodine SCC of the 7AH11-S Zircaloy-2 tubing. Thus, speci-mens Zr-2S-6 through Zr-2S-8 failed by ductile rupture even though they contained 250 mg iodine. However, iodine SCC was promoted in subsequent tests in which smaller stress increments were used. The results of those tests, and of the subseuqent con-stant pressure tests, indicated that 282 MPa was the smallest hoop stress that would cause iodine-induced failure within testing times up to 190 hours. The smallest failure strain observed was 3 percent.

All of the unirradiated specimens discussed thus far were tested as-etched. Therefore, at the beginning of the tests their surfaces were protected only by the thin oxide formed by exposure to air at room temperature. Unlike the 7FD11

Table 5-4

RESULTS OF PRESSURIZATION TESTS AT 590 K ON 7AH11-S ZIRCALOY-2 TUBING SPECIMENS

Specimen Number[1]	Test Type[2]	Amount of Iodine (mg)	Pressurization History[3]		Failure Strain (%)	Remarks[4]
			Time (hr)	σ_{nom} (MPa)		
Zr-2S-1	1	0	0	367†	32	Ductile failure
Zr-2S-6	2	250	24	194		
			24	259		
			24	323		
			–	~355†	38	Ductile failure during pressure increase.
Zr-2S-7	2	250	24	302		
			–	~370†	33	Ductile failure during pressure increase.
Zr-2S-8	2	250	2	256		
			2	288		
			1.8†	319†	36	Ductile failure--no SCC.
Zr-2S-9	2	250	1.5	275		
			0.25†	294†	3	SCC-1 failure mode.
Zr-2S-10	2	250	24	301		
			3.6†	307†	6	SCC-2 type failure.
Zr-2S-11	2	250	1.5	290		
			2.3†	322†	24	Ductile failure--no SCC
Zr-2S-14	2	250	190	275		
			0.08†	288†	7	SCC-2 type failure
Zr-2S-15	3	250	0.25†	290†	4	SCC-1 type failure
Zr-2S-16	3	250	100†	282†	5	SCC-2 type failure
Zr-2S-17	3	250	61†	286†	5	Preoxidized specimen--SCC-2 failure

[1]The missing numbers in this sequence are those of specimens used for the investigation of oxide film fracture reported in Section 4 of this report.

[2]See Figure 5-4 and text.

[3]Values identified with a dagger† are associated with specimen failure.

[4]All failures occurred within the central gage region of the specimen.

Zircaloy-4 and 7AH11-H Zircaloy-2 tubing lots, the annealing temperature used for the 7AH11-S Zircaloy-2 was high enough to permit the thermal growth of a substantial oxide film without degrading the mechanical properties of the tubing. Specimen Zr-2S-17 was therefore oxidized for 5 hours at 770 K in oxygen to form a ~ 1.5-μm-thick oxide. Then 250 mg of iodine was placed in the specimen and it was pressure-tested to failure to investigate whether the relatively thick oxide film affected the susceptibility to iodine SCC. As indicated in Table 5-4, failure occurred after 61 hours at a hoop stress of 286 MPa, and the failure strain was ~ 5 percent. Both values are within the ranges observed with unoxidized specimens.

The two modes of SCC failure noted for the other test materials were also observed in 7AH11-S Zircaloy-2. Although the fine details of the fracture surfaces were generally obscured by corrosion products, SEM examination indicated that the SCC regions did not penetrate very far through the cladding wall in these specimens and contained more features suggestive of intergranular crack growth than the SCC regions in 7FD11 or 7AH11-H specimens. For example, Figure 5-12 shows the part of the SCC region adjacent to the inside surface in specimen Zr-2S-16. The appearance of this fracture is quite different from that of the stress-relieved Zircaloy-4 specimen shown in Figure 5-8.

DISCUSSION AND CONCLUSIONS

Comparison of Possible Threshold Criteria for Iodine SCC of Zircaloy Tubes

The data in Table 5-1 provide convincing evidence that hoop stress is a more useful parameter than nominal stress intensity for predicting the conditions that will lead to iodine-induced failure of Zircaloy tubing under internal pressurization. Consider, for example, the behavior of the preflawed specimen Zr-4-17 and the unflawed specimen Zr-4-27. The former specimen failed at a nominal stress intensity of 5.4 MPa·m$^{1/2}$ and had previously survived an exposure of 168 hours at 4.8 MPa·m$^{1/2}$. The as-fabricated flaws present in the inside surface of 7FD11 Zircaloy-4 are very small (see Figure 3-5) and at an applied hoop stress of 320 MPa, the nominal stress intensity associated with these flaws in specimen Zr-4-27 certainly would not exceed 2 MPa·m$^{1/2}$. Therefore, since specimen Zr-4-17 survivied for 168 hours at 4.8 MPa·m$^{1/2}$, the failure time predicted for specimen Zr-4-27

SA-4197-306
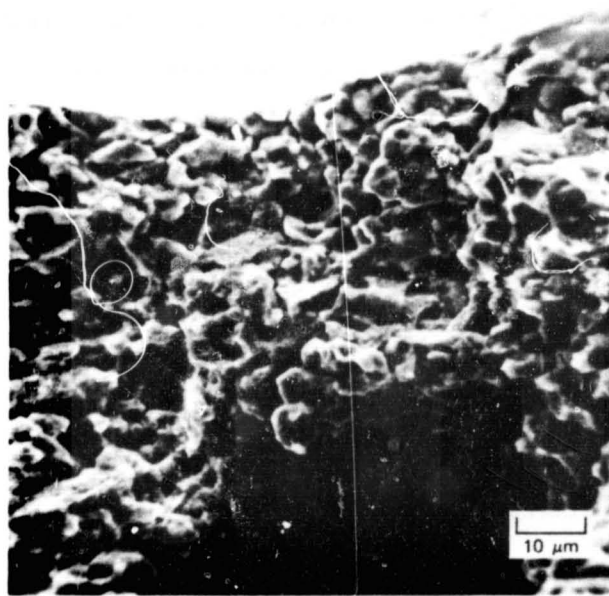
FIGURE 5-12   FRACTURE SURFACE OF SPECIMEN Zr-2S-16 (UNIRRADIATED
ZIRCALOY-2) TESTED IN THE PRESENCE OF IODINE AT 590 K

on the basis of stress intensity would be $\gg$ 168 hours. In contrast, the actual failure time was only 27.6 hours. However, the failure time of specimen Zr-4-27 is entirely predictable if one relates failure time to hoop stress rather than to stress intensity. Thus, specimen Zr-4-17 survived an exposure of 168 hours at a hoop stress[*] of 290 MPa and failed after an additional 21.6 hours at 325 MPa. The failure time predicted for specimen Zr-4-27 at a nominal hoop stress of 320 MPa therefore would be slightly more than 21.6 hours, in agreement with the actual observation.

It might be argued that stress is a more useful predictive parameter than stress intensity in the present experiments because of the blunt character of the machined preflaws. However, difficulties have also been encountered in using stress intensity to predict the times to iodine-induced failure of specimens containing fatigue-sharpened preflaws of different sizes (5-6). Therefore, the deficiences of K_{Inom} as a predictive parameter are likely due to the departures from an ideal linear elastic situation that exist under the present test conditions.

As mentioned earlier, none of the present K_{Inom} measurements satisfy the empirically based acceptance criteria recommended by ASTM (5-5), which provide a check of whether or not the test under consideration was performed under conditions leading to an acceptable approximation of a linear elastic, plane strain stress state. In all the present tests, the preflaw depth was not sufficiently larger than the plastic zone associated with the preflaw to achieve an acceptable linear elastic, plane strain approximation. Practical experience (5-2) and theoretical considerations (5-7, 5-8) suggest that the K_{Iscc} threshold concept breaks down in this small-flaw regime and is replaced by a threshold stress that must be exceeded for stress corrosion cracking to occur. Under these circumstances, it is expected that the minimum value of K_{Inom} at which stress corrosion cracking can be induced will decrease with decreasing flaw depth because of the increasing departure from linear

---

[*]As explained earlier, σ_{net} is considered to be a more meaningful measure of the hoop stress than σ_{nom} for preflawed specimens that failed at the preflaws.

elastic conditions. It is therefore not surprising that the values of K_{Iscc} for iodine-SCC of Zircaloys that have been deduced from experiments on thin-walled tubing specimens containing fatigue-sharpened preflaws (5-6) and natural flaws (5-9) are much smaller than the value of 9 to 10 MPa·m$^{1/2}$ that has been obtained at reactor operating temperatures in valid, fracture mechanics type tests (5-10, 5-11, and see Section 6).

Table 5-2 shows that the irradiated specimen HBR-1 failed at a nominal stress intensity of 7.9 MPa·m$^{1/2}$. Because of the high yield stress of the HBR cladding (~ 600 MPa according to reference 5-12), this test was only marginally invalid in terms of the ASTM acceptance criteria (5-5) at a stress intensity of 7.9 MPa·m$^{1/2}$ and was valid at the lower values of stress intensity (2.4 to 3.3 MPa·m$^{1/2}$) that did not promote iodine SCC failure in a total exposure period of over 50 hours. Thus, the result of the test on specimen HBR-1 seems to indicate that K_{Iscc} for iodine SCC of irradiated Zircaloy at reactor operating temperatures is not dramatically lower than the values that have been reported for unirradiated Zircaloy (5-10, 5-11).

The data in Tables 5-1 and 5-3 also offer convincing evidence that a threshold stress rather than a threshold strain must be exceeded to induce iodine SCC of internally pressurized Zircaloy tubing. Compare, for example, the results of the tests on specimens Zr-4-16 (an incrementally pressurized preflawed specimen) and Zr-4-20 (a preflawed specimen held at constant pressure). The test results are consistent with the idea of a stress threshold in that both specimens failed after about 20 hours at a hoop stress of 315 MPa, even though specimen Zr-4-16 was exposed for 72 hours at lower stresses. The same test results are not consistent with a threshold strain concept. The strains at failure should be nearly identical if attainment of a critical strain is a sufficient criterion for the onset of SCC, whereas the actual failure strains differ by a factor of three. Similarly, the behavior of specimens Zr-2H-4 through Zr-2H-13 (Table 5-3) suggests a threshold stress at about 320 MPa, whereas the failure strain values for the same specimens show a minimum at intermediate failure times that is inconsistent with the behavior that would be expected if the onset of SCC occurred at a critical strain.

Although it seems possible to conclude that attainment of a certain critical strain is not a sufficient condition for iodine SCC of Zircaloy tubing, all four of the materials studied exhibited significant plastic strains at failure. Therefore, we cannot exclude the possibility that attainment of a strain threshold is a necessary but not sufficient condition for the occurrence of iodine SCC.

Dependence of the Threshold Stress and Iodine SCC Failure Time on
Materials and Other Variables

Figures 5-13 through 5-16 illustrate the dependence of time to failure on hoop stress for the four materials investigated. Values of σ_{net} are plotted for pre-flawed specimens that failed at the preflaw--in all other cases the nominal hoop stress values are plotted. All four figures indicate the yield stress (YS) and burst stress (BS) of the tubing in short-time pressurization tests at the same temperatures.

Although the data exhibit some scatter, Figure 5-13 shows that a well-defined threshold for iodine SCC of 7FD11 Zircaloy-4 at 630 K exists at a hoop stress of about 300 MPa. At stresses just above this threshold, exposure to iodine results in failure in much shorter times than those required for creep-rupture failure in an inert environment. At higher stresses, the iodine SCC and creep rupture failure curves converge, and at stresses close to the burst stress (~ 525 MPa), the failure times are similar. As indicated in Table 5-1, the decreased failure time in iodine environments is accompanied by a decrease of failure strain of up to a factor of 10 for both preflawed and unflawed test specimens.

The creep rupture behavior of 7AH11-H Zircaloy-2 was not investigated but its per-formance in iodine-containing environments at ~ 590 K is qualitatively similar to that of the 7FD11 tubing at ~ 630 K (compare Figures 5-13 and 5-15). However, the 7AH11-H material shows a somewhat larger threshold stress (~ 330 MPa) and generally longer failure times than the 7FD11 material. These effects may be attributable either to the difference of the chemical compositions of the two materials (differ-ences in other metallurgical characteristics were found to be very slight--see Section 3 and Appendix A) or, more likely, to the difference of test temperature.
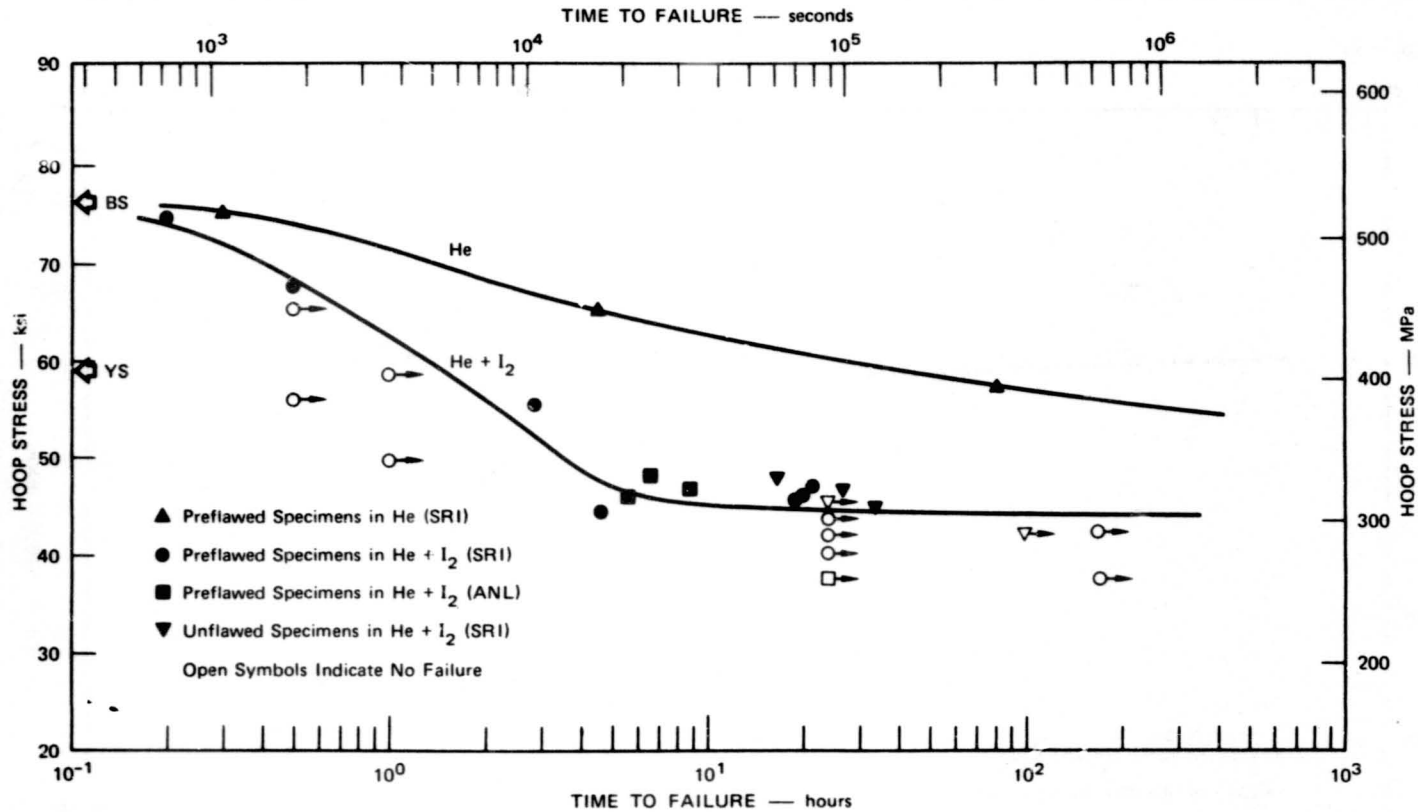
FIGURE 5-13   RESULTS OF TUBE PRESSURIZATION TESTS ON 7FD11 ZIRCALOY-4 SPECIMENS AT 630 K

The He + I₂ curve approximately defines the minimum conditions required for iodine-induced failure and may be somewhat conservative because of the scatter in the data.

SA-4197-307

5-33
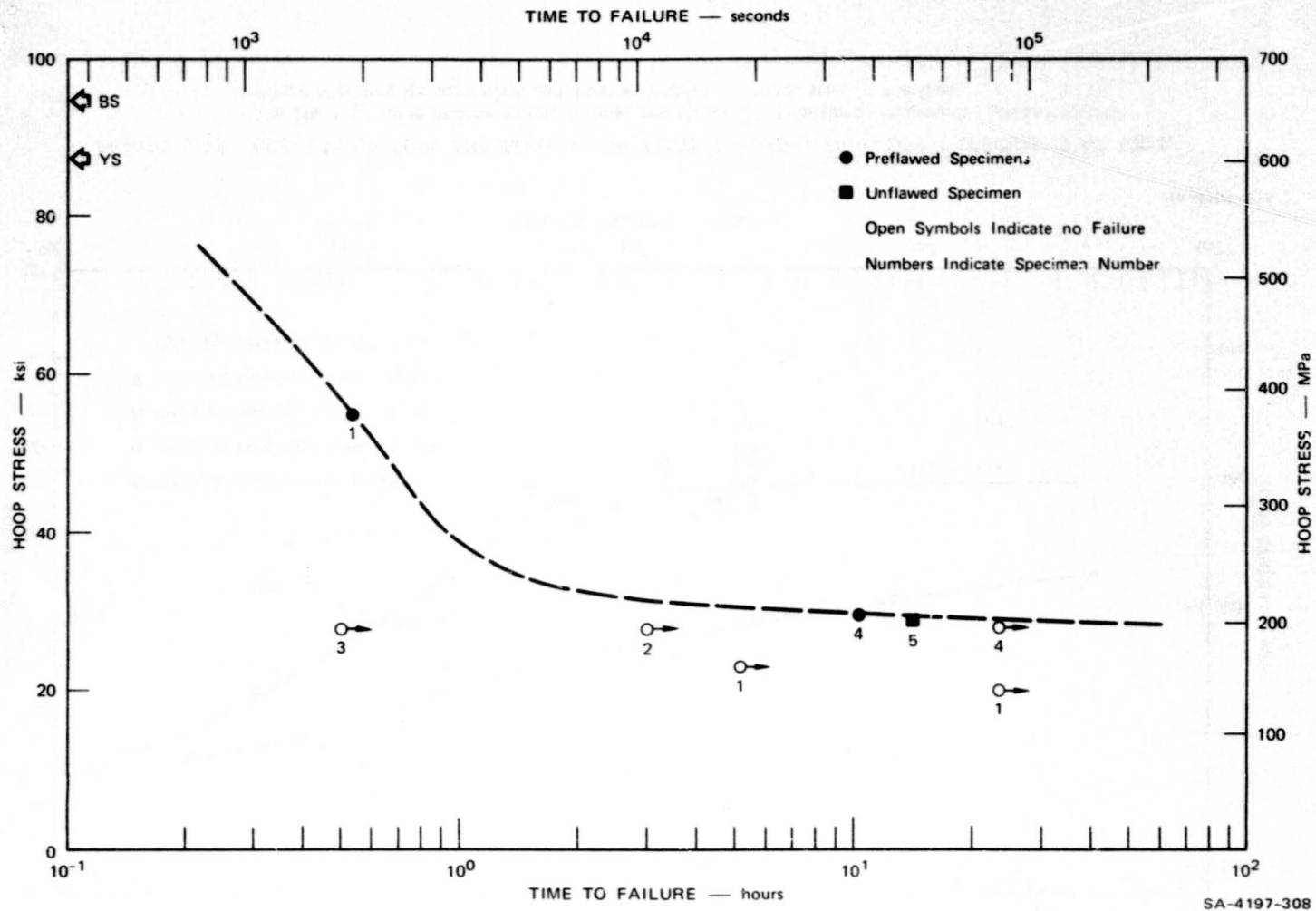
FIGURE 5-14 RESULTS OF TUBE PRESSURIZATION TESTS AT ANL ON IRRADIATED H.B. ROBINSON CLADDING SPECIMENS EXPOSED TO IODINE AT 630 K
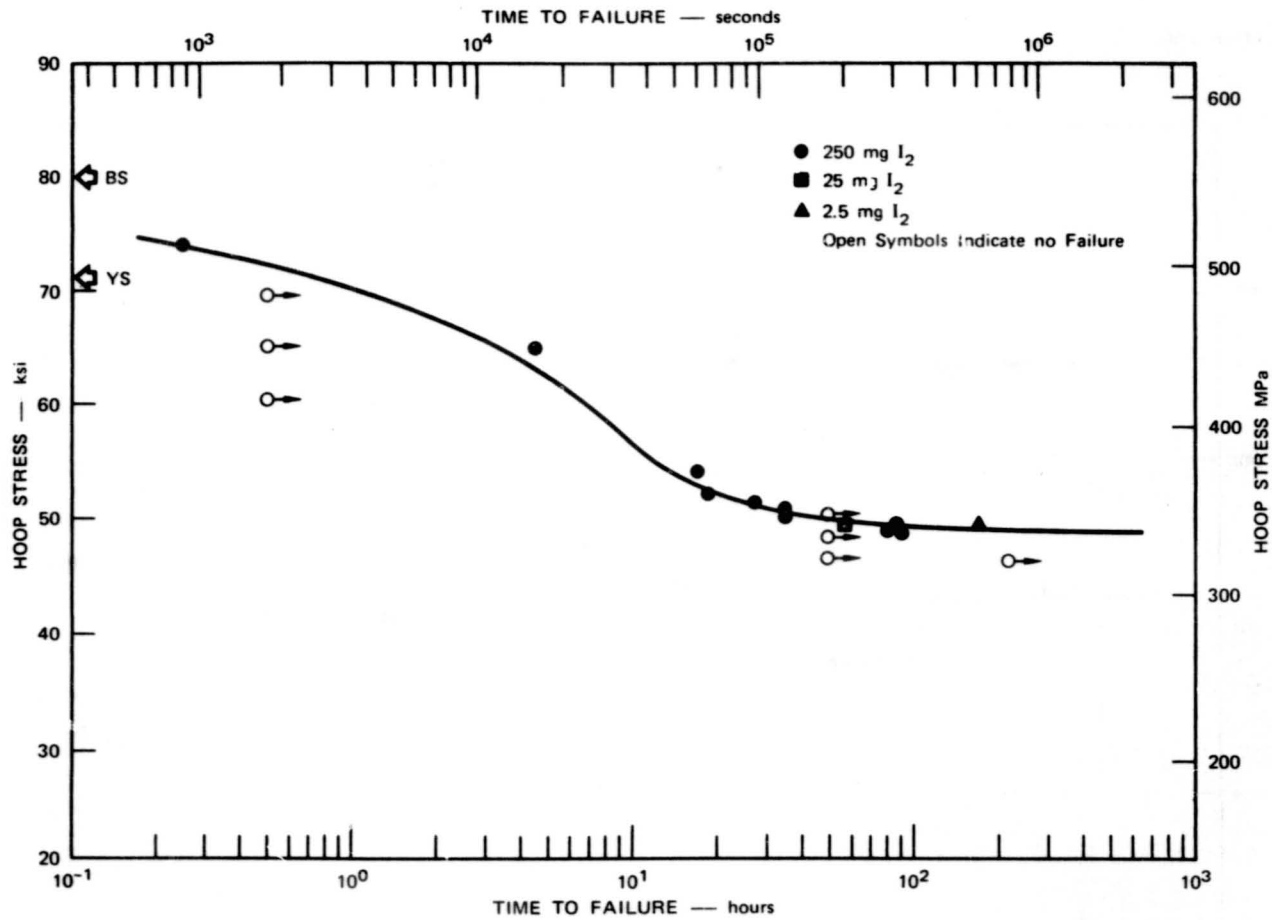
FIGURE 5-15   RESULTS OF TUBE PRESSURIZATION TESTS ON UNFLAWED 7AH11-H
ZIRCALOY-2 SPECIMENS EXPOSED TO IODINE AT 590 K

SA-4197-309
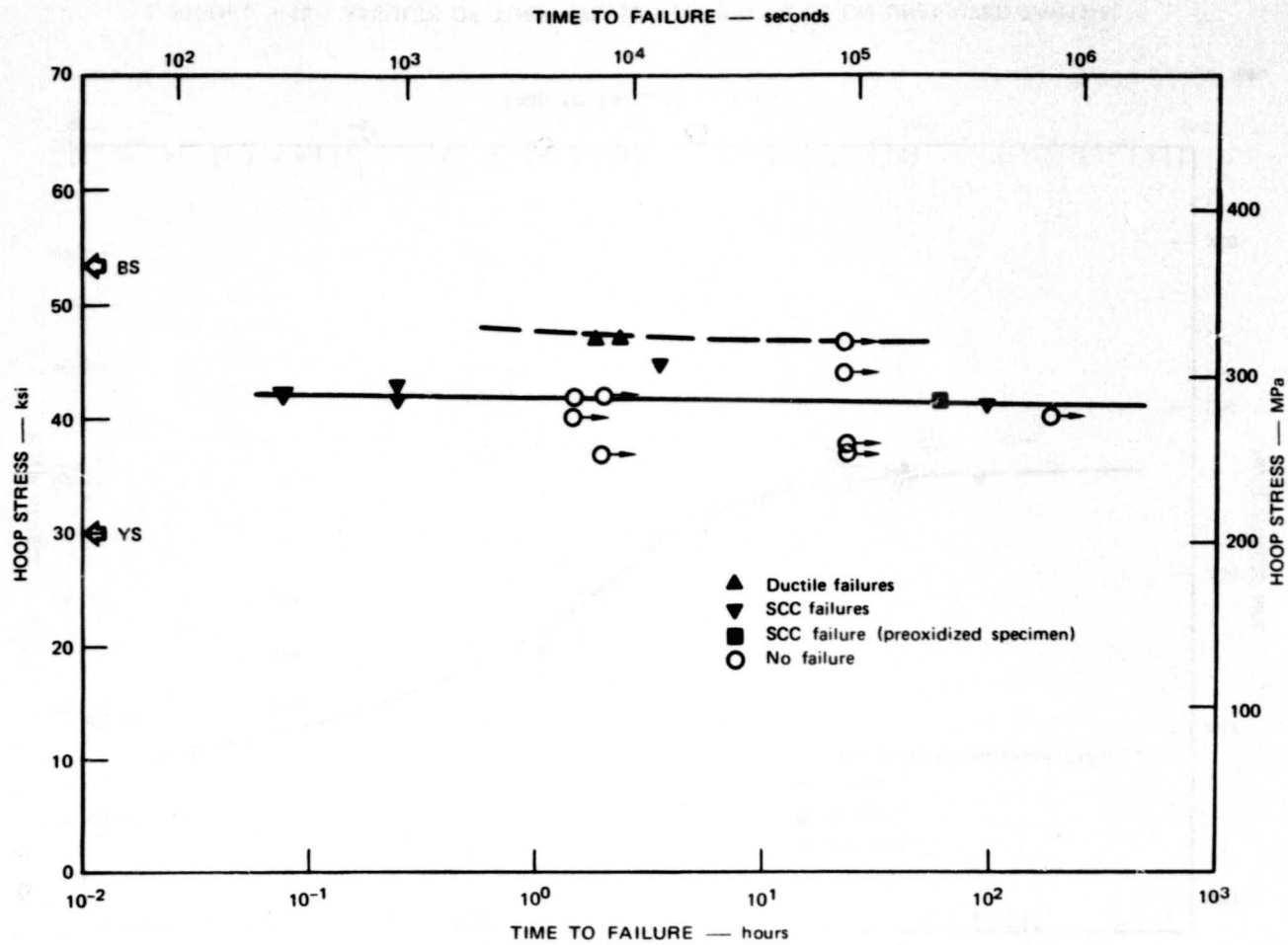
FIGURE 5-16   RESULTS OF PRESSURIZATION TESTS ON UNFLAWED SPECIMENS OF 7AH11-S ZIRCALOY-2
EXPOSED TO IODINE AT 590 K

Figure 5-15 also indicates that decreasing the iodine concentration from 250 mg I_2 to 2.5 mg I_2 ($\sim$ 6.0 to 0.06 mg I_2 per cm^2 of Zircaloy surface) tends to increase the failure time at a stress close to the threshold, but does not significantly increase the threshold itself. An increase in failure times with decreasing iodine concentration in the same range has also been reported by Cox and Wood (5-3).

Although additional data clearly are required, the behavior of the irradiated HBR Zircaloy-4 specimens (Figure 5-14) suggests a similar trend to that of the unirradiated 7FD11 Zircaloy-4 specimens (Figure 5-13) at the same test temperature. Based on the limited number of results available, the threshold stress for iodine SCC of the HBR tubing at 630 K appears to be about 200 MPa, which is about 30 percent less than the threshold stress for the unirradiated 7FD11 tubing. The threshold stress also is a much smaller fraction of the yield stress for the irradiated material (0.33 for HBR tubing compared with 0.75 for 7FD11 tubing). Moreover, the failure strains at stresses just above threshold were lower in the HBR specimens and the time to failure for specimen HBR-1 (0.53 hours) was much less than that for specimen Zr-4-18 (2.9 hours) at the same net stress. Tests on 7FD11 in the hot cell gave results that were indistinguishable from those obtained in out of cell tests (see Table 5-1). Thus, the differences between the behavior of the 7FD11 and HBR specimens cannot be attributed to differences in test procedure and we can conclude that the irradiated HBR tubing is markedly more susceptible to iodine SCC at 630 K than the unirradiated 7FD11 Zircaloy-4 tubing. Although the greater susceptibility of the HBR material is probably a direct effect of neutron irradiation during service, no definite conclusion can be reached in the absence of information on the susceptibility to iodine SCC of unirradiated tubing from the same lot as the HBR cladding. Unfortunately, such unirradiated material is not available for testing.

The behavior of the 7AH11-S Zircaloy-2 (Figure 5-16) differed from that of the other three materials in that iodine SCC was consistently observed only within a very narrow range of stresses. No failures occurred below 282 MPa, which appears to be the threshold stress for iodine SCC. Stress corrosion cracking was observed at stresses between 282 MPa and 307 MPa, but all four specimens tested at stresses greater than 307 MPa failed by ductile processes even though iodine was present in

the test environment. We believe that crack blunting due to rapid creep suppressed iodine SCC in these specimens. Support for this theory is provided by the results of the crack initiation studies on 7AH11-S Zircaloy-2 reported in Section 4 of this report. Those studies showed that iodine-induced stress corrosion crack nuclei became wider rather than deeper when increasing local stresses were applied for a constant time. Suppression of iodine SCC at high strain rates has been reported by others (5-3, 5-13, 5-14) and is observed in many other metal/environment systems. The present results suggest that a strain rate of about 3×10^{-5} sec^{-1} will suppress iodine SCC of Zircaloy-2 at 590 K, in reasonable agreement with published data (5-13).

Another aspect of the behavior of the 7AH11-S Zircaloy-2 that differed from the other materials was the very wide spread of failure times observed in tests at stresses just above the threshold stress. Of particular interest is the observation that iodine SCC failure of 7AH11-S Zircaloy-2 tubing sometimes can proceed to completion in periods of only a few minutes. Moreover, the times to failure seem to show a bimodal distribution at stresses in the range 282 MPa to 294 MPa--three of the five specimens tested in this stress range failed in 15 minutes or less, whereas the other two required 61 and 100 hours for failure. This suggests that different pieces of the 7AH11-S Zircaloy-2 tubing have different susceptibilities to iodine-SCC, an idea that is supported to some extent by the results of the crack initiation studies on this material (see Section 4) as well as by literature references to "susceptible" batches of Zircaloy (5-3, 5-13).

One of the two 7AH11-S specimens that showed long-time SCC failures just above the threshold stress was the preoxidized specimen. Therefore, we can conclude that the presence of a 1.5-μm oxide film has little or no effect on the threshold stress for iodine-induced SCC of 7AH11-S Zircaloy-2 tubing at 590 K but may have an effect on the failure time.

Since the only difference between the 7AH11-S and 7AH11-H lots of Zircaloy-2 tubing was the final heat treatment temperature, a comparison of the behavior of those two tubing lots provides an indication of the effect of microstructure on the

susceptibility of Zircaloy-2 to iodine SCC. The test data in Tables 5-3 and 5-4 and Figures 5-15 and 5-16 indicate that

- The threshold stress for iodine SCC of the annealed tubing was slightly lower than that for the stress relieved material.

- The shortest failure times for stress-relieved specimens were nearly two orders of magnitude larger than the shortest failure times for annealed specimens at stresses just above the iodine SCC stress thresholds.

- Stress-relieved specimens showed smaller failure strains than annealed specimens in tests at stresses just above the iodine SCC stress thresholds.

Thus two out of three indicators of relative SCC susceptibility favor the stress-relieved 7AH11-H material over the annealed 7AH11-S tubing. It can be concluded that Zircaloy-2 tubing becomes more susceptible to iodine SCC in internal pressurization tests as the heat treatment temperature of the tubing is increased from 770 K to 840 K and the microstructure changes from a stress-relieved to a recrystallized condition.

It might be argued that failure strain is the most relevant indicator of SCC susceptibility as far as the fuel cladding application of Zircaloy tubing is concerned because cladding is subjected to a fixed displacement type of loading (imposed by the fuel) in reactor service. However, the larger failure strain of the 7AH11-S tubing is mainly due to the fact that the iodine SCC stress threshold is above the yield stress of this material. It is likely that the failure strain of 7AH11-S tubing would fall as the yield stress was increased by radiation hardening and that the lower threshold stress and failure time of 7AH11-S Zircaloy-2 would then make it more prone than 7AH11-H tubing to iodine-induced failure even under fixed-displacement loading.

Origin of the Threshold Stress

In many instances of the stress corrosion cracking of reactive metals that form highly protective oxides, it is observed that a certain minimum strain rate must be sustained to continually rupture the oxide formed at the crack tip so that SCC can continue (5-15). In some cases (5-15), SCC threshold stresses have been shown

to be the smallest stresses that could generate the required rates of strain. Wood (5-16) has indicated that iodine SCC of Zircaloys can be suppressed at very small strain rates, thus suggesting that the threshold stresses observed in the present experiments might be associated with the attainment of a certain critical strain rate.

The data provide mixed support for this idea. For example, the average diametral (hoop) strain rates in specimens Zr-2H-7 through Zr-2H-12, which were tested at stresses just above threshold, were all about 3×10^{-8} sec^{-1} based on the failure strains and times to failure; this is consistent with a critical strain rate concept. However, if attainment of this strain rate were a sufficient condition for iodine SCC of Zircaloy-2 at 590 K, the stress threshold for the 7AH11-S Zircaloy-2 would have been much lower than that actually observed because the average strain rates in specimens of this material at stresses just above threshold were up to 100 times faster than 3×10^{-8} sec^{-1}. Moreover, the behavior of specimens Zr-2S-15 and Zr-2S-16 (Table 5-4), for which the average strain rates differ by more than two orders of magnitude, is much easier to explain in terms of a threshold stress than in terms of a threshold strain rate.

The present observations seem less consistent with the idea of a critical strain rate than with the concept that the threshold stress is the minimum stress that is capable of forming a propagatable crack in Zircaloy exposed to iodine, as suggested by Ranjan and Smith (5-8). However, if a critical strain rate is required for iodine SCC of Zircaloy tubing, the present data indicate that it is material- and/or temperature-dependent and has the following values: $\leq 3 \times 10^{-8}$ sec^{-1} for 7AH11-H at 590 K; $\leq 10^{-7}$ sec^{-1} for 7AH11-S at 590 K; $\leq 2 \times 10^{-7}$ sec^{-1} for HBR at 630 K; and $\leq 10^{-7}$ for 7FD11 at 630 K.

REFERENCES

5-1 S. R. Novak and S. T. Rolfe, Corrosion, 26, 121 (1970).

5-2 R. W. Staehle, "Materials-Environment Viewpoint," in Stress Corrosion Cracking Problems and Research in Energy Systems, L. C. Ianniello, ed. (ERDA 76-98, February 1976), p. 108.

5-3   B. Cox and J. C. Wood, "Iodine Cracking of Zircaloy Fuel Cladding--
      A Review," in Corrosion Problems in Energy Conversion and Generation,
      Craig S. Tedman, Jr., ed. (Electrochemical Soc., New York 1974),
      p. 275.

5-4   A. S. Kobayashi, N. Polvanich, A. F. Emery, and W. J. Love, "Inner and
      Outer Cracks in Internally Pressurized Cylinders," presented at the 1976
      Conference on Pressure Vessels and Piping in Petroleum Mechanical
      Engineering, Mexico City, (September 1976).

5-5   ASTM Recommended Test Method E-399-72, "Plane Strain Fracture Toughness
      Testing of Metallic Materials" (1972).

5-6   K. Videm and L. Lunde, "Stress Corrosion Cracking of Zircaloy Fuel
      Cladding under Power Ramps and in Lab Tests," Proceedings: ANS Topical
      Meeting on Water Reactor Fuel Performance, St. Charles, Illinois,
      May 1977.

5-7   B. A. Bilby, A. H. Cottrell, and K. H. Swinden, Proceedings of the Royal
      Society, A272, 304-314 (1963).

5-8   G. V. Ranjan and E. Smith, "Fracture of Zircaloy Cladding During Power
      Ramps by Interactions with Uranium Dioxide Pellets in Water Reactor Fuel
      Rods," Proceedings: ANS Topical Meeting on Water Reactor Fuel Performance,
      St. Charles, Illinois, May 1977.

5-9   P. H. Kreyns, G. L. Spahr, and J. E. McCauley, J. Nuclear Materials, 61
      202-212 (1976).

5-10 J. C. Wood, J. Nuclear Materials, 45, 105 (1972/73).

5-11 H. Wachob and H. G. Nelson, "Halogen Stress Corrosion Cracking of
      Zircaloy-4," Proceedings: TMS-AIME Symposium on Environment Sensitive
      Fracture of Engineering Materials, Chicago, Illinois, October 1977.

5-12 A. A. Bauer, L. M. Lowry, and J. S. Perrin, "Evaluating Strength and
      Ductility of Irradiated Zircaloy," Battelle Columbus Quarterly Report
      BMI-NUREG-1984, March 1976.

5-13 J. C. Wood, B. A. Surette, I. M. London, and J. Baird, J. Nuclear Materials,
      57, 155 (1975).

5-14 A. Garlick, J. Nuclear Materials, 49, 209 (1973/74).

5-15 H. I. Logan, "The Stress Corrosion of Metals" (J. Wiley and Sons Inc.,
      New York, 1966).

5-16 J. C. Wood and D. G. Hardy, "Characteristics of Fuel Cladding After Power
      Ramping," Proceedings: ANS Topical Meeting on Water Reactor Fuel Performance,
      St. Charles, Illinois, May 1977.

Section 6

SCREENING TESTS FOR STRESS CORROSION CRACKING IN SEVERAL ENVIRONMENTS

INTRODUCTION

As discussed in Section 2 of this report, the Zircaloy cladding of a light water reactor fuel rod can be exposed in service to a variety of chemical substances, some of which cause embrittlement or stress corrosion cracking (SCC) of Zircaloy. The tests reported in this section were undertaken to screen the aggressiveness toward Zircaloy of a wide variety of fission products and fuel impurities, with the goals of identifying the chemical agents most likely to be responsible for PCI fuel cladding failures and selecting the test environments for detailed laboratory studies of SCC behavior. Zircaloy-4 was used for the screening tests because there is less information available in the literature on the SCC behavior of this alloy than for Zircaloy-2. Most of the tests were performed at NASA-Ames Research Center using sheet and plate specimens but the aggressiveness of cesium and to a lesser extent, cadmium was also investigated at SRI in tests on tubing specimens.

SLOW CRACK GROWTH IN GASEOUS HYDROGEN ENVIRONMENTS

Hydrogen gas, formed by the decomposition of moisture introduced with the UO_2 fuel, is one of the components of the internal environment of fuel cladding. Hydrogen is capable of embrittling zirconium alloys and cladding failures due to the formation of massive "sunburst" hydrides were a significant problem until steps were taken to minimize the moisture content of the fuel pellets. Failures of CANDU pressure tubes have also been attributed to embrittlement due to stress-induced hydride formation (6-1).

Although the embrittlement of Zircaloys by hydrogen charging and subsequent precipitation of hydrides has been widely studied, comparatively little attention has

been paid to the possibility that gaseous hydrogen environments may be capable of promoting slow crack growth in Zircaloys with low internal hydrogen contents. Accordingly, the study described below was undertaken.

Experimental Procedures and Results

"Off the shelf" annealed Zircaloy-4 plate (12.7-mm thick) obtained from TWCA was used for most of the experiments. This material had a grain size of about 12 μm and showed a fairly intense basal texture in which maximum basal pole concentrations of about five times random were located at about $\pm 30°$ from the plate normal direction toward the plate transverse direction. Later in the test series, some experiments were performed with the 9912-4B lot of stress-relieved Zircaloy-4 plate. The history and characteristics of this 12.7-mm-thick plate are described in Section 3 and Appendix A.

Hydrogen-induced slow crack growth was studied in precracked compact-tension specimens prepared from the annealed Zircaloy-4 plate. Variables investigated were applied stress intensity, hydrogen pressure, and temperature (within the range 296 to 343 K). The results obtained in these tests, which were conducted in accordance with ASTM procedures,[*] are summarized in Figures 6-1 through 6-3.

No subcritical crack growth was observed at temperatures of 393 K and above in the experiments on the annealed Zircaloy-4. Tests on stress relieved Zircaloy-4 specimens at 573 and 658 K confirmed that under static loads and at high hydrogen pressures, subcritical crack growth did not occur at reactor operating temperatures. However, under cyclic loading (1 Hz, tension-tension, R = 0.1), crack growth was observed at 573 K at hydrogen pressures less than 66 Pa. Interestingly, the crack velocity at constant nominal peak stress intensity fell with increasing hydrogen pressure as shown in Figure 6-4. The pressure dependence was found to be slightly greater at 658 K than at 573 K.

---

*ASTM Recommended Test Method E-399-72, "Plane Strain Fracture Toughness Testing of Metallic Materials," 1972.
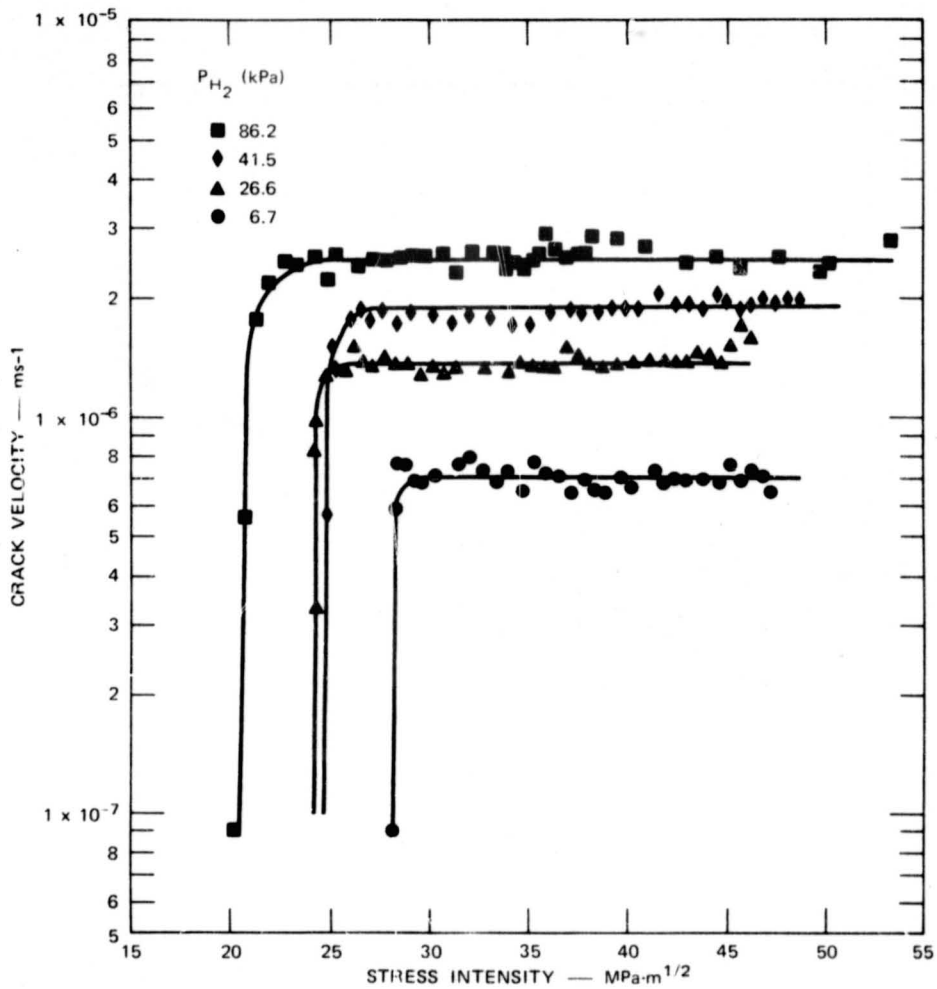
FIGURE 6-1   INFLUENCE OF HYDROGEN PRESSURE ON THE SLOW CRACK GROWTH
BEHAVIOR OF ANNEALED ZIRCALOY-4 AT 297 K
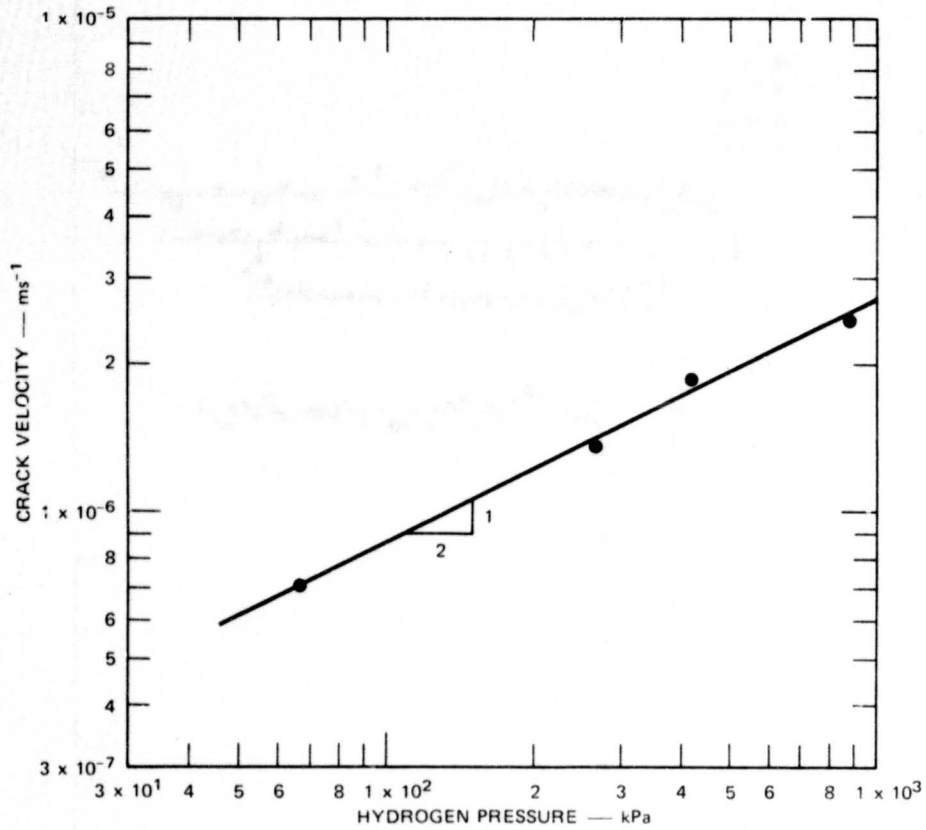
FIGURE 6-2 HYDROGEN PRESSURE DEPENDENCE OF STAGE 2 CRACK GROWTH
IN ANNEALED ZIRCALOY-4 at 297 K
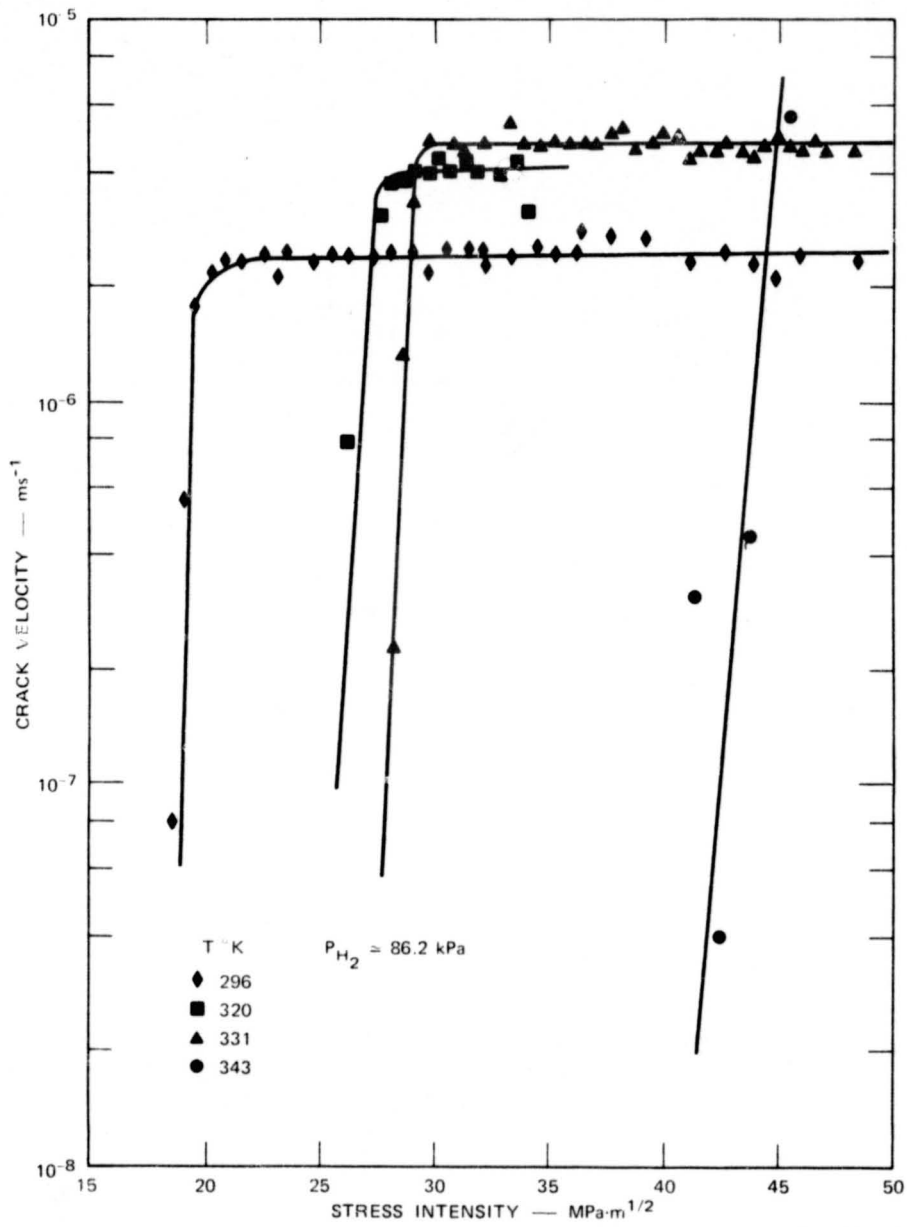
FIGURE 6-3 EFFECT OF TEMPERATURE AND STRESS INTENSITY ON CRACK VELOCITY
FOR ANNEALED ZIRCALOY-4 TESTED IN HYDROGEN
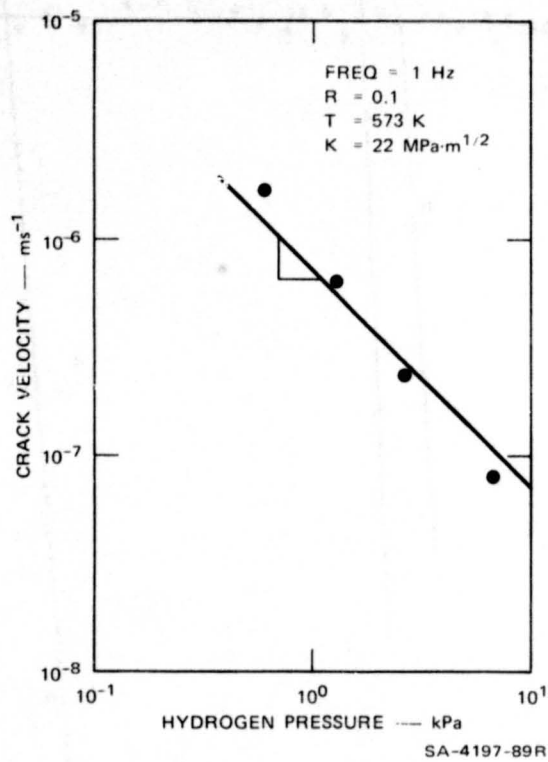
FIGURE 6-4   HYDROGEN PRESSURE DEPENDENCE
OF FATIGUE CRACK GROWTH RATE
IN STRESS-RELIEVED ZIRCALOY-4

Discussion

The form of the crack velocity versus stress intensity curves obtained at low tem-
perature (Figure 6-1) is similar to that observed in many other cases of stress
corrosion cracking. A threshold stress intensity must be exceeded to obtain slow
crack growth, and a diffusion-limited plateau (Stage 2) in the rate of crack growth
is encountered at higher stress intensities. The threshold stress intensity
decreased with increasing hydrogen pressure, whereas the Stage 2 growth rate
increased approximately with the square root of the hydrogen pressure (Figure 6-2).
Increases of test temperature up to 343 K at constant gas pressure increased both
the threshold stress and the Stage 2 growth rate (Figure 6-3). Figure 6-5, which
is an activation plot for the Stage 2 crack growth rate, gives a value of $\sim$ 15.5 kJ/
mole for the activation energy of the rate-controlling process.

Several processes could account for an activation energy of 15.5 kJ/mole. The first
possibility is stress-induced hydride formation: Nelson and Williams (6-2) have
reported activation energies of < 20 kJ/mole for stress-induced hydride formation
in titanium and it would not be surprising to find a similar value for stress-
induced hydride formation in Zircaloy. A second possibility is the short-circuit
diffusion of hydrogen, which has an activation energy about one-half that for bulk
diffusion. Thus, one would predict an activation energy of 17 to 20 kJ/mole for
the short-circuit diffusion of hydrogen in zirconium. The final possibility is
the chemisorption of hydrogen on the Zircaloy surface. Shanabarger (6-3) has
measured an activation energy of $\sim$ 24 kJ/mole for the chemisorption of hydrogen on
iron. Because zirconium is an exothermic hydride former, the activation energy for
chemisorption on Zircaloy is probably less than that for iron and a value of
$\sim$ 15 kJ/mole would not be unreasonable.

Fractographic observations did not completely clarify the nature of the rate con-
trolling process, but they did demonstrate that hydride formation is involved in
hydrogen-induced slow crack growth. Figure 6-6 shows that the process is very
crystallographic with many cleaved facets and unidirectional slabs of zirconium
hydride on the fracture surface. Moreover, the cross section in Figure 6-7 shows
that the entire fracture surface was covered with a 10-μm-thick layer, which was
identified as ZrH by x-ray diffraction.
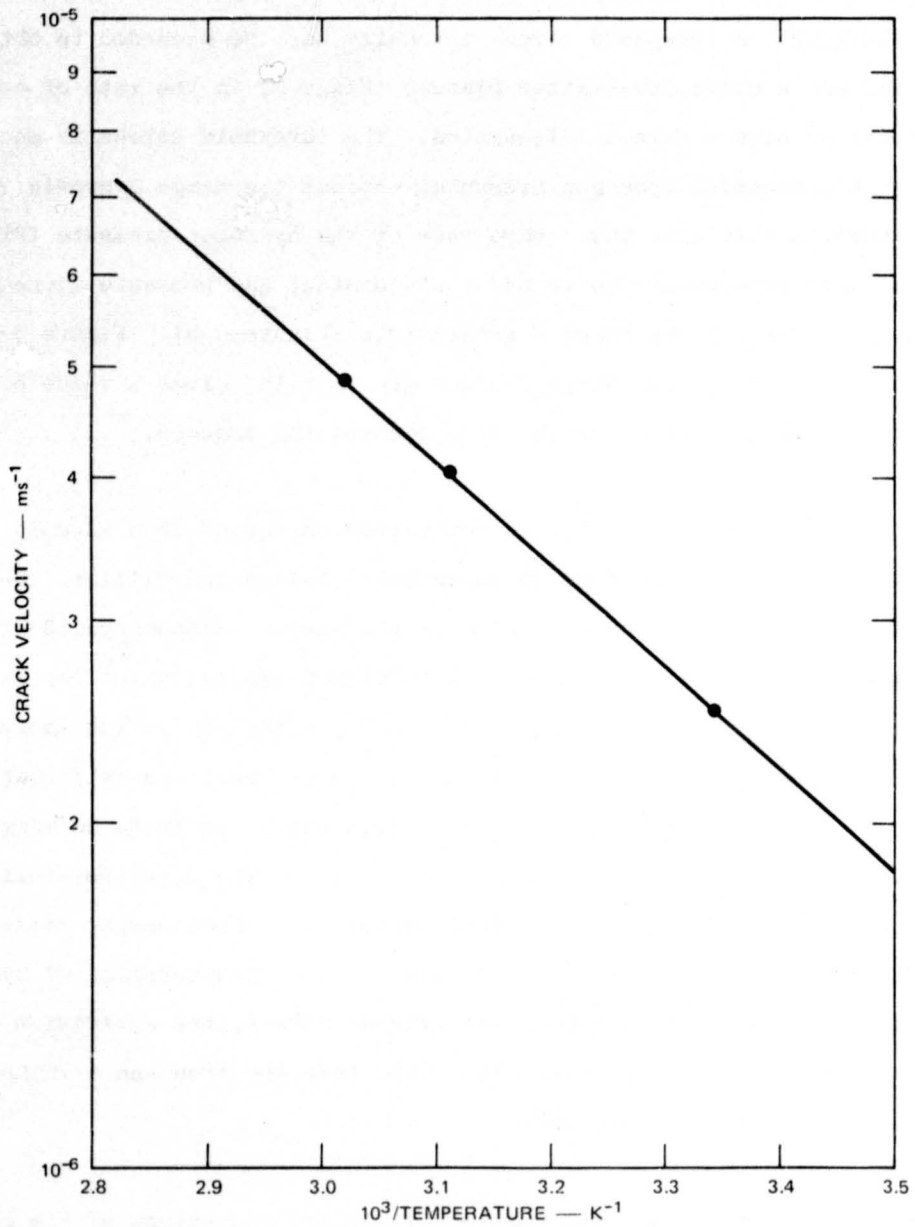
FIGURE 6-5   ACTIVATION ENERGY PLOT FOR STAGE 2 CRACK GROWTH RATE IN
ANNEALED ZIRCALOY-4 EXPOSED TO HYDROGEN AT A PRESSURE OF
~86 kPa
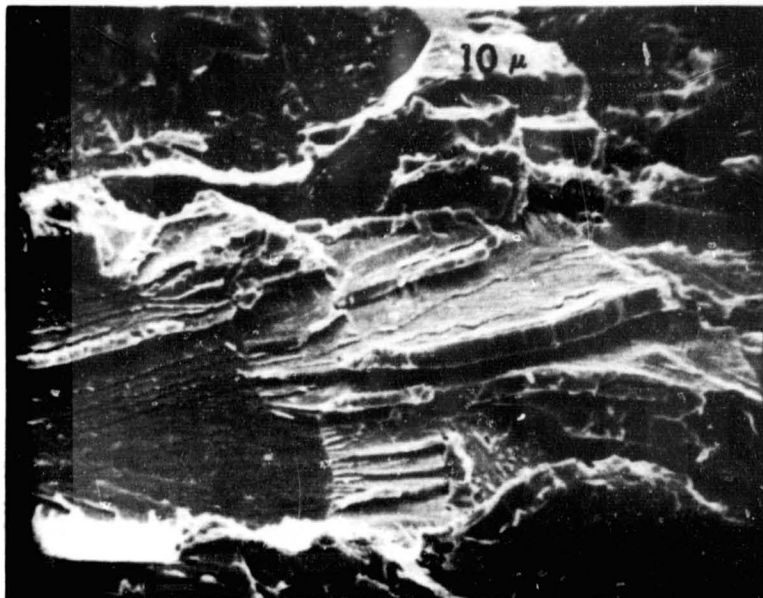
SA-4197-86

FIGURE 6-6   FRACTURE SURFACE OF ANNEALED ZIRCALOY-4
              PLATE FOLLOWING SLOW CRACK GROWTH IN
              HYDROGEN AT 297 K AND A PRESSURE OF ~86 kPa
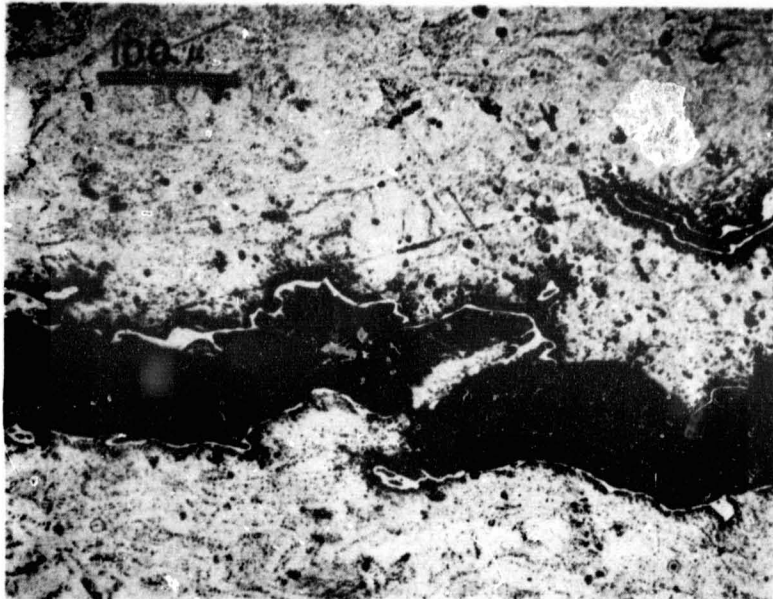
SA-4197-87

FIGURE 6-7   LONGITUDINAL SECTION PERPENDICULAR TO THE
CRACK FRONT SHOWING A LAYER OF ZrH THAT
COMPLETELY COVERS THE FRACTURE SURFACE

Hydride formation also plays a key role in the crack growth behavior at higher temperatures. Figure 6-8 is a cross section through the midsection of a stress-relieved specimen that was statically loaded in hydrogen at 573 K. A ball of hydride, which in this case proved to be ZrH_2, has formed at the crack tip and has completely blunted it. The resulting decrease in stress intensity is the probable reason why no slow crack growth occurred in the statically loaded specimens at the higher test temperatures.

Figure 6-8 also suggests a possible explanation for the unusual negative hydrogen pressure dependence observed in the fatigue crack growth studies (Figure 6-4). At high hydrogen partial pressures, the hydride may form too rapidly to be broken by the mechanical action at the crack tip. The formation of a hydride ball leads to blunting of the crack tip, thus reducing the stress intensity. As the hydrogen pressure is decreased, mechanical fatigue can crack the zirconium hydride at the crack tip as fast as the hydride is formed. Therefore, an increase in crack velocity occurs with a decrease in hydrogen partial pressure.

Summary

Statically loaded precracked specimens of Zircaloy-4 exhibit subcritical crack growth at stress intensities $\gtrsim$ 20 MPa·m$^{1/2}$ when exposed to hydrogen gas at ambient temperature. The threshold stress intensity increases with decreasing hydrogen pressure and increasing temperature. The Stage 2 crack growth rate increases with both hydrogen pressure and temperature. The activation energy of the process that controls the rate of Stage 2 cracking at near-ambient temperatures is about 15.5 kJ/mole and the fracture surfaces are completely covered with a thin layer of ZrH.

Hydrogen-induced slow crack growth in statically loaded specimens is suppressed at reactor operating temperatures, apparently because of crack blunting associated with the formation of ZrH_2 at the crack tip. However, subcritical crack growth is observed in cyclically loaded, precracked specimens exposed to low hydrogen pressures. The crack velocity in this regime increases with decreasing hydrogen pressure, probably because crack blunting by hydride formation occurs less readily at low hydrogen pressures.
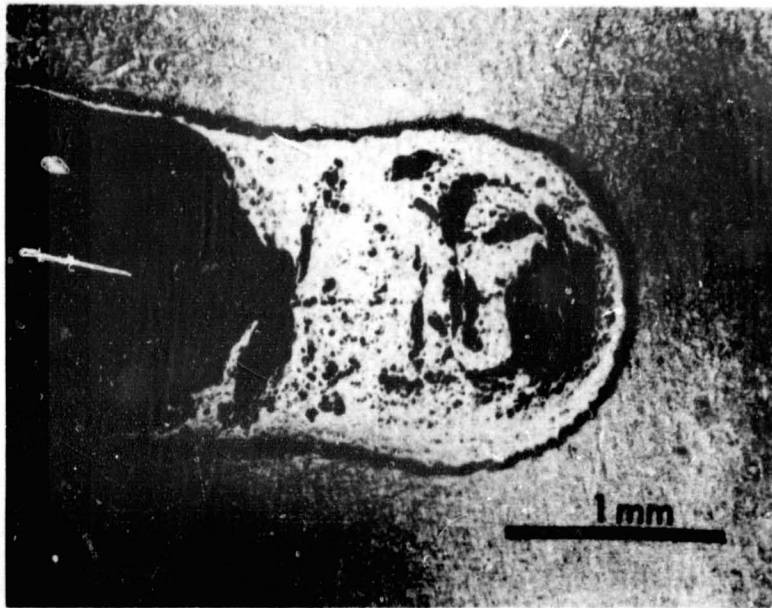
SA-4197-88

FIGURE 6-8 CRACK TIP REGION OF A STRESS-RELIEVED
ZIRCALOY-4 SPECIMEN STATICALLY LOADED AT
573 K IN HYDROGEN AT A PRESSURE OF 13.3 kPa

STRESS CORROSION CRACKING IN HALOGEN VAPORS

Rosenbaum (6-4) was the first to show that Zircaloys are susceptible to stress corrosion cracking (SCC) in iodine vapor at reactor operating temperatures. Since iodine is a major fission product, Rosenbaum's observation suggested the possibility that iodine is the active substance in PCI fuel cladding failures. This posssibility was reinforced when it was found that the details of iodine SCC fracture surfaces resembled the features found on the fracture surfaces of cladding that had suffered PCI failure. Therefore, iodine SCC of Zircaloys has received wide attention and studies have been conducted of the effects of iodine concentration (6-5), temperature (6-6), residual stress (6-6), stress state (6-7), and crystallographic texture (6-7).

An important discrepancy in the research literature concerns the value of the threshold stress intensity K_{Iscc}, the lowest value of stress intensity at which iodine-induced slow crack growth can occur under plane strain, linear elastic conditions. Wood, et al. (6-8) reported a value of ~ 10 MPa$\cdot$m$^{1/2}$ at 573 K, whereas Videm and Lunde (6-9) detected crack growth at nominal stress intensities as low as 4 MPa$\cdot$m$^{1/2}$. Other workers (6-10) have claimed that K_{Iscc} must be less than 1 MPa$\cdot$m$^{1/2}$ to explain the behavior of thin-wall tubing. It was considered essential to firmly establish the value of K_{Iscc} under valid plane strain linear elastic conditions to provide a sound basis for understanding iodine-induced crack growth in fuel cladding. Therefore the study described below was undertaken. In addition to determining K_{Iscc} for iodine SCC, slow crack growth tests were conducted in bromine and chlorine (present in the fuel rod environment to a lesser extent than iodine), in zirconium iodide, and in the combined environments of iodine with iron, iodine with oxygen, and iodine with cadmium. A paper describing the results obtained has been accepted for publication (6-11).

Experimental Procedures

The 9912-4B lot of stress-relieved Zircaloy-4 plate was used for this investigation. The fabrication history and metallurgical characteristics of this 12.7-mm-thick plate material are described in Section 3 and Appendix A.

Wedge-opening loaded, compact tension (WOL-CT) fracture mechanics specimens 1.25 cm thick were cut from the Zircaloy-4 plate so that the crack would propagate in the rolling direction on a plane normal to the plate width. The specimens were of sufficient thickness to ensure that the ASTM guidelines for plane strain conditions would be met at all values of stress intensity less than about 18 MPa·m$^{1/2}$. In accordance with ASTM recommended procedures, specimens were fatigue-precracked in air and a wedge was driven into the initial machined notch to produce a fixed crack opening displacement (COD). The wedge was made of a molybdenum alloy known to be chemically inert to halogens. The specimens were encapsulated in individual 3.8-cm-diameter Pyrex capsules. After the appropriate environment had been introduced (iodine, bromine, chlorine, zirconium iodide, or a combined environment of iodine and iron, iodine and oxygen, or iodine and cadmium), the capsules were sealed and placed in a furnace at 633 ± 5 K for various lengths of time. After removal from the furnace, the specimens were air-cooled and then reloaded to determine the actual final load.

The load on the specimen at 633 K was estimated to be 75% of the load at room temperature. This factor is based on the reduced material modulus at the test temperature and the difference between the thermal expansion coefficients of molybdenum and zirconium. Specimens were fatigue cracked post test in order to protect the region of stress corrosion crack growth and then were failed by overload. The final value of stress intensity during the SCC part of the test was calculated from the estimated load at temperature, and from the location of the stress corrosion crack tip, which was determined by examining the fracture surface of the failed specimen. An average crack growth rate for each test was determined by dividing the total length of environment-induced slow crack growth observed on the fracture surface by the total time the specimen had been exposed to the test environment. Detailed fractography was conducted using a scanning electron microscope.

Results and Discussion

Stress corrosion crack growth in Zircaloy-4 was observed at approximate PWR fuel cladding operating temperature (633 K) in all the environments investigated. Table 6-1 summarizes the tests and lists the chemical substances and concentrations (mg

Table 6-1

SUMMARY OF ENVIRONMENTALLY INDUCED CRACK GROWTH BEHAVIOR OF
ZIRCALOY-4 IN HALOGEN AND HALOGEN CONTAINING ENVIRONMENTS
AT 633 K

| Chemical Environment | | K_{Final} | Average Crack |
Substance	Concentration (mg/cm^2)	$(MPa \cdot m^{1/2})$	Growth Rate (ms^{-1})
I_2	4.4	14	2×10^{-7}
		10	6×10^{-9}
		9	4×10^{-10}
		7	No growth
		5	No growth
I_2 + Fe	4.4	10	1×10^{-9}
		9	No growth
I_2 + O_2	4.4	15	3×10^{-7}
		9	No growth
I_2 + Cd	1.1	11	5×10^{-9}
ZrI_4	30	15	1×10^{-7}
		11	4×10^{-8}
		9	1×10^{-9}
Br_2	30	11	3×10^{-8}
		10	3×10^{-9}
		9	9×10^{-10}
Cl_2	20	15	1×10^{-8}

of halogen per cm^2 of Zircaloy) initially present in each capsule, the final value of stress intensity at the termination of each test (estimated to be accurate to about ± 0.5 $MPa \cdot m^{1/2}$), and the observed average crack growth rate. As can be seen, the behavior of Zircaloy-4 was somewhat similar in all environments. Differences do exist, however, when the influence of each environment is compared separately and fracture topography is also considered.

In an iodine environment at ~ 633 K, the value of K_{Iscc} appears to be approximately 9 $MPa \cdot m^{1/2}$. This value is similar to the value of 10 $MPa \cdot m^{1/2}$ observed by Wood et al. (6-8) for Zircaloy-2 at 573 K. Thus the present observations support the data of Wood, et al. (6-8) and also suggest that K_{Iscc} may be fairly insensitive to temperature (between 573 K and 633 K) and material (stress-relieved Zircaloy-4 and cold-worked Zircaloy-2). As discussed in detail in Section 5, the lower values of "K_{Iscc}" reported by Videm and Lunde (6-9) and Kreyns et al (6-10) probably are attributable to departures from plain strain linear elastic conditions in their thin-walled tubing specimens. Since crack propagation in thin-walled tubes occurs at nominal stress intensities that are well below the true value of K_{Iscc}, it seems clear that the onset of iodine-induced crack growth in Zircaloy cladding tubes is controlled by a parameter other than stress intensity, and indeed the evidence presented in Section 5 suggests that stress is the key parameter.

The fracture surface of a specimen exposed under load to an environment containing iodine is shown in Figure 6-9. The general topography of this surface is typical of that observed in all halogen-containing environments investigated in this study. Two rather unusual features are evident in the region of stress corrosion crack growth. First, the fracture surface is extremely rough with deep troughs extending into the specimen, perpendicular to the plane of macroscopic crack growth. These troughs probably are evidence of preferred cracking on or near the basal planes. The second unusual feature is the highly irregular stress corrosion crack front. Cracking appears to have occurred along preferred channels ahead of the macroscopic crack front leaving microscopic ligaments of unfailed material behind. Again the preferred crack paths appear related to the texture of the material.

MACHINED NOTCH

PREFATIGUE

I_2 – SCC

POSTFATIGUE

OVERLOAD

3 mm
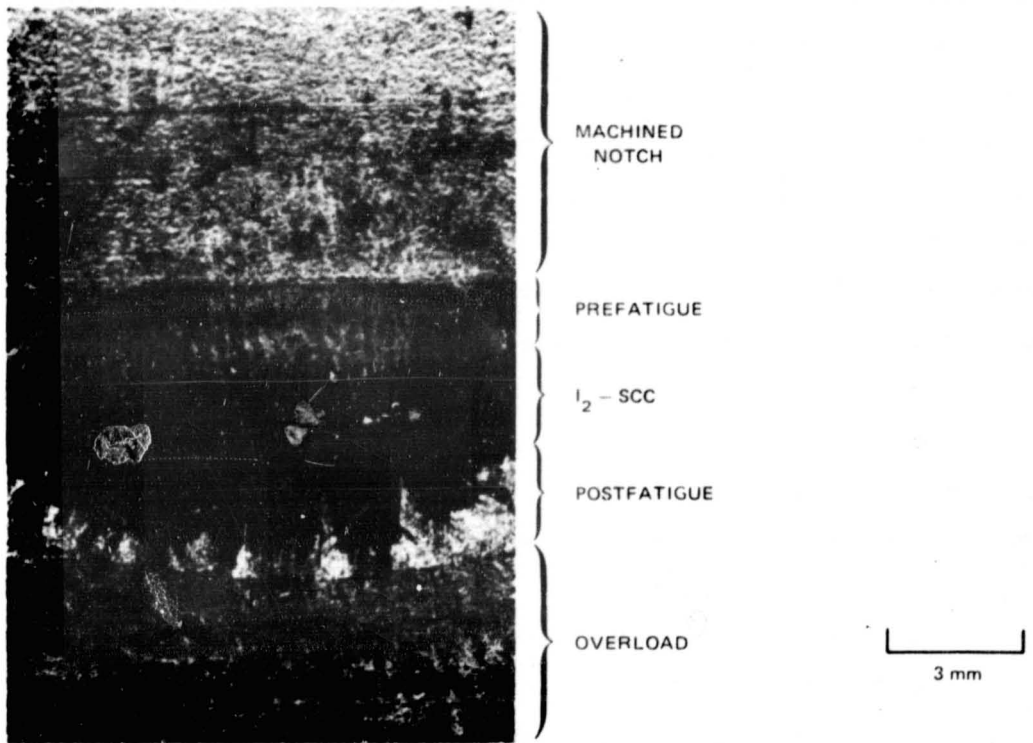
SA-4197-82

FIGURE 6-9   STRESS CORROSION CRACK GROWTH IN STRESS-
RELIEVED ZIRCALOY-4 EXPOSED TO IODINE VAPOR
AT 633 K FOR 7 DAYS

Figure 6-10, a fractograph taken using a scanning electron microscope, is a typical magnified view of the stress corrosion fracture surface. As can be seen, the primary mode of failure is by transgranular cleavage interconnected by regions of ductile failure. No evidence was observed of the intergranular failure reported by Videm and Lunde (6-9). A discussion of the origin of this discrepancy is presented in Section 5. It seems probable that recrystallized material of the kind studied by Videm and Lunde (6-9) is more susceptible to intergranular cracking than stress-relieved material but the underlying reason for this effect of microstructure is not understood.

Chemical interaction between iodine and zirconium in the absence of stress was observed on the machined notch surface of the specimen. Figure 6-11 is a magnified view of this region and shows severe pitting, numerous breaks in the corrosion product film, and corrosive attack with some undercutting of precipitates. These observations are consistent with those reported in Section 4 and provide further evidence that iodine can penetrate thin oxide films on as-received Zircaloy surfaces.

The stress corrosion crack growth behavior of stress-relieved Zircaloy-4 in the combined environments of iodine plus iron, iodine plus oxygen, and iodine plus cadmium appears to be similar to that observed in an iodine environment alone. Although no stress corrosion crack growth was observed in either iodine plus iron or iodine plus oxygen at $9 \text{ MPa} \cdot \text{m}^{1/2}$, crack growth in iodine at this level was extremely slow. Thus, this stress intensity is considered to be the threshold stress intensity. A similar value of K_{Iscc} probably exists for the three combined environments investigated. Qualitatively the data suggest that iron retards the crack growth rate in an iodine environment. In contrast, results reported by other workers indicated that the presence of iron wool increased the probability of stress corrosion cracks in an iodine environment (6-5). This difference suggests that iron may enhance crack initiation (as proposed in Section 4) but reduces the crack growth rate once the crack has been initiated. Oxygen does not appear to have a significant effect on iodine stress corrosion cracking. Cadmium alone, in either the liquid or vapor phase has recently been observed to cause embrittlement of Zircaloy (6-12, 6-13). In the present study, no evidence of a major synergistic influence of cadmium is indicated.

20 μm
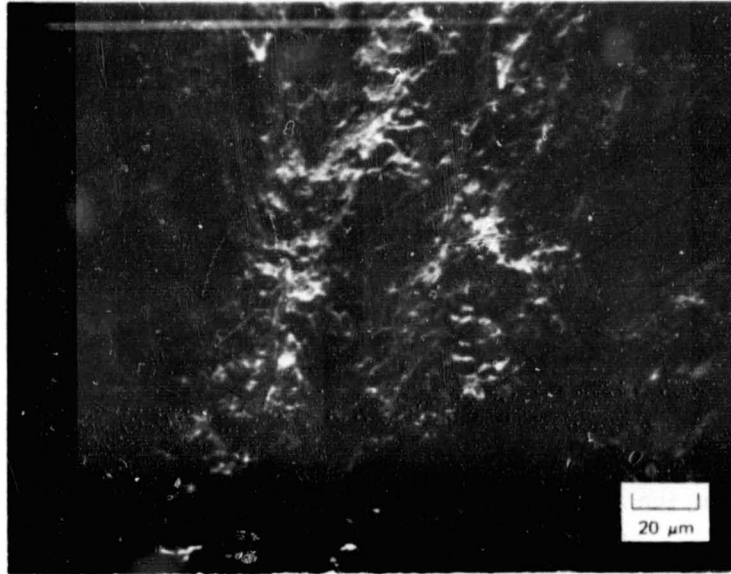
SA-4197-84

FIGURE 6-10   FRACTOGRAPH OF STRESS CORROSION CRACKED REGION
PRODUCED IN STRESS-RELIEVED ZIRCALOY-4 AFTER 14 DAYS
EXPOSURE TO IODINE AT 633 K

25μ
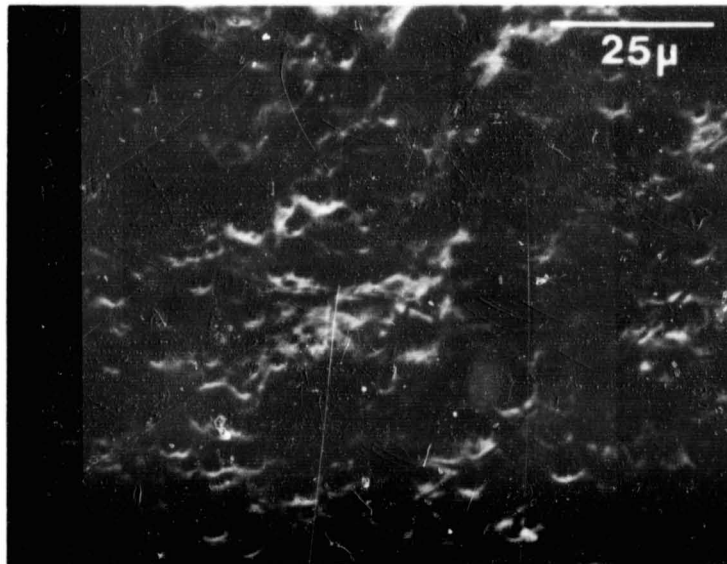
WACHOB/NASA
SA-4197-160

FIGURE 6-11   AN UNSTRESSED SURFACE OF A ZIRCALOY-4 SPECIMEN
AFTER EXPOSURE TO IODINE AT 633 K FOR 28 DAYS

The fracture mode observed in the three combined environments of iodine plus iron, iodine plus oxygen, and iodine plus cadmium was identical to that observed in iodine alone with failure occurring by cleavage combined with ductile rupture.

The presence of oxygen does have a definite effect on the chemical reaction of iodine with zirconium. When the environmental capsules were opened in laboratory air, in those originally containing only iodine the zirconium iodide that had formed on the fracture surface began to hydrolyze giving off hydrogen iodide and forming a white zirconium oxide that masked the fracture surface detail. When oxygen was originally present in the capsule, subsequent exposure of the fracture surfaces to air did not result in hydrolysis. The surfaces remained free from heavy oxide and hydrogen iodide was not evolved. Oxygen originally present in the capsule appeared to hinder the formation of a heavy layer of zirconium iodide by rapidly converting zirconium iodide to a thin layer of zirconium oxide as the crack tip propagated.

In tests in an environment initially containing zirconium iodide (ZrI_4) and no free iodine, average crack growth rates at comparable stress intensities are essentially identical to those observed for an environment initially containing iodine alone. Additionally, the primary fracture mode of zirconium iodide-induced stress corrosion cracking of Zircaloy-4 is transgranular cleavage interconnected by ductile rupture, identical to that observed in iodine. Free iodine should be converted to zirconium iodide at the temperature of these tests. In zirconium iodide no evidence was found of gross surface pitting on the machined notch surface as was observed in an iodine environment (Figure 6-11). The similarity in stress corrosion behavior suggests that cracking in an iodine environment occurs through the formation of zirconium iodide and free iodine is not necessary.

The aggressiveness of bromine and chlorine toward Zircaloy-4 at ~ 633 K is similar to that of iodine. The average crack growth rates at comparable final stress intensities are similar for all three halogens, as seen in Table 6-1. Like iodine, the value of K_{Iscc} for bromine appears to be about 9 MPa·m$^{1/2}$. Wood (6-5) and Cox and Wood (6-7) have investigated the influences of bromine and chlorine, respectively on the crack growth behavior of Zircaloy-2 at room temperature. In

bromine plus air at 296 K, the observed value of K_{Iscc} was approximately 14 MPa·M$^{1/2}$. In moist chlorine at 296 K, K_{Iscc} was observed to be approximately 28 MPa·m$^{1/2}$. Thus both halogens appear to become more aggressive at higher temperatures.

Crack growth in bromine and chlorine occurs by transgranular cleavage interconnected by ductile rupture as shown in Figures 6-12 and 6-13, respectively. Thus the SCC failure modes in the three halogen environments are qualitatively identical. However, long-term exposure of the fracture surface to bromine suggests that bromine reacts chemically with Zircaloy more rapidly than do iodine and chlorine. The angular features of the bromine-induced fracture become rounded and the cleavage facets become more difficult to identify. Additionally, bromine produced heavy pitting on the prefatige crack surface. Such pits did not appear on the stress corrosion cracked region and so must have either occurred before the onset of cracking or are associated with an oxide film. The pits due to bromine are much rounder and smoother than those produced by iodine.

In an effort to establish whether or not subcritical crack growth can occur in stress-relieved Zircaloy-4 exposed to an inert environment, a WOL-CT specimen was loaded to an initial stress intensity of approximately 25 MPa·m$^{1/2}$ at room temperature. The specimen was placed in a capsule, which was evacuated, sealed, and raised to a temperature of ∼ 633K. The specimen was held for four weeks and then removed and examined for the existence of subcritical crack growth. No perceptible crack growth was observed at a calculated final stress intensity of approximately 17 MPa·m$^{1/2}$. Therefore, the crack growth observed in the halogen environments at lower values of stress intensity must be due to the aggressive nature of the environments and is not the result of purely mechanical instability at the crack tip.

Summary

Iodine, bromine and chlorine environments at ∼ 633 K appear to be similarly aggressive in their ability to promote stress corrosion crack growth in stress-relieved Zircaloy-4. The threshold stress intensity under plane strain conditions for both iodine and bromine is about 9 MPa·m$^{1/2}$. An environment initially containing zirconium iodide (ZrI$_4$) is as aggressive as an environment initially containing
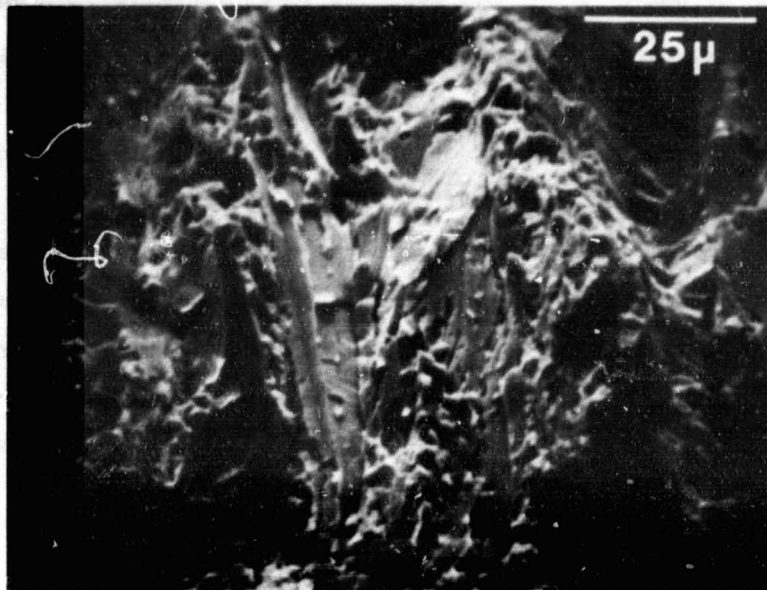
WACHOB/NASA
SA-4197-164

FIGURE 6-12   STRESS CORROSION CRACKED REGION PRODUCED IN A STRESS-RELIEVED
ZIRCALOY-4 SPECIMEN AFTER EXPOSURE TO BROMINE FOR 4-1/2 HOURS
AT 633 K
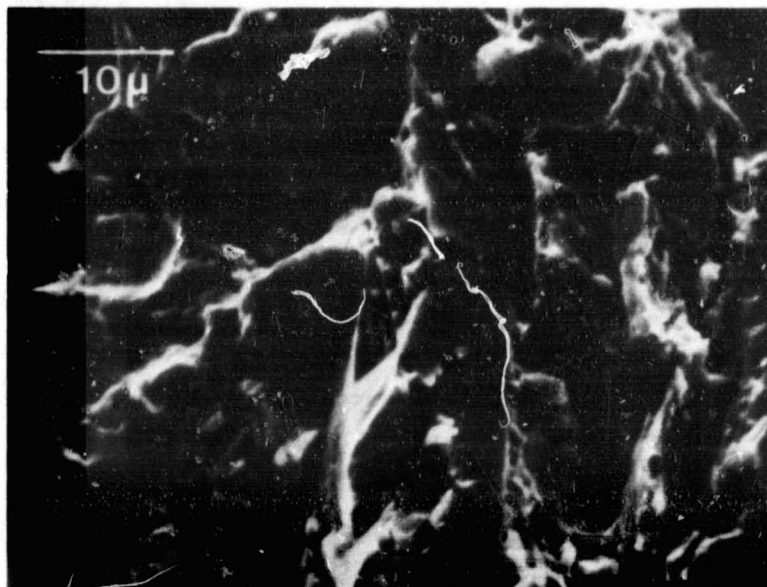
WACHOB/NASA
SA-4197-165

FIGURE 6-13   STRESS CORROSION CRACKED REGION PRODUCED IN A STRESS-RELIEVED
ZIRCALOY-4 SPECIMEN AFTER EXPOSURE TO CHLORINE FOR 4-1/2 HOURS
AT 633 K

free iodine, which suggests that cracking of Zircaloy in an iodine environment occurs through the formation of zirconium iodide and that free iodine is not necessary. A similar conclusion is reported in the literature (6-7). In tests of combined environments, no strong evidence of synergistic effects of iron, oxygen, or cadmium was observed. The macroscopic fracture topography and the microscope fracture mode were essentially identical in all the halogen-containing environments investigated. On the macroscopic scale the fracture surfaces were extremely rough with deep troughs and an uneven crack front related to the basal plane texture in the material and/or chemical fibering. The primary failure mode in all environments was transgranular cleavage with interconnecting regions of ductile failure. Both iodine and bromine were capable of causing localized corrosion (pitting) of unstressed Zircaloy-4 at ~ 633 K.

PRELIMINARY TESTS IN LIQUID METALS AND METAL VAPORS

As discussed in Section 2, the inside surface of nuclear fuel cladding can be exposed in service to a variety of substances that contain the metals Se, Sn, Cs, Te, Sb, Ag, and Cd. Of these elements only Cd and Cs are known to be capable of promoting subcritical crack growth in Zircaloys. We therefore conducted a series of preliminary screening tests in which 12.5-mm-thick WOL-CT specimens cut from the 9912-4B lot of stress-relieved Zircaloy-4 plate were stressed in the presence of various metals at ~ 633 K for 1 week. The results of these tests are summarized in Table 6-2. This table lists the estimated final values of stress intensity (calculated as outlined in the previous subsection and estimated to be accurate to ±0.5 MPa·m$^{1/2}$) as well as pertinent comments concerning each test.

The static wedge-loading technique used in this investigation failed to produce any preceptible crack growth in any of the test environments. An energy dispersive X-ray analysis (EDX) of the exposed precracked specimen surface indicated that, following their respective tests, Se, Sn, and Cs were present on the surfaces, whereas Ag, Sb, Te, and Cd were not. In addition, both Se and Cd produced growths on the unstressed, machined surfaces of the test specimens. The Se growths are shown in Figure 6-14: EDX analysis indicated only Zr and Se present, with a peak ratio of 8:7. An EDX semiquantitative analysis of the Cd growths indicated that

Table 6-2

RESULTS OF WOL-CT TESTS IN LIQUID METALS
AND METAL VAPORS

Environment	Final K $(MPa \cdot m^{1/2})$	Comments
Se	10	"Wets" the surface; surface growths prominent; NPCG[1]
Sn	10	"Wets" the surface; surface growths prominent; NPCG
Cs	13	"Wets" the surface; probably oxidized cesium; NPCG
Te	8	Did not appear to "wet" the surface; NPCG
Sb	9.5	Did not appear to "wet" the surface; NPCG
Ag	8	Did not appear to "wet" the surface; NPCG
Cd	9	Did not appear to "wet" the surface; Cd foil used to obtain Cd vapor, NPCG
Cd	11	Did not appear to "wet" the surface; lots of Cd vapor deposition on cooling; prepumped to a hard vacuum before sealing; NPCG
Cd	11	Did not appear to "wet" the surface; specimen submerged in liquid Cd; NPCG
Cd	5	Did not appear to "wet" the surface; specimen submerged in liquid Cd; NPCG
Cd	12-13	Did not appear to "wet" the surface; special 347SS wedge and machined mating surface to obtain increasing COD upon going to temperature; NPCG

[1] NPCG signifies no perceptible crack growth.
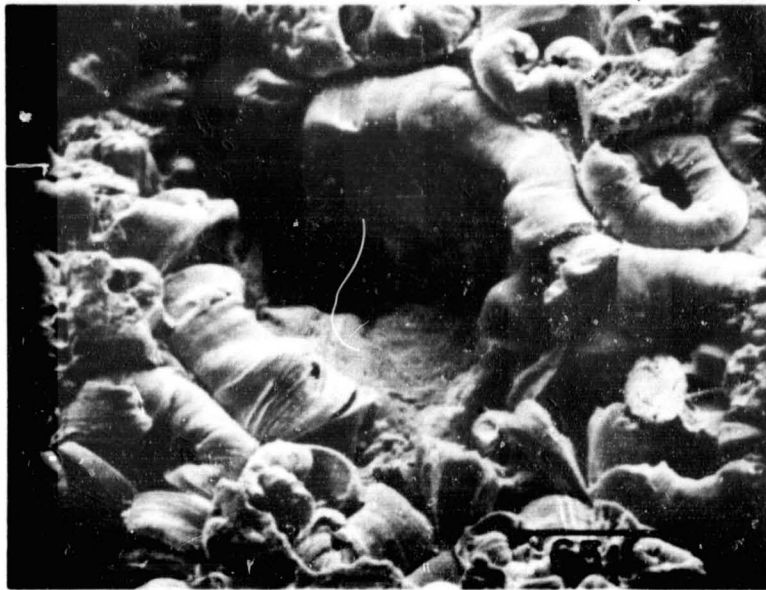
WACHOB/NASA
SA-4197-167

FIGURE 6-14   AN UNSTRESSED SURFACE OF ZIRCALOY-4
SPECIMEN AFTER EXPOSURE TO SELINIUM AT
633 K FOR 7 DAYS

the outer surface had two phases; one having a 1:3 and the second a 2:3 ratio of Zr to Cd. A similar analysis of the interior region indicated a 1:10 ratio of Zr to Cd. This evidence suggests that corrosion of Zircaloy is likely in many fission product environments in the absence of an applied stress.

Because embrittlement by cadmium at similar test temperatures has been reported by other workers (6-12, 6-13), a special effort was made to induce cadmium cracking in WOL-CT specimens of stress-relieved Zircaloy-4. However, as shown in Table 6-2, all tests in cadmium environments failed to promote cracking. No perceptible crack growth was observed in vapor-phase cadmium, in liquid-phase cadmium, with cadmium rubbed onto the surface of the Zircaloy, in a cadmium environment with very low oxygen, and in a special expanding-mated-wedge test.

The major differences between the test method used by Grubb and Morgan (6-13) and that used here are: (1) the existence of a significant tensile strain rate in the rising-load tests used by Grubb and Morgan (6-13) and (2) the use of a getter (6-13) to reduce the oxygen partial pressure to very low values. Both these differences could affect the extent to which the cadmium can penetrate the surface oxide film on the Zircaloy. Tensile deformation will cause continuous cracking of the oxide and a low oxygen partial pressure will decrease the rate at which the oxide cracks can be repaired. Thus, the present results suggest that oxide film penetration is an extremely important step in cadmium-induced cracking of Zircaloy.

EMBRITTLEMENT BY CESIUM IN RISING-LOAD TESTS

Cesium is an abundant fission product and embrittlement of Zircaloy by liquid cesium has been reported by other workers (6-8, 6-14, 6-15). However, attempts (including those reported in the previous subsection) to induce embrittlement at reactor operating temperatures (573 to 633 K) were not successful and the comparative work of Wood, et al. (6-8) suggested that cesium is much less aggressive than iodine toward Zircaloy.

In other cases of liquid metal embrittlement (LME) it is frequently observed that the aggressiveness of the molten metal is very sensitive to its composition (6-16).

Since the effect of composition variations had not been investigated for the cesium-Zircaloy system, it seemed possible that under some circumstances cesium might be much more aggressive toward Zircaloy than the previous work had indicated. The lack of any information on the influence of the oxygen content of the cesium was considered to be of particular concern because this variable will strongly affect the ease with which the cesium can penetrate the protective oxide film. We therefore undertook the limited investigation described below. A complete description of this work has been published elsewhere (6-17).

Experimental Procedures

The material studied was the 7FD11 lot of stress-relieved Zircaloy-4 tubing. The characteristics of this tubing are discussed in Section 3 and Appendix A. Test specimens were prepared by cutting ~ 12.7-mm lengths from the tubing, degreasing with acetone, rinsing with ethyl alcohol, and drying in warm air.

The tests were conducted by diametrally compressing the specimens at a constant displacement rate in one of the controlled environment chambers shown in Figure 6-15. The test environment was either argon, air (room temperature only) or liquid cesium overpressured with 69 kPa argon. When cesium was used, the chamber was assembled in an inert environment.

Most of the rings were tested at a displacement rate of 0.51 mm/min. A few rings were tested at a displacement rate of 12.7 mm/min and one ring was notched before testing. The two 60-degree notches had a root radius of about 0.03 mm and were positioned at the ends of a diameter. When this specimen was tested, it was oriented so that the diameter joining the notches was perpendicular to the loading axis. The load was monitored as a function of displacement at a controlled temperature in the range of room temperature to ~ 633 C. A large-displacement, finite element model was used to estimate the stress and strain distributions in unnotched rings tested at 313 K and 573 K. The accuracy of the model was verified by comparing the finite element solutions with analytical solutions [elastic strain (6-18)] and experimental local strain measurements (elastic and plastic strains up to 3 percent).

CROSSHEAD

STAINLESS
STEEL
BELLOWS

TO VACUUM
AND GAS

CESIUM
LEVEL

CAGE FOR
DEOXIDANT

RING SPECIMEN

HEATING
COILS

CERAMIC
INSULATORS

MONITORING
THERMOCOUPLE

LOAD CELL

(a)

CROSSHEAD

TEFLON O-RING
(SLIDING SEAL)

AUSTENITIC
STAINLESS
STEEL

TO VACUUM
AND GAS

ZIRCALOY-4
LINER

ZIRCALOY-4 END
TO LOADING PISTON

CESIUM
LEVEL

HOLES TO
RETAIN
DEOXIDANT

HEATING
COILS

RING
SPECIMEN

MONITORING
THERMOCOUPLE
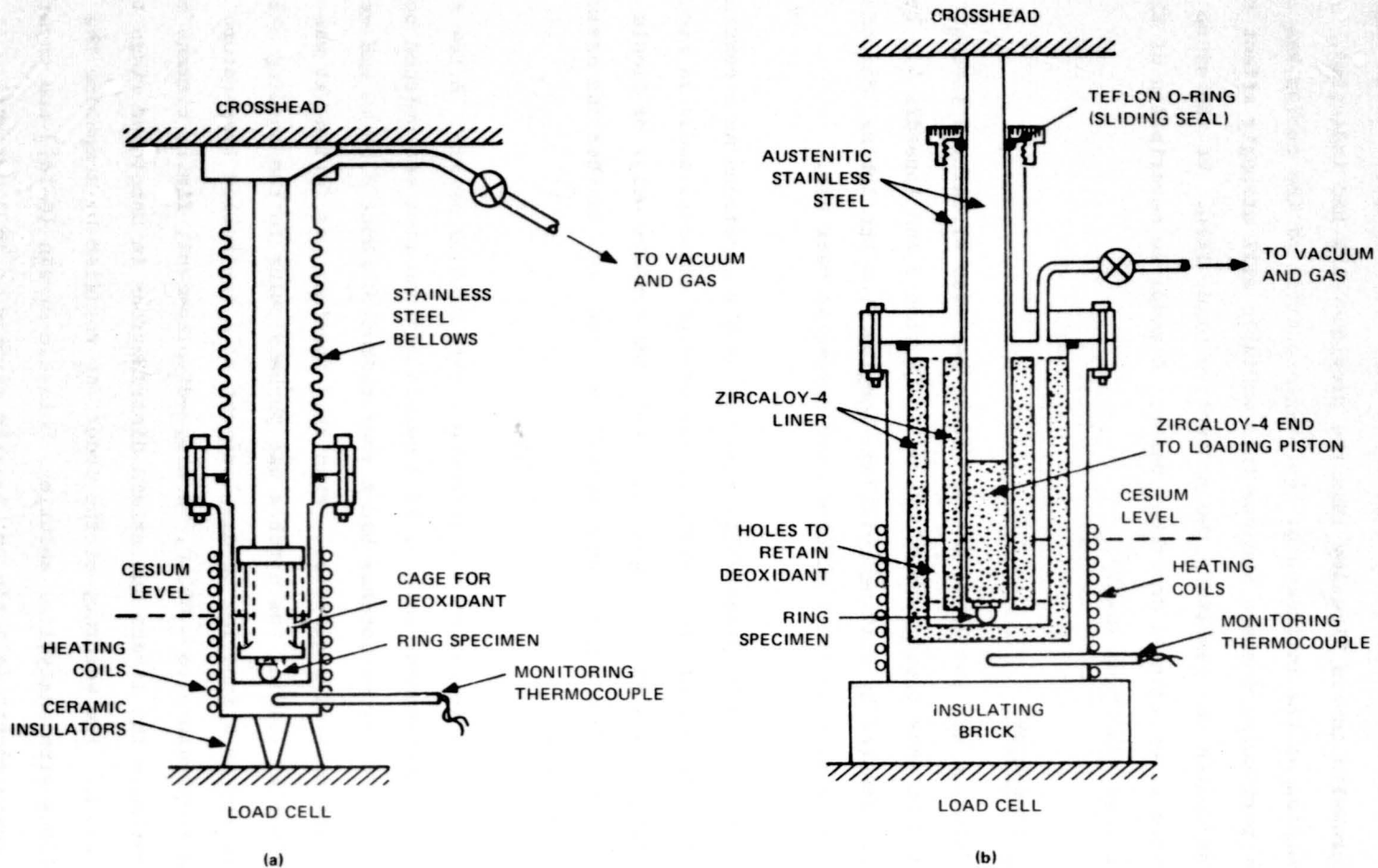
INSULATING
BRICK

LOAD CELL

(b)

TA-350522-162

FIGURE 6-15   CONTROLLED ENVIRONMENT CHAMBERS USED IN THIS TEST PROGRAM

Experimental Results

Three types of load-displacement curves were observed and are illustrated in Figure 6-16. Load-displacement curves of Type 1 were observed for specimens tested in air or argon. As discussed by DeRuntz and Hodge (6-18), this is the type of load-displacement curve expected for the diametral compression of a moderately thin-walled, ductile tube between two parallel, rigid plates. The exact form of the curve depended on the test temperature but failure of the specimens, which originated in the outer surface of the ring near the horizontal diameter, was always of the ductile type shown in Figure 6-17a.

Six series of tests were conducted in liquid cesium, each series beginning with a fresh batch of cesium. Table 6-3 summarizes the test conditions and the results of the tests. The behavior of the rings was found to depend in a complex manner on the exact nature of the test environment and on the test chamber used.

The first series of tests was conducted using the stainless steel test chamber. When no attempt was made to deoxidize the cesium, Type 1 load-displacement curves were obtained that were indistinguishable from those obtained in the control tests in air and argon. However, when the cesium was deoxidized using the calcium deoxidation treatment discussed earlier, ring specimens consistently were embrittled in tests at 313 K and 573 K and showed Type 2 load-displacement curves. The change in load-displacement behavior was accompanied by a change to a brittle microfracture mode as seen in Figure 6-17(b) and 6-17(c). The finite-element model was used to generate estimates of the peak plastic strains at the onset of fracture. For smooth specimens tested at the slower displacement rate the plastic strain estimates (tensile) at the onset of cracking were 0.3 ± 0.05 percent (573 K) and 0.4 ± 0.05 percent (313 K). For a smooth specimen tested at 313 K at the faster crosshead speed, the plastic strain at the onset of cracking was estimated as 2.5 ± 0.5 percent. Estimates of the strain rate in the plastic regions near the ends of the horizontal diameter were also obtained from the finite-element model. At the onset of cracking, the strain rate in the specimens tested at the slower crosshead speed was about 2×10^{-4} sec^{-1}. The corresponding figure for the smooth specimen tested at the faster crosshead speed was about 6×10^{-3} sec^{-1}.
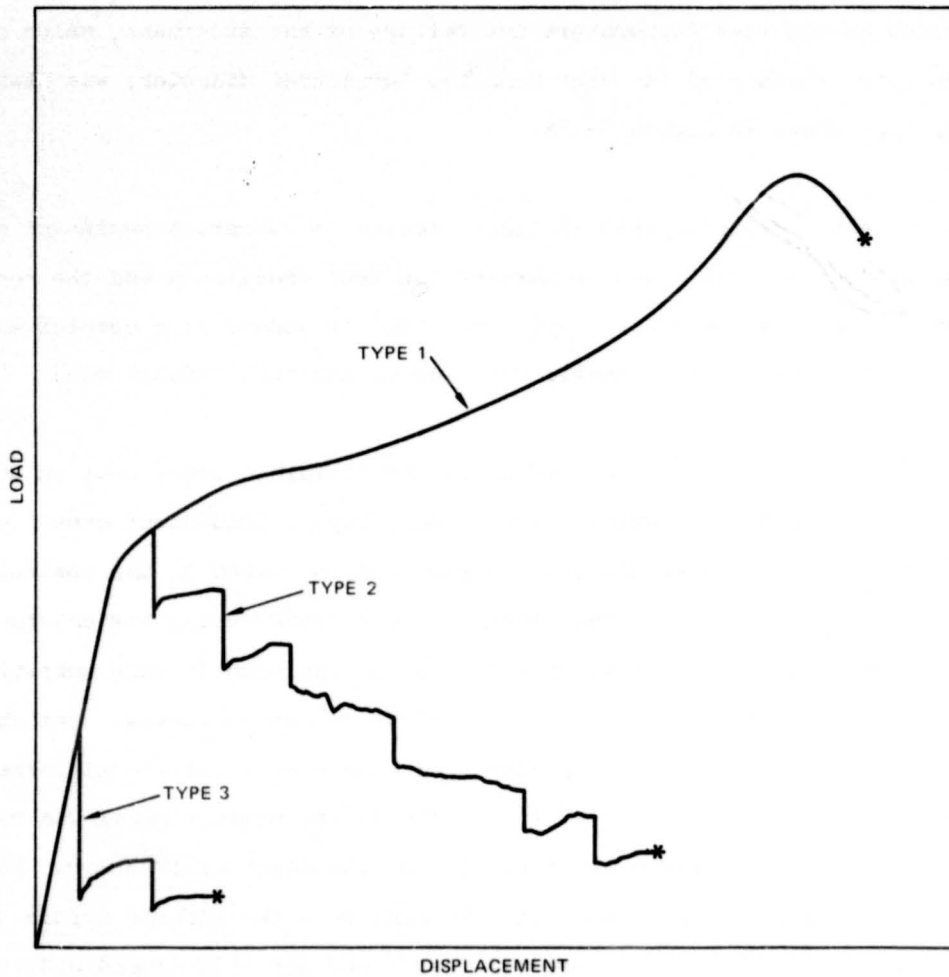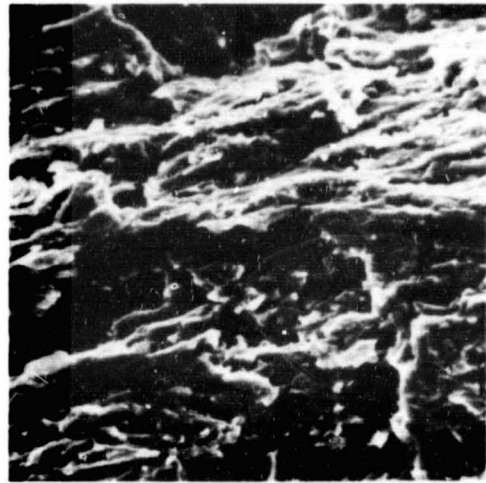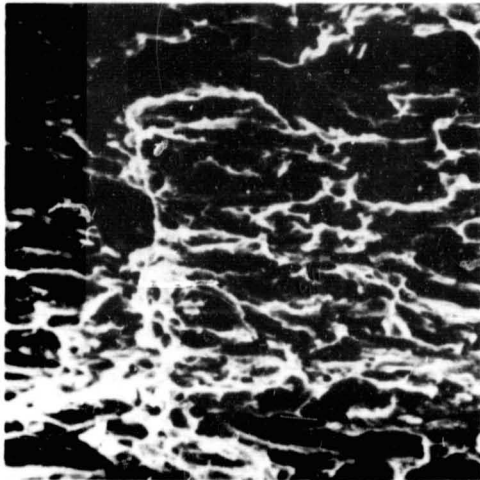
FIGURE 6-16   THREE TYPES OF LOAD-DISPLACEMENT CURVES OBSERVED IN
DIAMETRAL COMPRESSION TESTS
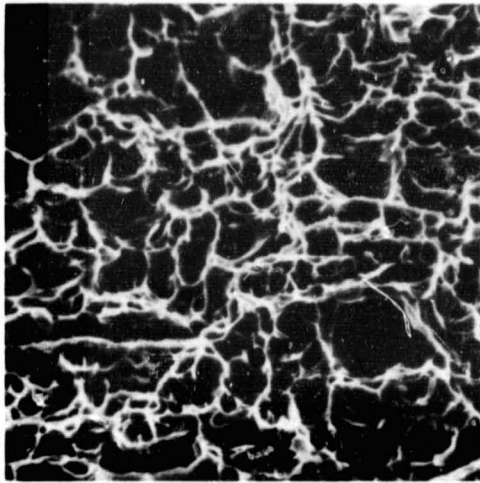
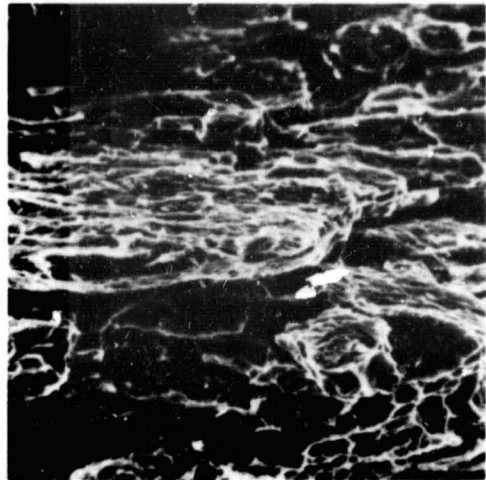FIGURE 6-17   SEM PHOTOGRAPHS OF ZIRCALOY-4 FRACTURE SURFACES
(SCALE MARKS INDICATE 10 μm)

(a) Control specimen fractured in air at room temperature.
(b) Specimen fractured in deoxidized cesium at 313 K during test series 1.
(c) Specimen fractured in deoxidized cesium at 573 K during test series 1.
(d) Specimen fractured in deoxidized, iron-contaminated cesium at 313 K
during test series 3.

Table 6-3

SUMMARY OF RESULTS OF DIAMETRAL COMPRESSION TESTS ON ZIRCALOY-4 RINGS IN
LIQUID CESIUM AT 313 K AND 573 K

Test Series[1]	Test Chamber	Condition of Cesium	Specimens Tested at 313 K		Specimens Tested at 573 K	
			Number Tested	Number Embrittled	Number Tested	Number Embrittled
1	Stainless steel	1.1 Not deoxidized. 1.2 Deoxidized and inadvertantly contaminated with Fe, Al, Cr.	6 3[2]	0 3[2]	0 1	0 1
2	Stainless steel with Zircaloy liner	2.1 Deoxidized but not contaminated. 2.2 Deoxidized and contaminated with Fe + Al.	1 1	0 1[3]	11 2	0 0
3	Zircaloy	3.1 Deoxidized but not contaminated. 3.2 Deoxidized and contaminated with 1% Fe.	4 4	0 2[3]	0 0	0 0
4	Zircaloy	4.1 Deoxidized and contaminated with 1% Fe. 4.2 Deoxidized and contaminated with a second addition of 1% Fe.	3 3	1[3] 0	0 1	0 0
5	Zircaloy	5.1 Deoxidized and contaminated with 0.1% Fe.	2	1[3]	0	0
6	Stainless steel	6.1 Deoxidized and contaminated with 0.1% Fe	0	0	2	2

[1] A fresh batch of 99.95% cesium was used in each of the six test series.
[2] One specimen was notched.
[3] In test series 2 through 5, embrittlement was observed only in the one or two tests immediately following the first addition of the contaminant.

After four tests had been conducted in calcium-deoxidized cesium using the stainless
test chamber, a sample of the cesium was taken for semiquantitative spectrographic
analysis. The cesium was > 99.5 percent pure and contained no calcium, but it did
contain traces of other elements, notably Fe, Al, and Cr. Since the initial purity
of the cesium was > 99.95 percent, this analysis suggested that the stainless steel
test chamber might be contaminating the cesium; therefore, the all-Zircaloy chamber
was designed. While the latter test chamber was under construction, a Zircaloy liner
was inserted in the barrel of the stainless steel chamber to reduce the area of stain-
less steel contacted by the cesium, the cesium was then replaced with a fresh batch,
and a second series of tests was conducted. In these tests, brittle behavior was
not observed in calcium-deoxidized cesium until the cesium was deliberately contam-
inated by adding iron and aluminum. The specimen tested immediately following the
addition of the contaminants showed Type 2 behavior--in two subsequent tests, the
Zircaloy-4 specimens exhibited ductile Type 1 load-displacement curves.

Test series 3 through 5, each starting with a fresh batch of cesium, were conducted
in the all-Zircaloy test chamber. These tests demonstrated that, at 313 K,
Zircaloy-4 was not embrittled by calcium-deoxidized cesium but that embrittlement
could be promoted if the deoxidized cesium was contaminated by iron. However, these
results also confirmed that the role of iron was more complex than the first series
of tests had suggested. Although an addition of about 1 weight percent iron to cal-
cium-deoxidized cesium consistently promoted embrittlement in the test immediately
following the addition, in subsequent tests the Zircaloy-4 specimens reverted to a
ductile failure mode. In Series 3, brittle behavior was observed in the two tests
following the iron addition, whereas in Series 4 brittle cracking occurred in only
one test before reversion to ductile behavior. A further addition of iron to the
same cesium (Series 4) did not lead to the reappearance of embrittlement. A smaller
(0.1 weight percent) addition of iron to a fresh batch of cesium (Series 5) resulted
in a similar sequence of events; that is, the iron addition promoted an immediate
transition from ductile to brittle behavior, but a reversion back to ductile behavior
occurred in the next test. When embrittlement occurred, the microfracture mode
(Figure 6-17d) was similar to that observed in the first test series: when Type 1
load-displacement curves were observed, the microfracture mode was always completely
ductile (Figure 6-17a)..

In the final series of tests (Series 6), which was conducted in the stainless steel chamber, it was confirmed that Zircaloy-4 shows brittle behavior in deoxidized cesium containing 0.1 weight percent iron at a test temperature of 573 K. However, the load-displacement curves obtained for the two specimens tested in Series 6 were of Type 3 (Figure 6-16) rather than the Type 2 curves associated with embrittlement in all other tests. Estimates of the strains at the onset of failure in these tests using the finite element model resulted in values of 0.1 to 0.2 percent which are equivalent to stresses of 75 to 105 MPa--well below the yield strength at 573 K.

Discussion

We anticipated that Zircaloy-4 might be more susceptible to embrittlement by cesium containing less dissolved oxygen since oxide film repair would be more difficult in a low-oxygen environment. Although the results of the Series 1 tests suggest that cesium does indeed become more aggressive toward Zircaloy-4 following calcium deoxidation, a more systematic study will be required to unequivocally prove that oxygen content is an important variable. The results of Series 2.1 and 3.1 (Table 6-3) show clearly that Zircaloy-4 behaves in a ductile manner when loaded in diametral compression in deoxidized, uncontaminated cesium. Since we do not know at what stage the cesium used in Series 1 became contaminated, we cannot completely rule out the possibility that the transition from ductile behavior in Series 1.1 to brittle behavior in Series 1.2 was associated with a change in the contaminant content of the cesium rather than with a reduction of dissolved oxygen content.

The results of Series 3 show that contamination of calcium-deoxidized cesium with a small amount of iron is accompanied by a transition from ductile to brittle behavior in tests at $\sim$ 313 K.

In test series 4, 5, and 6, freshly contaminated, deoxidized cesium consistently caused embrittlement in tests at both 313 K and 573 K. Iron was also present in the cesium environments that caused embrittlement in Series 1 and 2. However, the effects of contaminating the cesium with chromium alone or aluminum alone were not investigated, so it is not known whether these contaminants contributed to the

embrittlement observed in the first and second test series. It is not clear why the specimens in test Series 6 were more severely embrittled than those in the earlier test series.

The origin of the effect of iron contamination is uncertain at present. However, at least two possible explanations can be suggested for the curious reversion behavior observed in test Series 2 through 5. The first explanation is based on the idea that dissolved iron promotes embrittlement only within a narrow concentration window. Thus, when iron is first added to the cesium, it slowly goes into solution, and at the initially low levels of contamination it promotes embrittlement. The iron continues to slowly dissolve, and eventually the critical concentration for embrittlement is exceeded so that, in the second or third test after the iron addition, no embrittlement occurs. Somewhat analogous behavior has been observed in other metal-environment systems that exhibit environmentally assisted fracture. For instance, Deegan and Wilde (6-19) showed that steel suffers stress corrosion cracking in anhydrous ammonia only if the ammonia contains oxygen and nitrogen in certain concentration ranges.

A second possible explanation was recently advanced by Douglass (6-20), who suggested that the observed behavior could readily be understood if a chemical reaction between iron and zirconium yielding a sparingly soluble reaction product was involved in the embrittlement process. Addition of iron to a fresh batch of cesium would promote embrittlement until the solubility limit of the Zr-Fe reaction product was reached. Thereafter, the cesium would no longer serve as a sink for the reaction product, which therefore would remain undissolved in the reaction zone to stifle further reaction and inhibit embrittlement. In addition to being consistent with the behavior observed in the Zircaloy test chamber and in the stainless steel test chamber that had been partially lined with Zircaloy, this explanation is attractive in that it also provides a possible reason why a reversion from brittle to ductile behavior was not observed in Series 1 or 6. In those series, the only zirconium encountered by the iron-contaminated cesium was the test specimens. Thus, saturation of the cesium with a Zr-Fe reaction product might require many more tests in the stainless steel chamber than in the Zircaloy

chamber, where the iron-contaminated cesium was exposed to a much larger surface area of zirconium.

Further experimentation will be required to determine whether or not embrittlement of Zircaloy-4 by deoxidized, iron-contaminated cesium is affected by strain rate or test temperature. Based on the four tests conducted in Series 1.2, the plastic strain at the onset of cracking does not seem to be very sensitive to test temperature but may increase somewhat with increasing strain rate. The load and displacement at the onset of cracking appeared to be reduced by the presence of notches as would be expected in view of their stress and strain concentrating effect.

Any future work in this area should also consider the possibility that embrittlement by iron-contaminated cesium could be a purely chemical phenomenon. All specimens that showed brittle behavior in the present tests were exposed to the iron-contaminated cesium for a prolonged period at ~ 650 K during the calcium deoxidation treatment. Therefore, we cannot dismiss the possibility that the unstressed rings were embrittled during the deoxidation treatment, that is, prior to mechanical loading at the final test temperature.

Summary

Zircaloy-4 exhibits brittle behavior in tests in liquid cesium at 313 K and 573 K if the cesium has a low oxygen content and is contaminated with iron. In diametral compression tests on smooth, Zircaloy-4 rings that were exposed to iron-contaminated cesium at ~ 650 K for 18 hours before testing, brittle fracture sometimes was initiated at tensile strains less than 0.2 percent in tests at 573 K. It is not clear whether iron is the primary embrittling agent and cesium is merely a vehicle for the iron, or whether cesium is the primary embrittling agent and the role of iron is related to oxide film penetration.

EMBRITTLEMENT BY CADMIUM IN RISING LOAD TESTS

As noted earlier, embrittlement of Zircaloy by cadmium has been reported by other workers (6-12, 6-13) but was not observed in our statically loaded WOL-CT screening tests. We speculated that this difference in behavior might be due to the difference

between our static tests and the continuously loaded tensile tests that had resulted in embrittlement (6-12, 6-13). As a preliminary test of this theory, four diametral compression tests were made on 12.7-mm-long rings of 7FD11 Zircaloy-4 tubing partly immersed in cadmium at ∼ 593 K. The experiments were conducted using the Zircaloy-4 chamber shown in Figure 6-15(b). The first ring was heated at ∼ 593 K in contact with the cadmium for 2 hours prior to the test and showed no embrittlement. The second specimen was heated for 26 hours before testing and showed severe embrittlement of a type similar to that illustrated by the Type 2 curve in Figure 6-16. The specimen was found to be noticeably oxidized after the test, which suggested that it had gettered dissolved oxygen from the cadmium during the 26 hour exposure period prior to the test. The final two tests showed no embrittlement but subsequent examination revealed that all the cadmium had reacted with the Zircaloy walls of the test chamber to form Zr-Cd intermetallics so that neither specimen had been exposed to the molten metal.

The results of the diametral compression tests encouraged us to believe that both a rising stress and a small dissolved oxygen content in the cadmium were prerequisits for cadmium embrittlement of Zircaloy. Accordingly, a series of experiments was undertaken at NASA-Ames Research Center in which dynamic four-point bend tests were performed on specimens cut from the 3.2-mm 9912-6B lot of stress-relieved Zircaloy-4 sheet (see Section 3 and Appendix A for details on this material) in an attempt to further elucidate the nature of cadmium embrittlement at reactor operating temperatures. A variety of notches, with or without fatigue precracks, was used and tests were undertaken at both high and low oxygen partial pressures.

Three types of load-displacement curves were observed in tests at ∼ 633 ± 5 K. A typical example of each curve is shown in Figure 6-18. The classic plastic beam, showing large stable deflections, was observed in an inert environment, in cadmium vapor, and in all environments with high oxygen partial pressures. No evidence of cracking was observed in subsequent examinations. The second and third type of curves were observed with liquid cadmium having a low oxygen content. The second type of load-displacement curve showed a maximum load followed by a slow load decay. Subsequent examination showed that a subcritical crack had propagated through the
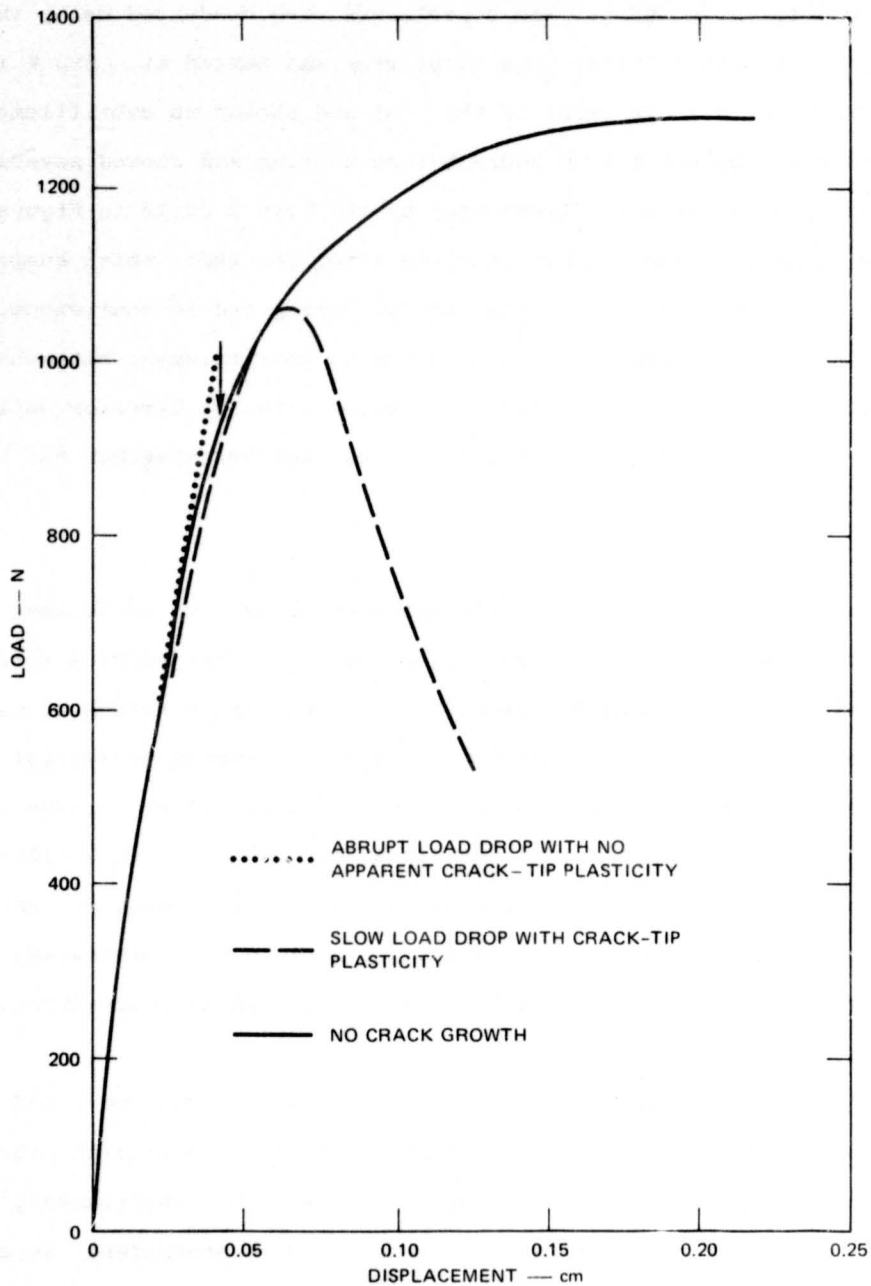
FIGURE 6-18   CURVES OBSERVED IN 4-POINT BEND TESTS IN CADMIUM AT 633 K

beam thickness, as shown in Figure 6-19. An interesting feature is the large amount of plastic deformation that accompanied the crack growth. The third type of curve showed essentially elastic or slightly plastic loading followed by an abrupt drop in load to a very low value. The concomitant crack extension is shown in Figure 6-20. This crack growth process showed very little plastic deformation adjacent to the crack. However, when the surface cracking was discontinuous, small plastic bridge regions were observed, as shown in Figure 6-21.

An exact value of the threshold stress intensity K_{Iscc} was difficult to obtain. As seen in Figures 6-19 to 6-21, crack branching dissipates much of the energy and leads to questionable values of K_I. Using the load at failure and the initial flaw length, estimates of the initial stress intensities were made. The spread in initial stress intensity values was ~ 16 to 24 MPa·m$^{1/2}$, with the average value being ~ 20 MPa·m$^{1/2}$. This value was obtained from specimens that were exposed to a low oxygen partial pressure and were either totally submerged in liquid cadmium or were deformed into the liquid cadmium upon loading. No failures were observed for specimens tested in cadmium vapor.

The fracture surface of a specimen fractured in a liquid cadmium environment at ~ 633 K is very complex. Several features appear frequently and therefore can be assumed to be characteristic of cadmium-induced failures. One feature often seen is cleavage. Figure 6-22 shows that cleavage regions have occurred at the interface of the fatigue precrack and the stress corrosion crack. The dominant feature on the fracture surfaces of specimens that have failed in cadmium is fluted regions of the type shown in Figure 6-23. At higher magnification the cleaved and plastically deformed areas of the flutes can be seen more clearly, as illustrated in Figure 6-24. Cadmium-induced failure generally appears to follow a transgranular path; however, in one instance evidence of intergranular failure was observed, as shown in Figure 6-25. Optical metallography of fracture surfaces using polarized illumination confirmed that intergranular features were present but were much less common than transgranular features.
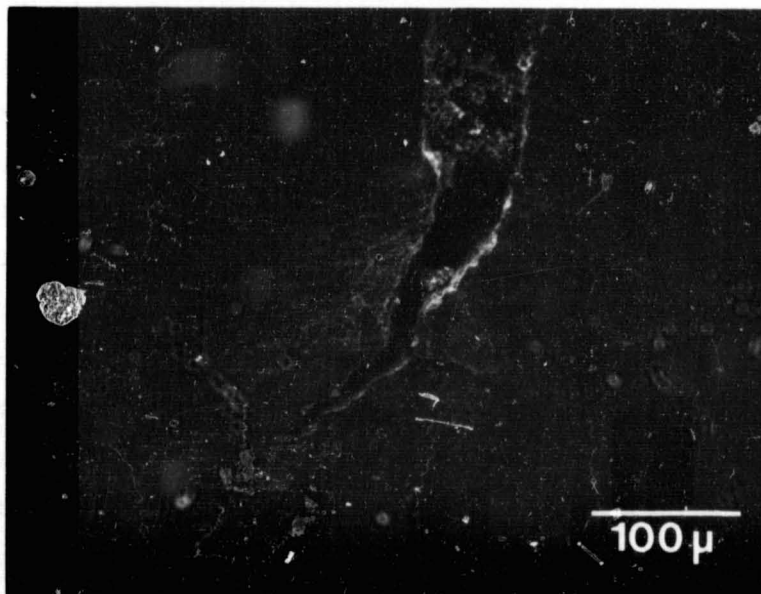
In summary, cadmium stress corrosion cracking of stress-relieved Zircaloy-4 will occur in rising load tests if the oxygen partial pressure is low and if the specimen
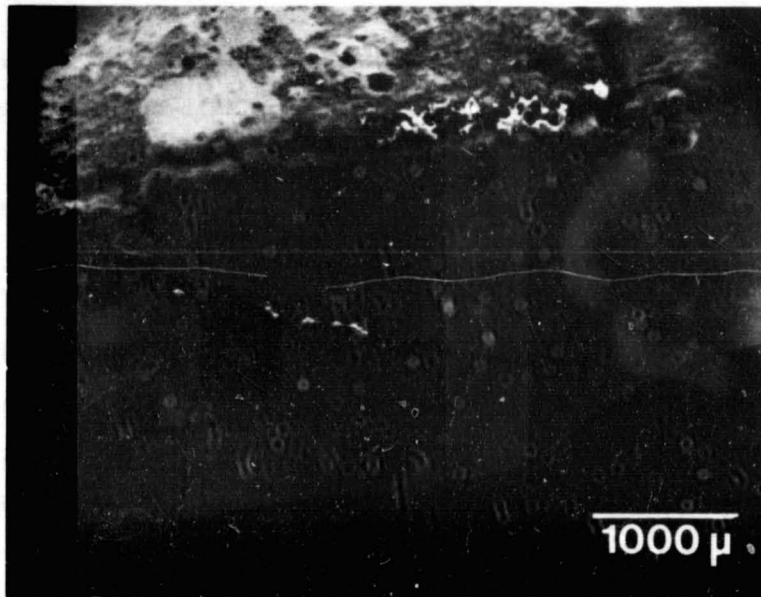
SA-4197-199

FIGURE 6-19   A 4-POINT BEND SPECIMEN OF STRESS-RELIEVED
ZIRCALOY-4 AFTER FAILURE IN CADMIUM AT 633 K
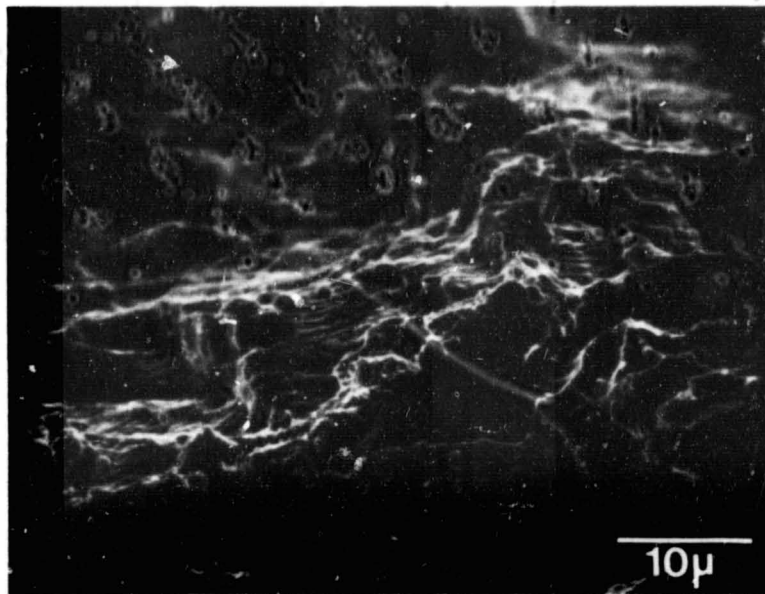

SA-4197-200

FIGURE 6-20   CRACK BRANCHING AND PLASTIC DEFORMATION THAT
OCCURRED UPON LOADING IN LIQUID CADMIUM AT 633 K
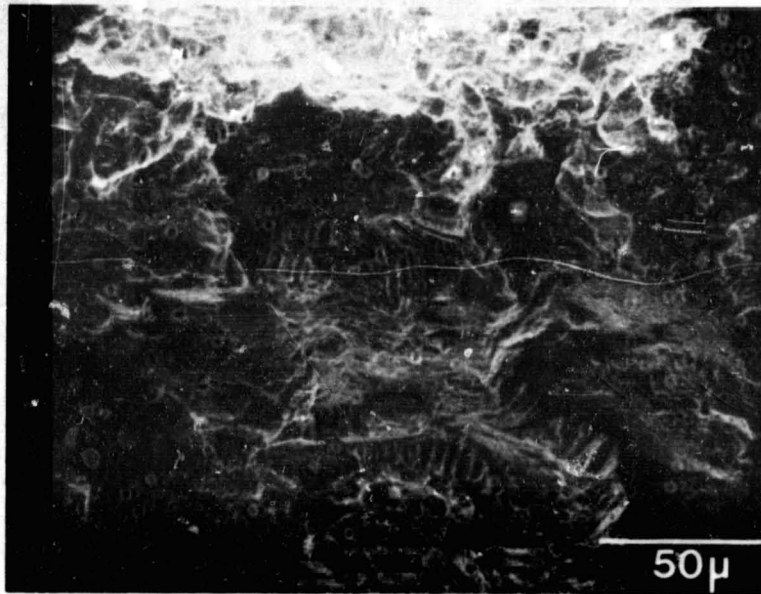
WACHOB/NASA   SA-4197-201

FIGURE 6-21   A PLASTICALLY DEFORMED BRIDGE IN A 4-POINT BEND SPECIMEN
              OF STRESS-RELIEVED ZIRCALOY-4 AFTER FAILURE IN THE ELASTIC
              REGION IN CADMIUM AT 633 K

WACHOB/NASA   SA-4197-202

FIGURE 6-22   THE PREFATIGUE CRACK — STRESS CORROSION CRACK REGION IN
              A 4-POINT BEND SPECIMEN OF STRESS-RELIEVED ZIRCALOY-4 AFTER
              FAILURE IN CADMIUM AT 633 K

SA-4197-203

FIGURE 6-23   A TYPICAL FRACTURE SURFACE OF A 4-POINT BEND SPECIMEN OF
STRESS RELIEVED ZIRCALOY-4 AFTER FAILURE IN LIQUID CADMIUM
AT 633 K
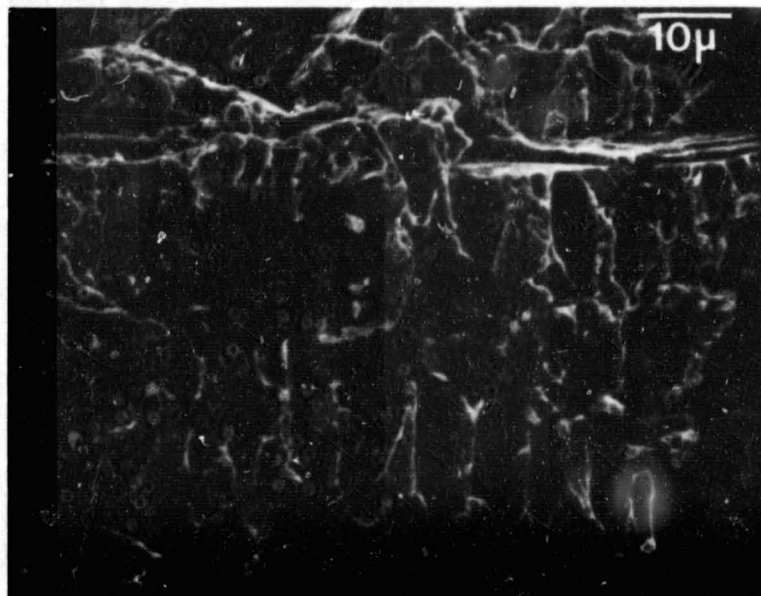
SA-4197-204

FIGURE 6-24   THE CHARACTERISTIC FLUTED REGIONS AFTER FAILURE
IN CADMIUM AT 633 K
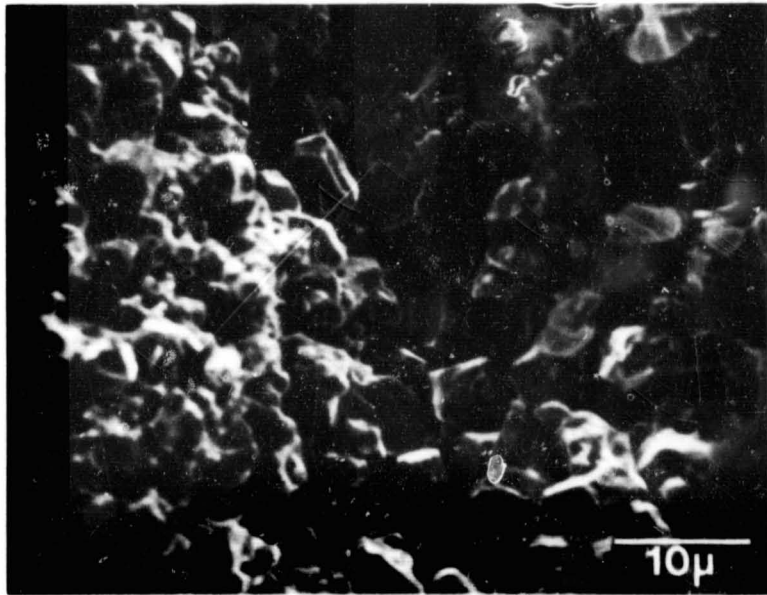
WACHOB/NASA   SA-4197-205

FIGURE 6-25   AN INTERGRANULAR FAILURE REGION OBSERVED IN STRESS-
RELIEVED ZIRCALOY-4 AFTER EXPOSURE TO CADMIUM AT 633 K

is deformed into or submerged in liquid cadmium. The average initial stress intensity for cadmium-induced cracking was ~ 20 MPa·m$^{1/2}$, which is more than a factor of 2 greater than that required for iodine-induced cracking. However, the ~ 20 MPa·m$^{1/2}$ value may be in error because of the large amount of crack branching that occurs during cadmium-induced cracking. The fracture surfaces generated in cadmium show both fluted and cleaved areas, which indicates that both environment-assisted cleavage and plastic deformation are important in the overall fracture process.

SUMMARY AND CONCLUSIONS

The gases H_2, I_2, Br_2, and Cl_2 and the liquid metals Cs and Cd were shown to be capable of promoting subcritical crack growth in stress-relieved Zircaloy-4 at reactor operating temperatures. Further, evidence was found that I_2, Br_2, Cd, and Se all are capable of corroding Zircaloy-4 at reactor operating temperatures in the absence of stress. The metals Se, Sn, Te, Sb, and Ag did not cause crack extension in statically loaded specimens.

It is difficult to compare the aggressiveness of the various species that caused subcritical crack growth because the differing natures of the cracking processes and the differing characteristics of the various species necessitated the use of different test methods. The halogens were the only species that caused crack extension in statically loaded specimens at reactor operating temperatures. They seemed to be similar in their aggressiveness toward Zircaloy and resulted in very similar fracture surfaces that contained a mixture of cleavage and ductile rupture. The threshold stress intensities (K_{Iscc}) for the halogens were estimated to be about 9 MPa·m$^{1/2}$ at 633 K and iodine-induced cracking proved to be essentially immune to the presence of oxygen.

In contrast, cadmium and cesium were aggressive toward Zircaloy at fuel cladding operating temperatures only when steps were taken to reduce the oxygen contents of the test environments to very small values. Furthermore, cesium and cadmium seemed to require a rising load type of test before embrittlement occurred and cesium had to be contaminated with a trace of iron. K_{Iscc} for cadmium cracking

at 633 K was estimated to be about 20 MPa·m$^{1/2}$, but this value was believed to be an overestimate. In tests on smooth specimens, cadmium and iron-contaminated cesium generally caused embrittlement at stresses just above the yield stress, although on two occasions much smaller failure stresses were observed in the iron-contaminated cesium environment.

Gaseous hydrogen proved to be much more aggressive toward Zircaloy at ambient temperature than at fuel cladding operating temperatures. Hydrogen was capable of promoting subcritical crack growth in statically loaded specimens at room temperature but an alternating stress was required to obtain any crack extension at 573 K.

The present evidence suggests that the halogens are more consistently aggressive toward Zircaloy at reactor operating temperatures than the other elements screened. Thus, the halogens were the only substances that caused cracking in the statically loaded WOL-CT tests and were relatively insensitive to the presence of contaminants. Iodine was therefore selected as the environment for the detailed studies reported in Sections 4 and 5. However, it cannot be concluded that I_2 is more aggressive than, say, Cd in the particular conditions that prevail inside an operating nuclear fuel rod. For instance both Cd and Fe-contaminated Cs caused embrittlement of 7FD11 Zircaloy-4 tubing in diametral compression tests at temperatures $\sim$ 600 K. In contrast, when a specimen was similarly tested in the presence of I_2, no evidence of embrittlement was observed. This result, which is probably a consequence of the sensitivity of iodine-induced SCC to both strain rate and mode of loading (6-5) shows that under some circumstances, Cd and Fe-contaminated Cs are more aggressive toward Zircaloy than the halogens. Consequently, the results of the present screening tests do not allow a positive identification of the chemical agent responsible for PCI cladding failures. However, when the present data are combined with the availability considerations reported in Section 2, we can tentatively conclude that the chemical substances most likely to be involved in PCI failure are I_2, Cd, and perhaps Fe-contaminated Cs.

REFERENCES

6-1 C. F. Coleman, "Susceptibility of Cold-Worked Zirconium-2.5 wt% Niobium Alloy to Delayed Hydrogen Cracking" AECL-5260, Atomic Energy of Canada Limited, January 1976.

6-2 H. G. Nelson and D. P. Williams, Met. Trans., 3, 2107 (1972).

6-3 M. R. Shanabarger, NASA-Ames Research Center, Private Communication (1976).

6-4 H. S. Rosenbaum, "The Interaction of Iodine with Zircaloy-2," Electrochemical Technology, 4, 153 (1966).

6-5 J. C. Wood, "Factors Affecting Stress Corrosion Cracking of Zircaloys in Iodine Vapour," J. Nuclear Materials, 45, 105 (1972/73).

6-6 A. Galick and P. D. Wolfenden, "Fracture of Zirconium Alloys in Iodine Vapour," J. Nuclear Materials, 41, 274 (1971).

6-7 B. Cox, and J. C. Wood, "Iodine Induced Cracking of Zircaloy Fuel Cladding," in Corrosion Problems in Energy Conversion and Generation, p. 275, C. S. Tedman, Jr., ed. (Electrochemical Society, New York, N.Y., 1974).

6-8 J. D. Wood, B. A. Surette, I. M. London, and J. Baird, "Environmentally Induced Fracture of Zircaloy by Iodine and Cesium: The Effects of Strain Rate, Localized Stresses and Temperature," J. Nuclear Materials, 57, 155 (1975).

6-9 K. Videm and L. Lunde, "Stress Corrosion Cracking of Zircaloy Fuel Cladding Under Power Ramps and in Lab Tests," Proceedings: ANS Topical Meeting on Water Reactor Fuel Performance, St. Charles, Illinois, May 1977.

6-10 P. H. Kreyns, G. L. Spahr, and J. E. McCauley, J. Nuclear Materials, 61, 202-212 (1976).

6-11 H. Wachob and H. G. Nelson "Halogen Stress Corrosion Cracking of Zircaloy-4," to be published in Proceedings, TMS-AIME Symposium on Environment Sensitive Fracture of Engineering Materials, Chicago, Illinois (October 1977).

6-12 W. T. Grubb, Nature, 265, 36 (1977).

6-13 W. T. Grubb and M. H. Morgan, III, "Cadmium Embrittlement of Zircaloy-2," Proceedings: ANS Topical Meeting on Water Reactor Fuel Performance, St. Charles, Illinois, May 1977.

6-14 D. W. Levinson, "Seal and Insulator Problems in Thermionic Converters," Illinois Institute of Technology Report IITRI-B215-22, 1964.

6-15 B. Cox, Corrosion, 28, 207 (1972).

6-16 W. Rostoker, J. M. McCaughey, and H. Markus, Embrittlement by Liquid Metals (Reinhold, New York, 1960).

6-17 B. C. Syrett, D. Cubicciotti, and R. L. Jones, "Embrittlement of Zircaloy-4 by Liquid Cesium at 300 C" Zirconium in the Nuclear Industry, ASTM STP 633, pp. 281-294 (1977).

6-18 J. A. DeRuntz and P. G. Hodge, "Crushing of a Tube Between Rigid Plates," ASME Paper No. 63-APM-2, Presented at the Summer Conference of the Applied Mechanics Division of ASME, Ithaca, N.Y. June 24-26, 1963.

6-19 D. C. Deegan and B. E. Wilde, Corrosion, 29, 310 (1973).

6-20 D. L. Douglass, University of California, Los Angeles, Private Communication, May 1976.

Section 7

DISCUSSION AND CONCLUSIONS

MECHANISM OF IODINE-INDUCED SCC OF ZIRCALOY TUBING

The present results support a model of iodine-induced SCC failure of Zircaloy clad-
ding tubes very similar to that proposed by Cox and Wood (7-1). Our model is
illustrated in Figure 7-1 and each stage of the model is discussed separately
below.

Oxide Penetration

Oxide cracking apparently is an essential first step. Although we have observed
the formation of pits in unstressed, unoxidized Zircaloy exposed to iodine (which
indicates that iodine is capable of penetrating thin, air-formed oxide films),
these isolated pits do not correlate with the locations of iodine-induced crack
nuclei in the metal. Moreover, iodine apparently cannot penetrate oxide films
with thicknesses in the range relevant to the inside surface of irradiated fuel
cladding (≥ 0.5 μm) unless the oxide is ruptured mechanically. We therefore believe
that before the oxide film can be penetrated during iodine-induced SCC, the cladding
must attain a sufficient level of strain to mechanically rupture the oxide film.

Experiments mentioned in Section 4 show that ~ 1-μm- and ~ 3-μm-thick oxides
(formed by thermal oxidation in dry oxygen) are detectably cracked when Zircaloy
samples are subjected to a total (elastic plus plastic) strain of $\gtrsim 0.4\%$ at
reactor operating temperatures. This strain would be reached at a stress of about
300 MPa in a perfectly elastic sample of Zircaloy. However, that is an upper limit
for the cladding stress required for oxide rupture because plastic flow and creep
usually are possible at smaller stress levels. For example, it was found that a
short time hoop stress of only ~ 200 MPa was required to generate a hoop strain of
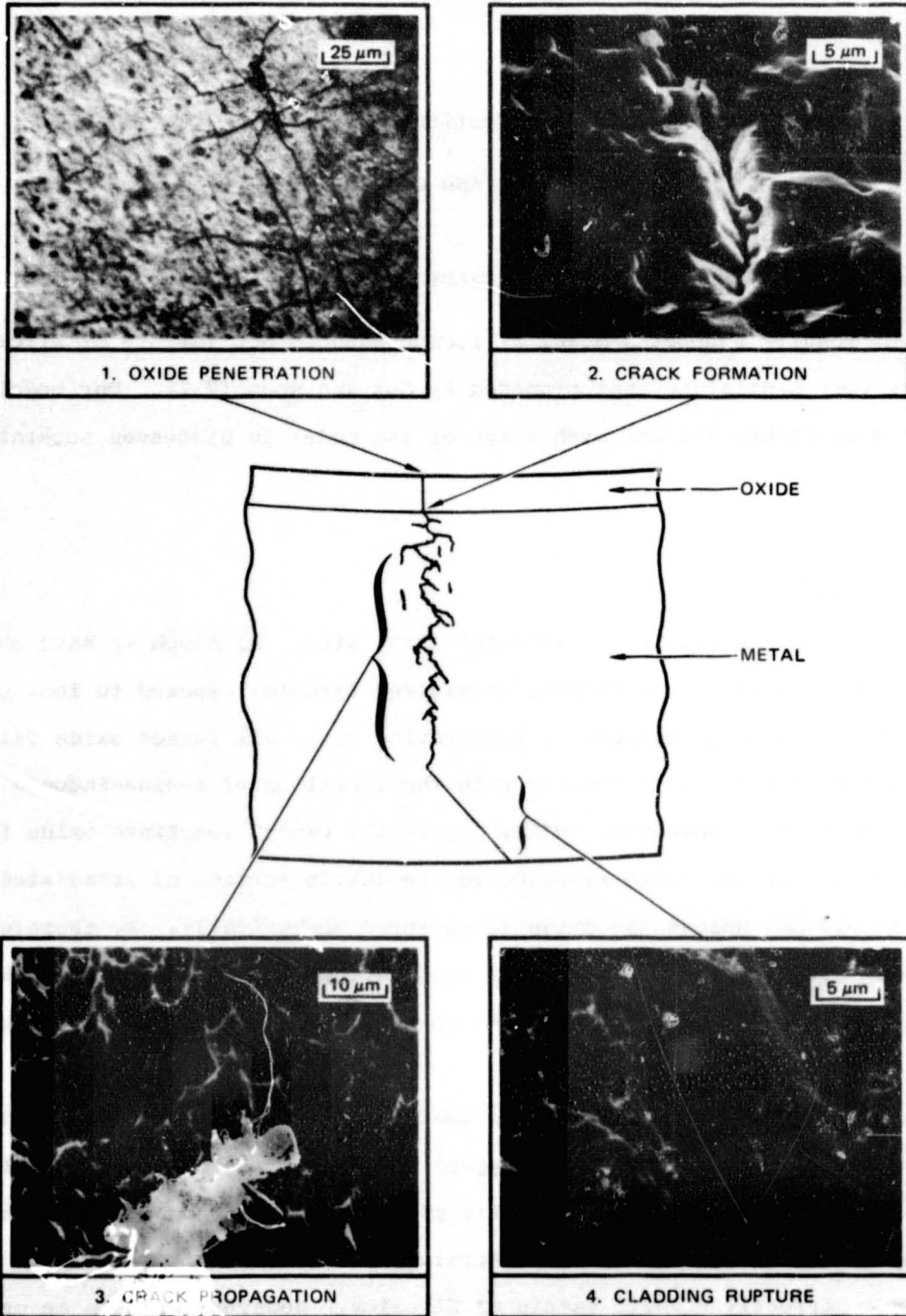
FIGURE 7-1 MICROGRAPHS ILLUSTRATING THE FOUR STATES OF IODINE-INDUCED
CLADDING FAILURE

0.4% in annealed Zircaloy-2 cladding at 590 K. Similarly, the data in Table 5-2 indicate that irradiated HBR cladding undergoes creep strains (plastic) of several tenths of a percent if stresses of ∼ 200 MPa are sustained for periods of several hours.

At higher strains, the number of cracks in the oxide increases systematically, as shown in Figure 4-19 and the number of cracks formed at a given strain depends on the oxide thickness (Figure 4-20). Thus, the amount of metal surface exposed to the environment depends both on strain and on the nature of the oxide film.

The threshold stress for iodine SCC of the annealed Zircaloy-2 tubing was about 280 MPa, whereas oxide cracking could be detected at a stress of ∼ 200 MPa. Moreover, the threshold stress was completely unaffected by preoxidation. We therefore believe that although oxide film fracture is necessary to allow contact between the metal and the aggressive environment, penetration of the oxide film does not automatically imply that SCC will occur. That is, oxide film penetration is not the critical step in the overall iodine-SCC process.

Our information on oxide penetration addresses the behavior of oxide films formed by thermal oxidation in dry oxygen at a pressure of about 0.1 MPa. We have no data on the strains required to rupture oxide films formed under the low oxygen potential conditions that prevail inside an operating nuclear fuel rod. However, there is no reason to believe that the resistance of such films to mechanical rupture is significantly superior to that of oxides formed at higher oxygen pressures. In fact, some of the observations reported in Section 2 suggest that the oxide films formed on the cladding in-reactor are rather imperfect. We therefore doubt that oxide film penetration is a critical step in PCI failure of nuclear fuel cladding.

Crack Formation

Cracking of the protective oxide film exposes a small area of Zircaloy metal surface in the metal-oxide interface to the iodine-containing environment. If the applied stress is sufficiently large, stress corrosion crack nucleation then occurs at certain favored sites in the exposed metal surface.

We think that the threshold stresses observed in the pressurization tests (Section 5) are associated with crack formation because the maximum stress for continued growth of a preexisting stress corrosion crack is expected to decrease with increasing crack depth. <u>Therefore, we regard crack formation as the critical step in the iodine-induced failure of internally pressurized Zircaloy tubes.</u>

Our tube pressurization data indicate that stress rather than strain or stress intensity is the key parameter in crack formation, as discussed in Section 5. The present data indicate that threshold stress depends on microstructure (annealed is inferior to stress relieved) and probably also on irradiation (irradiated is inferior to unirradiated) but is not sensitive to iodine concentration in the range 6 to 0.06 mg per square centimeter of Zircaloy surface.

The indenter studies discussed in Section 4 indicate that two populations of crack nuclei are formed in unirradiated Zircaloy. Small nonpropagating cracks form at stresses well below the threshold stress for iodine-induced failures of internally pressurized tubes. These small cracks generally seem to be intergranular and occur at sites such as certain grain boundaries in recrystallized material where the local stresses generated during plastic deformation are exceptionally large.

Crack nuclei of the second type are larger than those of the first type, generally seem to be transgranular, and always occur at sites in the metal surface that contain higher-than-normal concentrations of alloying elements or impurities. These crack nuclei are observed only in specimens stressed at levels above the threshold stress for iodine-induced failure of internally pressurized tubes. <u>We therefore believe that the threshold stress is the stress required to form crack nuclei at chemical inhomogeneities and that their propagation causes iodine-induced failure.</u>

The exact mechanism that results in the formation of cracks at local concentrations of impurities and alloying elements is not currently known. In Section 4 we suggested a mechanism based on the formation of brittle mixed metal iodies. This mechanism probably can account for many of the experimental results but it is not obvious why the threshold stress for recrystallized Zircaloy-2 should be lower

than that for stress-relieved Zircaloy-2 from the same tubing batch. Perhaps interdiffusion at the higher annealing temperature used for the recrystallized material increases the effective size of the chemical inhomogeneities. Also, the mechanism suggested in Section 4 does not provide an immediate explanation for the effect of irradiation. Possibly oxygen is picked up by the local inhomogeneities during long-term in-reactor exposure and this makes them more susceptible to embrittlement by iodine. Another possibility is that the small crack nuclei that are formed at lower stresses but do not propagate in unirradiated Zircaloy are capable of growth in irradiated material, perhaps as a consequence of intense local stresses associated with dislocation channeling and flow localization.

Whatever the exact mechanism, crack formation is a rapid process. Crack nuclei were observed after times under load above the threshold stress as short as 5 minutes. This suggests that the time to failure in pressurized tube experiments may be associated chiefly with the time required to grow the largest crack nucleus formed in the specimen to a sufficient size for final rupture of the tube to occur. In that case, the very consistent times to failure observed in the tube pressurization tests (see, for example, Table 5-3) must indicate that the largest crack nuclei formed in ~ 3 cm lengths of tubing (the uniformly stressed region in our tube pressurization specimen) are always of very similar size. This is not unreasonable if the number of nucleation sites in such tube lengths is very large, as the results of the indenter tests (Section 4) suggest.

Crack Propagation

Once a stress corrosion crack has been initiated, crack growth will occur if the stress remains sufficiently large and the specimen continues to be exposed to a sufficiently aggressive environment. In the present work, an iodine concentration of 0.06 mg I_2 per cm^2 Zircaloy was found to be more than sufficient to allow the stress corrosion process to proceed; the results of Busby et al. (7-2) indicate that the iodine concentration threshold is less than 0.005 mg/cm^2. Crack propagation occurs on a surface approximately perpendicular to the principal applied stress (Figure 5-9) and more crack branching occurs at higher stress levels.

The results of our tube pressurization tests on preflawed specimens suggest that the minimum value of nominal hoop stress for continued crack growth initially falls linearly with flaw size in such a way that the net section stress remains essentially equal to the crack formation threshold stress. Similar behavior has been reported by Videm and Lunde (7-3), who showed that the presence of fatigue-sharpened flaws up to 100 μm in depth did not reduce the net section stress threshold for iodine SCC of annealed Zircaloy-2 at 613 K.

At larger crack sizes, one would expect that the minimum nominal stress for continued crack growth σ_{min} would be related to the stress intensity threshold K_{Iscc} through a relation of the type

$$\sigma_{min} = \frac{K_{Iscc}}{f(\frac{a}{W}) \sqrt{\pi a}} \quad , \quad (7-1)$$

where a is the crack depth, and f is a geometry-dependent function of a and the wall thickness W. Probably the crack tip conditions would control the value of the stress required for continued propagation when σ_{min} in equation 7-1 is less than the net section threshold stress σ_{onet} defined as

$$\sigma_{onet} = \sigma_0 (1 - \frac{a}{W}) \quad , \quad (7-2)$$

where σ_0 is the nominal threshold stress for iodine SCC of unflawed specimens. Taking typical values of $K_{Iscc} = 9$ MPa·m$^{1/2}$ (Section 6), $f(\frac{a}{W}) = 1.1$ (Figure 5-5), $\sigma_0 = 300$ MPa (Section 5), and W = 700 μm (Section 3), we can deduce that the transition from stress control to stress intensity control should occur at a crack depth of about 100 to 200 μm. Support for this conclusion is provided by Videm and Lunde's data (7-3), which indicate that iodine-induced propagation of sharp flaws ~ 300 μm deep requires a significantly smaller net section stress than the propagation of flaws $\lesssim$ 100 μm deep.

If the failure times in the pressurization tests depend mainly on the time required to propagate crack nuclei of almost constant size (as suggested in the previous subsection), the data in Section 5 suggest that the crack growth rate is more

rapid in recrystallized Zircaloy-2 than in stress-relieved Zircaloy-2 and probably increases with iodine concentration, irradiation, and an increase of testing temperature from 590 to 630 K. The effects of testing temperature and iodine concentration probably relate to the availability of iodine at the crack tip, whereas the effects of irradiation and heat treatment probably reflect changes in the deformation behavior of the metal in the vicinity of the crack tip.

Crack propagation occurs by a mixture of cleavage and ductile tearing in stress-relieved materials (e.g., Figure 5-11) but may involve intergranular processes in recrystallized Zircaloy-2 (Figure 5-12). Videm and Lunde (7-3) report predominantly intergranular fracture in recrystallized thin-wall Zircaloy tube specimens.

The mechanism by which iodine promotes intergranular fracture and transgranular cleavage in Zircaloy is not understood at present nor do we clearly understand the distinction between the two crack propagation paths. Iodine-induced crack propagation at stress intensities above K_{Iscc} in fracture mechanics specimens is always transgranular (7-1, and see also Section 6). Perhaps propagation tends to be intergranular in recrystallized Zircaloy tube specimens because the low yield stress and small cross section combine to relax the stress state at the crack tip to such an extent that transgranular failure (which probably requires the expenditure of more energy because of the involvement of plastic processes) becomes very difficult. In both intergranular and transgranular crack propagation, we presume that the presence of iodine at the crack tip in some way weakens the interatomic bonding sufficiently to permit the local stress to break Zr-Zr bonds.

Cladding Rupture

Stress corrosion crack propagation continues until plastic instability occurs, resulting in rapid, ductile fracture of the uncracked ligament ahead of the crack, usually on a shear surface (Figure 5-9). We observed two modes of final failure--pinholes, which were more common at low stresses, and short axial splits, which were more common at high stresses.

Two criteria have been proposed previously to define the conditions required for cladding rupture. Videm and Lunde (7-3), use a critical apparent stress intensity criterion, whereas Kreyns, et al. (7-4) prefer a critical net section stress, which they regard as equal to the ultimate tensile strength (UTS) of the cladding. Neither of these criteria is entirely satisfactory.

The presence of X-marks on the outside surface of cladding specimens prior to failure in internal pressurization SCC tests and at failure sites in test reactor experiments (7-5) indicates that the uncracked ligament becomes fully plastic before final failure. The use of a linear elastic stress intensity failure criterion is clearly inappropriate in this situation. The UTS criterion is probably a good approximation at high stress levels where the stress corrosion crack does not penetrate very far into the metal before plastic instability occurs, but it seriously underestimates the net section stress required for instability at low stress levels because the plastic constraint associated with deep cracks is ignored. As Cottrell (7-6) has pointed out, plastic constraint in a deeply notched tensile member can raise the apparent yield strength of the uncracked ligament by about a factor of 3. Thus, if we assume that in the present case plastic instability immediately follows net section yielding, ductile failure of the tube will occur when the net section stress reaches approximately $3\sigma_y$ (where σ_y is the yield strength of the tube material) in a deep-notch, low-stress situation. Therefore, the net section stress required for final cladding failure should rise from a value close to the cladding UTS for shallow cracks to a value close to three times the yield strength for deep cracks.

The results of our pressurization tests on stress-relieved Zircaloy-4 tubing ($\sigma_Y \approx 350$ MPa; UTS ≈ 540 MPa) provide good support for the cladding rupture criterion proposed above. The net section stress at instability for a specimen that failed when the stress corrosion crack depth was $\sim 16\%$ of the wall thickness was 530 MPa-- very close to the UTS. A specimen that failed when the crack depth was $\sim 40\%$ of the wall thickness showed a slightly higher net section stress at final failure of about 560 MPa. Finally, several specimens failed when the stress corrosion crack had penetrated $\sim 70\%$ of the wall thickness. For these specimens the net section stress at instability was ~ 1000 MPa, which is slightly less than three times the yield stress.

The threshold stress for crack formation defines the minimum stress that can be applied to the cladding during the later states of the SCC fracture process in constant pressure tests. In tests at stresses close to the threshold, we found that the largest crack depth that could be tolerated before final cladding rupture occurred was ~ 70% of the wall thickness in the stress-relieved materials and ~ 30% of the wall thickness for recrystallized Zircaloy-2. However, it is clear that if the stress falls as the crack propagates (as would normally be the case in a constant-displacement situation), the crack will penetrate to a depth greater than 70% of the wall thickness before ductile rupture of the uncracked ligament occurs. It is even possible to envisage a situation where the stress corrosion crack could penetrate the entire thickness of the tube wall because the stress required for continued SCC propagation is expected to be less than that for ductile rupture of the uncracked ligament at all crack depths. (Both stresses are zero when the crack depth equals the wall thickness, but we believe that the minimum stress for ductile rupture rises more rapidly with increasing crack size than does the minimum stress for SCC.) However, in most practical cases, final fracture of the cladding is expected to occur rapidly by purely mechanical (environment-insensitive) ductile rupture.

RELEVANCE OF THE RESULTS TO PCI FAILURE

The results of power-ramping experiments in test reactors (7-1, 7-7) provide convincing evidence that PCI failures are due to the combined action of stresses in the cladding associated with the power ramp and the chemical environment to which the inside cladding surface is exposed. That is, PCI failures occur under conditions where neither the stress applied to the cladding nor the chemical environment would alone cause failure. The general picture of the mechanism of PCI failure that is beginning to gain wide acceptance is as follows. As the power increases, the temperature at the fuel center rises and causes the fuel to expand. Fuel expansion generates tensile strains and stresses in the cladding that are locally intensified at the inside cladding surface at locations such as pellet-pellet interfaces and fuel chips and over pellet cracks. The protective ZrO_2 film is ruptured at such locations, exposing the underlying metal to a corrosive environment that either has been released previously from the fuel or is released during the ramp as a result

of the temperature increase in the fuel center. If the local stress/strain state is severe enough and the environment is corrosive enough, and if both stress and environment are sustained long enough, a small stress corrosion crack will form at the inside surface of the cladding and grow until it penetrates the cladding wall.

In the context of this model of PCI failure, the most important observations of the present work are:

- Significant quantities of a number of fission products and fuel impurities can reach the cladding of power reactor fuel under some operating conditions (Section 2) and several of these substances can embrittle Zircaloy (Section 6)
- Crack nuclei form at specific sites in the metal surface when stressed Zircaloy is exposed to iodine (Section 4)
- A stress threshold exists for iodine SCC of Zircaloy at reactor operating temperatures below which the metal is immune to SCC failure (Section 5).

The significance of each of these observations is amplified below.

The Chemical Environment

The availability of sufficient concentrations of embrittling substances is one of the prerequisites for the occurrence of PCI failure and if contact between the cladding and the embrittling substances could be prevented, PCI failure would be suppressed. Our results indicate that several embrittling substances can potentially reach the cladding in sufficient concentrations to promote failure. Therefore, to be successful, any remedial measures must be broad-based rather than specific. That is, they must be effective in preventing contact between the cladding and several different fission products and impurities. One way in which this could be accomplished would be by suppressing the release of the aggressive substances, either by keeping fuel center temperature below the levels at which fission products are released or by interfering with the processes involved in the release of fission products and impurities from the fuel. Another approach would be to place a physical barrier of some sort between the fuel and the cladding, e.g., a coating on the cladding. Both concepts are currently being investigated. For instance, the CANLUB graphite coating system is believed to be successful in part because it prevents fission products from reaching the cladding (7-8). Fuel

modifications in which the centers of fuel pellets have smaller enrichment of fission isotopes, are being tested in Denmark and as a consequence of our results, EPRI has initiated PCI-related tests with a similar United Kingdom fuel in the Halden Reactor under project EPRI-RP 355 (7-9). The function of the low central enrichment is to reduce the temperature of the fuel center, which will allow higher power operation without fission product release to the cladding. EPRI also has experiments underway in the Halden Reactor to test the ability of large grain size fuel, produced by doping, to minimize fission product release.

Sites of Initiation of PCI Cracks

The results reported in Section 4 show that when Zircaloys are strained in the presence of iodine at reactor operating temperatures, stress corrosion cracks form beneath cracks in the oxide at locations in the metal surface that contain concentrations of alloying elements and impurities. It is interesting to compare the distribution of the sites observed in our crack formation studies with the dimensions of the regions of stress and fission product concentration that exist at pellet-pellet interfaces in fuel cladding. In the indenter tests (Section 4), the larger cracks coincident with concentrations of impurities and alloying elements were observed about one-third of the samples examined. The area of strain produced and examined in each sample was typically ~ 1 mm^2. Therefore, there must have been one large crack for every ~ 3 mm^2 of Zircaloy surface. Thus, at the relatively large strains used in the indenter tests, oxide cracking exposed about 30 SCC initiation sites per square centimeter of Zircaloy surface. Since the area of the inside surface of a 0.1-mm length of Zircaloy cladding is ~ 3 mm^2, we can tentatively conclude that there is likely to be ~ 1 crack initiation site within an axial distance of about ±0.05 mm from every pellet-pellet interface.

This crack site density is in reasonable agreement with observations made on severely ramped test reactor fuel rods. In such rods, up to ~ 10 cracks are sometimes observed at a single pellet-pellet interface. At a density of 0.3 site/mm^2, 10 cracks would be expected at one pellet-pellet interface if the region of strain concentration (ridging) associated with that interface extended for an axial distance of about ±0.5 mm, which is of the order of magnitude observed in profilometer

measurements on ridges in severely ramped fuel rods. Thus, the data are not inconsistent with the idea that the sites at which PCI cracks form are the same sites as those at which we observed initiation of iodine-induced stress corrosion cracking in unirradiated Zircaloy tubings.

It has yet to be confirmed that the initiation of PCI failure in power reactor fuel rods occurs at sites in the surface of the cladding that contain abnormal concentrations of alloying elements and impurities. In project EPRI RP 829 incipient defects from power reactor fuel rods are being examined to address that question (7-9). In the interim it is worthwhile pursuing methods of eliminating these sites to improve the PCI resistance of cladding. In an EPRI funded follow-on program at SRI International, the effect on SCC susceptibility of state-of-the-art surface treatments that could be applied to homogenize or modify the inside surface of commercial tubing will be evaluated prior to test reactor demonstration of improved PCI resistance.

Although this remedy appears promising, it is possible that features other than chemical inhomogeneities in the metal surface are important, and so it is appropriate to proceed with caution. The literature reports that SCC by iron iodide and aluminum iodide is more severe than by iodine alone (7-1). That result may indicate that elements transported to the metal surface through the vapor are effective in promoting crack initiation, which means that crack initiation in metal halide environments may not require the presence of a chemical inhomogeneity in the metal surface. Therefore, in addition to investigating the origin of chemical inhomogeneities in Zircaloy and developing ways of eliminating them it would be highly desirable to clarify the reason why iodine stress corrosion cracks preferentially initiate at such inhomogeneities.

The Stress Threshold

Our experiments with pressurized tubes (Section 5) show that a stress threshold exists for iodine SCC of Zircaloy at reactor operating temperatures below which the Zircaloy is immune to iodine SCC and above which the failure time decreases systematically with increasing stress. If PCI failure exhibits similar

characteristics, the present results suggest it should be possible to optimize the PCI resistance of the Zircaloy cladding by modifying its microstructure.

PCI failures are not encountered if rates of power change are kept very small. Although this may be because fission products are not released from the fuel during slow power ramps, it is also clear that a small rate of power change will result in the generation of small cladding stresses because creep of the cladding and fuel can largely accommodate the thermal strains if the strain rate is slow. Thus, the effectiveness of vendor-recommended power-change restrictions in suppressing PCI failure provides some support for the idea that a threshold stress for PCI failure does exist. Whether or not there is a PCI threshold, any steps that reduce local stress concentrations in the cladding should reduce the incidence of PCI failure under given operating conditions. Hence, lubricants that prevent fuel-cladding bonding, chamfered fuel pellets that reduce ridging at pellet-pellet interfaces, and ductile fuel-cladding interlayers ("barriers") that reduce local stresses by plasticly deforming should all be somewhat effective in alleviating PCI.

Three aspects of iodine-induced failure of Zircaloy that are particularly relevant to PCI failure require further work before optimum operating procedures can be properly defined. First, additional data are required to define the stress threshold for irradiated Zircaloy more exactly and to position the stress versus failure-time envelope at stresses above the threshold. Second, the effect of iodine concentration on the stress threshold and failure time for irradiated Zircaloy should be studied, particularly at very small iodine concentrations. Finally, a damage accumulation law* is needed at stresses above the threshold so that the behavior observed in constant stress laboratory tests can be related to the variable stress situation encountered in fuel cladding service. These needs are being addressed under EPRI Projects RP 1027 and RP 971 (7-9).

---

*That is, we need to know how prior exposure at one stress above the threshold affects the life of a specimen that is subsequently exposed at a different stress.

If iodine SCC and PCI behavior are similar, one approach to optimizing the PCI resistance of cladding would be to change the microstructure so as to maximize both the threshold stress and the time to failure at stresses above threshold. As shown in Section 5, unirradiated stress-relieved Zircaloy has a higher threshold stress than recrystallized Zircaloy and also shows longer failure times. It would be desirable to confirm the superiority of a stress-relieved microstructure with tests on irradiated material, and the data being generated on RP 1027 should resolve the question of the optimum microstructure in the irradiated condition (7-9).

In the fuel cladding application, Zircaloy tubing is subjected to a constant displacement type of loading. Since SCC failure requires that the applied stress be sustained above a crack size dependent minimum value, any attempt to optimize the cladding characteristics must consider the stress relaxation characteristics of the cladding (which determine the stress-time history under fixed displacement loading) as well as the threshold stress and failure time. Present evidence suggests that the crystallographic texture of the cladding is one of its key characteristics. In particular, there is evidence that a 0° basal texture is more resistant to iodine SCC than a ±30° texture (7-10). As texture also affects stress relaxation behavior, the effects of texture variations on iodine SCC and stress relaxation will be studied in detail during the follow-on to the present program.

REFERENCES

7-1   B. Cox and J. C. Wood, "Iodine Induced Cracking of Zircaloy Fuel Cladding," in Corrosion Problems in Energy Conversion and Generation, C. S. Tedman, Jr., ed. (Electrochemical Society, New York, New York, 1974), p. 275.

7-2   C. C. Busby, R. P. Tucker, and J. E. McCauley, J. Nuclear Materials 55, 64 (1975).

7-3   K. Videm and L. Lunde, "Stress Corrosion Cracking of Zircaloy Fuel Cladding Under Power Ramps and in Lab. Tests," Proceedings: ANS Topical Meeting on Water Reactor Fuel Performance, St. Charles, Ill. May 1977.

7-4   P. H. Kreyns, G. L. Spahr, and J. E. McCauley, J. Nucl. Mat. 61, 203 (1976).

7-5   P. Knudsen, C. Bagger, and M. Fisher, "Characterization of PWR Power Ramp Tests," Proceedings: ANS Topic Meeting on Water Reactor Fuel Performance, St. Charles, Illinois, May 1977.

7-6   A. H. Cottrell, <u>The Mechanical Properties of Matter</u> (Wiley, New York, 1964), p. 328.

7-7   J. H. Davies, et al., "Irradiation Tests to Characterize the PCI Failure Mechanism," <u>Proceedings: ANS Topic Meeting on Water Reactor Fuel Performance</u>, St. Charles, Illinois, May 1977.

7-8   B. Cox., et al. "Summary of Panel Discussion on the Pellet–Cladding Interaction Problem," <u>Proceedings: ANS Topic Meeting on Water Reactor Fuel Performance</u>, St. Charles, Illinois, May 1977.

7-9   J.T.A. Roberts, et al., "Planning Support Document for the EPRI Light Water Reactor Fuel Performance Program," EPRI NP-370-SR Electric Power Research Institute, Palo Alto, California, January 1977.

7-10 A. K. Miller and E. Smith, "Stress Corrosion Fracture of Zircaloy Cladding in Fuel Rods Subjected to Power Increases.--II An Interpretation of the Effect of Texture on Crack Formation in Irradiated Zircaloy in an Iodine Environment," submitted to J. Nucl. Mat.

Appendix A

FABRICATION HISTORIES AND METALLURGICAL
CHARACTERISTICS OF THE EXPERIMENTAL MATERIALS

A complete listing of the materials obtained for use on projects RP 455 and RP 456
is shown in Table 3-1 in Section 3 of this report. The tables and illustrations
in this appendix provide details of (1) the reduction schedules used by TWCA to
fabricate the flat products (Tables A-1 to A-3), (2) the compositions of the ingots
from which the tubes and flat products were fabricated (Tables A-4 to A-7), (3) the
results of chemical analyses on 11 of the products (Table A-8), and (4) basal pole
figures, optical micrographs, and hardness measurements for 28 of the products
(Figures A-1 to A-28). A discussion of the significance of these results is pre-
sented in Section 3 together with additional metallurgical characterization informa-
tion on some of the experimental materials that was generated during the program.

Table A-1

FABRICATION SCHEDULES USED FOR 12.7-mm PLATE PRODUCTS

Beta-Quenched 100-mm Slab (Zr-2 or Zr-4)

(Schedule C)	(Schedule J)	(Schedule K)
Heat at 1170 K and Roll to 33 mm	Heat at 1170 K and Roll to 33 mm	Heat at 1170 K and Roll to 33 mm
Condition	Reheat at 1070 K and Quench	Reheat at 1070 K and Quench
Heat at 620 K and Roll to 12.7 mm	Heat at 620 K and Roll to 12.7 mm	Heat at 620 K and Cross Roll to 12.7 mm
Heat Treat	Heat Treat	Heat Treat
Condition	Condition	Condition
Saw	Saw	Saw

Table A-2

FABRICATION SCHEDULES USED FOR 3.2-mm SHEET PRODUCTS

Beta-Quenced 100-mm Slab (Zr-2 or Zr-4)

(Schedule C)	(Schedule J)	(Schedule K)
Heat at 1170 K and Roll to 25.4 mm	Heat at 1170 K and Roll to 25.4 mm	Heat at 1170 K and Roll to 25.4 mm
Condition	Condition	Condition
Heat at 1170 K and Roll to 5.5 mm	Heat at 1170 K and Roll to 5.5 mm	Heat at 1170 K and Roll to 5.5 mm
Stress Relieve 2 hours at 780 K	Reheat at 1070 K and Quench	Reheat at 1070 K and Quench
Condition	Condition	Condition
Cold Roll to 3.2 mm	Cold Roll to 3.2 mm	Cross Cold Roll to 3.2 mm
Heat Treat	Heat Treat	Heat Treat
Condition	Condition	Condition
Shear	Shear	Shear

Table A-3

FABRICATION SCHEDULES USED FOR 0.8-mm SHEET PRODUCTS

Beta-Quenched 100 mm-Slab (Zr-2 or Zr-4)

|
Heat at 1170 K and Roll to 19 mm

|
Condition

|
Heat at 1170 K and Roll to 2.5 mm

(Schedule C)	(Schedule J)	(Schedule K)
Stress Relieve 2 hours at 780 K	Reheat at 1070 K and Quench	Reheat at 1070 K and Quench
Condition	Condition	Condition
Cold Roll to 1.9 mm	Cold Roll to 1.9 mm	Cross Cold Roll to 1.9 mm
Stress Relieve 2 hours at 780 K	Stress Relieve 2 hours at 780 K	Stress Relieve 2 hours at 780 K
Cold Roll to 0.8 mm	Cold Roll to 0.8 mm	Cross Cold Roll to 0.8 mm
Heat Treat	Heat Treat	Heat Treat
Condition	Condition	Condition
Shear	Shear	Shear

Table A-4

COMPOSITION OF TWCA INGOT NUMBER 395481Q USED
TO FABRICATE ZIRCALOY-2 TUBING

Composition (percent)		
	Top	Bottom
Sn	1.56	1.41
Fe	0.14	0.14
Cr	0.12	0.11
Ni	0.05	0.05
Impurities (ppm)		
Al	45	41
B	0.3	0.2
Cd	< 0.2	< 0.2
Ca	< 10	< 10
C	120	100
Cl	< 5	< 5
Co	< 10	< 10
Cu	12	14
Hf	73	74
H	7	7
Pb	< 25	< 25
Mg	< 10	< 10
Mn	< 25	< 25
N	39	22
Si	< 50	< 50
Ti	< 25	< 25
W	< 25	< 25
U	< 0.5	< 0.5
O	1160	990
Cb	< 50	< 50
Mo	< 10	< 10
Ta	< 100	< 100
V	< 25	< 25
Na	< 10	< 10

Table A-5

COMPOSITION OF TWCA INGOT NUMBER 397598Q USED TO
FABRICATE ZIRCALOY-2 PLATE AND SHEET

Composition (percent)		
	Top	Bottom
Sn	1.53	1.49
Fe	0.14	0.14
Cr	0.11	0.10
Ni	0.05	0.05
Impurities (ppm)		
Al	50	47
B	< 0.25	< 0.25
C	120	140
Cd	< 0.25	< 0.25
Ca	< 10	< 10
Cl	< 5	< 5
Cb	< 50	< 50
Co	< 10	< 10
Cu	13	18
H	< 5	< 5
Hf	92	74
N	37	36
Na	< 10	< 10
P	8	8
O	1250	1370
Mg	< 10	< 10
Mn	< 25	< 25
Mo	< 10	< 10
Si	69	73
Ti	< 25	< 25
Ta	< 100	< 100
W	< 25	< 25
V	< 25	< 25
U	1.0	1.2
Pb	< 25	< 25

Table A-6

COMPOSITION OF TWCA INGOT NUMBER 394597Q USED TO
FABRICATE ZIRCALOY-4 TUBING

Composition (percent)		
	Top	Bottom
Sn	1.52	1.39
Fe	0.20	0.19
Cr	0.12	0.11
Impurities (ppm)		
Al	38	< 35
B	0.2	0.2
Cd	< 0.2	< 0.2
Ca	< 10	< 10
C	110	120
Cl	< 5	< 5
Co	< 10	< 10
Cu	17	17
Hf	44	44
H	7	< 5
Pb	< 50	< 50
Mg	< 10	< 10
Mn	< 25	< 25
Ni	< 35	< 35
N	33	34
Si	81	69
Ti	< 25	< 25
W	< 25	< 25
U	1.0	0.9
O	1260	1270
Cb	< 50	< 50
Mo	< 25	< 25
Ta	< 100	< 100
V	< 25	< 25
Na	< 10	< 10

Table A-7

COMPOSITION OF TWCA INGOT NUMBER 397523Q USED TO FABRICATE ZIRCALOY-4 PLATE AND SHEET

Composition (percent)		
	Top	Bottom
Sn	1.53	1.52
Fe	0.21	0.20
Cr	0.11	0.11
Impurities (ppm)		
Al	45	40
B	0.2	0.2
C	120	120
Cd	< 0.2	< 0.2
Co	< 10	< 10
Cu	14	12
Ca	< 10	< 10
Cl	15	< 5
Cb	< 50	< 50
H	7	7
Hf	57	52
Mg	< 10	< 10
Mn	< 25	< 25
Mo	< 10	< 10
N	35	37
Ni	< 35	< 35
Si	< 50	< 50
Ti	< 25	< 25
Ta	< 100	< 100
Na	< 10	< 10
W	< 25	< 25
V	< 25	< 25
Zn	< 50	< 50
O	1150	1160
U	1.1	0.7
Pb	< 25	< 25

Table A-8

INTERSTITIAL IMPURITY CONTENTS OF SHEET, PLATE,
AND TUBE PRODUCTS

Identification Number[1]	Interstitial Content (ppm)		
	O	N	H
7FD11	1300	33	21
7AH11-S	1160	32	13
7AH11-H	1190	34	15
9908-3B	1280	37	7
9908-4B	1480	32	8
9908-5A	1310	44	10
9912-2B	1280	34	14
9912-4B	1180	40	10
9912-6A	1150	39	7
9913-3A	1150	42	17
9913-3B	1160	39	20

[1]See Table 3-1 for additional details.

(a)

(b)
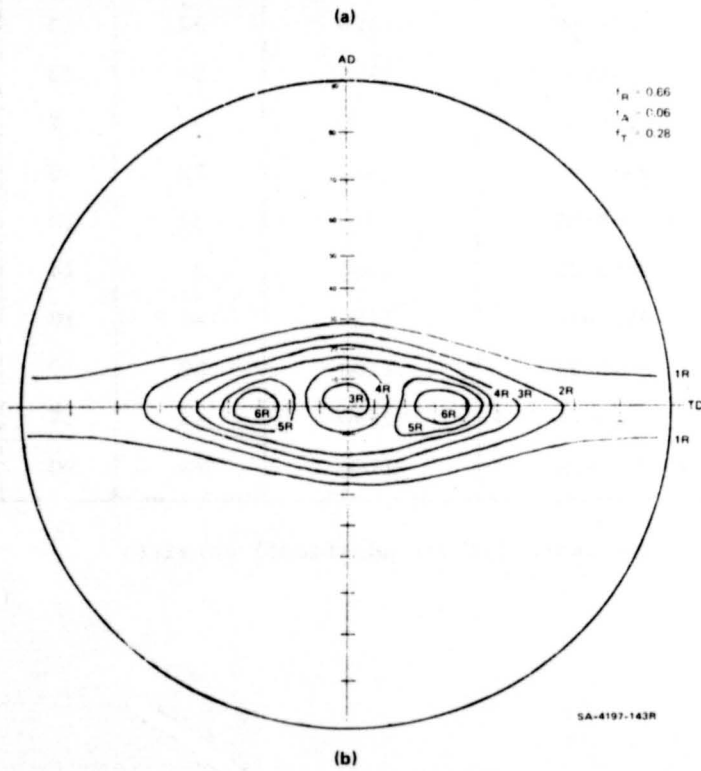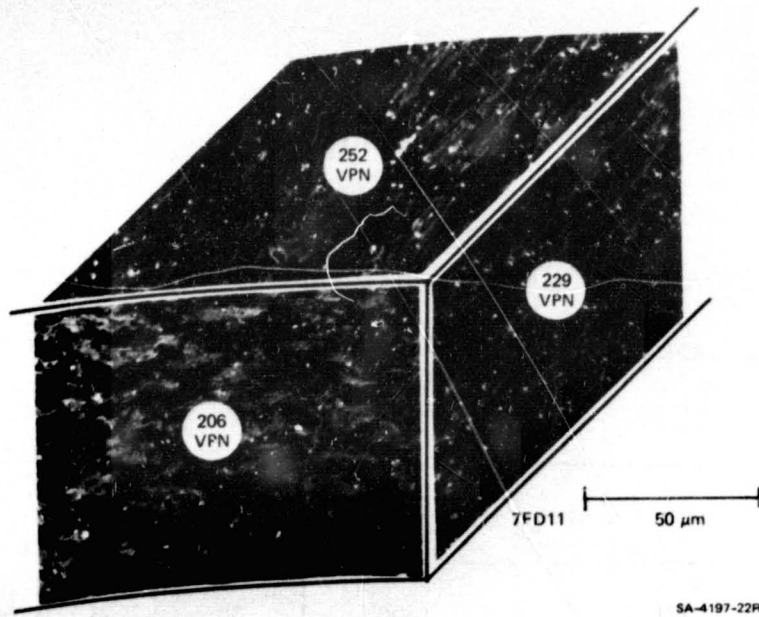
FIGURE A-1   MICROSTRUCTURE AND HARDNESS (a) AND BASAL POLE FIGURE
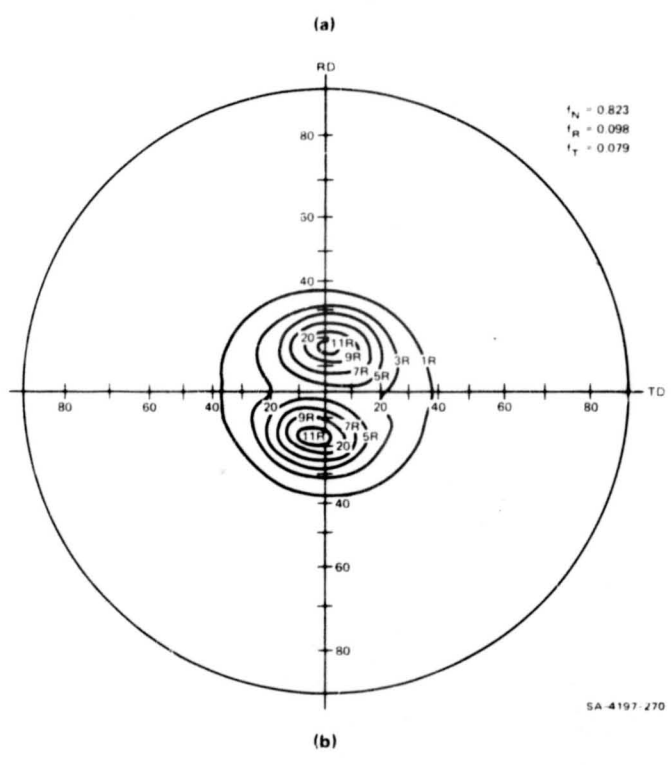(b) FOR THE 7FD11 LOT OF ZIRCALOY-4 TUBING

(a)

(b)
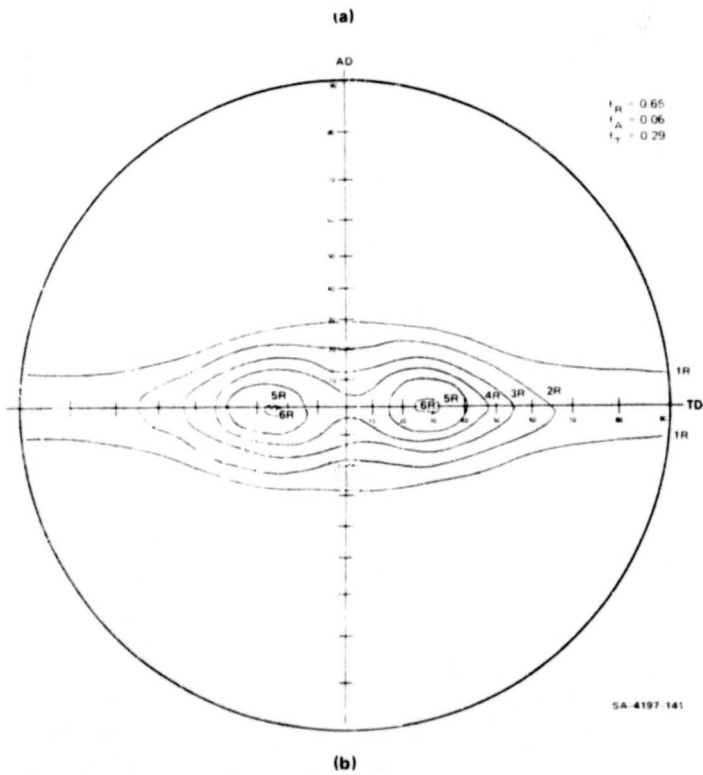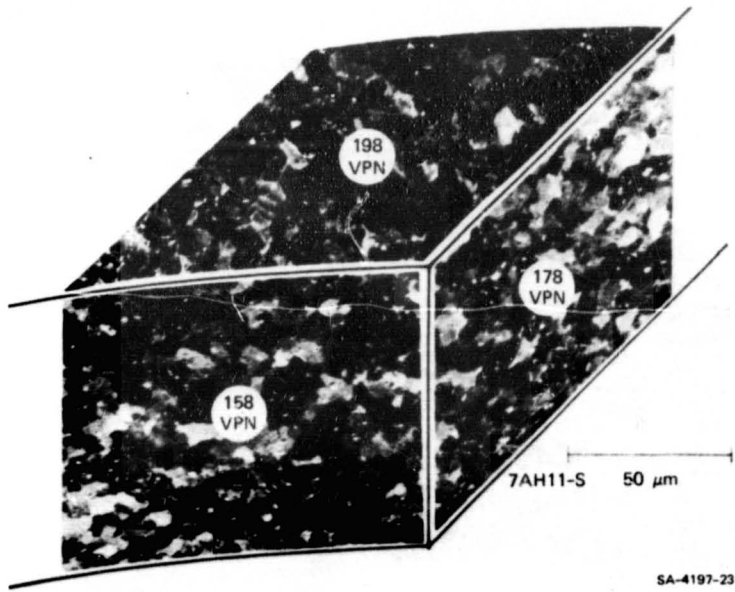
FIGURE A-2   MICROSTRUCTURE AND HARDNESS (a) AND BASAL POLE FIGURE
(b) FOR THE 7AH11-S LOT OF ZIRCALOY-2 TUBING

(a)

(b)
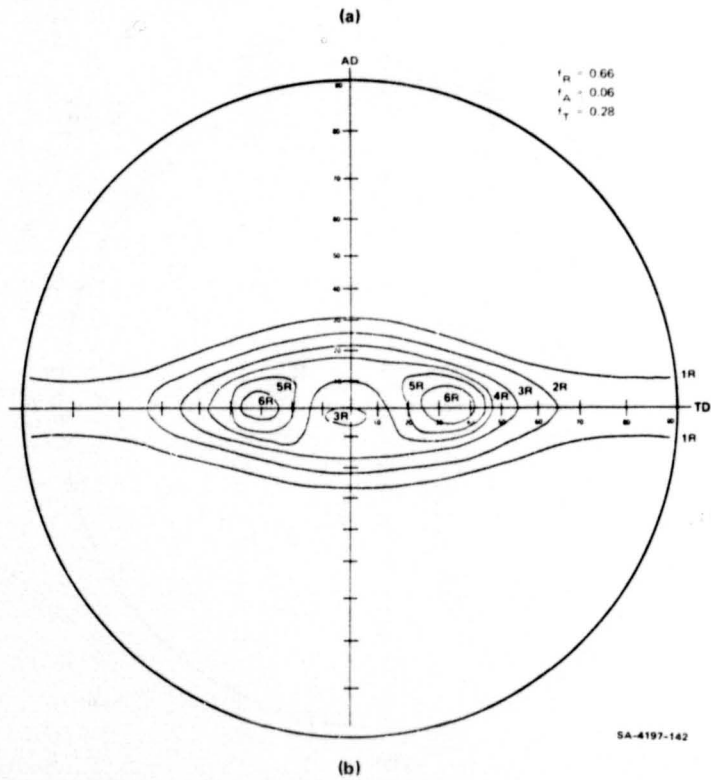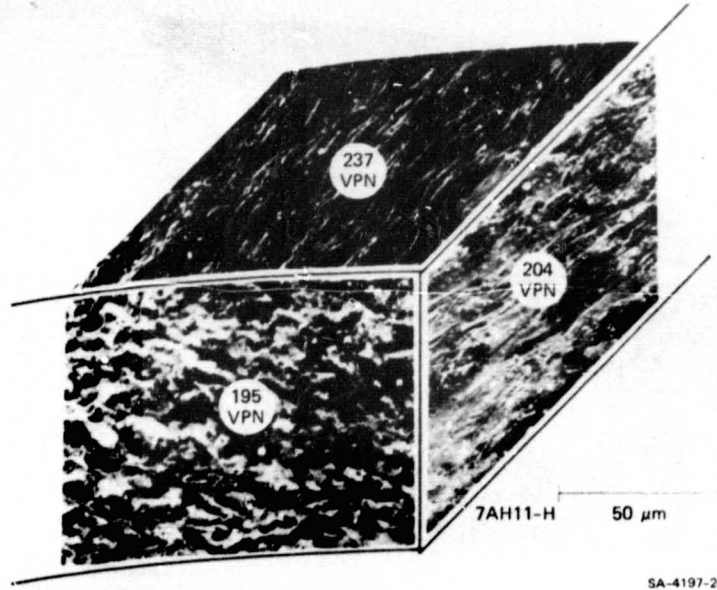
FIGURE A-3   MICROSTRUCTURE AND HARDNESS (a) AND BASAL POLE FIGURE (b)
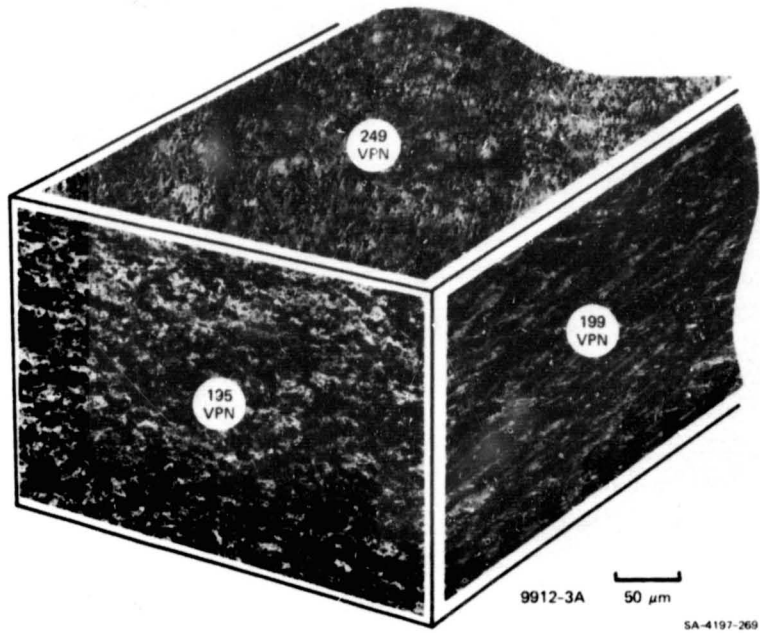FOR THE 7AH11-H LOT OF ZIRCALOY-2 TUBING
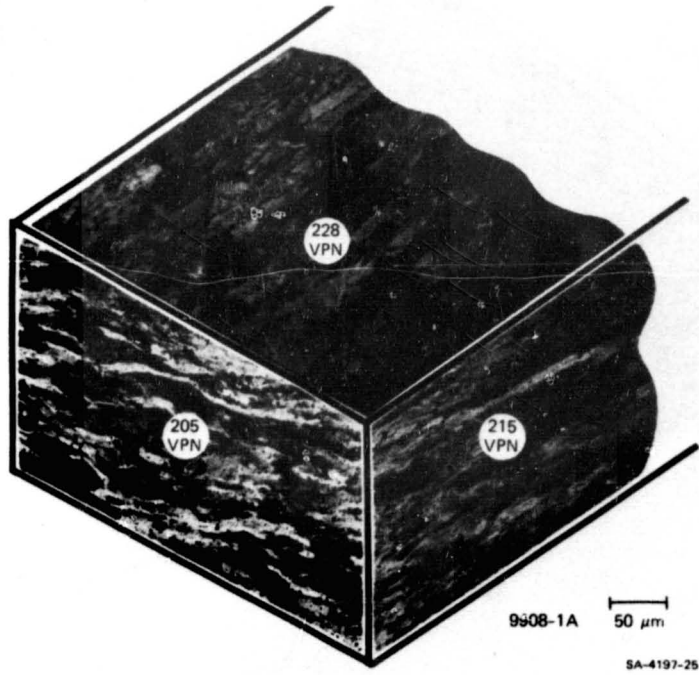
(a)
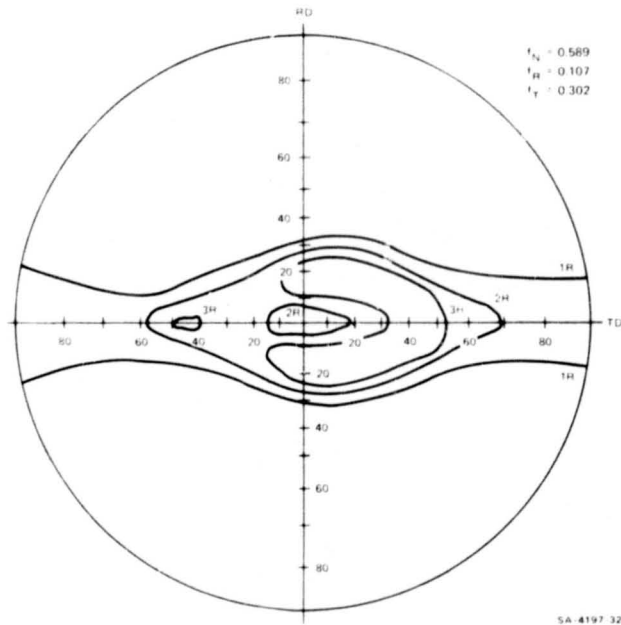
(b)

FIGURE A-4   MICROSTRUCTURE AND HARDNESS (a) AND BASAL POLE FIGURE (b)
FOR THE 9908-1A LOT OF ZIRCALOY-2 PLATE
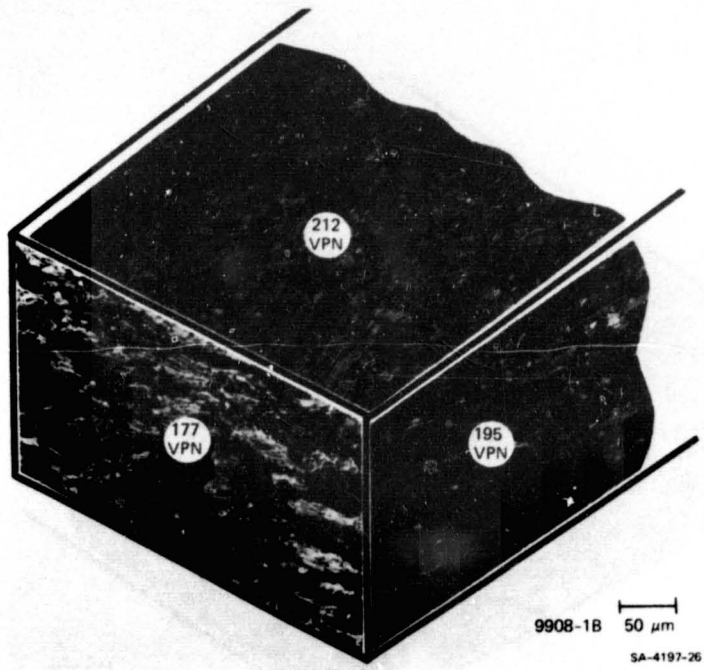
(a)
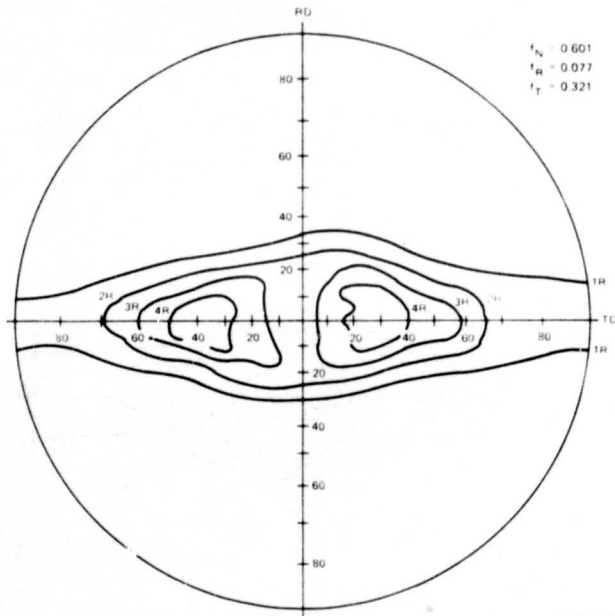
(b)
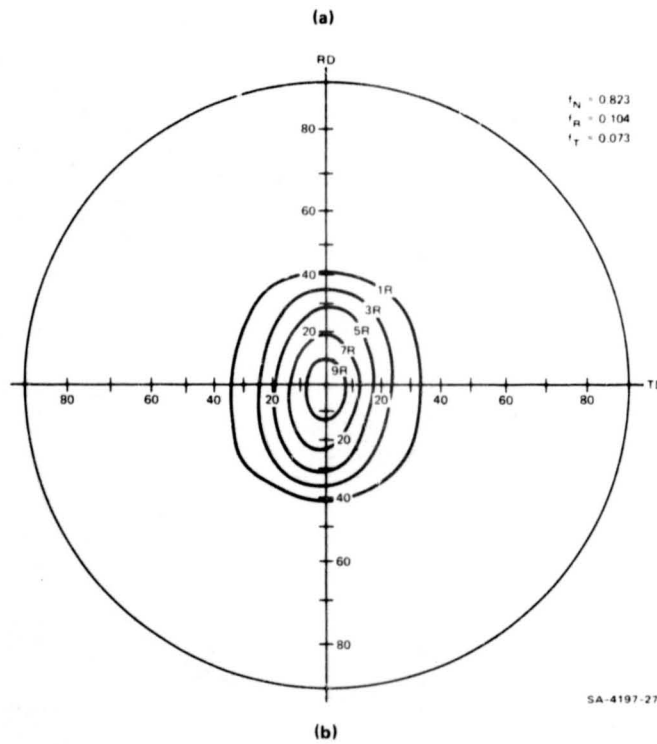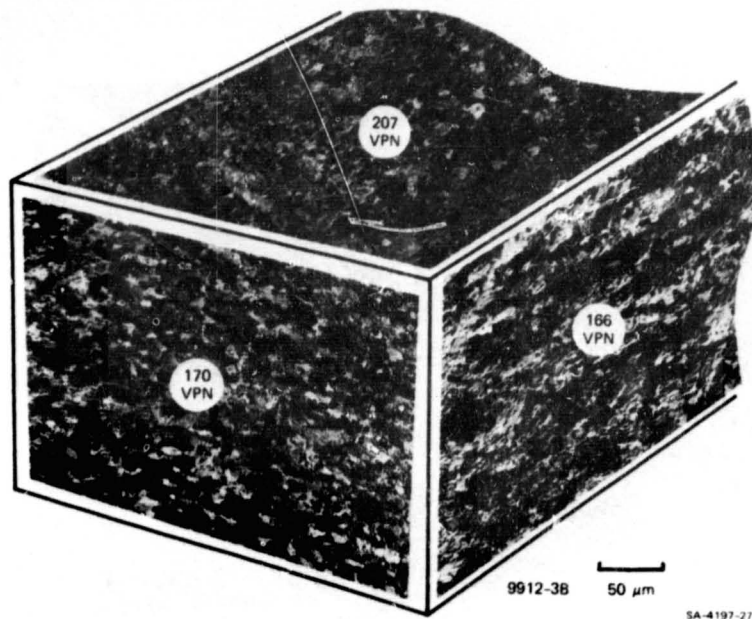
FIGURE A-5 MICROSTRUCTURE AND HARDNESS (a) AND BASAL POLE FIGURE (b)
FOR THE 9908-1B LOT OF ZIRCALOY-2 PLATE

9908-2A 50 μm

SA-4197-27

(a)

(b)
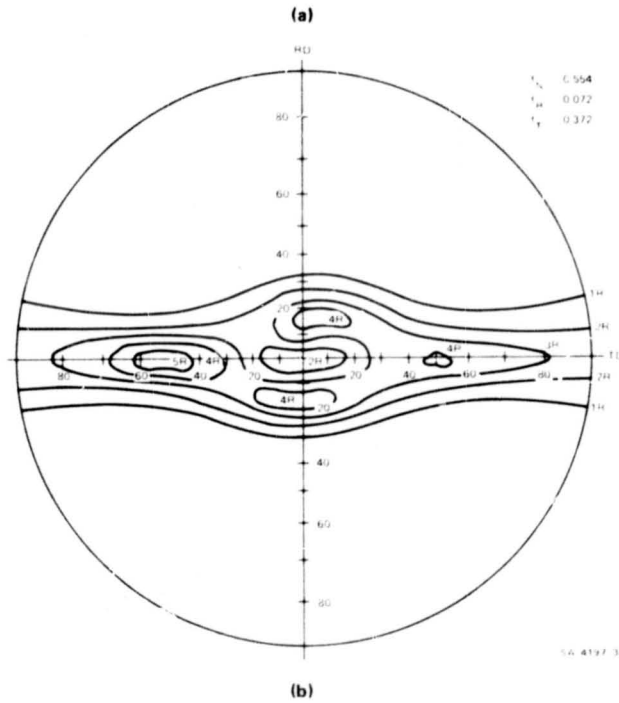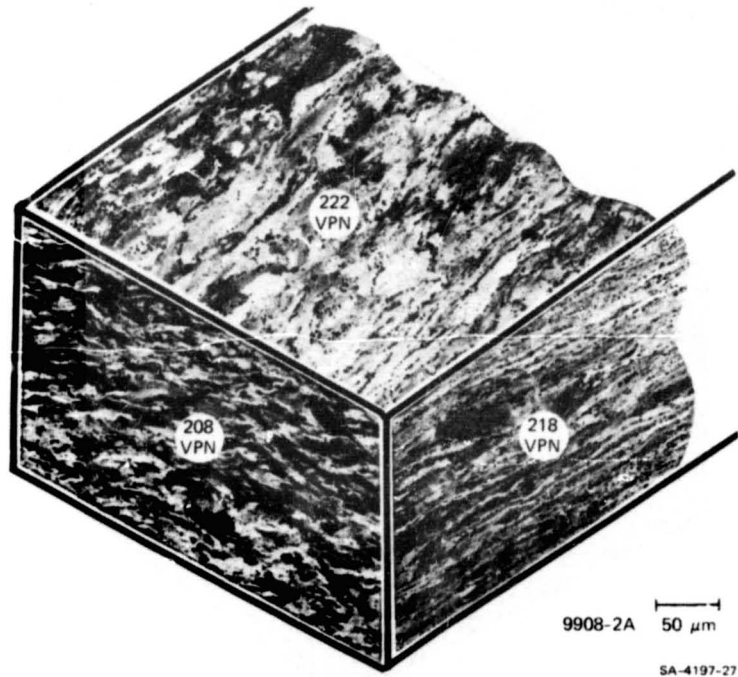
FIGURE A-6   MICROSTRUCTURE AND HARDNESS (a) AND BASAL POLE FIGURE (b)
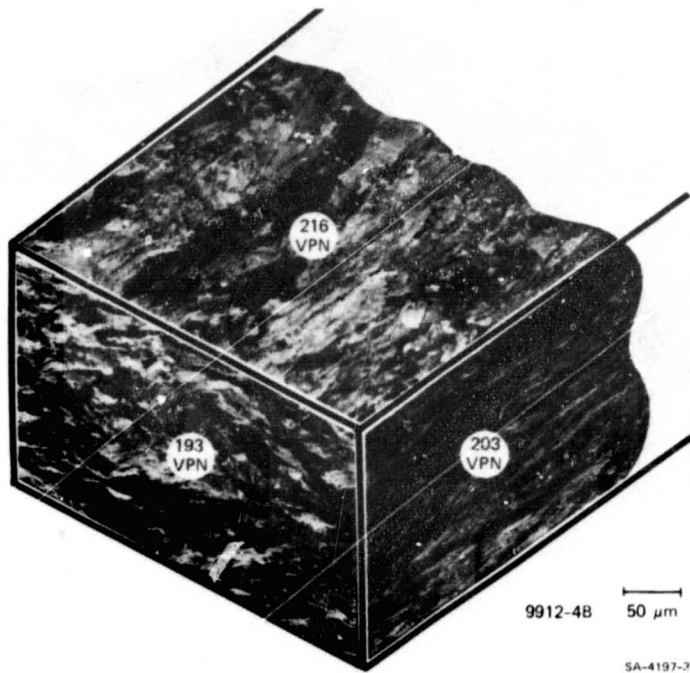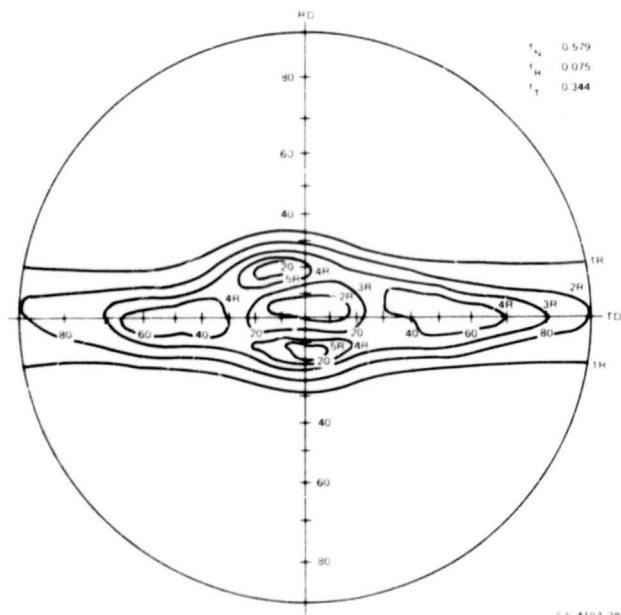FOR THE 9908-2A LOT OF ZIRCALOY-2 PLATE

(a)

(b)

FIGURE A-7   MICROSTRUCTURE AND HARDNESS (a) AND BASAL POLE FIGURE (b)
FOR THE 9908-2B LOT OF ZIRCALOY-2 PLATE
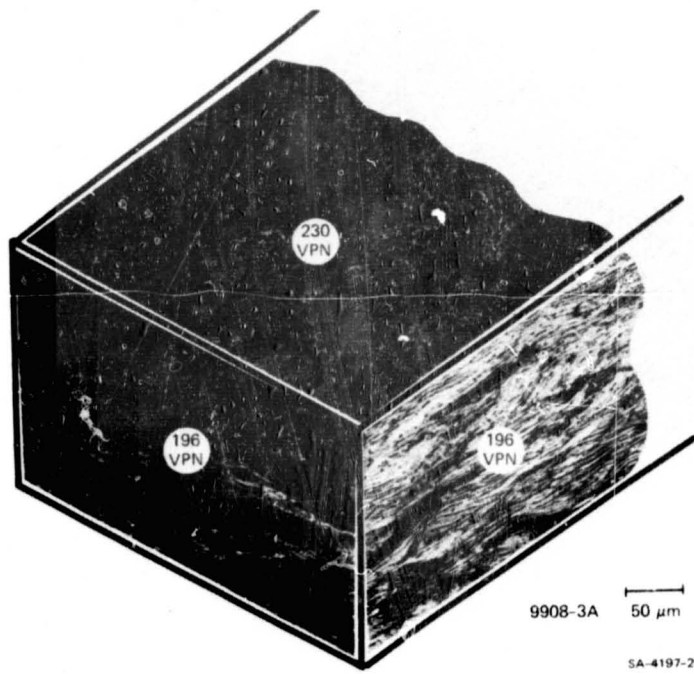
(a)
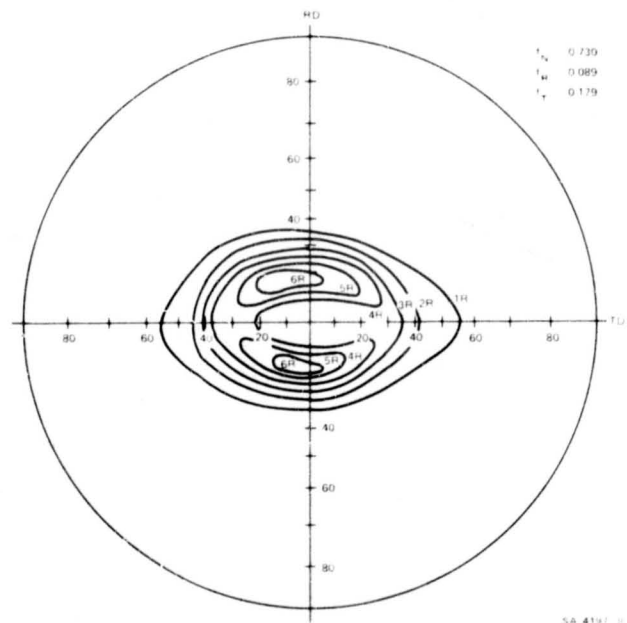
(b)

FIGURE A-8   MICROSTRUCTURE AND HARDNESS (a) AND BASAL POLE FIGURE (b)
FOR THE 9908-3A LOT OF ZIRCALOY-2 PLATE

(a)

(b)
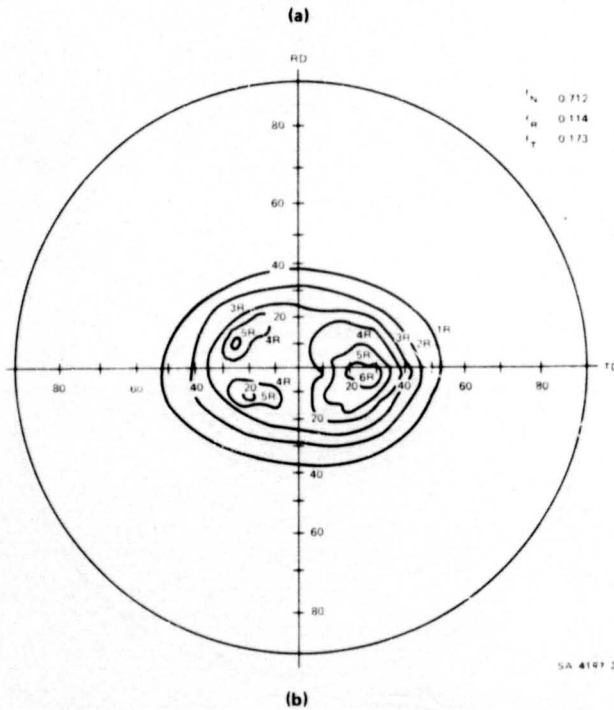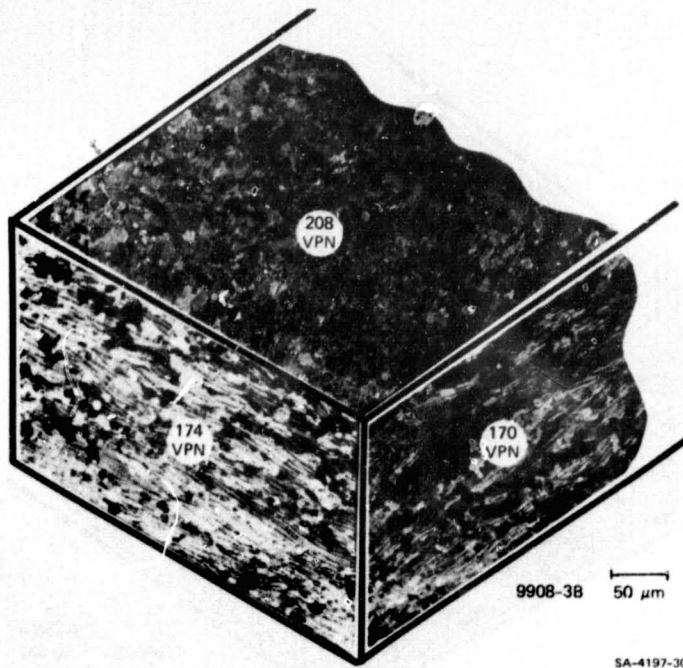
FIGURE A-9   MICROSTRUCTURE AND HARDNESS (a) AND BASAL POLE FIGURE (b)
FOR THE 9908-3B LOT OR ZIRCALOY-2 PLATE

(a)

$t_N = 0.576$
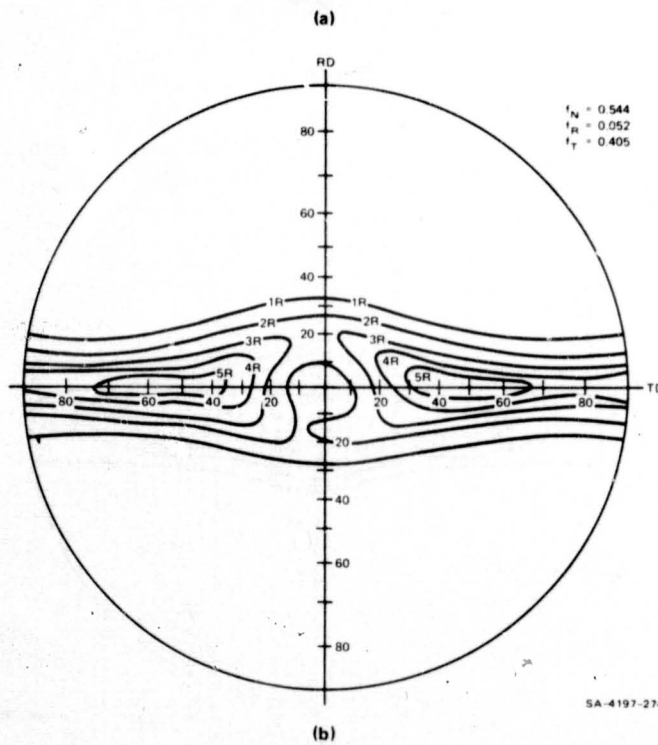$t_R = 0.056$
$t_T = 0.368$
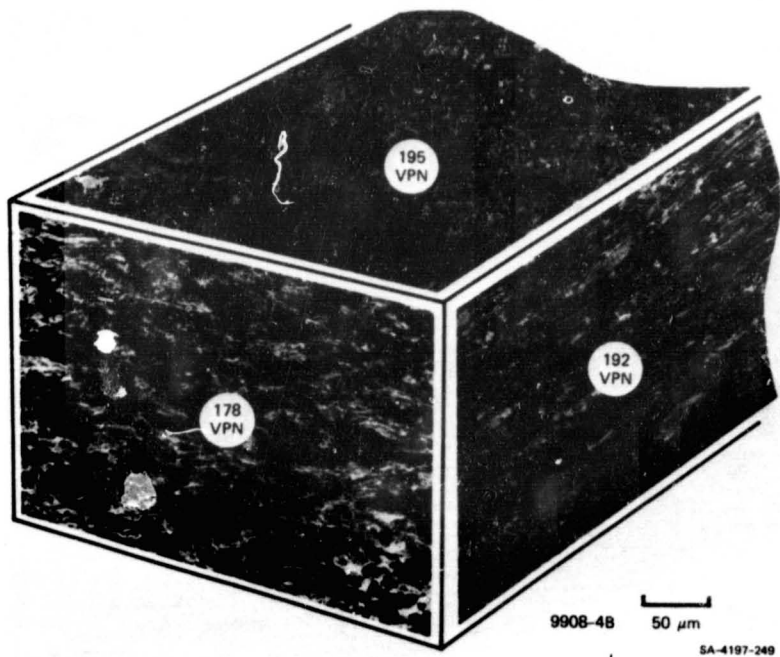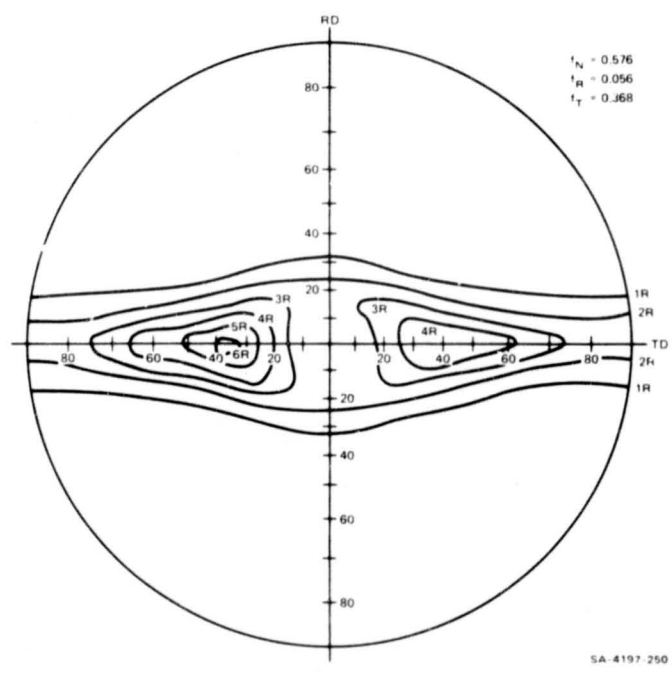
(b)

FIGURE A-10   MICROSTRUCTURE AND HARDNESS (a) AND BASAL POLE FIGURE (b)
FOR THE 9908-4B LOT OF ZIRCALOY-2 SHEET

(a)

(b)
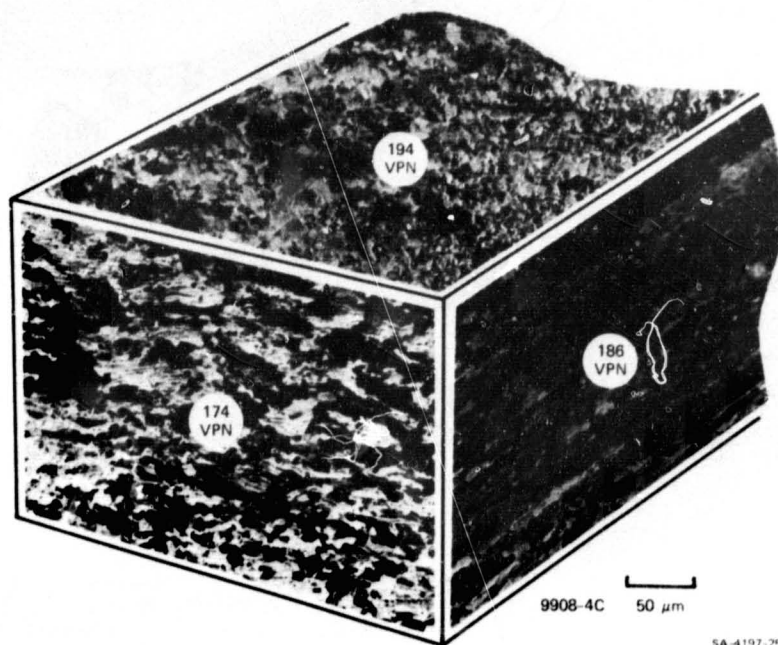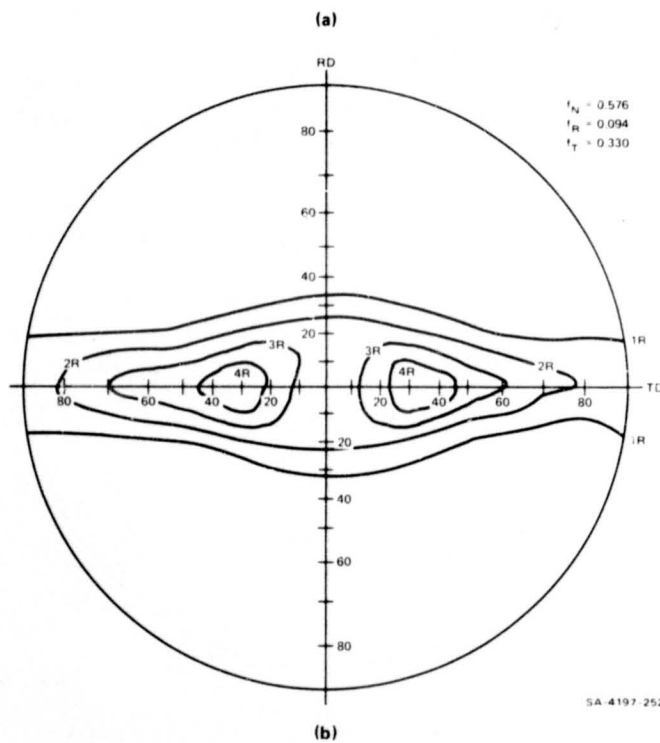
FIGURE A-11   MICROSTRUCTURE AND HARDNESS (a) AND BASAL POLE FIGURE (b)
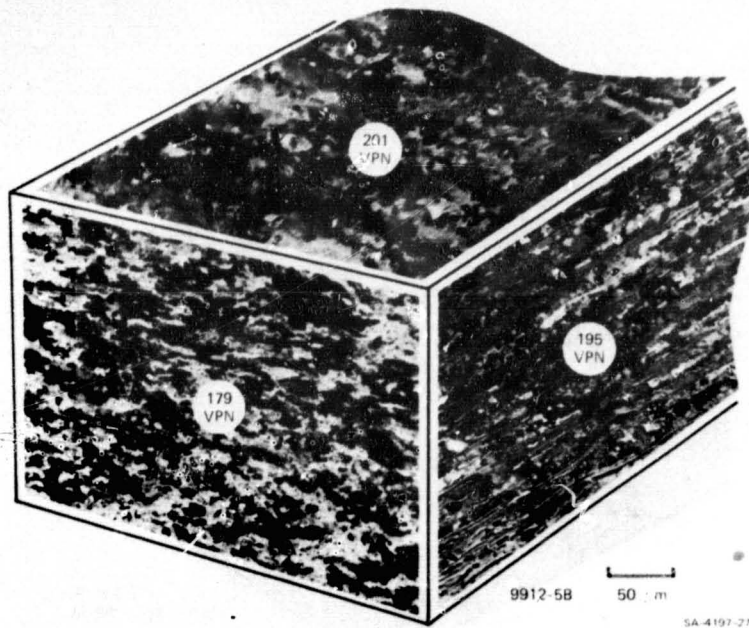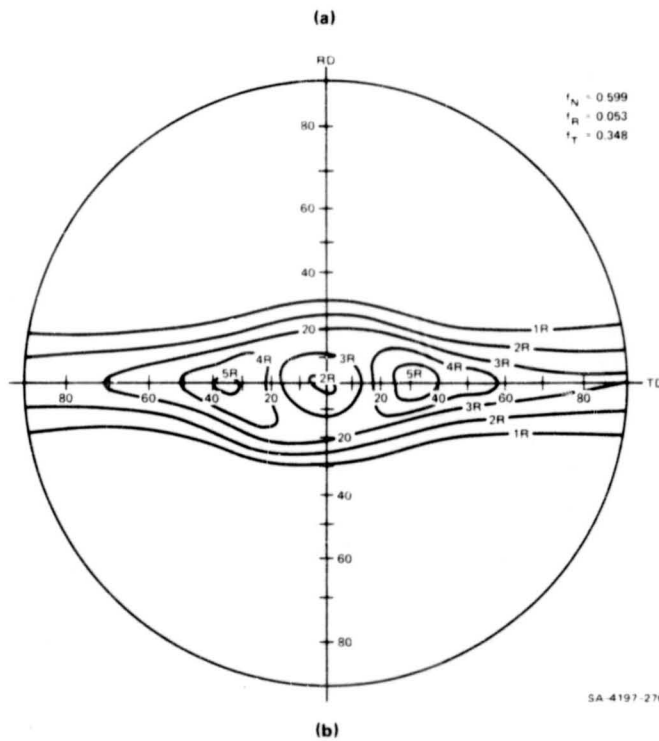FOR THE 9908-4C LOT OF ZIRCALOY-2 SHEET

(a)

(b)
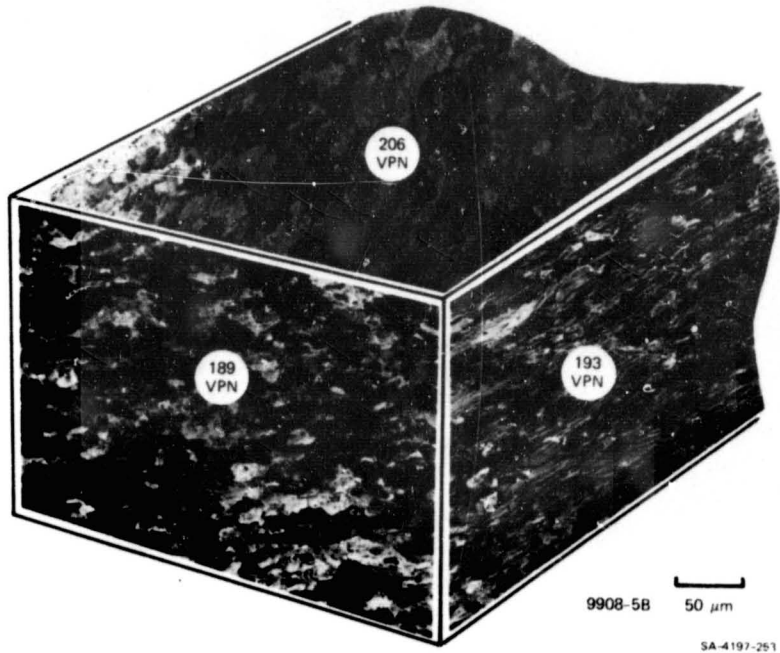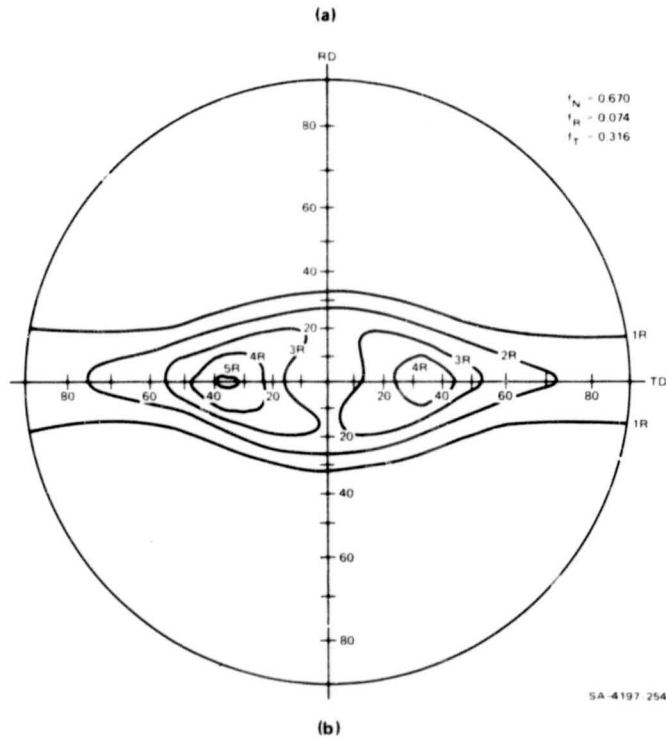
FIGURE A-12   MICROSTRUCTURE AND HARDNESS (a) AND BASAL POLE FIGURE (b)
FOR THE 9908-5B LOT OF ZIRCALOY-2 SHEET
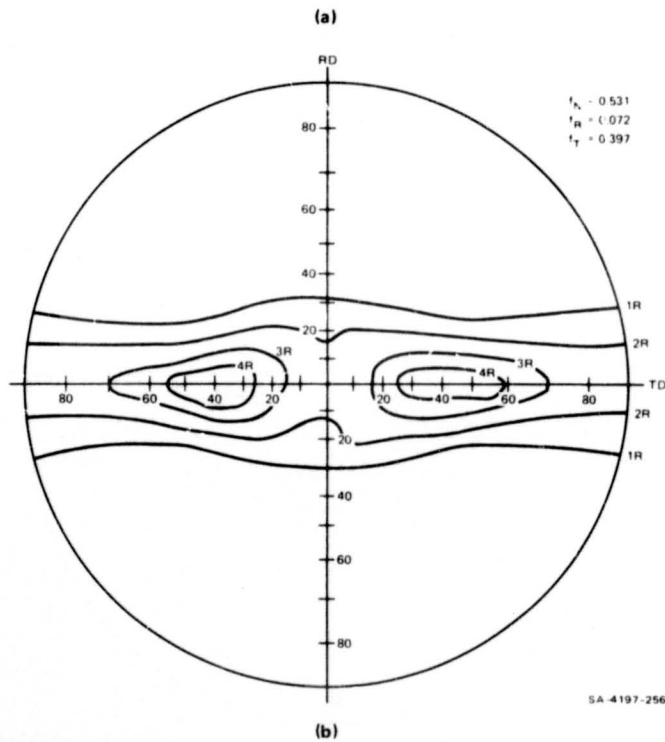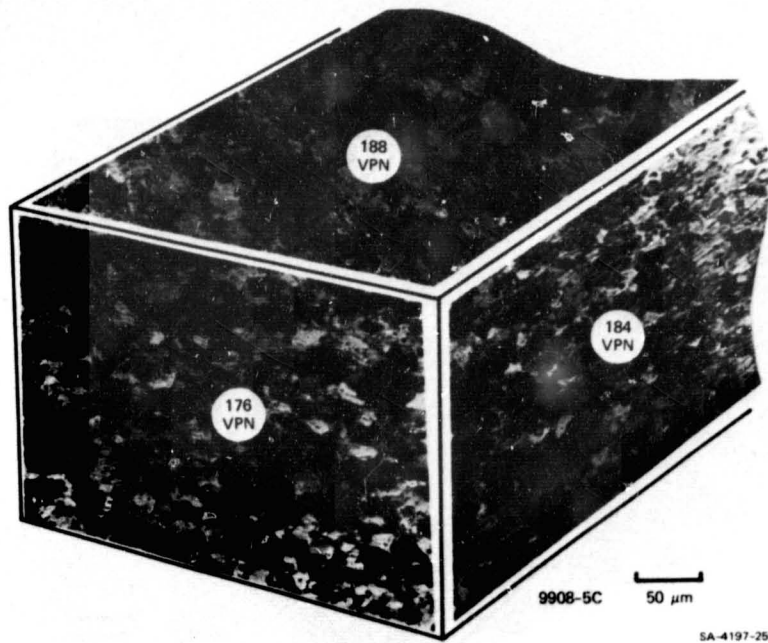
FIGURE A-13   MICROSTRUCTURE AND HARDNESS (a) AND BASAL POLE FIGURE (b)
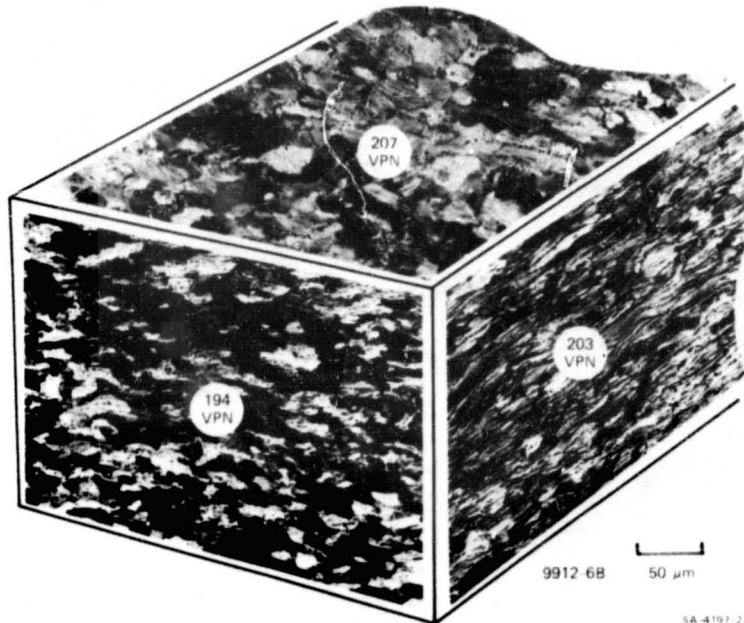FOR THE 9908-5C LOT OF ZIRCALOY-2 SHEET

A-22

(a)
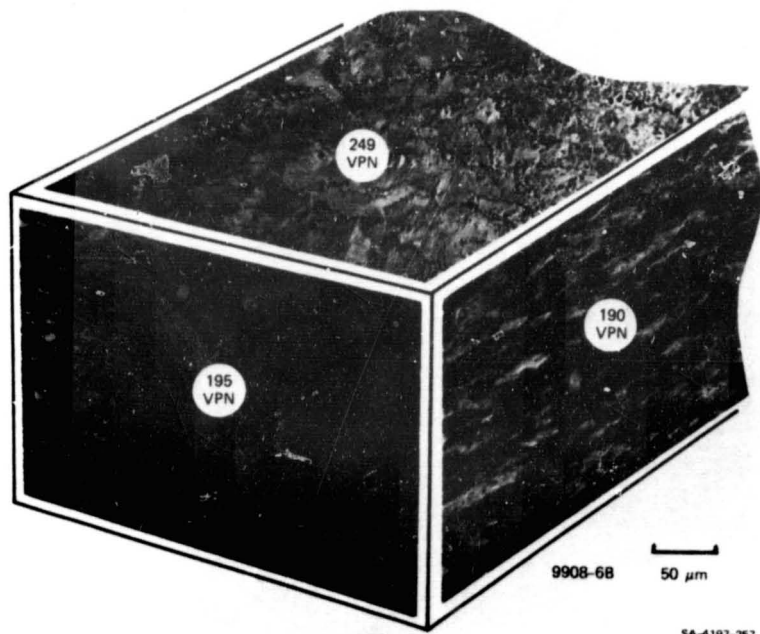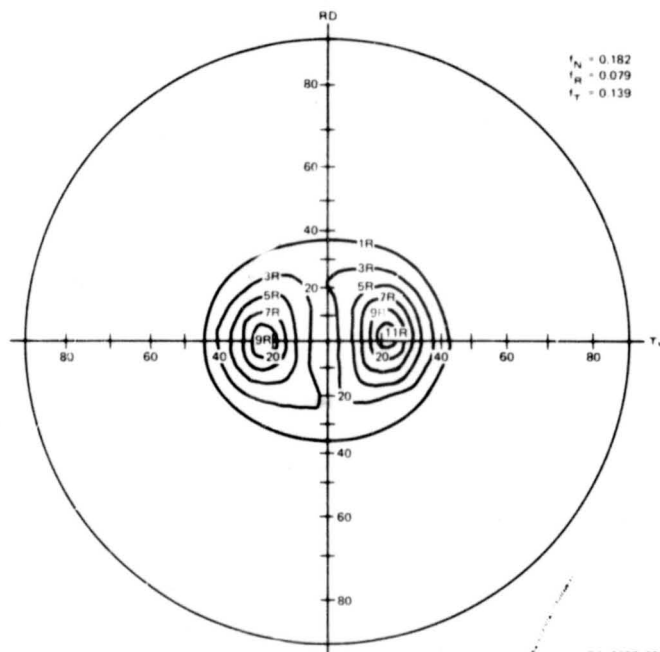
(b)

FIGURE A-14   MICROSTRUCTURE AND HARDNESS (a) AND BASAL POLE FIGURE (b)
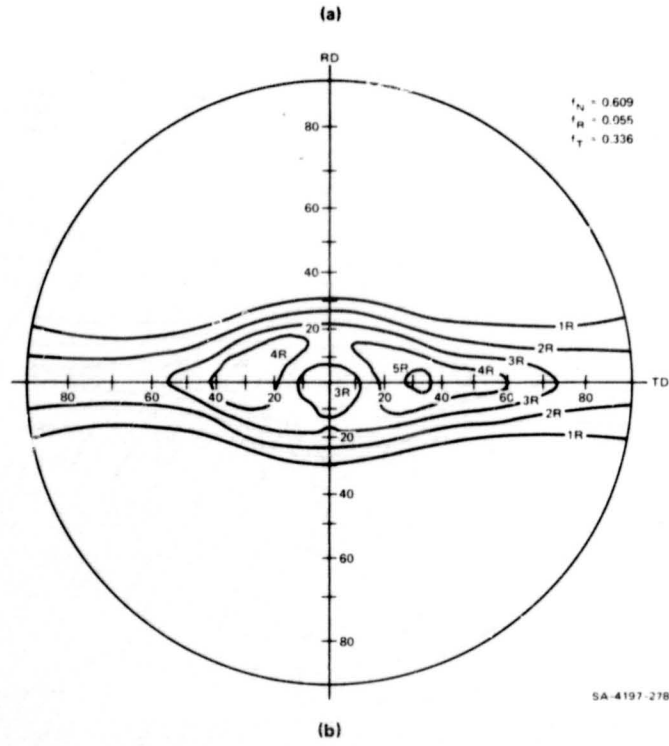FOR THE 9908-6B LOT OF ZIRCALOY-2 SHEET
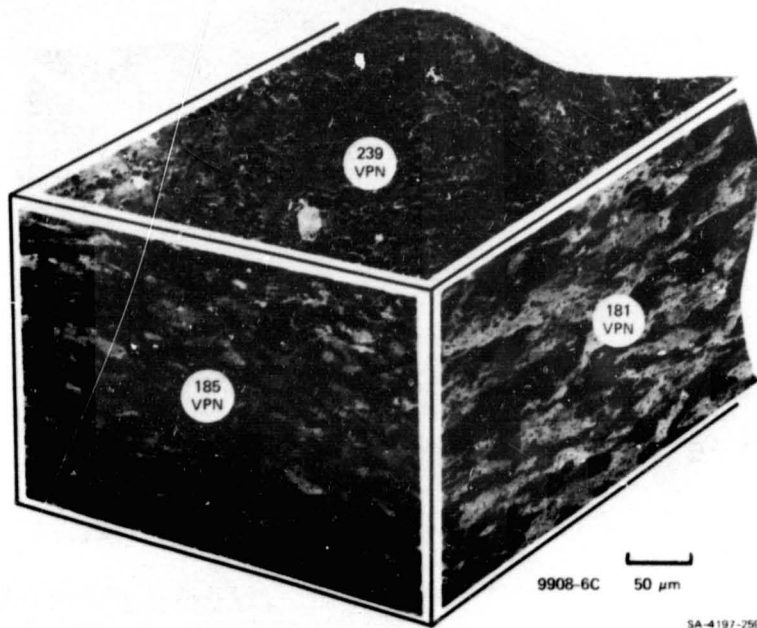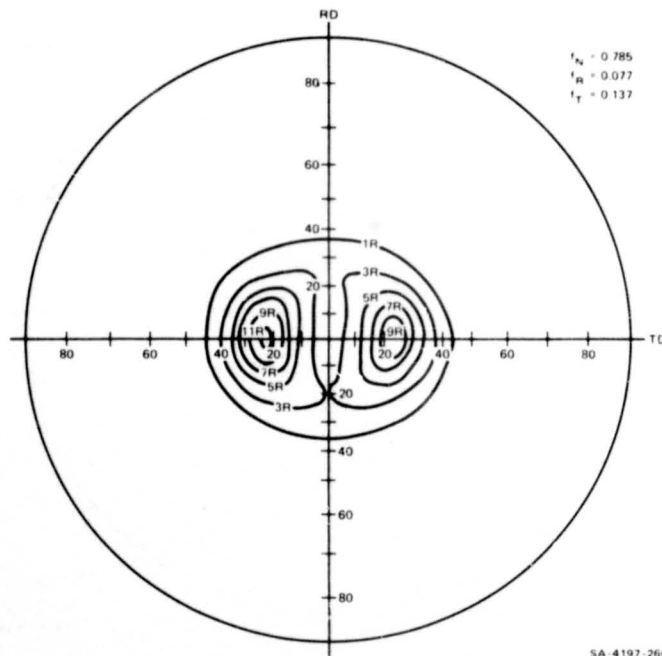
FIGURE A-15   MICROSTRUCTURE AND HARDNESS (a) AND BASAL POLE FIGURE (b)
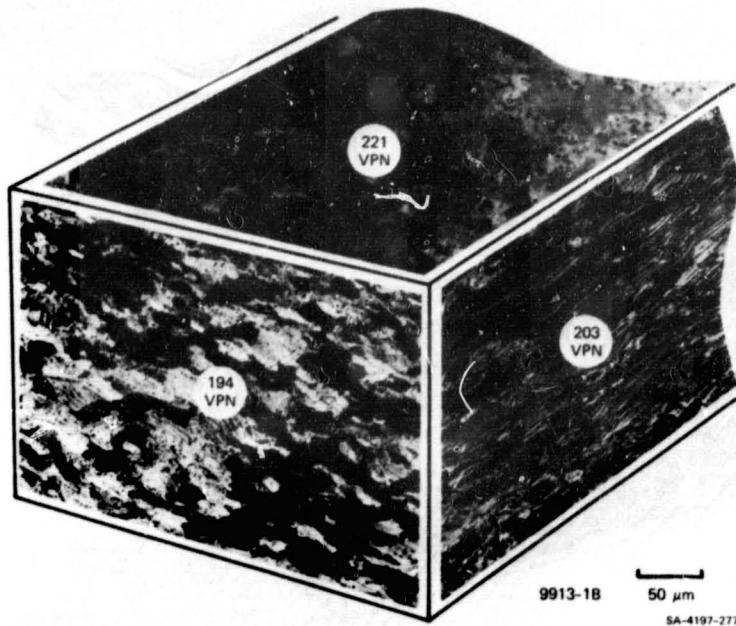FOR THE 9908-6C LOT OF ZIRCALOY-2 SHEET
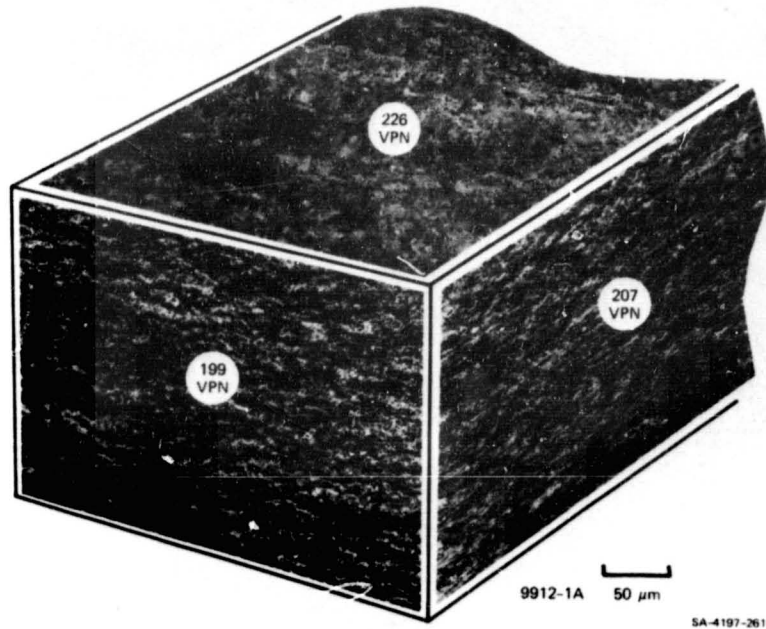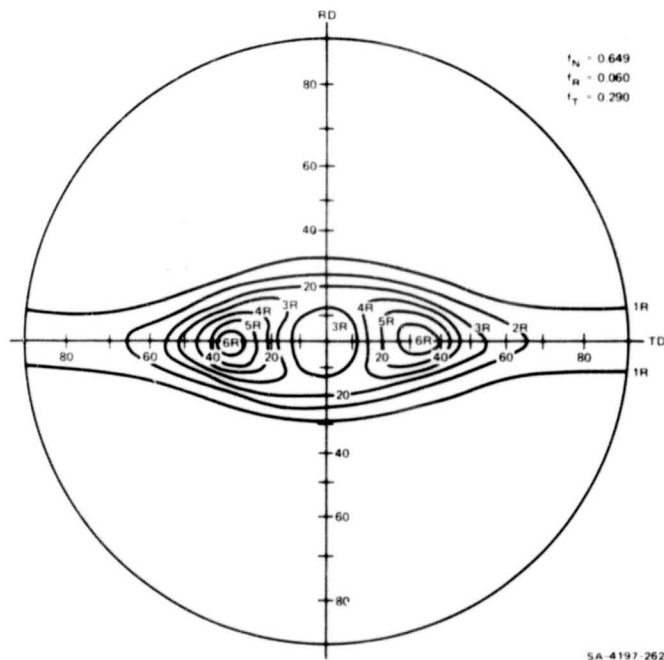
FIGURE A-16   MICROSTRUCTURE AND HARDNESS (a) AND BASAL POLE FIGURE (b)
FOR THE 9912-1A LOT OF ZIRCALOY-2 SHEET

(a)

(b)
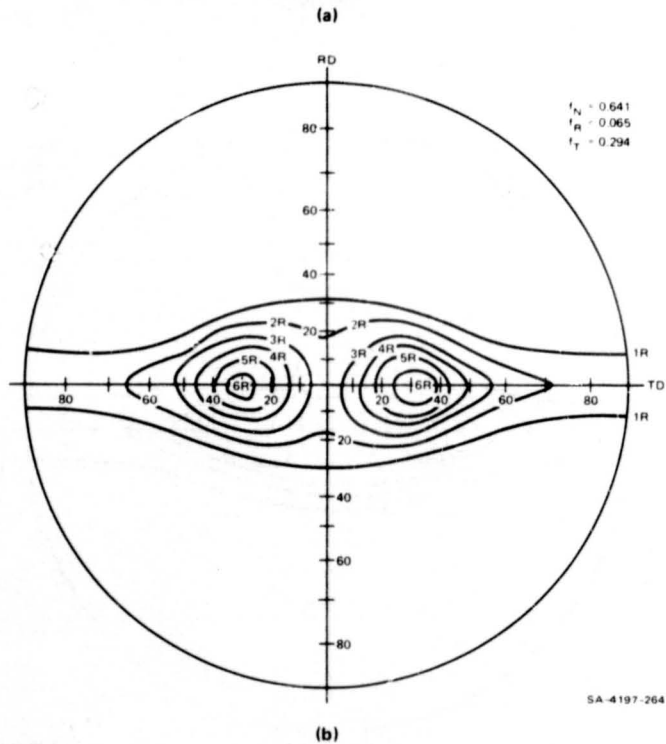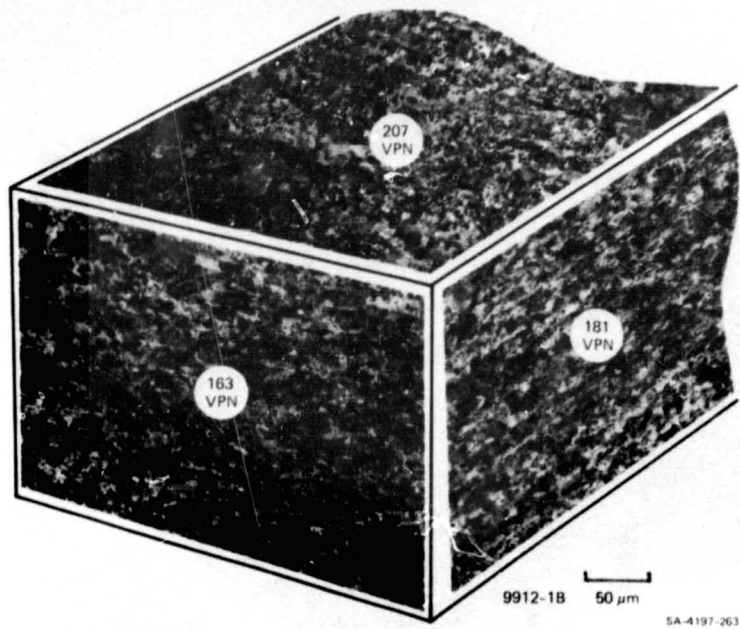
FIGURE A-17 MICROSTRUCTURE AND HARDNESS (a) AND BASAL POLE FIGURE (b)
FOR THE 9912-1B LOT OF ZIRCALOY-2 SHEET

(a)

(b)
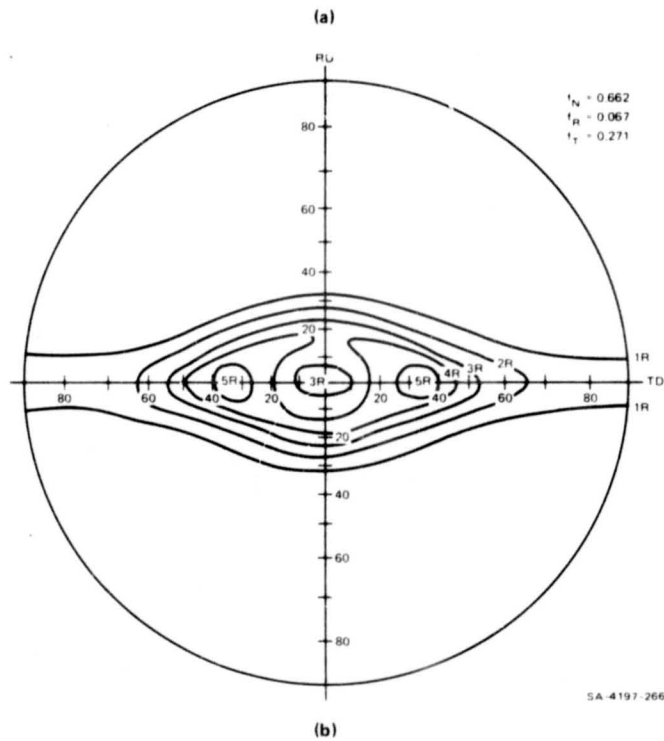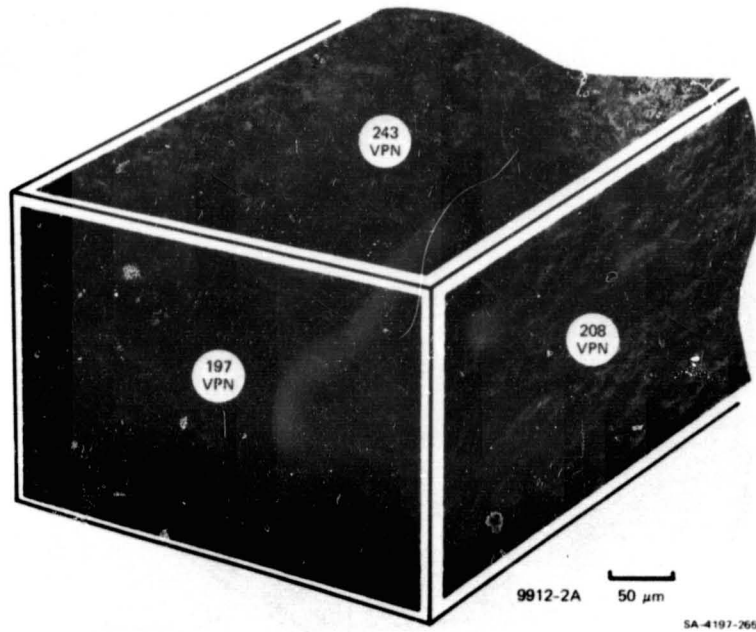
FIGURE A-18   MICROSTRUCTURE AND HARDNESS (a) AND BASAL POLE FIGURE (b)
FOR THE 9912-2A LOT OF ZIRCALOY-2 SHEET

(a)
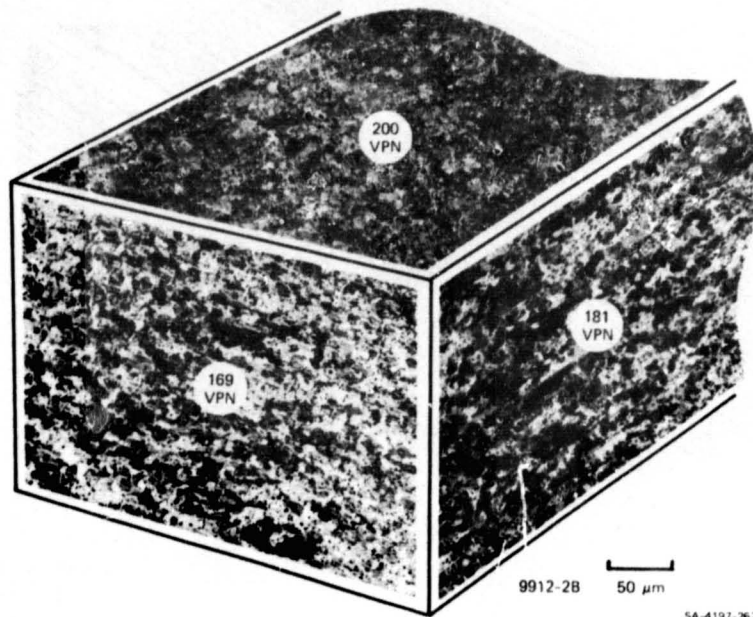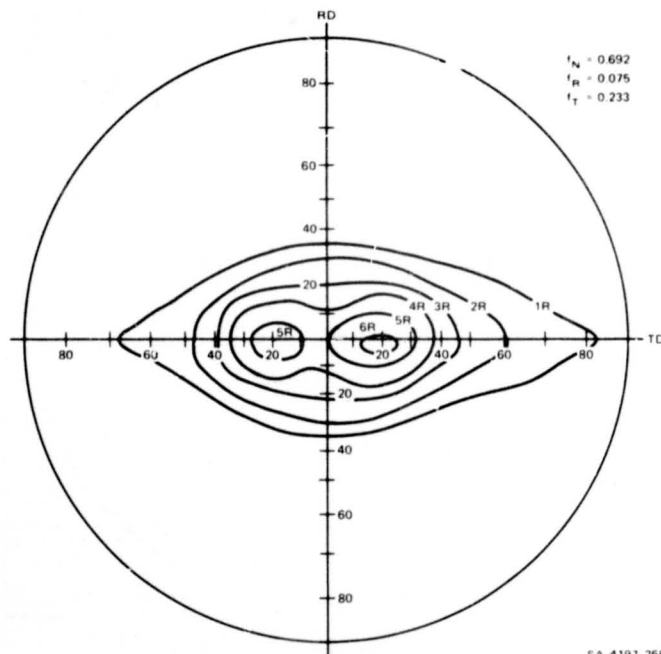
(b)

FIGURE A-19   MICROSTRUCTURE AND HARDNESS (a) AND BASAL POLE FIGURE (b)
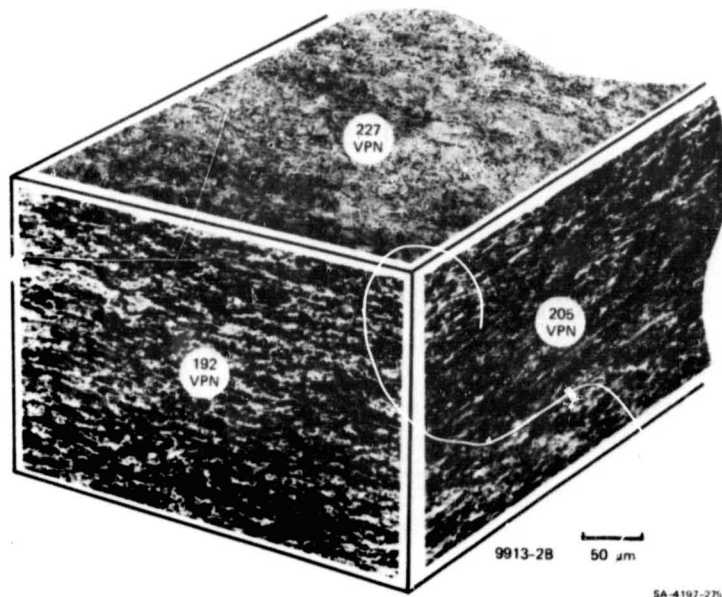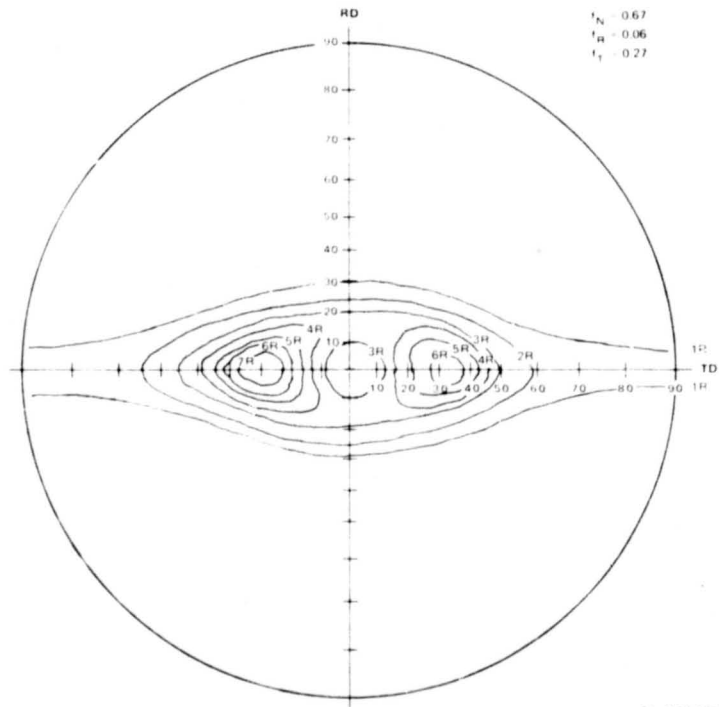FOR THE 9912-2B LOT OF ZIRCALOY-2 SHEET

(a)

(b)

FIGURE A-20   MICROSTRUCTURE AND HARDNESS (a) AND BASAL POLE FIGURE (b)
FOR THE 9912-3A LOT OF ZIRCALOY-2 SHEET

(a)

(b)

FIGURE A-21   MICROSTRUCTURE AND HARDNESS (a) AND BASAL POLE FIGURE (b)
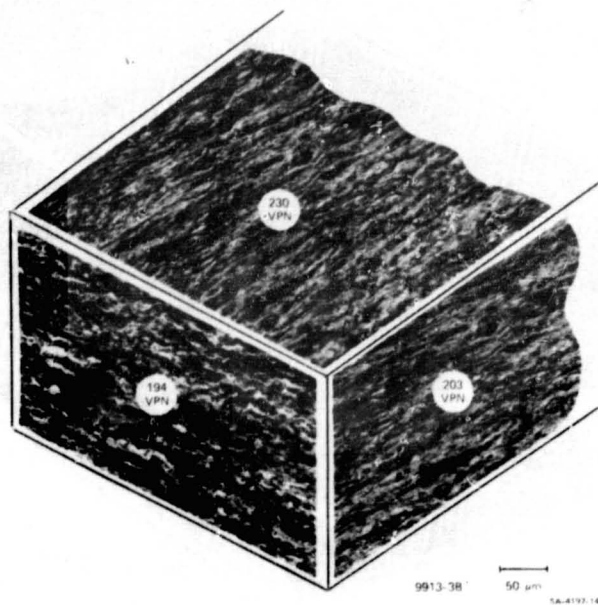FOR THE 9912-3B LOT OF ZIRCALOY-2 SHEET

(a)

(b)

FIGURE A-22   MICROSTRUCTURE AND HARDNESS (a) AND BASAL POLE FIGURE (b)
FOR THE 9912-4B LOT OF ZIRCALOY-4 PLATE

FIGURE A-23   MICROSTRUCTURE AND HARDNESS (a) AND BASAL POLE FIGURE (b)
FOR THE 9912-5B LOT OF ZIRCALOY-4 SHEET

(a)
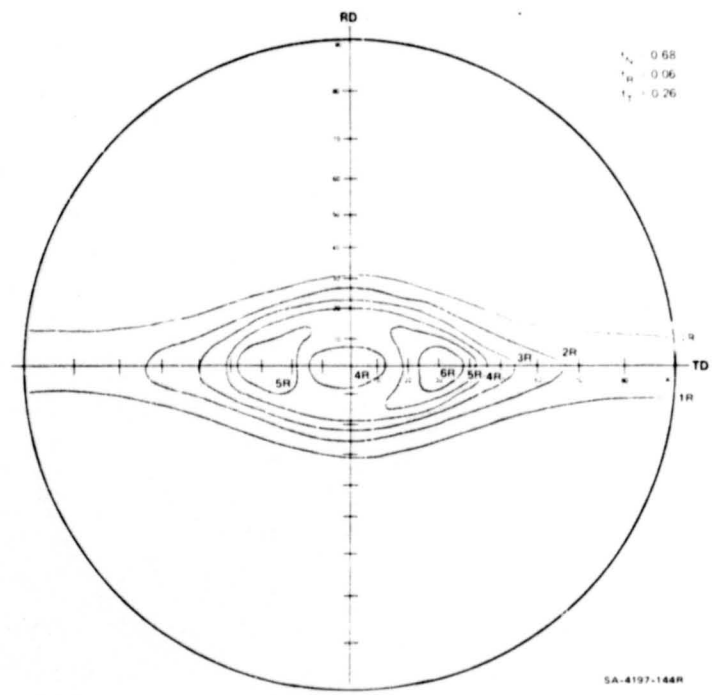

(b)

FIGURE A-24   MICROSTRUCTURE AND HARDNESS (a) AND BASAL POLE FIGURE (b)
FOR THE 9912-6B LOT OF ZIRCALOY-4 SHEET

(a)

(b)

FIGURE A-25   MICROSTRUCTURE AND HARDNESS (a) AND BASAL POLE FIGURE (b)
FOR THE 9913-1B LOT OF ZIRCALOY-4 SHEET

FIGURE A-26   MICROSTRUCTURE AND HARDNESS (a) AND BASAL POLE FIGURE (b)
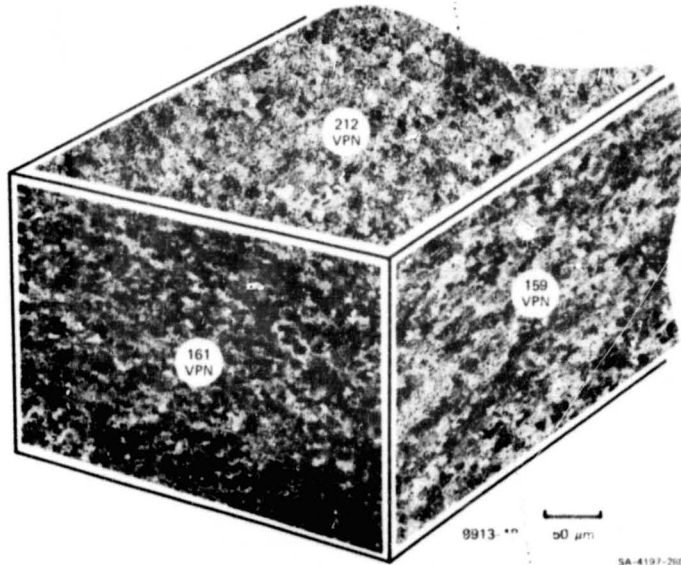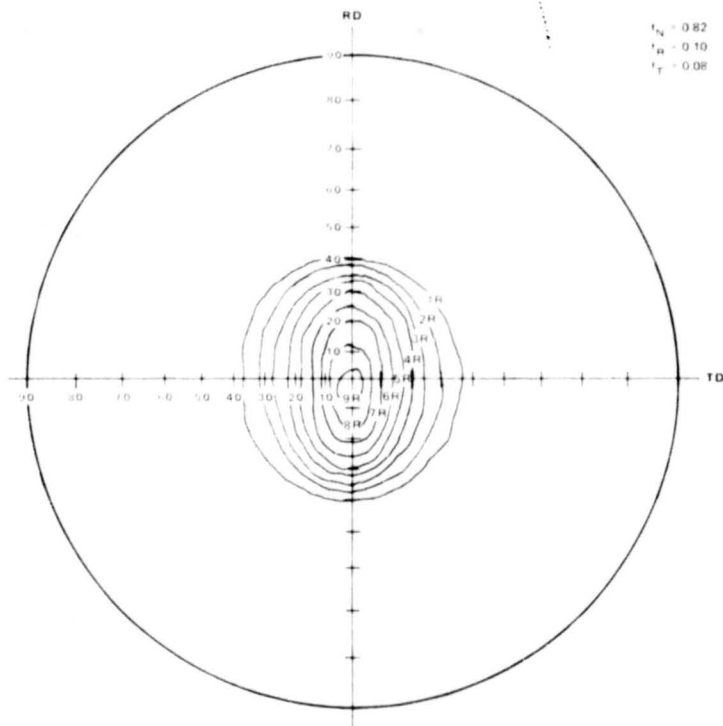FOR THE 9913-2B LOT OF ZIRCALOY-4 SHEET

(a)

(b)

FIGURE A-27   MICROSTRUCTURE AND HARDNESS (a) AND BASAL PULSE FIGURE (b)
FOR THE 9913-3B LOT OF ZIRCALOY-4 SHEET

(a)

(b)

FIGURE A-28   MICROSTRUCTURE AND HARDNESS (a) AND BASAL POLE FIGURE (b)
FOR THE 9913-4B LOT OF ZIRCALOY-4 SHEET

Appendix B

SCC OF STRESSED ZIRCALOY RINGS
EXPOSED TO IODINE

During his stay at MIT, Professor Shingo Namba of Osaka University conducted a study of iodine-induced stress corrosion cracking (SCC) in ring samples of Zircaloy. Short lengths (from 0.25 to 1.2 cm long) of 7FD11 Zircaloy-4 tubing (see Section 3 and Appendix A) were forced onto stainless steel or aluminum tapered mandrels that had been chilled to liquid nitrogen temperature. The sample was stressed by heating it and the mandrel to a temperature in the range 590 K to 750 K. Stressed samples were exposed to iodine vapor for various times from 40 to 200 hours and were periodically examined for cracking.

It proved to be very difficult to achieve iodine SCC by this technique. In all 122 samples were tested. Early experiments at a temperature of 590 K were unsuccessful; hence, the test conditions were made increasingly severe. A few cracks were finally obtained in specimens that had bee notched longitudinally, stressed with stainless steel mandrels, and heated to 750 K in an argon gas stream containing iodine at a pressure of 300 Pa ($\sim$ 2 torr). The tests were run on batches of seven samples. In one batch, two samples out of seven failed in 41 hours, and in another batch, five out of seven samples failed in 94 hours. The sporadic incidence of cracking may indicate that the susceptibility of the samples of tubing is variable.

After the tests, the samples were examined in a scanning electron microscope (SEM). The surfaces were found to be coated with a layer of corrosion product that contained patches of acicular crystals of FeI_2. In some areas of the outside surface of a sample that suffered SCC, there were cracked protuberances that seemed to have been formed by a reaction that caused localized swelling. An example is shown in Figure B-1. A sample of that material was cleaned of surface corrosion products
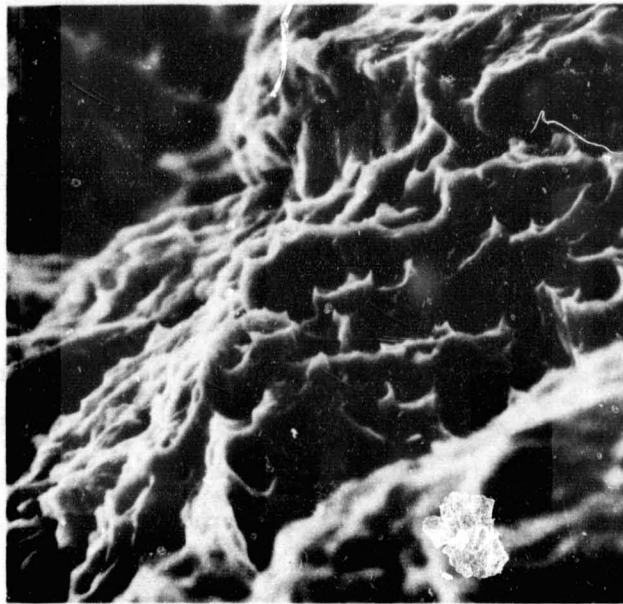
SA-4197-233

FIGURE B-1   SEM PHOTOGRAPH OF CRACKED PROTUBERANCES
FORMED ON ZIRCALOY-4 RING EXPOSED TO
IODINE (3000X)

by argon ion milling and the underlying metal was examined in the SEM. The locally raised regions were found to contain iron in concentrations as large as 20%. Apparently iron had been vapor transported from the stainless steel mandrel, probably as FeI_2, and had reacted with the Zircaloy surface in localized spots to form the iron-containing regions, which swelled because of the increase in volume due to the added Fe.

Two of the ring samples from one batch were studied in detail. One sample (N-1) did not have a visible crack; the other (N-3) had a hairline crack extending longitudinally from the root of the notch about halfway along the length. Sample N-1 (uncracked) was broken so that a longitudinal crack was formed extending the notch the entire length of the ring. The fractured surface of the ring was examined in the SEM. Most of the fracture surface showed features typical of ductile tearing, as seen in Figure B-2. However, scattered in the dimpled regions there were areas of flat cleavage, as shown in Figure B-3. The cleavage areas covered about a tenth of the total fracture surface. Analysis of the cleaved regions showed the presence of a few percent iron and iodine or tin and iodine. Cleaved regions were observed in the middle of the tubing wall with no obvious access to the surface of the metal and yet iodine and iron were present and presumably involved in the cleavage.

Sample N-3 was broken mechanically so that the hairline crack was extended longitudinally, and the resultant fracture surface was examined in the SEM. The fracture surfaces showed a combination of ductile dimples and cleavage as illustrated in Figure B-4. The area fraction of ductile fracture increased with distance along the crack from the root of the notch to the mechanically broken region. However, even in the region broken after the test, about half the fracture area consisted of cleavage. Analysis of the dimpled areas showed almost pure Zr with some Fe. The cleaved areas were rich in Fe, in some cases to the extent that Zr could not be detected.
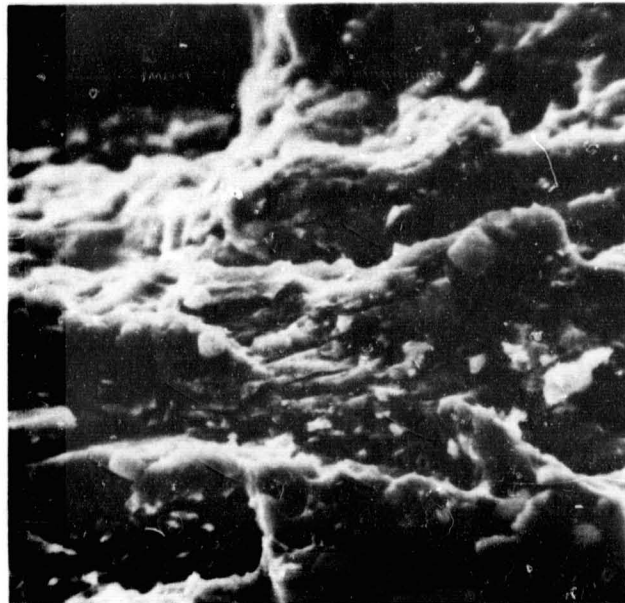
A piece of as-received tubing was broken mechanically and the fracture surface was examined in the SEM. Fracture was almost entirely ($\sim$ 99% by area) by ductile

SA-4197-283

FIGURE B-2   SEM PHOTOGRAPH OF THE DIMPLED FRACTURE SURFACE
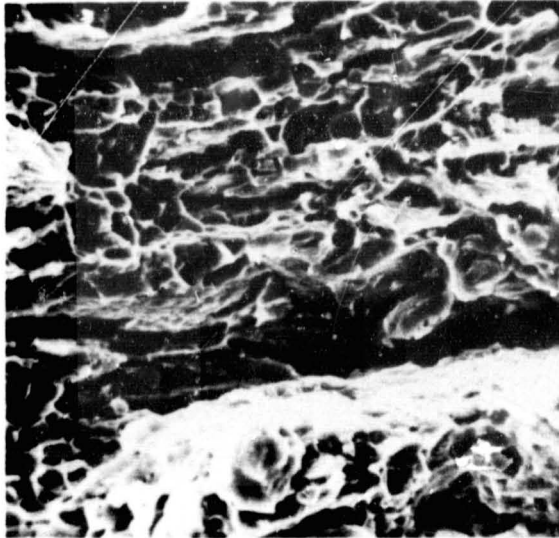OF RING SAMPLE N-1 (5000X)

Analysis showed no Fe and a trace of I.

SA-4197-284

FIGURE B-3   SEM PHOTOGRAPH OF CLEAVAGE FEATURES OCCASIONALLY
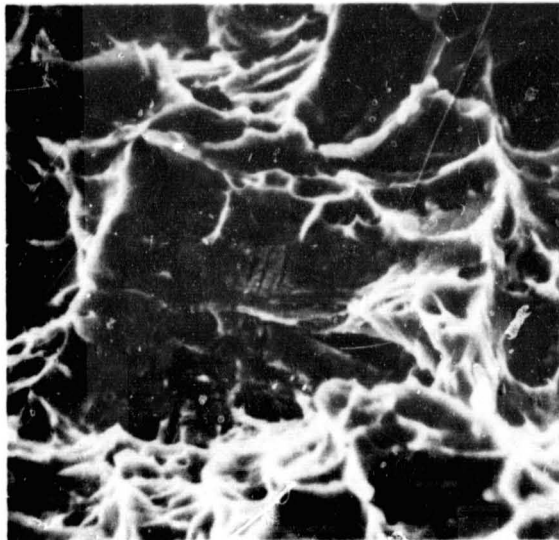PRESENT ON FRACTURE SUFACE OF SAMPLE N-1 (2000X)

Analysis of the center region showed a few percent of Fe and I.

SA-4197-285

FIGURE B-4   SEM PHOTOGRAPH OF THE FRACTURE SURFACE OF SAMPLE
N-3 (2000X)

Analysis of the flat regions just below the center of the photo showed all
Fe with a trace of Al (no Zr). The dimpled regions showed Zr with a few
percent Fe.

SA-4197-286

FIGURE B-5   SEM PHOTOGRAPH OF FEATURE FOUND IN FRACTURE SURFACE
OF AS-RECEIVED ZIRCALOY-4 TUBING (2000X)

Analysis showed only Zr.

processes. Occasionally a feature like the one in Figure B-5 was observed. Analysis of such features showed only Zr.

These stressed ring tests show that under the conditions of the tests, iron was transferred from the stainless steel mandrel to the Zircaloy by the iodine. In addition, Fe was found in the regions of the fracture that occurred by cleavage but was not found in the ductile regions. It seems likely that the iron contributed in some way to the occurrence of cleavage; however, it can also be argued that the iron was deposited on the freshly formed surfaces after cracking had occurred.